



HAL
open science

Number statistics and momentum correlations in interacting Bose gases

Jan-Philipp Bureik

► **To cite this version:**

Jan-Philipp Bureik. Number statistics and momentum correlations in interacting Bose gases. Optics [physics.optics]. Université Paris-Saclay, 2024. English. NNT : 2024UPASP014 . tel-04552932

HAL Id: tel-04552932

<https://pastel.hal.science/tel-04552932>

Submitted on 19 Apr 2024

HAL is a multi-disciplinary open access archive for the deposit and dissemination of scientific research documents, whether they are published or not. The documents may come from teaching and research institutions in France or abroad, or from public or private research centers.

L'archive ouverte pluridisciplinaire **HAL**, est destinée au dépôt et à la diffusion de documents scientifiques de niveau recherche, publiés ou non, émanant des établissements d'enseignement et de recherche français ou étrangers, des laboratoires publics ou privés.

Number Statistics and Momentum
Correlations in Interacting Bose Gases
*Statistiques du nombre et corrélations en impulsion
dans des gaz de Bose interagissants*

Thèse de doctorat de l'université Paris-Saclay

École doctorale n° 527 Ondes et Matière
Spécialité de doctorat : Physique
Graduate School : Physique, Référent : Institut d'Optique Graduate School

Thèse préparée dans l'unité de recherche **LCF (Université Paris-Saclay, Institut d'Optique Graduate School, CNRS)**, sous la direction de **David CLÉMENT**, Maître de conférence.

Thèse soutenue à Paris-Saclay, le 26 février 2024, par

Jan-Philipp BUREIK

Composition du jury

Membres du jury avec voix délibérative

Ariel LEVENSON

Directeur de recherche, Université Paris-Saclay

Jan ARLT

Professeur, Aarhus University

William GUERIN

Chargé de recherche, Université Côte d'Azur

Anna MINGUZZI

Directrice de recherche, Université Grenoble Alpes

Président & Examineur

Rapporteur & Examineur

Rapporteur & Examineur

Examinatrice

Membres du jury sans voix délibérative

David CLÉMENT

Maître de conférence, Université Paris-Saclay

Directeur de thèse

Titre : Statistiques du nombre et corrélations en impulsion dans des gaz de Bose interagissants
Mots clés : Statistique du nombre, Corrélations en impulsion, Physique à N corps, Réseau optique, Gaz quantiques, Détection d'atomes uniques

Résumé :

Ce travail de thèse est dédié à l'étude des statistiques du nombre et corrélations en impulsion dans des gaz de Bose sur réseaux interagissants. Le modèle de Bose-Hubbard est simulé en chargeant des condensats de Bose-Einstein (BEC) d'atomes d'Hélium-4 métastables dans un réseau optique tridimensionnel (3D). Ce modèle présente une transition de phase quantique d'un superfluide à un isolant de Mott induite par des fluctuations quantiques provoquées par l'interaction. L'objectif de ce travail est de comprendre le rôle de ces fluctuations quantiques en analysant leurs signatures dans l'espace des impulsions. Le schéma de détection original utilisé à cette fin fournit la distribution d'impulsion résolue à l'échelle de l'atome unique en 3D. À partir de ces jeux de données composés de milliers d'atomes individuels, les statistiques du nombre d'occupation de différents sous-volumes de l'espace des impulsions fournissent des informations sur les propriétés de corrélation ou de cohérence du gaz de Bose interagissant. À impulsions proches, ces probabilités d'occupation permettent l'identification de statistiques d'état

pur sous-jacentes dans le cas d'états many-body classiques tels que les superfluides en réseau et les isolants de Mott. Dans le régime faiblement interagissant, des corrélations bien établies entre les paires d'atomes à impulsions opposées sont observées. De plus, on constate que ces corrélations entre paires diminuent en faveur de corrélations plus complexes entre plus de deux particules lorsque les interactions sont augmentées. Une observation directe de corrélations non-Gaussiennes encapsule la nature statistique complexe des superfluides fortement interagissants bien en amont de la transition de phase vers l'isolant de Mott. Enfin, lors de la transition de phase, on constate une augmentation des fluctuations du nombre d'occupation du mode du BEC, constituant une signature directe des fluctuations quantiques induisant la transition. Des quantités indépendantes de la taille du système, telles que le cumulatif de Binder, présentent des variations abruptes même dans un système de taille finie et semblent prometteuses pour constituer des observables appropriés permettant de déterminer le comportement universel lorsqu'elles sont mesurées dans un système homogène.

Title : Number statistics and momentum correlations in interacting Bose gases
Keywords : Number statistics, Momentum correlations, Many-body physics, Optical lattice, Quantum gases, Single-atom detection

Abstract :

This thesis work is dedicated to the study of number statistics and momentum correlations in interacting lattice Bose gases. The Bose-Hubbard model is simulated by loading Bose-Einstein condensates (BECs) of metastable Helium-4 atoms into a three-dimensional (3D) optical lattice. This model exhibits a quantum phase transition from a superfluid to a Mott insulator that is driven by interaction-induced quantum fluctuations. The objective of this work is to comprehend the role of these quantum fluctuations by analyzing their signatures in momentum space. The original detection scheme employed towards this aim provides the single-particle resolved momentum distribution of the atoms in 3D. From such datasets made up of thousands of individual atoms, the number statistics of occupation of different sub-volumes of momentum space yield information about correlation or coherence properties of the interacting Bose gas. At close-by momenta these occupation probabilities permit the identification of underlying pure-state

statistics in the case of textbook many-body states such as lattice superfluids and Mott insulators. In the weakly-interacting regime, well-established correlations between pairs of atoms at opposite momenta are observed. Furthermore, these pair correlations are found to decrease in favor of more intricate correlations between more than two particles as interactions are increased. A direct observation of non-Gaussian correlations encapsulates the complex statistical nature of strongly-interacting superfluids well before the Mott insulator phase transition. Finally, at the phase transition, fluctuations of the occupation number of the BEC mode are found to be enhanced, constituting a direct signature of the quantum fluctuations driving the transition. System-size independent quantities such as the Binder cumulant are shown to exhibit distinctive sharp features even in a finite-size system, and hold promise for constituting suitable observables for determining universal behavior when measured in a homogeneous system.

Acknowledgments

Completing this PhD thesis would not have been possible without the incredible support and guidance I received from countless individuals. Their encouragement and insights played a crucial role in shaping this work, and I want to express my sincere appreciation to all who contributed to this endeavor.

First and foremost, I am profoundly grateful to my supervisor, David Clément, for accepting me as a member of the Helium Lattice team. I am thankful for your unwavering support and encouragement throughout both the joyful and the challenging phases of my thesis. Your enthusiasm for the physics we do in the lab has been a significant source of motivation for me over these years. In choosing my thesis project, working with people whom I genuinely liked and who made each day enjoyable was equally as important to me as any academic success, and I have never regretted joining your team. Your leadership style of holding all team members to high standards while maintaining a positive atmosphere brings out the best in everyone and makes our work enjoyable. In addition to your inexhaustible knowledge in experimental physics, I am grateful for the invaluable lessons you have taught me in presenting and communicating our research results. These skills will undoubtedly benefit me in all future endeavors.

This work was carried out at the Laboratoire Charles Fabry (LCF), where I am grateful to director Patrick Georges for welcoming me, as well as for his dedicated efforts in fostering a friendly atmosphere and personally engaging with and supporting each of the PhD students. I extend equal thanks to Chris Westbrook for welcoming me to the quantum gases group. Additionally, I am thankful to Jan Arlt and William Guérin for agreeing to serve as referees for my thesis, and to Anna Minguzzi and Ariel Levenson for their contributions as members of my thesis committee.

Experiments with ultracold atoms are complex machines that rarely can be operated by a single individual. When issues arise, troubleshooting can be complicated, tiresome, and time-consuming. In such circumstances, having the right colleagues is invaluable.

I would like to express my deep gratitude to the other members of the Helium Lattice team

with whom I have had the privilege of spending the past three years. First and foremost, a big thank you to Antoine and Gaétan, with whom I formed the HBT team (Hercé-Bureik-Tenart) upon beginning my PhD. Working alongside you in the lab has been an absolute pleasure, and I will forever cherish the memories of the countless hours spent aligning optical lattices, debugging the experimental sequence, and moving the experiment to the new lab room.

I would also like to thank the new generation of PhD students, Maxime and Géraud, who have swiftly taken over the experiment and will undoubtedly advance it to new heights with the inclusion of the fermionic isotope. I couldn't have asked for better co-workers during my PhD journey than all of you.

My thanks also extend to the post-docs with whom I had the pleasure of collaborating during my thesis, Alexandre and Raphaël, as well as our recurring theory collaborator, Tommaso Roscilde. I am equally grateful to all the members of the quantum gases and quantum optics groups for creating an enjoyable work atmosphere in the basement and hallways of the LCF. In the same spirit, I would like to express my appreciation to the members of the LEnsE (Fabienne, Julien, Cedric, and Thierry) for their support during my teaching activities at Institut d'Optique.

Reflecting upon my journey in physics, I am grateful to acknowledge former teachers and mentors who have significantly contributed to fostering my interest and knowledge in this field. I extend my sincere thanks to Christian Casimir, Henning Moritz, Christoph Becker, Klaus Sengstock, Ian Spielman, and Jakob Reichel.

The challenges and demands of a PhD would be difficult to endure without some form of external support or compensation.

Merci beaucoup à mes amis parisiens: Jun, Laure, Thomas, Guillaume, Britton, Sylvain, Clarisse, Hadriel, Mélissa et Tom. Vielen Dank an die Freunde aus alten Hamburger Zeiten: René, Felix und Leon. Thanks to Paco, Anna, and Alina for some great memories in the land of the free.

And finally, I am endlessly grateful to my family for their unwavering support throughout all stages of my life. Ohne Eure Unterstützung wäre ich nie soweit gekommen. Vielen Dank für alles, Paps, Maman, Juli, Nicki, Karin, Oma, meine Opas, Bernd, Damian, Oliver, Frédo, Josiane, Alex, Flo, Ju und Pascal.

Résumé

Ce travail de thèse est dédié à l'étude des statistiques du nombre et corrélations en impulsion dans des gaz de Bose sur réseaux interagissants. Le modèle de Bose-Hubbard est simulé en chargeant des condensats de Bose-Einstein (BEC) d'atomes d'Hélium-4 métastables dans un réseau optique tridimensionnel (3D). Ce modèle présente une transition de phase quantique d'un superfluide à un isolant de Mott induite par des fluctuations quantiques provoquées par l'interaction. L'objectif de ce travail est de comprendre le rôle de ces fluctuations quantiques en analysant leurs signatures dans l'espace des impulsions. Le schéma de détection original utilisé à cette fin fournit la distribution d'impulsion résolue à l'échelle de l'atome unique en 3D. À partir de ces jeux de données composés de milliers d'atomes individuels, les statistiques du nombre d'occupation de différents sous-volumes de l'espace des impulsions fournissent des informations sur les propriétés de corrélation ou de cohérence du gaz de Bose interagissant. À impulsions proches, ces probabilités d'occupation permettent l'identification de statistiques d'état pur sous-jacentes dans le cas d'états many-body classiques tels que les superfluides en réseau et les isolants de Mott. Dans le régime faiblement interagissant, des corrélations bien établies entre les paires d'atomes à impulsions opposées sont observées. De plus, on constate que ces corrélations entre paires diminuent en faveur de corrélations plus complexes entre plus de deux particules lorsque les interactions sont augmentées. Une observation directe de corrélations non-Gaussiennes encapsule la nature statistique complexe des superfluides fortement interagissants bien en amont de la transition de phase vers l'isolant de Mott. Enfin, lors de la transition de phase, on constate une augmentation des fluctuations du nombre d'occupation du mode du BEC, constituant une signature directe des fluctuations quantiques induisant la transition. Des quantités indépendantes de la taille du système, telles que le cumulants de Binder, présentent des variations abruptes même dans un système de taille finie et semblent prometteuses pour constituer des observables appropriés permettant de déterminer le comportement universel lorsqu'elles sont mesurées dans un système homogène.

Avec l'avènement de la mécanique quantique au début du 20^e siècle, les physiciens en sont

venus à considérer la lumière et la matière sur un pied d'égalité. De Broglie a énoncé pour la première fois le concept de dualité onde-particule en 1924 [1]. Après que Bose a dérivé la distribution de Planck pour les photons sur la base de l'hypothèse des quanta de lumière [2], Einstein a utilisé son résultat pour dériver une théorie quantique du gaz de Bose idéal, prédisant une condensation des atomes dans l'état fondamental en dessous d'une température critique [3]. Il a fallu presque tout le reste du siècle pour que la technologie laser et les techniques de refroidissement [4-6] progressent suffisamment pour permettre les premières réalisations expérimentales de la condensation de Bose-Einstein [7, 8]. Depuis, les expériences sur les gaz quantiques ont progressé et sont maintenant régulièrement capables d'atteindre la dégénérescence quantique, un régime caractérisé par une longueur d'onde de Broglie λ_{dB} des atomes de l'ordre de la distance interparticulaire moyenne, $n\lambda_{dB}^3 \sim 1$, avec n la densité du gaz et λ_{dB} croissant inversement avec la température et la masse de la particule. Dans une telle situation, le caractère ondulatoire des particules massives devient crucial et les effets de la mécanique quantique dominant. Ces expériences ont ouvert la voie au domaine de la simulation quantique.

Simulation quantique

Les systèmes présents dans la nature sont généralement constitués d'un grand nombre de particules en interaction et sont souvent caractérisés par des phénomènes complexes qui résultent de l'interaction complexe de ces interactions entre leurs composants. Étant donné la faible masse de l'électron, les systèmes de matière condensée ont tendance à entrer dans cette catégorie, car leur densité de particules peut être suffisamment élevée pour atteindre la dégénérescence quantique, même à température ambiante. Les systèmes d'électrons fortement corrélés dans la matière condensée présentent des phénomènes émergents tels que la supraconductivité [9] ou la physique de Hall quantique [10]. Les grands ensembles de nombreux corps sont notoirement difficiles à décrire exactement, car la taille de l'espace de Hilbert associé croît de façon exponentielle avec le nombre de degrés de liberté, ce qui met souvent le calcul de la fonction d'onde de nombreux corps hors de portée des ordinateurs classiques. Les approches de champ moyen qui remplacent l'effet des interactions particule-particule par un effet d'interaction moyen offrent un équilibre entre la précision et la faisabilité informatique, mais sont incapables de capturer les corrélations et fluctuations quantiques complexes [11-13].

Une solution possible à ce problème remonte à une suggestion de Feynman [14], qui a proposé d'utiliser un système quantique sous contrôle presque parfait pour imiter et simuler le comportement d'un second système quantique intéressant. Dans ces situations, les expériences peuvent montrer la voie et simuler des problèmes quantiques trop complexes pour être résolus numériquement [15]. Grâce au contrôle précis des paramètres microscopiques tels que le paysage énergétique ou les interactions dans le système, ainsi qu'à la capacité de mesurer de nombreuses observables d'intérêt, la boîte à outils que représentent les ensembles d'atomes ultrafroids s'est avérée constituer un banc d'essai bien adapté pour cartographier des hamiltoniens complexes [16].

Interactions et transitions de phase quantiques

Malgré la percée dans le domaine des atomes ultrafroids qui a été réalisée par la mise au point des premiers condensats de Bose-Einstein (BEC), ces systèmes peuvent difficilement être considérés comme des "nombreux corps" du point de vue de la mécanique quantique, puisque presque tous les atomes se trouvent dans le même état quantique décrit par une fonction d'onde macroscopique. La possibilité de simuler des transitions de phase quantiques avec des ensembles d'atomes ultrafroids permet l'étude expérimentale d'assemblages d'atomes qui sont véritablement "à plusieurs corps", dans le sens où, malgré l'hypothèse réductionniste de pouvoir tout ramener à des lois fondamentales, l'inverse ne s'applique pas : Ces systèmes sont caractérisés par des phénomènes émergents qui résultent uniquement de l'interaction de grands ensembles de particules en interaction qui ne peuvent être décrits sur la base des lois fondamentales pour les seuls constituants individuels. Dans les systèmes où les interactions entre les particules dominent leurs énergies cinétiques individuelles, l'interaction entre les particules peut devenir si dominante que des états quantiques fortement corrélés émergent.

L'un des hamiltoniens les plus simples d'un point de vue conceptuel, mais qui contient néanmoins des caractéristiques complexes de nombreux corps quantiques, est l'hamiltonien de Bose-Hubbard, qui décrit des particules dans un paysage potentiel périodique avec deux échelles d'énergie concurrentes : Le couplage tunnel J entre les sites adjacents, et l'interaction sur site U

de deux particules partageant le même site. Le système subit une transition de phase quantique d'un superfluide à un isolant de Mott à une valeur critique de U/J qui a été observée expérimentalement dans l'une des premières mises en œuvre réussies de la simulation quantique [17] après sa proposition [18], en utilisant des treillis optiques pour simuler le paysage potentiel périodique [19]. La transition de phase de l'isolant de Mott est induite par des interactions et des fluctuations quantiques, et constitue donc un type de transition de phase fondamentalement différent de celles induites par un paramètre thermodynamique externe et des fluctuations de température.

Fluctuations quantiques et corrélations de nombreux corps dans l'espace des quantités de mouvement

Les corrélations dans les systèmes à plusieurs corps sont généralement le résultat de la non-commutabilité des parties de l'hamiltonien, par exemple la partie d'interaction qui ne commute pas avec la partie de non-interaction. Elles s'accompagnent de fluctuations quantiques lorsque la partie du hamiltonien qui interagit ne commute pas avec la partie qui n'interagit pas, ce qui entraîne une compétition entre les deux échelles d'énergie associées qui peut induire une transition de phase quantique, c'est-à-dire une transition dans l'état fondamental du système à plusieurs corps qui n'est pas déterminée par la température. Dans le cas du modèle de Bose-Hubbard, cette transition sépare un état fondamental conducteur d'un état fondamental isolant. Il est donc naturel d'examiner cette transition de phase dans l'espace des quantités de mouvement. Dans les expériences, on peut y parvenir en désactivant le piège qui maintient le système en place et en le laissant tomber sous l'effet de la gravité pendant un temps suffisamment long. Les particules ayant une vitesse initiale élevée seront plus éloignées du centre après la chute libre, ce qui permet d'établir une correspondance entre la position après l'expansion et la distribution de la quantité de mouvement dans le piège [17, 20, 21].

Les corrélations peuvent coder une multitude d'informations sur l'état du système. Dans certaines circonstances, elles peuvent même présenter des statistiques similaires à celles des états purs, ce qui n'est pas évident dans une expérience réelle. L'émergence de corrélations à partir de l'interaction des interactions et de l'énergie cinétique est l'un des aspects centraux de l'in-

térêt et de l'étude de l'expérience sur le treillis d'hélium au LCF. Dans le cas de la physique de Bose-Hubbard, le régime d'interaction faible est caractérisé par des corrélations de paires entre atomes à des moments opposés [22, 23]. L'augmentation des interactions au-delà du domaine des fluctuations quantiques linéarisées devrait produire des corrélations plus complexes, car les paires corrélées sont brisées dans des processus d'interaction d'ordre supérieur. L'augmentation continue des interactions permet de réaliser la transition de phase d'un superfluide à un isolant de Mott. Dans le régime critique quantique, on s'attend à des fluctuations accrues résultant des fluctuations quantiques à l'origine de la transition. L'étude de ces sujets est au cœur des travaux de recherche présentés dans ce manuscrit.

Statistiques numériques et détection d'atomes uniques en trois dimensions

Les plateformes d'atomes froids ont mis en œuvre avec succès une variété de techniques d'imagerie destructives et non destructives. Les microscopes à gaz quantique résolus en un seul site sont capables de détecter des particules uniques dans des dimensions inférieures à trois [24–27]. En trois dimensions (3D), cependant, les expériences reposant sur l'interaction des atomes avec la lumière pour sonder les atomes sont soumises à l'intégration de la ligne de visée des caméras et nécessitent généralement de nombreux photons par atome pour atteindre une force de signal suffisante. Pour évaluer les signaux de corrélation à corps multiples entre plusieurs particules, il est nécessaire d'observer la dynamique de chaque composant individuel au sein du système [28–30], ce qui implique en principe une mesure de la distribution complète des particules dans le degré de liberté considéré. Cela constitue un formidable défi dans le cas des systèmes 3D, où la détection d'une seule particule n'est pas réalisable par des moyens optiques.

Pour contourner ce problème, cette expérience utilise de l'hélium métastable comme espèce atomique, ce qui permet une détection électronique dans le champ lointain puisque son énergie interne est suffisante pour qu'un seul atome arrache un électron d'une plaque métallique; une technologie développée à l'Institut d'Optique au début du millénaire [31]. Avec une efficacité quantique du détecteur de $\eta = 53(2)\%$, la précision des mesures du nombre d'atomes dans l'espace des quantités de mouvement est suffisante pour que la densité moyenne des quantités de mouvement s'étende sur quatre ordres de grandeur en amplitude. Elle permet également d'ac-

céder à la distribution d'occupation complète dans l'espace des quantités de mouvement pour les grands systèmes de $10^3 - 10^5$ atomes, ce qui permet d'analyser les moments d'ordre supérieur au-delà de la moyenne et de la variance et constitue un atout inestimable dans l'analyse des corrélations quantiques à partir des statistiques de nombre de l'état préparé.

Ce manuscrit est divisé en quatre chapitres : Le chapitre 2 présente le dispositif expérimental. Les séquences de refroidissement et de piégeage sont décrites et conduisent à la production de BECs avec des temps de cycle aussi bas que quatre secondes. La configuration du réseau optique et le schéma de détection électronique sont détaillés, ainsi que le système de surveillance du laboratoire récemment mis en place qui a permis une surveillance continue de l'équipement expérimental critique et des conditions de la salle de laboratoire à partir de n'importe quel endroit. Les trois chapitres suivants sont consacrés aux résultats expérimentaux obtenus dans le cadre de l'expérience sur le réseau d'hélium : Dans le chapitre 3, le sort du signal de corrélation de paires de Bogoliubov [22] qui caractérise le régime d'interaction faible des gaz de Bose [23] est examiné dans le contexte d'interactions plus fortes. Il s'avère que le signal d'appariement est supprimé avec l'augmentation des interactions en faveur de corrélations plus complexes entre plus de deux particules, signalant le début du régime fortement corrélé. Une observation directe d'un cumulatif de quatre opérateurs non nul lors d'interactions fortes est présentée, constituant une signature directe de corrélations non gaussiennes [32]. Le chapitre 4 présente une analyse des statistiques de comptage complet des gaz de treillis en interaction préparés dans l'expérience. Les états quantiques à grand nombre de corps emblématiques tels que les BEC de réseau et les isolants de Mott sont caractérisés par leurs propriétés de cohérence à grand nombre de corps lorsqu'ils sont sondés dans de petits volumes de l'espace des quantités de mouvement après une expansion. Le rôle de l'appauvrissement du condensat est mis en évidence dans les petites déviations des statistiques de Poisson pour les BEC à partir des corrélations normalisées à distance nulle jusqu'au sixième ordre. Enfin, le chapitre 5 présente une analyse des fluctuations des paramètres d'ordre du condensat mesurées à travers la transition de phase de l'isolant de Mott. Ces fluctuations, mesurées via le nombre d'occupation du condensat, sont renforcées vers la transition de phase, présentant un pic d'amplitude $\Delta N_0 \sim \sqrt{\langle N \rangle}$ incompatible avec le bruit expérimental modélisé, reflétant les observations faites dans le contexte de la transition

de condensation du gaz normal [33,34]. En outre, le cumulatif de Binder est extrait pour sonder les propriétés statistiques du paramètre d'ordre BEC et il s'avère qu'il présente une forte variation à la transition de phase, ce qui ouvre la voie à l'analyse de la mise à l'échelle de la taille finie dans les systèmes homogènes. Les annexes contiennent des informations supplémentaires sur les thèmes de la statistique et de la programmation.

Contents

1	Introduction	17
2	The Helium Lattice Experiment	23
2.1	Bose-Einstein Condensation of Metastable Helium	26
2.1.1	Metastable Helium Source	27
2.1.2	Cooling and Trapping He^4	29
2.1.3	Imaging techniques	37
2.2	Helium in Optical Lattices	38
2.2.1	The Bose-Hubbard model	39
2.2.2	The Harmonic Trapping Potential	46
2.2.3	Lattice alignment and calibration	49
2.2.4	Finite temperature effect	50
2.2.5	Time-of-flight dynamics	53
2.3	Individual atom detection in 3D	55
2.3.1	Raman transfer	56
2.3.2	Description of the Detector	57
2.3.3	Automating the data pipeline for large quantities of data	61
2.4	Expmonitor: A Python library for the lab room	63
2.4.1	System setup	63
2.4.2	Surveillance of lab equipment	65
2.4.3	Automatic alerts	67
3	Bogoliubov Pairing and Non-Gaussian Correlations	69
3.1	Description of the weakly-interacting Bose gas	71
3.1.1	Bogoliubov approximation	71
3.1.2	Many-body ground state	73
3.1.3	The excitation spectrum	75

3.2	Normalized two-body correlation functions	78
3.2.1	Initial observation of anomalous two-body correlations	80
3.2.2	Evolution of normalized two-body correlations with interactions	82
3.3	Suppression of Bogoliubov pairing and non-Gaussian correlations	86
3.3.1	Connected correlation functions	87
3.3.2	Extracting two-body connected correlations from momentum distributions	90
3.3.3	Two-body connected correlations at opposite momenta	92
3.3.4	Experimental signature of non-zero four-particle correlators	94
3.4	Comparison with numerical simulations	95
3.4.1	QMC simulations on the 3D quantum rotor model	96
3.4.2	Comparison between theory and experiment	96
3.4.3	Three-mode connected correlations	98
3.5	Conclusion	100
4	Full-Counting Statistics and High-Order Correlations	101
4.1	FCS approach for identifying quantum states in the experiment	102
4.1.1	FCS for ideal BECs and Mott insulators	103
4.1.2	Measurement volume for pure state FCS	105
4.2	FCS of Mott Insulators	107
4.2.1	Multimode thermal FCS in large measurement volumes	108
4.3	FCS of weakly interacting BECs	110
4.3.1	Deviation of condensate FCS from Poissonian statistics	111
4.4	Many-Body Coherence of BECs and Mott Insulators	112
4.4.1	Normalized correlation functions	113
4.4.2	Measurement volume for fully contrasted correlation functions	116
4.4.3	High-order correlation functions of BECs and Mott insulators	119
4.4.4	Establishing the limit of the experimental statistics	124
4.5	Deviation from Coherent Statistics in Correlations of Lattice BECs	125
4.5.1	The incoherent statistical properties of the depletion	126
4.5.2	Increasing the incoherent contribution via interactions	129
4.5.3	Modeling the role of condensate depletion in many-body coherence	130

<i>CONTENTS</i>	15
4.5.4 Establishing the predictive capacities of the model	133
4.5.5 Extrapolating depletion densities below the BEC	135
4.5.6 Relationship between the condensed and the coherent fraction	137
4.6 Conclusion	140
5 BEC Atom Number Fluctuations Across the Mott Transition	143
5.1 Second order phase transitions	144
5.1.1 Classical phase transitions	145
5.1.2 Quantum phase transitions	147
5.1.3 Finite-size scaling	150
5.1.4 The role of the order parameter	151
5.1.5 Spontaneous symmetry breaking and Goldstone modes	152
5.1.6 The Binder cumulant	153
5.2 BEC number fluctuations across BEC transitions	155
5.2.1 The superfluid to normal gas transition	155
5.2.2 The superfluid to Mott insulator transition	158
5.3 Measurement of ΔN_{BEC}^2 across the Mott transition	162
5.3.1 The measurement volume for condensate number fluctuations	162
5.3.2 Post-selection and noise modeling	166
5.3.3 Measurement of order parameter fluctuations	173
5.3.4 Scaling of the number fluctuations with varying system size	180
5.4 Measurement of the Binder cumulant across the Mott transition	182
5.5 Conclusion	188
6 Conclusion	189
Appendices	191
A Correlations and Statistics	193
A.1 Law of total variance	193
A.2 Standard error of variance	193

B Evolution of the in-situ cloud size with interactions	195
List of Figures	197
List of Publications	201
Bibliography	203

1 - Introduction

With the advent of quantum mechanics at the beginning of the 20th century, physicists came to see light and matter on a similar footing. De Broglie first stated the concept of wave particle duality in 1924 [1]. After Bose derived the Planck distribution for photons based on the hypothesis of light quanta [2], Einstein used his result to derive a quantum theory of the ideal Bose gas, predicting a condensation of the atoms into the ground state below a critical temperature [3]. It took nearly the entire remainder of the century for laser technology and cooling techniques [4–6] to advance sufficiently to enable the the first experimental realizations of Bose-Einstein condensation [7, 8]. Ever since, quantum gas experiments have been on the advance, and are now routinely able to reach quantum degeneracy; a regime characterized by a de Broglie wavelength λ_{dB} of the atoms on the order of the average interparticle distance, $n\lambda_{dB}^3 \sim 1$, with n the density of the gas and λ_{dB} growing inversely with temperature and particle mass. In such a situation the wave-like character of massive particles becomes crucial and quantum mechanical effects dominate. Such experiments have opened the door for the field of quantum simulation.

Quantum simulation

Systems that occur in nature are typically made up of large numbers of interacting particles and are often characterized by complex phenomena that emerge based on the intricate interplay of these interactions among their components. Given the small mass of the electron, condensed matter systems tend to fall into this category, since their particle density can be sufficiently high to reach quantum degeneracy even at ambient temperature. Strongly-correlated electron systems in condensed matter exhibit emergent phenomena such as superconductivity [9] or quantum Hall physics [10]. Large many-body ensembles are notoriously difficult to describe exactly, since the size of the associated Hilbert space grows exponentially with the number of degrees of freedom, often putting the calculation of the many-body wavefunction out of reach of classical computers. Mean-field approaches that replace the effect of particle-particle interactions with an average interaction effect provide a balance between accuracy and computational feasibility, but are unable to capture complex quantum correlations and fluctuations [11–13].

One possible solution to this problem dates back to a suggestion by Feynman [14], who proposed making use of one quantum system under near-perfect control to mimick and simulate the behavior of a second quantum system of interest. In those situations experiments can lead the way and simulate quantum problems too complex to solve numerically [15]. With their precise control over microscopic parameters such as the energy landscape or interactions in the system, as well as the ability to measure many observables of interest, the toolbox represented by ensembles of ultracold atoms has proven to constitute a well-suited testbed onto which to map complex Hamiltonians [16].

Interactions and quantum phase transitions

Despite the breakthrough in the field of ultracold atoms that was delivered by the realization of the first Bose-Einstein condensates (BECs), these systems can hardly be considered to be "many-body" from a quantum mechanical point of view, since nearly all the atoms are in the same quantum state described by a macroscopic wavefunction. The possibility to simulate quantum phase transitions with ensembles of ultracold atoms enables the experimental study of assemblies of atoms that are truly "many-body" [35] in the sense that, despite the reductionist hypothesis of being able to break everything down to fundamental laws, the inverse does not apply: These systems are characterized by emergent phenomena that arise solely from the interplay of large ensembles of interacting particles that cannot be described on the basis of the fundamental laws for the individual constituents alone. In systems where interactions between particles dominate over their individual kinetic energies, the interplay between the particles can become so dominant that strongly correlated quantum states emerge.

One of the conceptually simplest Hamiltonians that hosts nonetheless complex quantum many-body features is the Bose-Hubbard Hamiltonian, which describes particles in a periodic potential landscape with two competing energy scales: The tunnel coupling J between adjacent sites, and the onsite interaction U of two particles sharing the same site. The system undergoes a quantum phase transition from a superfluid to a Mott insulator at a critical value of U/J that was observed experimentally in one of the first successful implementations of quantum simulation [17] following its proposal [18], using optical lattices to simulate the periodic potential landscape

[19]. The Mott insulator phase transition is induced by interactions and quantum fluctuations, and thereby constitutes a fundamentally different type of phase transition than those induced by an external thermodynamic parameter and temperature fluctuations.

Quantum fluctuations and many-body correlations in momentum space

Correlations in many-body systems are typically the result of non-commuting parts of the Hamiltonian, e.g. the interaction part not commuting with the non-interacting part. They are accompanied by quantum fluctuations when the interacting part of the Hamiltonian does not commute with the non-interacting part, leading to a competition between the two associated energy scales that can induce a quantum phase transition, i.e. a transition in the many-body ground state of the system that is not driven by temperature.

In the case of the Bose-Hubbard model, this transition separates a conducting from an insulating ground state. It is therefore a natural setting to examine this phase transition in momentum space. In experiments this can be achieved by switching off the trap holding the system in place and letting it fall under gravity for a sufficiently long time. Particles with high initial speed will be further from the center after the free fall, mapping the position after the expansion onto the momentum distribution in the trap [17, 20, 21].

Correlations can encode a multitude of information about the state of the system. Under specific circumstances, they can even exhibit statistics similar to those of pure states; a feat that is not obvious in any real experiment.

The emergence of correlations from the interplay of interactions and kinetic energy is one of the central aspects of interest and study of the Helium Lattice experiment at LCF. In the case of Bose-Hubbard physics, the weakly-interacting regime is characterized by pair correlations between atoms at opposite momenta [22, 23]. Increasing the interactions beyond the realm linearized quantum fluctuations is expected to produce more complex correlations as the correlated pairs are broken up in higher-order interaction processes. Continuing to increase the interactions results in realizing the phase transition from a superfluid to a Mott insulator. In the quantum critical regime enhanced fluctuations are expected as a result of the quantum fluctuations driving the transition. The investigation of these topics is at the heart of the research work presented in this manuscript.

Number statistics and single atom detection in three dimensions

Cold atom platforms have successfully implemented a variety of both destructive and non-destructive imaging techniques. Single-site resolved quantum gas microscopes are able to achieve single particle detection in dimensions lower than three [24–27]. In three dimensions (3D), however, experiments relying on the interaction of atoms with light to probe the atoms are subject to the line-of-sight integration of the cameras and typically require many photons per atom to achieve sufficient signal strength.

To assess many-body correlation signals among multiple particles, it is necessary to observe the dynamics of each individual component within the system [28–30], implying in principle a measurement of the full particle distribution in the considered degree of freedom. This constitutes a formidable challenge in the case of 3D systems, where single-particle detection is not feasible by optical means.

To circumvent this issue, this experiment uses metastable Helium as atomic species, which allows for electronic detection in the far field since its internal energy is sufficient for a single atom to strike out an electron of a metal plate; a technology developed at Institut d’Optique at the beginning of the millennium [31]. With a quantum efficiency of the detector of $\eta = 53(2)\%$ the ensuing precision on measurements of the atom number in momentum space is sufficient for the average momentum density to span four orders of magnitude in amplitude. It also provides access to the full occupation distribution in momentum space for large systems of $10^3 - 10^5$ atoms, enabling the analysis of higher order moments beyond mean and variance and constituting an invaluable asset in the analysis of quantum correlations from the number statistics of the prepared state.

Outline of the manuscript

This manuscript is divided into four chapters:

- In chapter 2 the experimental apparatus is presented. The cooling and trapping sequences are outlined that lead to the production of $^4\text{He}^*$ BECs cycle times as low as four seconds. The optical lattice setup and electronic detection scheme are detailed, as well as the newly-implemented lab monitoring system that has enabled continuous surveillance

of critical experimental equipment and lab room conditions from anywhere.

The following three chapters are dedicated to experimental results achieved on the Helium Lattice experiment:

- In chapter 3 the fate of Bogoliubov's pair correlation signal [22] that characterizes the weakly-interacting regime of Bose gases [23] is examined in the context of stronger interactions. The pairing signal is found to be suppressed with increasing interactions in favor of more complex correlations between more than two particles, signaling the onset of the strongly correlated regime. A direct observation of a non-zero four-operator cumulant at strong interactions is presented, constituting a direct signature of non-Gaussian correlations [32].
- In chapter 4 an analysis of the Full Counting Statistics of the interacting lattice gases prepared in the experiment is presented. Iconic many-body quantum states such as lattice BECs and Mott insulators are characterized by their many-body coherence properties when probed in small volumes of momentum space after an expansion. The role of the condensate depletion is highlighted in the small deviations from Poisson statistics for the BEC from the normalized zero-distance correlations up to sixth order [36].
- Finally, in chapter 5 an analysis of the condensate order parameter fluctuations measured across the Mott insulator phase transition is presented. These fluctuations, measured via the condensate occupation number, are found to be enhanced towards the phase transition, exhibiting a sharp peak of amplitude $\Delta N_0 \sim \sqrt{\langle N \rangle}$ incompatible with the modeled experimental noise, mirroring the observations made in the context of the normal gas condensation transition [33, 34]. Additionally, the Binder cumulant is extracted to probe the statistical properties of the BEC order parameter and found to exhibit a sharp variation at the phase transition, paving the way for finite-size scaling analysis in homogeneous systems.
- The appendices contain additional information on the topic of statistics, as well as some additional measurement results not included in the main text.

2 - The Helium Lattice Experiment

Helium is an exotic element in the community of ultracold quantum gases. As of the writing of this text, there are only six of experiments in the world that work with degenerate Helium gases [36–41], as opposed to the hundreds that work with conventional alkaline metals such as Rubidium, Sodium or Lithium. More generally, noble gases as a whole are a rarity in this domain. The reason for this lies in the atomic energy level structure of these elements. Their filled electron shells make them less reactive and more challenging to cool and manipulate at the low temperatures required for ultracold atom physics. They have high-lying first excited states that are not ideally suited for laser cooling and trapping, since their transitions lie in the ultraviolet (UV) (as is the case for Helium and Neon) or vacuum ultraviolet (VUV) (Argon, Krypton and Xenon) range of the electromagnetic spectrum. There are sometimes further inconveniences apart from the lack of suitable transitions from the ground state, such as the absence of usable Feshbach resonances in the case of ^4He [42,43]. Feshbach resonances are a phenomenon where the scattering properties of atoms can be dramatically altered by the presence of a magnetic¹ field [44]. They are typically associated with atoms or molecules with hyperfine structure and magnetic moments, and occur when the energy of a bound state of the system coincides with the energy of a scattering state, leading to significant changes in the scattering length and interaction strength between atoms. Since Helium is a noble gas with no nuclear spin ($I \simeq 0$) and no hyperfine structure², its interactions with magnetic fields do not lead to Feshbach resonances³ as seen for instance in alkali metals with more complex electronic and nuclear properties. Other drawbacks of ^4He include the presence of two-body losses from light-assisted collisions in the metastable state and the small efficient cross-sections of the imaging transitions (both detailed later in this chapter).

1. Magnetic tuning is the most common method, but optical Feshbach resonances exist as well.

2. Of the noble gases only Xenon exhibits nuclear spin and hyperfine structure, with the most common isotope ^{129}Xe possessing a nuclear spin of $I = 1/2$.

3. Specifically, the absence of hyperfine coupling between different Born-Oppenheimer potentials is not favorable for accessible s -wave Feshbach resonances for the fully spin-stretched states used in the experiment (see below), with the molecular bound state separated by large energy distances on account of the small mass of Helium. Experimental investigations of theoretically predicted d -wave Feshbach resonances [42] have not been able to establish their experimental accessibility [45].

Why then, with all these apparent disadvantages, would some research groups still choose such an (in some aspects rather inconvenient) atomic species as fundamental building block for their experimental platform? There are several answers to this question: For one thing, as the second element of the periodic table its simple electronic structure leads to Helium being one of the only atoms where energies and interaction properties can be calculated *ab initio* with extreme precision, making it an ideal testbed for exploring fundamental theories of atomic structure. The answer that has turned out to be decisive in choosing it for the purposes of this experiment, however, lies not in the state preparation, nor in the physical systems that can be explored, but in the detection: The atomic energy level structure of Helium contains a metastable state whose internal energy is considerably larger than the work functions of most common metals, which are typically on the order of 2-5 electronvolts (eV). This means that a single atom has a high probability of striking a single electron out of a metal plate upon contact. The ability for a single particle of the system to trigger a single, discernible (within limits) detection event in both space and in time paves the way for single-particle detection in all three dimensions.

Experiments with ultracold atoms inherently strive to isolate the atoms from the environment in order to be able to manipulate and probe them with as little destructive interference from the outside world as possible. Such an experimental apparatus usually consists of a series of vacuum pumps, tubes and viewports inside which the atoms are prepared and detected. Therefore, one of the prominent means of interacting with the particles is to make use of their interaction with electromagnetic radiation, i.e. to shine light on them. This works extremely well for the preparation stages, often in conjunction with the use of magnetic fields, but it represents a drawback for the detection of a three-dimensional (3D) system: The signal usually consists of many photons per atom, and ensemble sizes for quantum gas experiments typically range from a few thousand to a few million atoms. This means that a large number of photons arrive in quick succession on the sensor of the camera, so quickly in fact that it is impossible to discern their arrival times, and thus the signal is almost always subject to line-of-sight integration. Additionally, the required signal strength of many photons per atom and limited resolution of cameras make it virtually impossible to infer the position of the specific emitting atom from the photon

signal for 3D systems. The only signals that can be extracted by optical means are thus photon counts that are integrated over the entire depth of the sample along the imaging axis (and in many cases also in the transverse plane within single pixels of resolution limited cameras), making single particle detection in 3D impossible with standard imaging techniques⁴.

Atoms in metastable states of Helium can be detected directly, without resorting to photons as intermediate information carriers between the system and the detector. Experiments with metastable Helium allow for single-particle detection in 3D for thousands of particles per experimental realization. In the absence of an information carrier between the system and the detector, the detection process necessarily implies that the system itself needs to come into contact with the metal plate. This makes *in situ* detection difficult to even conceptualize: The metal plate would have to move across the atomic cloud without inducing any interference that could perturb the system in the moment of detection, such as blocking off any laser light. Instead, the way to bring the atoms into contact with the metallic plate is to let them fall onto it under gravity. In this case, the position of an atom on the detector after a long time-of-flight (TOF) can be related not to its original position, but rather its momentum, with an atom with a high initial velocity being detected further from the center and vice versa.

The detectability without photons is the key attribute that sets Helium apart from other atomic species. The advantage is such that, for physical systems that can greatly benefit from having access to the entire 3D momentum distribution, some groups choose to take upon themselves all of the inconvenient factors that come along with the use of Helium for an ultracold atom experiment. One of the more significant of these disadvantages is the absence of Feshbach resonances that allow for a precise tuning of the interaction strength between atoms. For atoms with no electrical dipole moment inter-atomic collisions are often the most prominent form of interaction. The strength (or rather: the rate) of these collisions depends on the atomic density. The density of colliding atoms can be increased by the use of an optical lattice, thereby lending (some) control over interaction strength in the system back to the experimentalist. As is outlined later in this chapter, the optical lattice also plays a significant role in the detection process,

4. Even though imaging systems have been able to extract some additional information along the imaging axis by making use of holography [46].

independently of any modification of the interaction strength in the system. The combination of these two aspects makes it thus rather natural for an ultracold atom experiment that uses Helium to also employ an optical lattice. In fact, three out of the six Helium experiments in the world use such a lattice in one way or another [36,41,47]. Thus the name of the setup on which this work has been carried out: The Helium Lattice Experiment.

The following section details the experimental setup used to bring ^4He to quantum degeneracy. The subsequent sections elaborate the optical lattice and the detection process, with a final section being accorded to the lab monitoring system that has been setup during this thesis.

2.1 . Bose-Einstein Condensation of Metastable Helium

The numerous challenges that have to be overcome in order to reach the quantum critical regime with Helium have been outlined above. This section now illustrates how these hurdles can be surpassed to produce Bose-Einstein condensates (BECs) of ^4He . In doing so, it follows the path of the atoms from the Helium gas bottle to the science chamber where the experiments are performed on them. Since the experimental sequence has not seen a significant evolution over the last years, the description of the individual stages is kept brief, with more detailed treatments being the subject of the team's previous theses [48-53].

In order for quantum effects to dominate the behavior of the gas, the ensemble of atoms has to be brought to quantum degeneracy, that is the phase space density has to be increased to a level where the spatial wavefunctions of the individual particles start to overlap. This is what it means in a quantum sense for the atoms to sense each other's presence. Quantum degeneracy occurs when the thermal de Broglie wave volume is on the order of the inverse density: $\lambda_{\text{dB}}^3 n \sim 1$, where $\lambda_{\text{dB}} = h/\sqrt{2\pi m k_{\text{B}} T}$. This immediately implies that the atoms have to be cooled down to very low temperatures in order to increase λ_{dB} , while at the same time increasing the density. The first of these concerns is addressed by cooling and the latter by trapping techniques for ultracold atoms, the relevant aspects of both of which are outlined below in the context of the Helium Lattice experiment at LCF.

The first BECs of metastable Helium were obtained simultaneously by groups at the Institut d'Optique [54] and the Laboratoire Kastler Brossel [55] in 2001. In 2006 the fermionic isotope ^3He was also brought to quantum degeneracy [56]. All of the experiments start by exciting Helium to the metastable state, denoted $^4\text{He}^*$ for the bosonic isotope, from which cooling transitions can be addressed using commercial lasers in the near-infrared range.

2.1.1 . Metastable Helium Source

As mentioned above, the electronic level structure for noble gases is such that transitions from the ground state lie in the UV or VUV regions of the electromagnetic spectrum and are thus not accessible using standard visible or near-infrared light sources. Furthermore, in the case of Helium, it is precisely the high internal energy of the metastable state 2^3S_1 of 19.8 eV [57], the largest of any metastable atom, that enables the unique single-atom detection techniques. The reliance on the metastable state is so significant that it is routinely referred to when citing the atomic species of the experiment: $^4\text{He}^*$, *metastable* Helium-4. The reason for this special treatment of the 2^3S_1 state of Helium-4 is its extremely long lifetime of more than 2 hours [47] compared to the experimental cycle duration (about 10 seconds) which obviates the need to contemplate the possibility of a $^4\text{He}^*$ atom spontaneously returning to the 1^1S_0 state during the experiment. The excitation of this metastable state is therefore the natural starting point for any quantum gas experiment with Helium, since it is only from the 2^3S_1 state that the toolbox of standard trapping and cooling techniques for ultracold atoms becomes available with standard wavelength lasers. This is illustrated in figure 2.1, which depicts the ^4He energy levels relevant for this experiment.

Since optical excitation is not a realistic option for the 2^3S_1 state, the universal method of choice is to use a plasma DC discharge. A high voltage of about 2.8 kV is applied to a metallic needle fixed inside a glass tube through which the Helium atoms flow. The tube ends in a small hole in a Boron-Nitride (BN) piece that directs the atoms onto a grounded skimmer (a perforated metallic plate that reduces the variance of the transverse velocity distribution). The high voltage ionizes the ^4He atoms and creates a fast flow of $^4\text{He}^+$ ions and electrons from the tip of the needle to the skimmer. These charged particles can recombine in the metastable 2^3S_1 state, creating a beam of very fast moving $^4\text{He}^*$ atoms behind the skimmer with a supersonic mean longitudinal

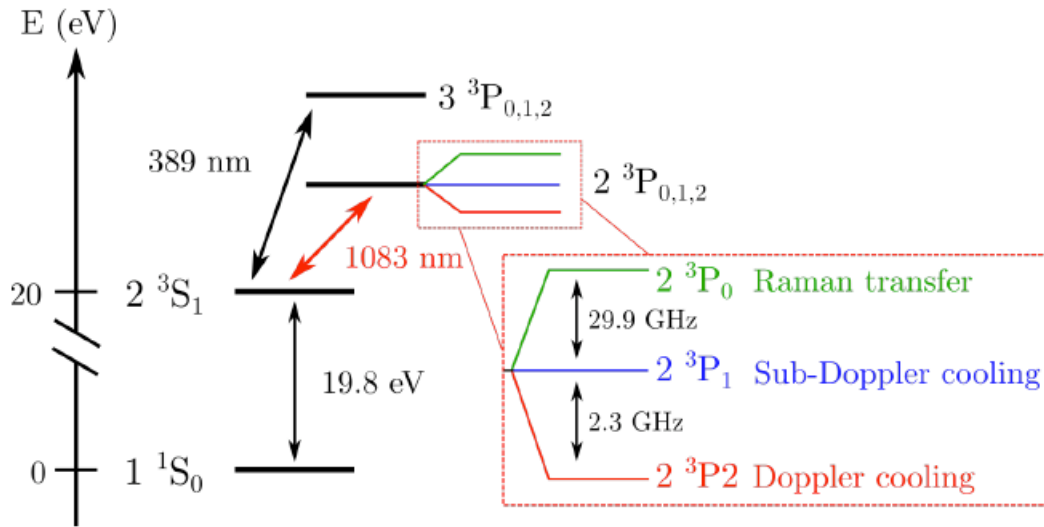


Figure 2.1 – Relevant energy levels of ^4He . The metastable state $2\ ^3S_1$ is the starting point for all cooling, trapping and imaging transitions towards the $2\ ^3P_{0,1,2}$ states, which can be accessed with standard near-infrared lasers at wavelengths around $1\ \mu\text{m}$. Taken from [52].

velocity of about 1200 m/s and transverse velocities around 50 m/s. The first cooling stage for metastable Helium occurs cryogenically using liquid nitrogen that flows through a copper tubing in contact with the BN piece. BN is chosen for its remarkable properties of being a good thermal conductor, allowing for heat transfer from the atoms in the plasma to the liquid nitrogen, while at the same time being an electrical insulator that does not interfere with the plasma creation process induced by the high voltage. The liquid nitrogen cooling stage sufficiently reduces the speed of the metastable atoms to allow for the application of standard laser cooling techniques in the subsequent steps. The entire source setup is schematically depicted in figure 2.2.

The source setup is in principle readily extensible to accommodate the fermionic species ^3He alongside its current bosonic counterpart. However, with the much more costly fermion the low conversion efficiency to the metastable state of only about 10^{-4} becomes a critical issue which necessitates a modification of the apparatus to reuse the non-converted atoms that are currently evacuated at every repetition of the experiment. He^4 is inexpensive enough to be able to discard 99.9% of every gas bottle.

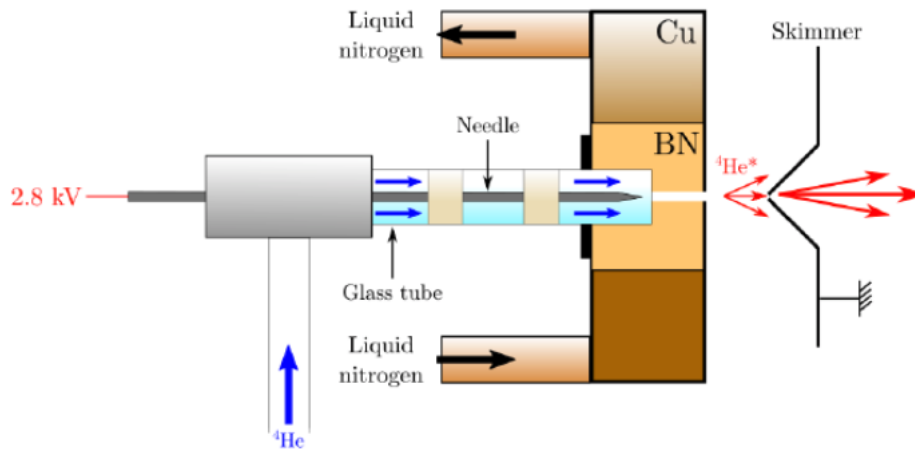


Figure 2.2 – Schema of the metastable Helium source. The Helium atoms are excited to the metastable state in the plasma that forms between the BN and the skimmer. Taken from [52].

2.1.2 . Cooling and Trapping He^4

One of the fundamental parts of every quantum gas experiment are the laser cooling stages. What may seem counter-intuitive to the uninitiated, that is being able to make something cold by shining light on it, has become the backbone of atomic physics experiments in recent decades. In its most basic variant, which is usually referred to as Doppler cooling, the atom is thought of as a two-level system that will absorb resonant light (and thereby momentum) in opposition to its movement direction and spontaneously re-emit in random directions that will tend to average out. In order for the momentum transfer to occur in the opposite direction of the atomic trajectory, the laser light is negatively detuned with respect to the atomic resonance, so that the moving atom sees the light shifted to resonance via the Doppler effect. This slowing by radiation pressure is limited by the natural linewidth Γ of the excited state, that is by the rate at which the atom absorbs and re-emits photons on this transition, with the temperature at the Doppler limit being given by $T_D = \hbar\Gamma/2k_B$.

Doppler Cooling Limit

Since the detuning of the cooling laser light is matched to the initial atomic velocity, the resonance condition is no longer fulfilled for an atom that has already been cooled, so that no re-heating by absorption occurs. The transition used for Doppler cooling in this experiment is the $2^3S_1 \rightarrow 2^3P_2$ transition (see fig. 2.1). The use of σ^+ polarized light makes the atoms cycle

between the $m_J = 1$ and $m_J = 2$ sublevels of the 2^3S_1 and 2^3P_2 states, respectively, and creates an effective two-level system. The natural linewidth of the excited state is $\Gamma_{2^3P} \simeq 2\pi \times 1.6$ MHz. This corresponds to a Doppler temperature of $T_D = \hbar\Gamma_{2^3P}/2k_B \simeq 39$ μ K, a theoretical limit for the use of this technique that was observed by the Helium Lattice experiment in 2014 [58].

Transverse Molasses and Zeeman Slower

After exiting the source the atoms are in a supersonic beam and have a significant transverse velocity spread that necessitates a collimation stage before the beam can be slowed down. This is achieved by the use of a transverse molasses setup made up of two counter-propagating beam pairs that Doppler cool the transverse velocity components of the beam. This increases the number of atoms that are able to reach the science chamber by a factor of about 20.

The atomic beam is thus collimated, but its longitudinal velocity is still supersonic. In order to be able to trap the atoms in a small cloud to perform experiments on them, the beam has to undergo significant deceleration. A widely used cooling method in the initial stages of an ultracold quantum gas experiment involves the use of a Zeeman slower, which is a lengthy tube encircled by magnetic coils to establish a consistently varying magnetic field. The Zeeman shift of the atomic energy levels induced by this field keeps the atoms resonant with a counter-propagating laser beam as they progress along the tube, thus allowing for their continuous deceleration. Due to the light mass of Helium and the small cross-section of its cooling transition, the atoms need to absorb many photons before their initial velocity of about 1200 m/s is reduced to the capture velocity of a Magneto-Optical Trap (MOT), which is around 50 m/s. This leads to metastable Helium experiments having some of the longest Zeeman slowers in the world with a length of around 2.5 m.

Magneto-Optical Trap

After exiting the Zeeman slower the atoms enter the science chamber. As outlined above, the two categories of steps required to achieve quantum degeneracy consist in cooling and trapping. The exit velocity of the Zeeman slower is sufficiently low to begin adding the latter to the former. This is realized with a Magneto-Optical Trap (MOT) that consists of three orthogonal pairs of counter-propagating red-detuned laser beams in conjunction with a quadrupole magnetic field.

The two components function jointly in such a way that atoms become more resonant with the light as they move away from the center of the trap, leading to a position-dependent net force towards the trap center as well as simultaneous cooling. The Helium Lattice experiment currently uses 25 G/cm magnetic gradients in a combination with laser beams at $15 I_{\text{sat}}$ per beam at a detuning of $\Delta = -60 \Gamma$, thereby capturing about 2×10^9 atoms in 1.5 s. In a final compression stage the density is increased by reducing the detuning by a factor of 5 while also decreasing the intensity to $0.1 I_{\text{sat}}$, which yields clouds at a temperature of $T \simeq 1.2$ mK and a density of $n \sim 7 \times 10^9$ atoms/cm³ while keeping roughly the same atom number as before the compression.

These values imply that in their current state the atoms are still several orders of magnitude below the quantum degeneracy limit of $\lambda_{\text{dB}}^3 n \sim 1$. For $^4\text{He}^*$, there exists no experimental technique capable of increasing phase-space density in such a way that the atoms can be brought to quantum criticality in one single step. Instead, as is the case for most ultracold atom experiments, a sequence of different techniques has to be employed one after the other, each one contributing to either reducing the temperature or increasing the density of the trapped ensemble (ideally both simultaneously). Figure 2.3 depicts the path of phase space density along the different steps of the cooling sequence.

As a general rule of thumb, the endpoint of an arrow in figure 2.3 to a given step in the cooling sequence is usually not far from the lowest or densest result that can be achieved by applying that specific cooling technique to $^4\text{He}^*$, implying that another type of cooling procedure has to be employed at this point to further cool or condense the cloud. The order of the sequence of different steps results from certain techniques requiring an appropriately low temperature of the ensemble to begin with in order to work efficiently, while others necessitate a specific global transformation of an internal degree of freedom of the cloud, such as spin-polarization (see below).

Red Molasses

Starting from the trapped cloud in the MOT, the magnetic quadrupole field is switched off and the detuning is reduced to $\Delta \simeq -\Gamma$, while at the same time the intensity is lowered by a factor of two to reduce light-assisted Penning collisions (more on these two-body losses below). As in the case of the MOT, the Doppler frequency shift experienced by an atom moving towards one of the

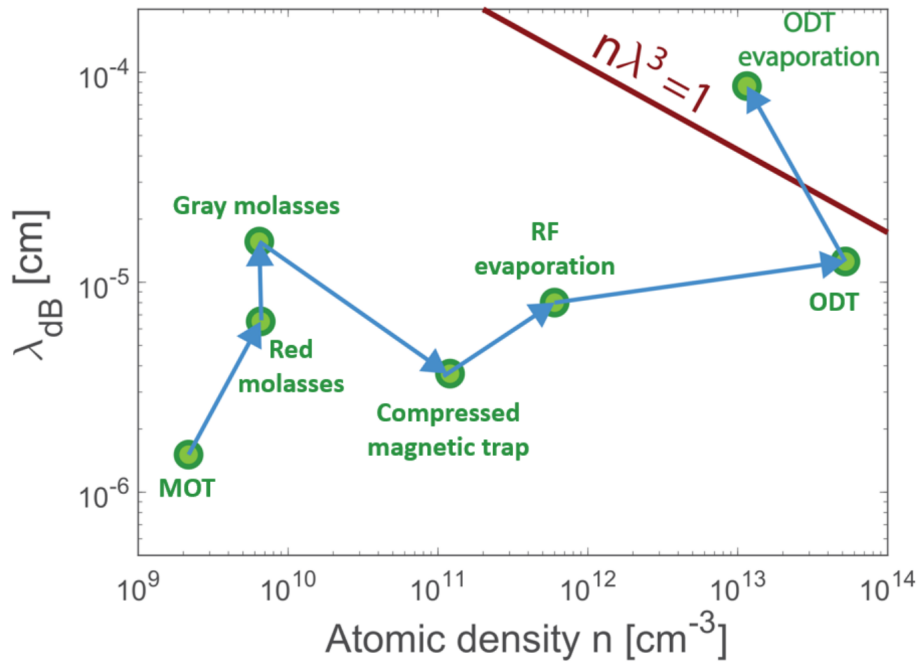


Figure 2.3 – Phase-space density at the different stages of the cooling sequence. A sequence of different cooling techniques has to be employed in order to be able to cross the quantum degeneracy limit of $\lambda_{dB}^3 n = 1$. Taken from [53].

laser beams shifts the balance of radiation pressure such that it is more likely to absorb momentum in the direction opposing its movement. On average this results in a friction-like force acting on atoms with trajectories away from the trap center, hence the name "optical molasses". About 90% of the atoms from the MOT are retained in this molasses stage, while the cloud temperature is reduced to $T \simeq 100 \mu\text{K}$ within 5 ms. This approaches the Doppler limit⁵ and corresponds to a sufficiently low temperature to proceed with sub-Doppler cooling techniques.

In other atoms sub-Doppler mechanisms would spontaneously take over at this point and further reduce the temperature, actually preventing the observation of the Doppler cooling limit. The observation of [58] indicates that these mechanisms do not occur spontaneously in red molasses of $^4\text{He}^*$. This fact is attributed to its low capture velocity, implying that in this case Doppler cooling yields too great a final velocity for sub-Doppler mechanisms to work efficiently

5. In order to attain the Doppler limit as in [58] the laser intensity has to be lowered to values that reduce the atom number too drastically for the purposes of the usual experimental sequence where large atom numbers are required to reach quantum degeneracy.

in the same conditions.

Grey Molasses

Sub-Doppler cooling is more involved than the mechanisms described so far, requiring a more complex target structure than a two-level system. In the case of $^4\text{He}^*$ the absence of hyperfine coupling leads to a perfectly degenerate "ground state" (the metastable state) that provides the lambda-like configuration between the 2^3S_1 and the 2^3P_1 states required for the implementation of a grey molasses stage, a name that stems from the recurring transitioning of the atoms between so-called bright and dark states. Fig. 2.1 illustrates that a different excited state is now addressed to proceed with sub-Doppler cooling techniques. More specifically, the lambda configuration is implemented using three pairs of counter-propagating $\sigma^+ - \sigma^-$ - polarized laser beams and leads to the population of a long-lived dark state, a superposition of the degenerate ground-states that does not interact with the laser light. A cooling technique consisting in repetitively cycling the atoms through a potential energy landscape to convert their kinetic into potential energy ("Sisyphus cooling") with motional coupling between the dark state and the state interacting with the laser light (the bright state) leads to the accumulation of slow-moving atoms in the dark state via velocity-selective coherent population trapping. The viability of this cooling procedure for ^4He has been well known for several decades [59,60].

Sisyphus cooling is implemented on the $2^3S_1 \rightarrow 2^3P_1$ transition using a detuning of $\Delta \simeq 8\Gamma$ and an intensity of $4.7 I_{\text{sat}}$ per beam. Atom numbers remain nearly constant with respect to the red molasses, and the sub-Doppler regime is reached with temperatures decreasing to $T \simeq 15 \mu\text{K}$.

Light-assisted Collisions

At this point the cloud is reasonably cold, but the phase-space density limited by the position-space density and therefore only on the order of $\sim 10^{-5}$. The limiting factor for the position-space density are light-assisted collisions that arise from the energy of the metastable state being greater than half the ionization energy of ^4He , meaning that it is energetically favorable for two metastable atoms to collide and Penning ionize [61] one of the atoms while leaving the other in the (true) ground state 1^1S_0 :



The centrifugal barrier renders this type of collision highly improbable and therefore negligible when both $^4\text{He}^*$ atoms are in the (metastable) ground state 2^3S_1 [62]. This barrier is removed, however, with the excitation by a near-resonant photon of one of the $^4\text{He}^*$ atoms to a 2^3P state, hence the name light-assisted collisions.

Since only $^4\text{He}^*$ atoms are trapped in the experiment, this type of collision leads to the loss of two metastable atoms and makes light-assisted collisions a considerably greater source of atom loss than for experiments that do not involve metastable states, constituting the limiting factor for the density in all laser cooling stages [63–66]. A different type of cooling procedure is thus required to be able to increase the density of the cloud without the need to rely on near-resonant light. In principle one could imagine charging the atoms into a far-off resonance optical dipole trap (ODT) in order to perform evaporative cooling to quantum degeneracy. However, the increase in the atomic density due to the tight confinement of such a trap has been shown in this experiment to increase the rate of Penning collisions to prohibitive levels when attempting such a transfer directly from the grey molasses stage, effectively ruling out an all-optical cooling approach for $^4\text{He}^*$ and suggesting the implementation of a hybrid solution involving a magnetic trap.

To circumvent the collision issue the gas is spin polarized, which has been shown to reduce the rate of Penning collisions by about 4 orders of magnitude when compared to a spin mixture [67], with spin-conservation leading to an effective suppression of Penning ionization⁶. The cloud is thus optically pumped to the magnetic sub-level $m_J = +1$ of the 2^3S_1 state before being transferred to a magnetic quadrupole trap, which acts as a reservoir from which the ODT can be filled in a subsequent step [68].

Magnetic Trap

Only the pumped sub-level $m_J = +1$ (about 85% of the cloud) is trapped by the magnetic quadrupole field, with the others being either insensitive to magnetic fields ($m_J = 0$) or anti-

6. When spin-polarized, the left-hand side of eq. 2.1 has a total spin of $S = 2$ and the right-hand side a total spin of $S = 1$, rendering the collision forbidden by conservation of total spin.

trapped ($m_J = -1$). A bias field is applied in the vertical z -direction to define the quantization axis. Magnetic gradients of ~ 5 G/cm trap the pumped atoms from the grey molasses and are increased to ~ 35 G/cm to increase the position-space density, with the density of the spin-polarized cloud no longer limited by Penning collisions. Radio-frequency (RF) evaporation removes the hottest atoms for a duration of 3 seconds during which the frequency is linearly decreased from 40 MHz down to 6 MHz. This cooling by evaporation works much like blowing on a cup of coffee: The most energetic particles are selectively expelled from the trap, while the remainder is left behind at a lower temperature. The relatively long duration of this step (nearly 50% of the total experimental sequence duration) stems from the slow ramp of the RF wave frequency, which has to be decreased in accordance with the time it takes for the gas to re-thermalize through collisions. The result of this first evaporation process is a slightly warmer cloud at $T \simeq 70$ μ K, but with a much larger density of $n \simeq 6.6 \times 10^{11}$.

Quadrupole magnetic traps are characterized by a zero-field crossing in the trap center that can induce spin flips to one of the untrapped magnetic sublevels ($m_J = 0, -1$) on account of the disappearance of the quantization axis in the zero field region [69]. These so-called Majorana spin flips result in atom losses at a rate inversely proportional to the particle mass [70, 71], making Helium particularly vulnerable to this effect. Furthermore, colder atoms are more susceptible to being lost in this way than hotter ones since they are more likely to stay around the zero field position in the trap center, leading to a heating of the cloud. Unsurprisingly, large Majorana losses have been observed in the experiment [68] and limit the density and lifetime in the magnetic trap, but the final atom number of about 10^8 coupled with the 50-fold increase in density over the grey molasses stage constitute a sufficient starting point in terms of phase-space density for a transfer to a crossed optical dipole trap (ODT).

Crossed Optical Dipole Trap

One of the main advantages of evaporative cooling in an ODT are the higher trapping frequencies⁷ that lead to increased densities and collision rates when compared to evaporation in a magnetic trap. The unique characteristics of $^4\text{He}^*$ that enable single-particle detection are a considerable advantage in the search for rare events such as multi-particle correlations that

7. In the initial stage at large intensities of the ODT beams.

require the acquisition of large amounts of data to achieve the necessary statistical significance. The faster and more robust production of degenerate ensembles of $^4\text{He}^*$ offered by an ODT is thus a significant asset in the ongoing quest to maximize the data acquisition rate for such signals.

The ODT consists of two far-off resonance Gaussian shaped beams at a wavelength of 1550 nm and an angle of 20° that are focused down to respective waists of $133\ \mu\text{m}$ and $63\ \mu\text{m}$ to trap the atoms in the maximum of the laser intensity. The loading process consists in a simultaneous increase of the ODT laser power (up to 18 W in the first beam and 8 W in the second) and a decrease of the quadrupole coil current creating the magnetic trap. One trap is slightly offset in the vertical direction with respect to the other to avoid the Majorana losses that would result from the accumulation of atoms in the zero-field center of the magnetic trap, with only a small magnetic bias field remaining to maintain the cloud in its spin polarized state. Only about 10% of the atoms are loaded into the narrow ODT, but this transfer results in an increase in density of two orders of magnitude and a two-fold decrease in temperature.

The final evaporation process to achieve Bose-Einstein condensation (BEC) consists in an exponential decrease of the ODT laser power over 600 ms, with the final value of the ramp determining the BEC atom number. For typical experiments with about 5000 atoms in the trap, the trapping frequencies amount to $(\omega_x, \omega_y, \omega_z) = 2\pi \times (41, 173, 180)$ Hz. In its current state the Helium Lattice experiment is capable of producing BECs of $N \simeq 10^6$ atoms every 4.8 seconds⁸ with technical fluctuations of about 8% in the atom number. However, the usual sequence duration for data acquisition with the single particle detector is extended to the range of 6 - 7 seconds in order to remove magnetic impurities in the $m_J = 0$ state from the trap.

Despite the drastic reduction of Penning collisions through spin polarization of the gas, these losses still represent the limiting factor for the lifetime of the BEC in the ODT ($\tau_{\text{BEC}} \simeq 5 - 10$ s), with the background pressure of the science chamber in principle admitting single-particle lifetimes on the order of 40 s.

8. The fastest BEC production time of the experiment is 2.8 seconds, but not in the stable mode of operation employed for data acquisition.

2.1.3 . Imaging techniques

Even though the single particle detector is the main workhorse of the Helium Lattice experiment (see below), fluorescence and absorption imaging techniques still prove invaluable for probing the cloud at various stages of the experimental sequence. The implementation of both techniques for $^4\text{He}^*$ is briefly summarized below.

Fluorescence Imaging

Fluorescence imaging is used to probe the initial stages of the experimental cycle. The atoms absorb resonant light from all six MOT beams for $100\ \mu\text{s}$ following a time-of-flight (TOF) of a few ms, and the resulting fluorescence in the vertical direction is captured by an InGaAs camera with a resolution of $125\ \mu\text{m}$ in the plane of the atoms that allows for measurements of the cloud temperature and atom number up until the loading of the ODT, at which point the fluorescence signal of the cloud is too small to be resolved by the imaging system.

Absorption Imaging

After transfer to the ODT the cloud can be probed using absorption imaging on the $2\ ^3\text{S}_1 \rightarrow 2\ ^3\text{P}_2$ transition with beam of intensity $4I_{\text{sat}}$ for a duration of $25\ \mu\text{s}$ in σ^+ polarization (so as to stay on a closed transition starting from $m_J = 1$), where the effect of stimulated emission is accounted for by a careful calibration. After a TOF of about 10 ms the shadow of the cloud is imaged by a second InGaAs camera with a resolution of $13\ \mu\text{m}$, which allows for the extraction of the BEC atom number by fitting Thomas-Fermi profiles to the cloud shape. *In situ* imaging would require an even higher resolution imaging system.

Helium in and of itself is far from an ideal candidate for high-quality absorption imaging, its low mass and resulting high recoil velocity making it more susceptible to being Doppler-shifted out of resonance for long imaging pulses. However, recent efforts on the experiment have led to an improvement of the absorption imaging by providing a numerical correction for the effect of stimulated emission at high intensities of the probe beam, rendering the peak optical depth in each shot independent of the probe intensity.

2.2 . Helium in Optical Lattices

Quantum simulation is one of the main application fields of ultracold atom experiments. The idea was originally brought forth by Richard Feynman [14] and consists in using one quantum system as a toolbox to mimic and study the behavior of other more complicated quantum systems. Ultracold atoms can be manipulated and controlled with high precision and are capable of modeling more complex systems, such as molecules or materials, that are challenging to study directly in the original systems. In this case the atoms are used as a means to an end more than as the primary object of research, since in many cases one is less interested in measuring the characteristics of an individual atom but more in the emergent properties of a larger ensemble of interacting particles. So called many-body systems are characterized by collective behaviors that are not present in systems of isolated or non-interacting particles, such as phase transitions [17, 18, 72], multi-particle entanglement [73, 74], topological order [75], quasiparticles [22, 23] or many-body localization [76–78]. The exponential growth of the associated Hilbert space with the number of degrees of freedom generally limits exact descriptions of such systems to ensembles no larger than a few dozen particles, making quantum simulation of the corresponding Hamiltonians one of only a few viable options to study quantum many-body physics in larger ensembles. Ultracold atoms are only one of a multitude of platforms that enable this approach [16], with very successful contributions stemming from experiments using Rydberg atoms [79], superconducting qubits [80] or trapped ions [81]. Some advantages of quantum gas platforms are the large particle numbers and control over the interactions and potential energy landscape they provide, with the latter often being implemented via optical lattices [19] that create a periodic energy profile in space similar to the Coulomb potential experienced by electrons in a crystal. As the name implies, optical lattices are a central aspect of the Helium Lattice experiment at LCF; this section is dedicated to their role and setup in the experiment.

Optical lattices are used for several purposes in the experiment: To tune the interactions between particles, to simulate a toy Hamiltonian from many-body physics called the Bose-Hubbard (BH) model, and to ensure the accurate detection of the atomic cloud in momentum space after a long TOF. The first of these points is necessitated by the absence of (usable) Feshbach reso-

nances in metastable Helium. The second enables the realization of a set of experiments on a very common solid-state model using a rather uncommon platform. The third is what enables the mapping of the impact positions and times on the detector onto the in-trap 3D momentum distribution. All of these points are detailed in the following subsections.

2.2.1 . The Bose-Hubbard model

Phase transitions are a macroscopic change in the properties of the system that is driven by microscopic fluctuations. For classical systems these fluctuations are linked to the competition between inner energy and entropy. Quantum phase transitions, on the other hand, are driven by quantum fluctuations that stem from the non-commutativity of different operators in the Hamiltonian of a system, and occur only in the ground state⁹. One of the most iconic of these ground-state phase transitions in condensed matter physics is the transition from a metal to an insulator driven by strong electron-electron interactions¹⁰. Conventional band theories of solids may fail in the description of materials where Coulomb interactions between electrons play a central role for the behavior of the system. The class of materials that come by their insulating nature as a result of these repulsive interactions between electrons are named after Sir Nevill Mott for his substantial contributions in explaining the occurrence of such insulators through the formation of an energy gap [82–84].

One of the simplest models that can account for the transition from a conducting state to a Mott insulator is the Hubbard model [85] that describes the behavior of strongly-correlated electrons in a lattice structure. Here the correlations in the system are a direct consequence of the interactions between the particles¹¹. In the context of superfluid-to-insulator transitions in liquid Helium this framework was extended to the Bose-Hubbard model [72], describing bosonic particles with repulsive contact interactions hopping through a lattice potential [86]. After a proposal that the phase transition described by this model might be observable with ultracold atoms in an optical lattice [18] the first experimental realization [17] marked the beginning of the field of

9. Though critical behavior such as power-law scaling of certain quantities may still be visible at finite temperature.

10. Besides the repulsive Coulomb interactions between electrons, phase transitions from a metal to an insulator can also be driven by disorder on the localization of the electrons or by the presence of frustration.

11. Consider for instance how spatial correlations arise from the mutual repulsion of electrons through their interaction.

simulating many-body physics using ultracold lattice gases [16].

The Bose-Hubbard Hamiltonian

The potential of a 3D cubic lattice of amplitude V_0 with separation d between adjacent sites writes:

$$V(\mathbf{r}) = V_0 \left[\sin^2 \left(\frac{k_d}{2} x \right) + \sin^2 \left(\frac{k_d}{2} y \right) + \sin^2 \left(\frac{k_d}{2} z \right) \right] \quad (2.2)$$

The corresponding reciprocal lattice vector is $k_d = 2\pi/d$. It is often convenient to express the lattice amplitude in units of the recoil energy $v_0 = sE_r$ where the latter is given by the lattice spacing and the atomic mass m : $E_r = \hbar^2/(8md^2)$ with the Planck constant \hbar .

An ensemble of N non-interacting bosons in the lattice is thus described by the band Hamiltonian

$$\hat{H}_{\text{Band, 3D}} = \sum_{i=1}^N \frac{\mathbf{p}_i^2}{2m} + \sum_{i=1}^N V(\mathbf{r}_i) \quad (2.3)$$

Cubic symmetry implies the separability of this Hamiltonian and in the absence of interactions it suffices to consider the 1D case for a single particle:

$$\hat{H}_{\text{Band, 1D}} = \frac{p_x^2}{2m} + \sin^2 \left(\frac{k_d}{2} x \right) \quad (2.4)$$

The eigenstates of $\hat{H}_{\text{Band, 1D}}$ are stated by Bloch's theorem [87] to be the Bloch waves $\psi_{n,q}(x) = e^{iqx} u_{n,q}(x)$, the product of a plane wave $e^{i\mathbf{r}\cdot\mathbf{q}}$ and a function reflecting the periodicity of the lattice $u_{\mathbf{q}}(\mathbf{r})$. Here $n \in \mathbb{N}$ corresponds to the band index and $q \in \mathbb{R}$ to the quasi-momentum of the Bloch wave. The eigenvalue equation for the Bloch wave writes:

$$\left[\frac{(p_x + \hbar q)^2}{2m} + V_0 \sin^2 \left(\frac{k_d}{2} x \right) \right] u_q(x) = E(q) u_q(x) \quad (2.5)$$

Since $u_{n,q}$ is periodic in $q \rightarrow q + k_d$, so are the eigenenergies $E_n(q)$, and the range of quasi-momenta can be limited to the First Brillouin Zone (FBZ): $q \in [-k_d/2, k_d/2]$. Numerical solutions for the first three energy bands are plotted in figure 2.4.

By design each Bloch wave represents a wavefunction that is spread out over the entire lattice. In many cases it can be useful to change to a basis of wavefunctions that are localized on

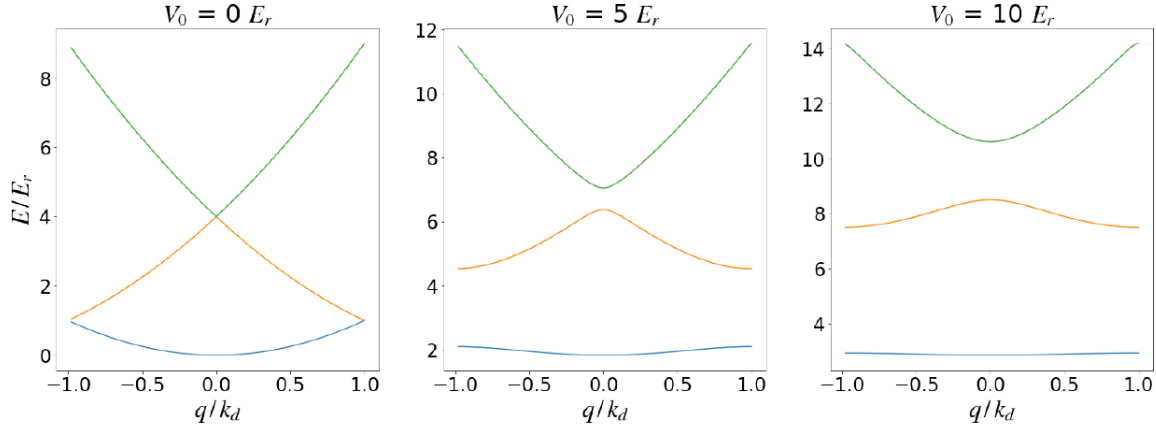


Figure 2.4 – Dispersion relations of the lowest three Bloch bands for increasing lattice amplitudes V_0 . The mean energy of the band grows with the band index. In 3D a gap opens up between the first two bands at the edge of the FBZ for $V_0 \gtrsim 2.2$. Taken from [53].

the individual lattice sites. These are the Wannier functions [88]:

$$w_{n,j}(x) = \sqrt{\frac{d}{2\pi}} \int_{\text{FBZ}} \psi_{n,q}(x) e^{-ijqd} dq \quad (2.6)$$

where $j \in \mathbb{Z}$ corresponds to the index of the lattice site. The $w_{n,j}$ correspond to the wavefunctions of a particle in band n on lattice site j . The delocalized Bloch waves can be decomposed into a sum over the localized Wannier functions:

$$\psi_{n,q}(x) = \sqrt{\frac{d}{2\pi}} \sum_j w_{n,j}(x) e^{-ijdq} \quad (2.7)$$

In second quantization the operator that creates a particle in the Bloch wave $\psi_{n,q}$ is denoted $\hat{c}_{n,j}^\dagger$. The band Hamiltonian in second quantization writes thus:

$$\hat{H}_{\text{Band, 1D}} = \int_{\text{FBZ}} E(q) \hat{c}_q^\dagger \hat{c}_q dq \quad (2.8)$$

The operator creating a particle in the Wannier function $w_{n,j}$ is denoted $\hat{b}_{n,j}^\dagger$ and its definition follows from (2.7):

$$\hat{c}_n^\dagger = \sqrt{\frac{d}{2\pi}} \sum_j \hat{b}_{n,j}^\dagger e^{-ijdq} \quad (2.9)$$

In the Wannier basis and using second quantization the band Hamiltonian now writes:

$$\hat{H}_{\text{Band, 1D}} = \sum_n \sum_{j,j'} J_n(j-j') \hat{b}_{n,j'}^\dagger \hat{b}_{n,j} \quad (2.10)$$

The tunneling amplitude $J_n(j-j')$ describes the process of a particle hopping from site j to another site j' via tunnel effect and decreases with the distance between the sites and the lattice amplitude:

$$J_n(j-j') = \frac{d}{2\pi} \int_{\text{FBZ}} e^{i(j-j')qd} E_n(q) dq \quad (2.11)$$

In the Tight-Binding (TB) limit where the lattice amplitude is large¹², the lowest energy band is considered with the excitation to higher bands made all but impossible by the large energy gap. Therefore the only tunneling processes taken into account are those between adjacent lattice sites, and the tunneling energy term is constant: $J = -J(-1) > 0$. In the ground state only the first band is populated ($n = 0$) and the band Hamiltonian in the TB limit simplifies to:

$$\hat{H}_{\text{Band, TB}} = -J \sum_{\langle i,j \rangle} \hat{b}_i^\dagger \hat{b}_j \quad (2.12)$$

with the sum being carried out over all adjacent lattice sites i and j .

Allowing for two-particle interactions adds a term to the band Hamiltonian (2.3):

$$\hat{H}_{\text{Band, 3D}} = \sum_{i=1}^N \frac{\mathbf{p}_i^2}{2m} + \sum_{i=1}^N V(\mathbf{r}_i) + \sum_i^N \sum_{j>i}^N U_{\text{int}}(\mathbf{r}_1, \mathbf{r}_2) \quad (2.13)$$

In second quantization the interacting part of the 1D band Hamiltonian writes:

$$\hat{H}_{\text{int}} = \frac{1}{2} \int dx \int dx' U_{\text{int}}(x, x') \hat{\Psi}^\dagger(x) \hat{\Psi}^\dagger(x') \hat{\Psi}(x') \hat{\Psi}(x) \quad (2.14)$$

where $\hat{\Psi}^\dagger(x)$ creates a particle at position x and relates to the creation operator in the Wannier basis via:

$$\hat{\Psi}^\dagger(x) = \sum_j w_j(x) \hat{b}_j^\dagger = \sum_j w_0(x-x_j) \hat{b}^\dagger(x) \quad (2.15)$$

12. Concretely $V_0 \geq 5E_r$.

using the property that for Wannier functions $w_0(x - jd) = w_j(x)$. Assuming a two-body contact interaction potential of the form $U_{\text{int}}(x_1, x_2) = g\delta(x_1 - x_2)$ with the coupling constant $g = 4\pi\hbar^2 a_s/m$ and s-wave scattering length a_s , the interaction Hamiltonian writes:

$$\hat{H}_{\text{int}} = \frac{g}{2} \sum_{j_1} \sum_{j_2} \sum_{j_3} \sum_{j_4} \hat{b}_{j_4}^\dagger \hat{b}_{j_3}^\dagger \hat{b}_{j_2}^\dagger \hat{b}_{j_1}^\dagger \int w_{j_4}^*(x) w_{j_3}^*(x) w_{j_2}(x) w_{j_1}(x) dx \quad (2.16)$$

In the TB regime the Wannier functions w_j are narrow due to the large lattice amplitude, and thus their overlap over different sites can be neglected. This collapses the four sums into the case of on-site interactions only with the sole contributing term stemming from $j_1 = j_2 = j_3 = j_4$. Introducing the on-site interaction energy $U_{1D} = g \int |w_{0,0}(x)|^4$ and atom number $\hat{n}_j = \hat{b}_j^\dagger \hat{b}_j$ the 1D interaction Hamiltonian in the TB limit simplifies to:

$$\hat{H}_{\text{int, TB}} = \frac{U_{1D}}{2} \sum_j \hat{n}_j (\hat{n}_j - 1) \quad (2.17)$$

In the 3D case the on-site interaction potential generalizes in a straightforward manner to:

$$U = g \left(\int |w_0(x)|^4 \right)^3 \quad (2.18)$$

Adding the interaction Hamiltonian to the band Hamiltonian in 3D yields the Bose-Hubbard Hamiltonian:

$$\hat{H}_{\text{BH}} = -J \sum_{\langle i,j \rangle} \hat{b}_i^\dagger \hat{b}_j + \frac{U}{2} \sum_j \hat{n}_j (\hat{n}_j - 1) \quad (2.19)$$

\hat{H}_{BH} describe an ensemble of bosons in the lowest band of a lattice of such amplitude that particles can move from site to site only via tunnel effect (J), with two-body contact interactions (U) occurring on sites with multiple occupation (see fig. 2.5). The macroscopic state of the system is dictated by the ratio of the two energy scales in \hat{H}_{BH} , $u = U/J$.

The Mott transition

A BEC is described by a single macroscopic wavefunction and exhibits long-range phase coherence. This superfluid can be loaded into an optical lattice where the atoms can move from

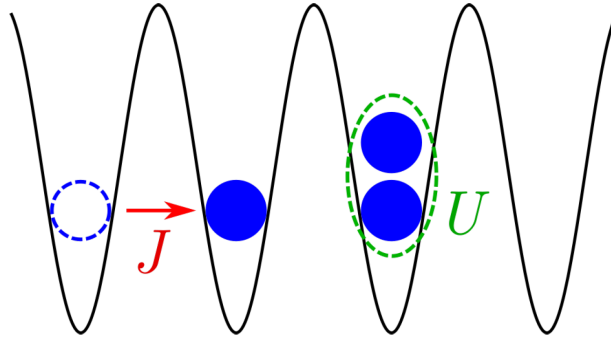


Figure 2.5 – Schematic representation of the two energy terms in the Bose-Hubbard Hamiltonian. Bosons can move around the lattice via tunnel coupling J and interact via two-body repulsive contact interaction U on doubly-occupied sites. Taken from [52].

one site to the next only via tunnel effect. If the repulsive interactions between atoms are small compared to the tunnel coupling, the system will remain in a superfluid state with kinetic energy being minimized by delocalization over many lattice sites. The excitation spectrum is gapless and long-range phase coherence persists, with large atom number fluctuations on every lattice site. If the interactions are large compared to the tunnel coupling, however, energy minimization leads to the atom number per site being pinned to the same integer value throughout the lattice, resulting in loss of phase coherence and a gap in the excitation spectrum. From these opposing limits it is clear that the collective behavior of the ground state of the system is determined by the competition between the kinetic energy J and the interaction term U in (2.19).

Taking the limiting case where the interactions U are vanishingly small before the tunnel coupling J , the ground state of the system of N particles in a lattice of M sites is a superfluid with a wave function corresponding to a Bloch wave at $\mathbf{q} = \mathbf{0}$:

$$|\Psi_0\rangle_{\text{SF}} = \frac{1}{\sqrt{N!}} \left(\hat{c}_{\mathbf{q}=\mathbf{0}}^\dagger \right)^N |0\rangle = \frac{1}{\sqrt{N!}} \left(\frac{1}{\sqrt{M}} \sum_{j=1}^M \hat{b}_j^\dagger \right)^N |0\rangle \quad (2.20)$$

The probability to find n atoms on site j is Poissonian:

$$P(n_j) \approx e^{-\bar{n}} \frac{\bar{n}^{n_j}}{n_j!} \quad (2.21)$$

where $\bar{n} = N/M$ is the average lattice filling. Equation (2.21) corresponds to the probability

distribution of a coherent state with mean atom number N :

$$|\Psi_{\text{coh}}\rangle = \mathcal{N} e^{\sqrt{N}\hat{c}_{\mathbf{q}=0}^\dagger} |0\rangle \quad (2.22)$$

that can be expressed in the Wannier basis of wavefunctions localized on each lattice site j :

$$|\Psi_{\text{coh}}\rangle = \mathcal{N} \prod_{j=1}^M e^{\sqrt{\bar{n}}\hat{b}_j^\dagger} |0\rangle = \prod_{j=1}^M \mathcal{N}_j \sum_{n_j=0}^{\infty} \frac{\alpha_j^{n_j}}{\sqrt{n_j!}} |n_j\rangle_j = \prod_{j=1}^M |\alpha_j\rangle_j \quad (2.23)$$

where the local coherent state on lattice site j is characterized by its amplitude $\alpha_j = \sqrt{\bar{n}}$ and is normalized by $\mathcal{N}_j = e^{-|\alpha_j|^2/2}$. The presence of long-range off-diagonal order becomes evident in the expression of the first order correlation function $G^{(1)}(i, j)$, which is independent of the separation between the considered lattice sites i and j :

$$G^{(1)}(i, j) = \langle \hat{b}_i^\dagger \hat{b}_j \rangle = \langle \Psi_{\text{coh}} | \hat{b}_i^\dagger \hat{b}_j | \Psi_{\text{coh}} \rangle = \alpha_i^* \alpha_j = \bar{n} \quad (2.24)$$

On the contrary, if it is the tunneling that is vanishingly small before the on-site interaction energy, (2.19) reduces in good approximation to (2.17), which is diagonal in the basis of Fock states with a ground state wavefunction given by [72]:

$$|\Psi_0\rangle_{\text{MI}} = \frac{1}{\sqrt{N!}} \prod_{j=1}^M \left(\hat{b}_j^\dagger \right)^{\bar{n}} |0\rangle \quad (2.25)$$

In the effective absence of tunnel coupling phase coherence between the sites is lost and the lattice filling is pinned to its lowest integer value $\bar{n} = N/M$ on each site. The absence of long-range off-diagonal order due to the large on-site phase fluctuations is once again visible from the first-order correlation function, which vanishes between different sites:

$$G^{(1)}(i, j) = {}_{\text{MI}} \langle \Psi_0 | \hat{b}_i^\dagger \hat{b}_j | \Psi_0 \rangle_{\text{MI}} = \delta_{i,j} \bar{n} \quad (2.26)$$

The phase transition between these two limiting cases results from the competition between the two energy terms U and J in (2.19). It is thus associated to the unitary dynamics of the system and occurs in the ground state, thereby constituting a quantum phase transition [89]. As such, it has an associated order parameter (the condensate wavefunction) that characterizes

the behavior of the system throughout the quantum critical regime. This order parameter will be the subject of detailed investigation in chapter 5.

Experimental implementation

The parameters of the model, i.e. the hopping strength J and the on-site interaction energy U , can be controlled experimentally. In the experiment, the lattice is created by making three perpendicular laser beams interfere with their own back-reflection, creating standing waves that form a periodic lattice potential with a cubic unit cell. The distance between two lattice sites is thus determined by the laser wavelength λ : $d = \lambda/2$. In the absence of any frequency modulation of the lattice laser to drive the system, the lattice amplitude s remains as the only tunable parameter to drive the system from a superfluid to a Mott insulator. Its relation to the energy terms of (2.19) can be seen in figure 2.6. Changing the lattice amplitude modifies both U and J , which means that the two energy terms of (2.19) are not independent: An increase in s leads to an exponential decrease in the tunnel coupling, while at the same time causing a narrowing of the Wannier function shape on each lattice site, which increases U following (2.18). The combination of both effects leads to a net exponential increase in u with s , which allows for the continuous variation of u over several orders of magnitude in the experiment by tuning the lattice amplitude. This enables an effective tuning of the interactions in the system even for situations where \hat{H}_{BH} is not necessarily the sole object of interest. In fact, the ability to tune U in this way opens up a whole range of possibilities to study interacting Bose gases outside of BH physics. Thus, in some way the lattice compensates somewhat for the absence of usable Feshbach resonances in $^4\text{He}^*$, albeit with slightly less flexibility than is offered by the latter.

When using this type of setup, the Gaussian shape of the laser beams leads to an additional external trapping potential that can have a non-negligible effect on the physics in the lattice, as is outlined in the following.

2.2.2 . The Harmonic Trapping Potential

One of the most important aspects of any quantum simulation experiment is the fidelity with which the target Hamiltonian can be mapped onto the actual physical system. Whilst great care is taken to isolate the atomic cloud as well as possible from the environment, the reality of lab work

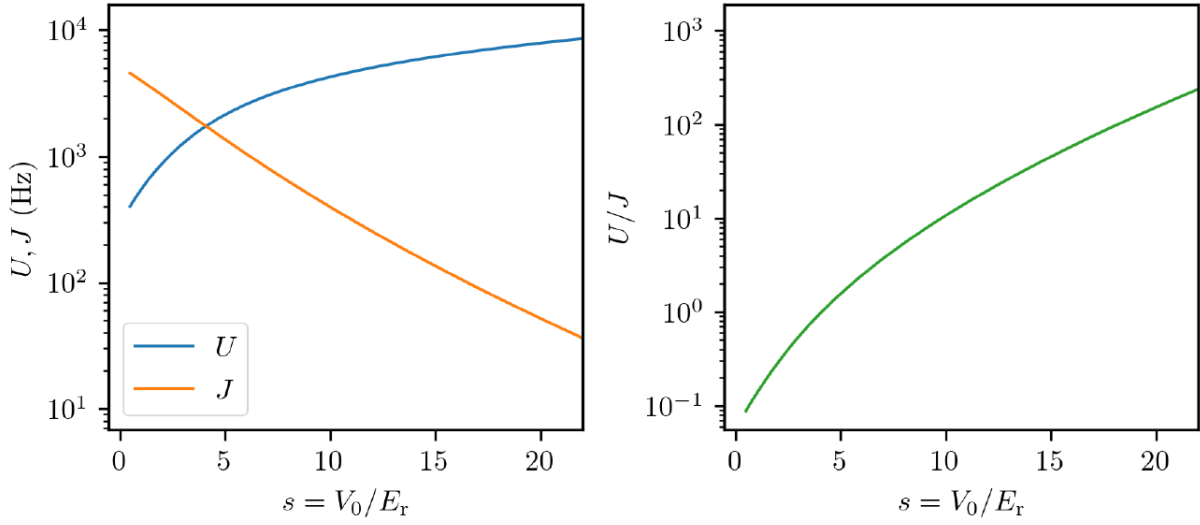


Figure 2.6 - Evolution of the Bose-Hubbard energy terms (a) and their ratio (b) with the lattice amplitude. From figure (a) it is clear that with the lattice amplitude (expressed here in units of the recoil energy) as only tunable parameter, the two energy terms J and U of (2.19) are not independent. Their ratio (b) is what determines the macroscopic state of the ground state. Taken from [52].

is often that there are no perfect solutions, only compromises. One such compromise applying to certain aspects of this experiment is the inherent superposition of a harmonic trapping potential with the optical lattice potential, which renders the system inhomogeneous. This superposition is due to the Gaussian profile of the laser beams used to create the lattice that leads to a weak external trapping potential of harmonic shape:

$$V_{\text{ext}}(\mathbf{r}) = \frac{1}{2}m\omega_{\text{ext}}^2\mathbf{r} \quad (2.27)$$

where the external trapping frequency depends on the laser intensity via $\omega_{\text{ext}} = 2\pi \times 140 \sqrt{s}$ Hz.

In principle this additional spatially varying potential would break the translational invariance of the lattice that is a fundamental prerequisite for Bloch's theorem. However, with $s \ll 100$ in our experiment these frequencies lie below the kHz, and V_{ext} can be considered to vary sufficiently slowly between neighboring lattice sites to allow for the incorporation of the external trapping potential into a position-dependent effective chemical potential via a Local Density Approximation (LDA) [90]:

$$\mu \rightarrow \mu_{\text{eff}}(\mathbf{r}) = \mu - V_{\text{ext}}(\mathbf{r}) \quad (2.28)$$

The LDA consists in treating the system as if being made up of individual cells that are both large enough to apply thermodynamics and at the same time small enough for their density to be quasi-homogeneous. This simplification breaks down in the vicinity of the quantum critical regime [91]. While μ_{eff} can vary locally, the global chemical potential is still fixed by the total atom number.

Since μ_{eff} is position-dependent, so is the lattice filling. This consequence leads to the superposition of different phases (both superfluid and Mott insulating) in the trap instead of the system-wide macroscopic change of state expected in the homogeneous case, as is illustrated in figure 2.7.

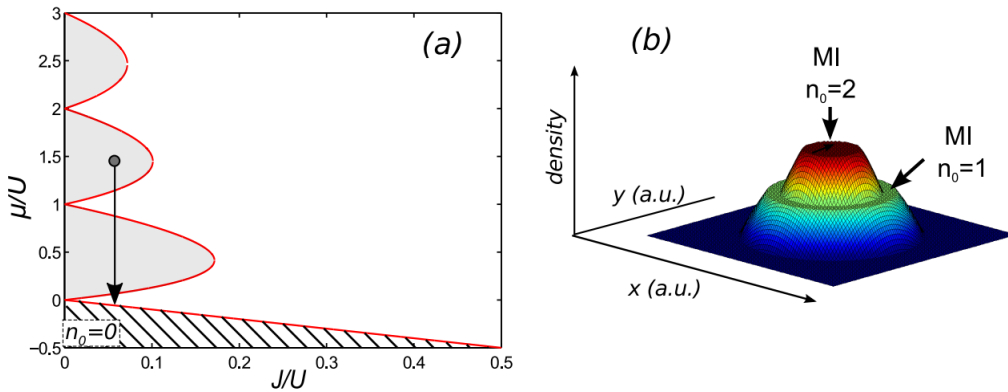


Figure 2.7 – Phase diagram (a) and spatial density profile (b) for the inhomogeneous system. (a) The phase diagram (chemical potential as a function of the tunnel coupling, both in units of the on-site interaction) shows the appearance of Mott insulating shells at integer filling. (b) In the inhomogeneous system a wedding-cake structure is formed with Mott shells surrounded by superfluid shells. Taken from [92].

From (2.28) it follows that the effective chemical potential and thus the filling take on their maximal values at the trap center¹³. As a consequence the highest-filling Mott insulating phase is located at this point in space. Moving further outward (following the arrow in fig. 2.7 (a)) the filling decreases continuously throughout the innermost superfluid shell, until forming the next Mott insulating shell at the next-lowest integer filling. Since the Mott phases are incompressible,

¹³. This is a direct result of V_{ext} increasing towards the edges of the system as per definition of a trapping potential.

their density remains constant even as V_{ext} increases, which leads to the so-called wedding cake structure in the density of the trapped cloud shown in fig. 2.7 (b).

This unintended feature occurs in position space, not in momentum space where the measurements are carried out in this experiment. The time-of-flight evolution induces an averaging of the different layers of the wedding cake as the distribution of the particle positions starts to map onto the in-trap momentum distribution, a side-effect that is not straightforward to correct in post-analysis. Fig. 2.7 (b) shows that even when the Mott transition is crossed in the center of the trap, a measurement of the system as a whole will also contain superfluid phases. In this case one refers to the system being in a Mott insulating state as soon as a single Mott shell has appeared.

Even though this effect might seem like an unequivocal experimental drawback on the surface, it brings with it some positive aspects in other areas: In a homogeneous system the gapped excitation profile of the Mott insulating state hinders the creation of excitations, which induces an increase in temperature in order to keep entropy constant. In the inhomogeneous system, however, the entropy can be absorbed in the superfluid shells (possibly even transitioning them to the normal gas phase), which prevents a significant temperature increase from occurring as the system is driven into the Mott regime.

2.2.3 . Lattice alignment and calibration

Figure 2.6 (b) shows the exponential relationship between the Bose-Hubbard parameter $u = U/J$ and the lattice amplitude s . Since it is s and not u that is under direct experimental control, precise knowledge of and control over the lattice laser power that is sent onto the atoms as a result of the calibration and alignment of the optical system is of utmost importance. An inaccurate power calibration can lead to a perceived shift of the phase diagram¹⁴, while a suboptimal alignment of the optical setup can lead to an undesirable heating of the cloud, as well as a decrease in intensity. While finding and maintaining an optimal alignment of the lattice requires some of the touch and instinct of an experimentalist¹⁵, the power calibration is conducted according to

¹⁴. For instance if the lattice light intensity in the science chamber is actually smaller than what is assumed, the system will still be in the superfluid state at values of u that one would expect to induce a Mott insulator.

¹⁵. Remember that all three lattice beams need to be simultaneously aligned (i) with their own back-reflection, (ii) with each other so as to insure orthogonality in 3D, and (iii) onto the micron-sized BEC

a standardized experimental procedure that employs parametric excitation of the atoms from the fundamental to the second excited band [93, 94]. This procedure is briefly outlined in the following.

In the usual experimental sequence the BEC is loaded from the ODT into the lattice by decrease the power of the optical dipole trap while at the same time ramping up the lattice laser power in all beams. For the power calibration, the lattice beam to be calibrated is kept at a higher value than the two others ($s = 10$ vs 7). After the ramp the amplitude of the higher beam is modulated for a duration of 20 ms, during which atoms can be parametrically excited from the fundamental to the second band when the modulation frequency equals twice the energy difference between the bands:

$$f_{\text{mod}} = 2f_{\text{res}} = 2(E_2(q=0) - E_0(q=0))/h \quad (2.29)$$

After the modulation the atoms remaining in E_0 are loaded back into the ODT while those excited to E_2 are lost, indicating the resonance frequency by a dip in the recaptured atom number as a function of f_{mod} (see fig. 2.8 (a)). Energy band calculations yield the relation between f_{res} and s (see fig. 2.8 (b)) and allow thus for a calibration of the power in the beam that is modulated.

2.2.4 . Finite temperature effect

While the preceding subsection dealt with a (in certain aspects) slightly detrimental aspect of the experimental setup, the undesirable effects brought on by the external trapping potential are something that can in principle be avoided. Experiments are technically capable of producing homogeneous lattice systems, and while the realization of Mott insulating states on such platforms brings with it its own set of experimental challenges, there is nothing intrinsically preventing the realization of such a system.

The story is a different one altogether when talking about the effect of a finite temperature. It goes without saying that any experiment takes place at non-zero temperature. How then can one hope to ever be able to observe the effects linked to a ground-state phase transition in an experiment? The answer lies in the critical behavior associated to the region of the phase diagram

formed in the ODT.

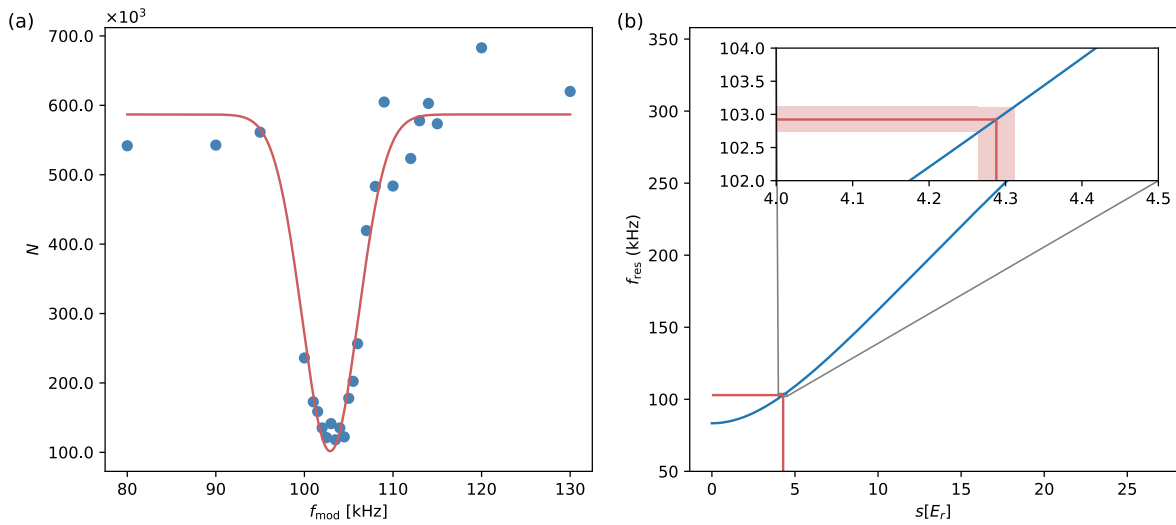


Figure 2.8 – Atom numbers (a) and band calculation (b) for the calibration of the optical lattice intensity via parametric heating. (a) Atom number as a function of the modulation frequency of one of the lattice beams. The pronounced dip is fitted with a Lorentzian curve to indicate the value of the resonance frequency according to (2.29). In this case $f_{\text{res}} = 102.9(2)$ kHz. (b) Band calculation relating the resonance frequency to the lattice beam intensity. The value for f_{res} determined in (a) corresponds to $s = 4.29(2)$. The fitting error on f_{res} leads to the uncertainty in s (red shaded area).

around the phase transition: Certain properties of the system, for instance correlation lengths, susceptibility or specific heat, follow power-law dependencies with temperature and other parameters. These dependencies are governed by critical exponents and scaling laws that characterize a universal behavior that is independent of the system’s microscopic details, with different physical systems undergoing the same type of phase transition exhibiting the same universal behavior. Different phase transitions are grouped together in distinct universality classes such that all members of a class share the same critical exponents and scaling laws. Concretely, the superfluid to Mott insulator phase transition of the BH model belongs to the 3D XY universality class [95], which is notable for short-range interactions, $\mathcal{O}(2)$ symmetry and a two-component order parameter.

This universal behavior is thus what leads to the critical properties of the ground-state phase transition being accessible at finite temperature [96], under the condition that the energy scale of the thermal fluctuations is smaller than the one associated to the critical scaling: If the

fluctuations of the order parameter at the critical point decay on a timescale of τ_c , the condition on the associated energy scale is:

$$\hbar/\tau_c = \hbar\omega_c > k_B T \quad (2.30)$$

However, this only shows that some critical behavior should be observable at some finite temperature; whether or not the temperature implied by (2.30) is in fact attainable in the experiment is not a straightforward question to answer.

Figure 2.9 shows the BH phase diagram at finite temperature. Increasing temperature leads to the system entering a normal gas phase starting from both the superfluid and the Mott insulator. In the first case, this corresponds to a phase transition similar to BEC, which is driven by temperature and thus classical in nature. In the latter case there is a smooth crossover, with the Mott melting temperature being equal to about $0.2 U/k_B$.

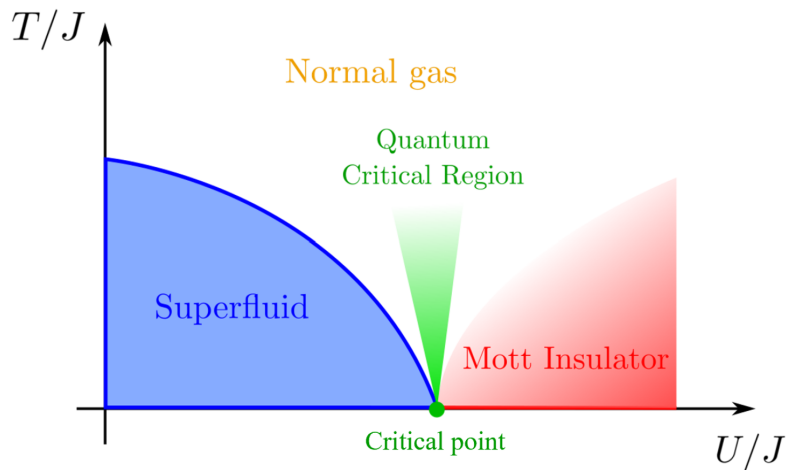


Figure 2.9 - Bose-Hubbard phase diagram. Temperature rescaled by the tunnel coupling as a function of the BH parameters $u = U/J$. The quantum phase transition is located on the x-axis. At finite T the superfluid and Mott insulating phases are separated by a normal gas phase. Above the quantum critical point there is a region where quantum critical phenomena can still be expected to be observable despite the finite temperature. Taken from [53].

Adiabatic preparation of equilibrium many-body states

It seems intuitive that in order for quantum mechanics to affect the behavior observed around the transition the temperature in the experiment should be kept as low as possible. This includes

the avoidance of unwanted heating effects such as the one associated to the alignment of the lattice. But even for a perfectly aligned lattice it is not obvious that the lattice ramps that charge the BEC from the ODT do not induce any type of undesirable change in the temperature or entropy of the prepared system.

This question has been studied in detail on the Helium Lattice experiment [97]. An approach using thermometry via the comparison of momentum densities obtained from experimental data with ab-initio Quantum Monte Carlo (QMC) simulations of the same quantity found the observed temperatures to align with isentropic lines reconstructed through the QMC simulations for the relevant experimental parameters. The entropy per particle was thus shown to be conserved throughout the BH phase diagram at a value of $S/N = 0.8(1) k_B$, affirming the capability of our experiment of adiabatically preparing equilibrium states of the BH model, even within the quantum-critical regime above the Mott transition where the thermometry method was in fact shown to be the most accurate. More details on this investigation can be found in [52, 53].

2.2.5 . Time-of-flight dynamics

A final point remains regarding the use of the lattice in this experiment. This aspect does not concern the ability to prepare a given physical system, but rather the one linked to the subsequent measurement of its momentum density. In fact, the lattice is a crucial element in enabling the single particle detection in momentum space with high fidelity that distinguishes the Helium Lattice experiment. However, what main seem like a simple premise on the surface, i.e. that the position of an atom after a long free fall can be related to its initial velocity, is only true if the free fall of the atoms is not perturbed by any interactions on the way. But the cloud that is released from the trap contains thousands of interacting atoms in a micron-sized volume and it is not obvious that some of them might not collide on their free fall path to the detector, which would obscure any information on their initial momentum in the trap.

The distance between the science chamber and the detector is such that the far-field condition is fulfilled¹⁶, and the time scale on which the trap is switched off¹⁷ to release the atoms

¹⁶. For ^4He the far-field time (the time it takes to pass from the Fresnel to the Fraunhofer regime of propagation) is less than 100 ms, and the distance from the trap center to the detector of 43 cm implies a fall duration of nearly 300 ms for an atom with no initial vertical velocity.

¹⁷. Less than 1 μs for optical potentials.

is much shorter than the one associated to the energies in the system. Thus, in the ideal case where no undesirable effects occur during the free fall, the spatial position \mathbf{r} of an atom after a fall time t_{TOF} can be related to its in-trap momentum $\hbar\mathbf{k}$ via the ballistic relation:

$$\hbar\mathbf{k} = \frac{m\mathbf{r}}{t_{\text{TOF}}} \quad (2.31)$$

The absence of accessible Feshbach resonances in $^4\text{He}^*$ rules out the commonly employed solution of tuning the interaction strength to zero as the atoms are being released from the trap, effectively turning off the interactions for the time-of-flight [43]. Instead, the lattice offers the possibility to rely on the rapid expansion of the cloud induced by trapping frequencies far above the mean-field interaction energy. When a trap with a frequency much larger than the chemical potential ($\hbar\omega_t \gg \mu$) is switched off, the wavefunctions expand on a time scale ($\sim 1/\omega_t$) that is much shorter than the one linked to the interaction-driven dynamics. Thus the rapid dilution of the expanding gas effectively suppresses any possibility of interactions. While the trapping frequencies of a 3D harmonic trap are generally insufficient to induce this effect, those associated to the single site of a sufficiently deep optical lattice meet the criteria¹⁸ [98].

While the above considerations apply at the mean-field level, it is still possible for two-body collisions to occur during the TOF, especially in the case of a superfluid being released from the lattice, where elastic s-wave scattering leads to the formation of scattering halos in the far-field momentum distribution. This effect has been investigated in the experiment [99], and the presence of said scattering halos was indeed confirmed. However, this effect was also shown to only be relevant at much higher atom numbers than those typically used in the experiment, concluding that the probability for these collisions to occur for the usual experimental parameters was on the order of 10^{-3} . Thus the lattice constitutes not only a means of tuning the interactions and simulating condensed matter systems in the experiment, but it also plays a vital role in accurately detecting the momentum distribution of the system under investigation. The analysis of these two-body collisions in the time-of-flight dynamics is covered in greater detail in [51, 52].

¹⁸. If the lattice filling is low, as is the case in this experiment.

2.3 . Individual atom detection in 3D

As outlined in the introduction to this chapter, it is the ability to achieve single particle detection in 3D for ensembles made up of thousands of atoms that is the decisive feature for building a quantum gas experiment around $^4\text{He}^*$. Thus, this section is dedicated to the measurement apparatus and procedure that enable this unique detection method, which is at the heart of nearly all the data being analyzed throughout this work.

In the absence of an information carrier between the atoms and the measurement apparatus such as photons in optical imaging, the electronic detection mechanism capable of sensing single atoms is almost inherently linked to a preceding free fall, since the atoms themselves have to come into contact with the detector. Even though subsection 2.2.5 detailed how the use of an optical lattice facilitates the accurate detection of momentum densities after a long TOF, these considerations pertained to possible sources of problems stemming from within the atomic ensemble itself, such as interactions between the particles during the TOF. Whilst eliminating the possibility of such undesirable effects occurring is indispensable, another possible source of disturbances exists that originates from outside the system: Since the atoms are spin-polarized during the final stages of the experimental sequence, they interact with magnetic fields, both in the desirable way designed into the experimental sequence, but also inadvertently with remaining stray magnetic fields in their environment. One can usually cope with the latter aspect during the duration of the experimental sequence, where all kinds of bias and gradient fields are deliberately employed to keep the atoms in an optimal state for manipulating them. However, the moment of the free fall leading up to the detection represents a challenge in this aspect, since traps are turned off in order to release the atoms in precisely the state they were prepared in, while at the same time the distance of nearly half a meter between the trap and the detector is much larger and thus considerably more difficult to control in terms of the magnetic environment than the center of the scienc chamber itself. Previous considerations pondered the possibility of turning off the interactions between atoms to eliminate unwanted effects during the TOF, and while this option is unavailable for $^4\text{He}^*$ in terms of interparticle interactions, it does exist when it comes to the interaction of the atoms with eventual stray magnetic gradient

fields on their way to the detector. The first step of the detection sequence implies thus transferring the atoms to a magnetically neutral sublevel so as to avoid any distortion of their impact positions on the detector due to the interaction with eventual stray magnetic fields during the TOF.

2.3.1 . Raman transfer

The original way of transferring the atoms to the $m_J = 0$ sublevel in the experiment consisted in separating the sublevels of the 2^3S_1 state by applying a magnetic bias field, and subsequently driving the transfer between the sublevels with an RF wave at a frequency corresponding to the Zeeman shift. While the implementation of such an RF transfer is straightforward, the population transfer to the $m_J = 0$ level is inherently limited to 50%, since the RF wave is also resonant with the $m_J = 0 \rightarrow m_J = -1$ transition. The atoms in $m_J = -1$ are (in absolute terms) just as susceptible to being perturbed by stray magnetic gradients during the TOF as the ones in $m_J = 1$ and are thus lost from a detection standpoint, decreasing the effective detection efficiency on the total atomic ensemble by 50%. This drawback represents a significant disadvantage in the search of faint signals such as multi-particle correlations that have a detection probability that decreases with the effective detection efficiency to the power of the number of correlated particles¹⁹. Circumventing this type of issue is thus crucial in the quest to observe such signals, and a solution has been put in place that consists in replacing the RF wave with a two-photon Raman transfer in order to achieve as efficient a transfer to the desired sublevel as possible.

The Raman transfer is implemented via the intermediate $|2^3P_0, m_J = 0\rangle$ state. The magnetic bias field remains to split the Zeeman sublevels, but now the $|2^3S_1, m_J = 0\rangle$ state is specifically addressed by a 2-photon process: A σ^- polarized pump beam couples the $|2^3S_1, m_J = 1\rangle$ to the intermediary $|2^3P_0, m_J = 0\rangle$ state, which is in turn coupled to the final $|2^3S_1, m_J = 0\rangle$ state via a π polarized Stokes beam. The transfer occurs coherently via absorption of a photon from the Pump beam and subsequent stimulated emission into the Stokes beam. In the experiment co-propagating beams for the Pump and Stokes imply that no significant amount of momentum

¹⁹. For instance if some effect decreases the detection efficiency by 50% in the analysis of three-body correlations, the detection probability of a correlation event decreases to $(1/2)^3 = 0.125$. To compensate for this effect, the experiment would thus have to accumulate 8 times more data to achieve the same statistics.

is transferred to the atoms with this process. In order to avoid one-photon absorption of the Pump beam, the one-photon detuning has to be kept large, $\Delta \gg \Gamma$, while the two-photon detuning is set so that the energy difference between Pump and Stokes matches the Zeeman shift $\Delta E \simeq h \times 13$ MHz induced by the magnetic bias field.

The successful implementation of the Raman transfer has enabled a refined measurement of the quantum efficiency of the single particle detector, which was found to be equal to $\eta_{\text{MCP}} = 0.53(2)$. A detailed description of this analysis and of the Raman setup as a whole is given in [52, 53].

2.3.2 . Description of the Detector

The last piece of the experimental puzzle is also arguably its centerpiece. Single particle detectors using micro-channel plates (MCPs) are much more common in particle physics [100–102] or for the detection of charged particles [103] or high-energy photons [104, 105] than in experiments with ultracold atoms [66]. The setup that enables the single-particle detection in 3D over a dynamic range of several orders of magnitude is outlined in this section²⁰.

Signal amplification: The Micro-Channel Plates

A metastable Helium atom in the 2^3S_1 state was measured to have a secondary electron coefficient of about 70% [106]. Such a signal has to undergo further amplification before it can be acquired, which is achieved by using micro-channel plates; metallic discs with holes in the surface leading to an ensemble of coated tubes with a diameter of a few microns [107]. When polarized with a high voltage on the order of a kV the electrons ejected by the impact of a $^4\text{He}^*$ atom are accelerated and create an electron avalanche that leads to a total gain on the order of $10^3 - 10^4$ per MCP. A stack of two MCPs on top of each other is sufficient to reach the gain saturated regime [108]. The specific models currently in use on the Helium Lattice experiment are the F9142-01 MOD6 fabricated by Hamamatsu. Its principal characteristic is the open-to-air ratio that is given by sum of the surface area of all holes relative to the total surface of the disc, a figure that amounts to 90% in this case. The disc diameter is 8 cm, with a single tube being only 12 μm wide. Drilling the tubes at a surface angle of 20° ensures that an atom falling onto the surface at a right angle will eventually hit the wall of one of the tubes. The amplification

²⁰. The detector setup has not seen any significant updates over recent years, therefore the discussion is kept brief at this point. A more detailed overview is given in [50].

process preserves the information about the spatial position of the initial impact of the atom, and is recorded using a set of cross delay lines [109].

In-plane positional resolution: The Delay Lines

The delay lines are placed under the MCP stack and consist of a plane of electrical wires interwoven at a right angle, with a single delay line being made up of two parallel wires forming a waveguide. The electron shower exiting a single MCP channel generates two electronic pulses propagating in opposite directions along each delay line (see fig. 2.10). With the length of the wires precisely known, recording the arrival times of these four pulses allows to reconstruct the impact position along the line, with the third coordinate in z direction given by the time of impact on the MCP surface that can equally be reconstructed from the arrival times of the four pulses. For a detailed description of the algorithm responsible for the reconstruction of the 3D atom coordinates from the arrival time quadruplets see [50]. The first implementation of this detection scheme for $^4\text{He}^*$ was achieved at Institut d'Optique in 2005 [31].

The Time-to-digital Converter

The arrival times of the four electronic pulses of the delay lines have to be read out at a maximum bandwidth so as to not limit the detectable particle flux. This is achieved using amplifiers and Constant-Fraction Discriminators that have a bandwidth of several hundred MHz. The bottleneck in the acquisition chain in terms of maximal detectable flux is given by the time-to-digital converter (TDC) developed from an FPGA chip. In its current state the highest achievable continuous acquisition rate is around 4×10^6 particles per second [111].

Resolution and limitations of the detector

With the reconstruction of the impact coordinates being based on the quadruplets of arrival times from the delay lines, it is clear that the ability of the detector to distinguish the impact positions of two atoms in space is directly linked to the temporal resolution of the arrival times²¹. The coding step of the TDC of 10 ps is the most significant irreducible time constant in the acquisition

21. For instance in order to distinguish two atoms with impact positions on the MCP that are 1 mm apart, a temporal resolution of 2 ns is necessary.

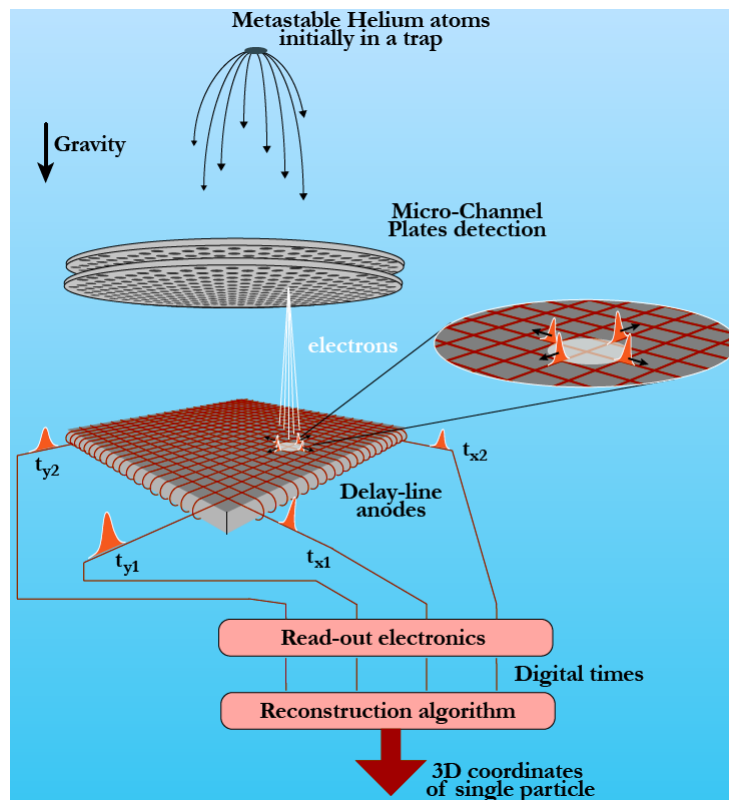


Figure 2.10 – Schematic representation of single particle detection of $^4\text{He}^*$ using MCPs and cross delay lines. The metastable atoms are measured after a long TOF and each extract an electron from the surface of an MCP. The resulting signal is amplified in the MCPs and triggers four electronic pulses on the cross delay lines below. From the arrival times of these pulses the impact positions on each of the orthogonal lines and the impact time on the MCP surface can be reconstructed, yielding the 3D position of the atom upon impact and thereby, via (2.31), its in-trap momentum. Taken from [110].

chain and limits the spatial resolution in the detector plane (referred to as the xy plane) to $60\ \mu\text{m}$. The vertical resolution is not subject to the same limitation as its coordinate is reconstructed differently from the x and y coordinates. Instead its resolution is governed by the geometric constraint of the 20° angle at which the tubes are drilled into the MCP that renders two atoms separated by less than $12\ \mu\text{m}/\tan(20)$ indistinguishable²², which limits the vertical resolution to about $33\ \mu\text{m}$. These spatial resolution limits can be converted to their corresponding in-trap momenta using (2.31), which gives a momentum resolution in k_x and k_y of about $1.5 \times 10^{-3} k_d$

²². This follows from a basic geometric consideration of the tube diameter and angle in the situation of two atoms arriving at the MCP surface at slightly different times but making contact with the inner tube wall at the same time at different depths along the tube.

and in k_z of about $9 \times 10^{-4} k_d$. These values have been confirmed experimentally, see [53].

The quantum efficiency of the detector is limited by the probability of an incoming $^4\text{He}^*$ atom to lead to a first signal in the form of an ejected electron. Once this electron has entered the chain of amplification and conversion to a quadruplet of arrival times, its detection is virtually guaranteed. Thus it is intuitive that the open-to-air ratio of the MCP plays a crucial role, since any electrons ejected from the metal surface can only be amplified if an atom falls into one of the tubes. The model currently in use is at the high end of the range of technological feasibility with an open-to-air ratio of 90%. The main factor that is currently limiting the single particle detection efficiency is the probability for the first ejected electron to continue its path down the tube, with the geometry of the MCP making it possible for this electron to escape to the outside of the tube. The quantum efficiency was measured after the implementation of the Raman transfer and found to be $\eta_{\text{MCP}} = 0.53(2)$ [52, 53], which indicates that the escape probability for an initial electron is considerable and presumably around 50%.

A further aspect to be considered for a detector capable of detecting such faint signals as a single atom is the possibility of any saturation effects at high particle flux. These are known to occur in MCPs [31, 112] due to the time that it takes for a single micro-channel to replenish its charge after a detection avalanche, which imposes an inevitable dead time within that tube during which any other atoms falling into the same tube have a lower probability of being detected. An investigation of the MCP saturation on the experiment concluded the critical flux to be on the order of 250×10^3 atoms/cm²/s [50, 51, 111], a threshold that is surpassed when working with BECs or lattice superfluids and leads to visible saturation of the densest features of the corresponding momentum distributions. Furthermore there is an additional saturation effect originating from the reconstruction algorithm, which encounters difficulties in identifying the correct time quadruplets for signals with high particle flux. These complications stem from the criteria for the assignment of delay line pulses not being error proof, as was shown in [50]. This can lead to incorrectly reconstructed atoms in the xy plane, which is why this small central plane of data is sometimes excluded in post-processing of experimental data.

On a final note, in the current setup with a distance of 43 cm between the positions of the ODT and the MCP, the ensuing long TOF leads to high-momentum parts of the distribution falling outside the detector on account of its finite size of 8 cm, which limits the accessible momentum range in the xy plane to little over the FBZ. This does not represent a significant drawback for most measurements where the essential physics of the system can be accessed from quantities measured within the FBZ, but it makes for a difference in the total detected and in-trap number that is larger than the factor given simply by the quantum efficiency η of the detector.

2.3.3 . Automating the data pipeline for large quantities of data

The ability to detect thousands of individual particles per experimental realization, coupled with the high sensitivity of a measurement apparatus capable of detecting single atoms, result in large quantities of data that make up a single dataset. This is all the more true in the search of faint signals where multi-particle correlations may have probabilities considerably below unity of being present in a single shot of the experiment. Furthermore, even if they are present, a large number of experimental repetitions is required in order to separate these signals consisting of only a handful of atoms per shot from the background made up of thousands of atoms with the necessary statistical significance. Additionally, when probing the critical regime around the phase transition where the most intriguing correlation signals are expected, the precise setup and calibration of the experiment is of utmost importance, since close to the transition a minute change in for instance the lattice intensity may drastically alter the macroscopic behavior of the system. This naturally leads to many datasets being taken in what are supposedly the same experimental conditions, but what is often only found out in post-analysis to contain a slight but crucial deviation in a key experimental parameter.

Consider for instance the lattice alignment: There exists currently no quantitative protocol for determining the best alignment of the three lattice beams with respect to the atoms and each other, with adjustments having to rely on the intuition of the experimentalist for the final steps of the fine-tuning procedure. as outlined above, an even slightly misaligned lattice can induce non-negligible heating effects in the ensemble; a fact that can only be determined after the acquisition of several hundreds of shots in the experiment since any kind of thermometry equivalent employed to gauge the temperature requires averaging over many repetitions to achieve a meaningful signal-to-noise ratio. In this case the selection of the most appropriate dataset for

any given analysis that involves probing the system across a range of configurations, such as traversing the BH phase diagram, has the potential to turn into a challenging task, and it is of vital importance that no mixup can occur in this data selection process.

There is a certain upper boundary to the efficiency range of a standard file-based organization system that stores data in directories on the computer. A given hierarchical level in such a file management system can only contain so many elements before it becomes impractical, a statement that is especially true if the characteristics by which the elements are sorted can vary across multiple dimensions. A concrete example for this experiment is a dataset taken at a certain ratio of interaction to tunnel coupling in the BH sense. The BH parameter U/J is usually the top hierarchical element in classing datasets, since the total atom number is often kept constant at the value that corresponds to unit filling in the trap center at the phase transition ($N = 5000$ atoms). If only U/J is made to vary for a series of datasets, then no complications arise in the organization. However, the level of complexity of a quantum gas experiment makes for a host of other parameters entering into contention for being possibly relevant. What is most often kept to tell different dataset at the same value of U/J apart is the acquisition date. In that sense the need to acquire a lot of shots of the experiment for a single dataset turns into an advantage, since it makes it extremely rare that multiple datasets can be taken in a single day. However, other experimental parameters may vary between datasets, and the scaling limit of the file-based organization limit has seemed within reach.

As a solution an automatic data pipeline has been set up to handle the acquisition and storage of all data without the need for manual intervention. The data is autonomously transferred from the acquisition computer to the team's main server, where it is systematically organized in an SQL database and stored in binary form. Any dataset can be accessed from anywhere on the local network, or from the outside using the lab's VPN. The database is backed up to the group's NAS, and any computer of the group can choose to automatically synchronize the database to keep local copies.

This system is extensible to any type of data storage and can be set up using the automation scripts contained in the project's [GitHub repository](#).

2.4 . Expmonitor: A Python library for the lab room

During the Covid-19 pandemic lab access was restricted, but a quantum gas experiment cannot simply be turned off in its entirety. Vacuum pumps have to keep on running to maintain the ultra-low vacuum in the experimental apparatus, especially in the science chamber. Lab temperatures need to be monitored to catch a possible A/C failure as early as possible. In this context an automatic lab monitoring system was designed and installed on the experiment that will be briefly detailed in the following. The software for the system described here is available on the project's [GitHub repository](#).

2.4.1 . System setup

The goal with the setup was to create a budget friendly fully autonomous solution that could run continuously in the background and provide essential insight into the state of lab equipment. In order to avoid having to rely on any of the existing lab computers which run the experiment and data acquisition, a new small server was installed²³ specifically for the lab monitoring. The server runs a program that polls data from all connected lab equipment periodically, stores the values in a local time-series database and displays the information on a graphical user interface that can be accessed both locally and from outside the institute via a VPN. The total cost of a new setup is below €100 and the automatic setup script builds most of what the server needs to start logging, with a setup script containing detailed instructions and total install time being less than 1h. The code base is open source and can be found at <https://www.github.com/JPBureik/experiment-monitoring>.

Most of the code base is written in Python, with only the setup script and the execution file for the Linux service being written in Shell script, while the script for the microcontroller is written in embedded C (see below). In the core of the program, each sensor is piloted via its own driver class. An abstract base class implements the abstract methods `connect`, `disconnect` and `rcv_vals` that every driver class has to overwrite in order for any of its members to be instantiated. This makes for a homogeneous interface across all connected devices that the main execution script can interact with. The abstract base class for all sensors defines the public methods `measure` and `to_db` that handle incoming values from the connected equipment and outgoing values to be written to

23. A Raspberry Pi 4B manufactured by the Raspberry Pi Foundation.

the database. In addition, it defines a public method `spike_filter` that has proven invaluable in the handling of data from analog sources. Each equipment-specific driver class defines its own conversion function and unit as class attributes (among other more specific equipment-related information such as the baudrate, timeout and port for serial connections) so that data is passed in the correct format to the main function.

The utility module contains the global the expetion handler and the driver class for the databae. InfluxDB was chosen for its optimization for storing and querying time-stamped data, which makes it a natural fit for any monitoring application. Its horizontal scalability, efficient retention policies and data downsampling allow for aggregation and reduction of data granularity as it ages, helping to manage long-term storage. In three years of data acquisition at a constant 5 second interval the net storage occupied by the database is only on the order of a handful of GB, an essential feature for ensuring compatibility with the small RaspberryPi server.

The storage solution on the server consists of a pair of USB thumb drives in RAID1 configuration, with any storage capacity over 100 GB ensuring sufficient overhead for years to come.

In order to be able to connect analog devices, a solution has been implemented that involves a microcontroller²⁴ connected to the local network. The analog devices are linked up to the analog-to-digital (ADC) ports of the microcontroller, using Zener diodes for overvoltage protection where necessary. The microcontroller executes a script that polls all analog input ports when prompted and returns the corresponding values. Communication with the server is established via TCP/IP. The server sends a message to the microcontroller that prompts the readout of the analog voltages. Network communication implies that the two devices need not be physically connected but can be placed anywhere in the local network. On the server side communication is handled by a specific driver class (`ArduinoADC`) for the microcontroller that defines the port and IP address for TCP/IP as class attributes. Using this driver class, any analog equipment will simply define an instance of the `ArduinoADC` as class attribute to handle all of the communication with the microcontroller. Since the converted signals from many analog devices might not be as precise as desired out of the box, especially in cases where a voltage conversion stage is required before the input of the ADC, a calibration script is provided in the utility module. This feature consists of a shell script that asks for the current true value (as seen on the display of the

24. Arduino Due fabricated by Adafruit, using the EthernetShield2 for TCP/IP communication.

equipment) and compares this to the value currently being read by the system. After a series of measurements it can fit the provided calibration function to the recorded data knowing the corresponding true values, and continuously update the fit parameters for the conversion function of the driver class.

If no new driver classes need to be written (see below), only the simple setup script has to be modified by the end user. This script imports the driver classes and instantiates the corresponding objects using the parameters provided in the `__init__` method. Additional settings (such as the spike filter) can be toggled via properties on the instantiated objects. This script also contains system wide parameters such as the acquisition interval and details for exception handling. A screenshot of part of the setup script is reproduced in fig. 2.11.

The system can be set up to automatically back up the contents of the server (especially the calibration settings and the InfluxDB database), either to a connected hard drive or to a NAS on the local network. The setup process for this feature is detailed in the documentation on GitHub.

2.4.2 . Surveillance of lab equipment

The main program executed by the server is completely agnostic as to the specific equipment that is connected, it simply executes the standard polling with the interface details being left to the equipment specific child class that is used to drive it. Currently the following interfaces are supported out of the box:

- Serial
- TCP/IP
- Analog
- SNMP
- USB

Polling occurs in a serial manner in order to avoid concurrency issues of multiple threads or processes trying to access the same periphery simultaneously. In principle a multi-threaded solution could be implemented so long as safeguards are put into place that ensure proper synchronization, but the time constants for most of the lab equipment are on the order of seconds when it comes to monitoring, which is fully within reach for the current solution. This situation is susceptible to change however in the case of a single long I/O operation blocking the execution, a scenario that has not occurred so far and would be specific to the connected equipment in

```

experiment-monitoring / src / expmonitor / config.py
Code Blame 59 lines (39 loc) · 1.53 KB Code 55% faster with GitHub Copilot
18
19 # Define interval [s] for data acquisition (+ execution time):
20 acq_interv = 0
21
22
23 """ ----- SENSOR SETUP ----- """
24
25
26 # Import all specific sensor classes:
27 from expmonitor.classes.phidget_tc import PhidgetTC
28 from expmonitor.classes.tpg261 import TPG261
29 from expmonitor.classes.tpg300 import TPG300
30 from expmonitor.classes.ups.eaton_ups import EatonUPS
31
32 # Setup Phidgets:
33 tc1 = PhidgetTC('Source', 4, 0)
34 tc2 = PhidgetTC('A/C', 4, 1)
35 tc3 = PhidgetTC('Lab', 4, 2)
36 tc4 = PhidgetTC('Water', 4, 3)
37
38 # Setup serial devices:
39 primary_vac = TPG261('Primary Pump', '/dev/ttyUSB0')
40 primary_vac.spike_filter.spike_threshold_perc = 1e3
41
42 # Setup analog devices via Arduino:
43 sc_vac = TPG300('Science Chamber', 2)
44 sc_vac.spike_filter.spike_threshold_perc = 1e3
45 sc_vac.spike_filter.spike_length = 2
46
47 # Setup batteries:
48 batteries = EatonUPS('Batteries', '10.117.51.129')
49
50
51 """ ----- DETAILS ----- """
52
53
54 # Exception logging:
55 overwrite_log_file = True # Replace old log file each time exec is run
56 log_full_tb = False # Log entire traceback for exceptions, not just one line
57
58 # Debugging:
59 verbose = False # Prints exception traceback to stdout

```

Figure 2.11 – Part of the configuration script for the experiment monitoring system. Each piece of equipment is instantiated from the imported driver classes. Options such as the spike filter can be toggled via properties on the instantiated objects.

question.

The continuous data acquisition is handled by a Linux Systemd service. The exception handler is set up in such a way that a measurement problem on a single piece of equipment does not block the execution; instead a report of the exception is written to the log file on the home directory

of the server.

Figure 2.12 shows a screen shot of the graphical user interface implemented using Grafana.



Figure 2.12 – Experiment monitoring GUI. The Grafana interface for the experiment monitoring system can be accessed locally or from outside the lab via a VPN. Gauges and time series plots indicate the current state of affairs of connected lab equipment, with the vertical lines corresponding to situations that trigger an automatic alert, here in the case of a lab-wide A/C failure. The limit for the lab temperature is passed at the yellow line, and after not falling below the limit in terms of its average value for a pre-set duration, an alert message is sent (red line). When the situation is back to normal, another e-mail is sent to inform the users (green line).

2.4.3 . Automatic alerts

The system also sends automatic alert e-mails in case of a pre-defined condition for any of the connected equipment. For instance, users can be rapidly alerted in case of an A/C failure in the lab or an issue with the vacuum system. A valid e-mail address from which to send the alerts

has to be provided. It is highly recommended to choose a dedicated new e-mail account for this feature, on the one hand for security reasons since in its current state the password is stored on the server, and on the other hand to avoid any issues in case of a multitude of alerts or a server malfunction²⁵. Furthermore compatibility has to be ensured between the SMTP host of the provided mail account and the security regulations of the network the server is connected to²⁶. The alert conditions for all equipment can be defined immediately through the Grafana web interface, obviating the need of modifying the server settings after its initial setup. The entire setup process for this feature is detailed in the documentation on GitHub.

The experiment monitoring system has been running with minimal maintenance for several years now and its modularity makes it readily extensible to new interfaces. The only currently known bug or problem consists in the Grafana Image Renderer is not being available for the ARM processor of the RaspberryPi. Therefore the alert e-mails do not contain a snapshot of the time series that causes the alert.

25. Some e-mail providers block users above a certain threshold of sent messages per time interval.

26. For instance, as of late 2023 Université Paris-Saclay only allows a single host, namely `smtps.universite-paris-saclay.fr` on port 465.

3 - Bogoliubov Pairing and Non-Gaussian Correlations in Interacting Bose Gases

The standout advantage of the Helium Lattice experiment presented in chapter 2 is its ability to study large many-body quantum systems that exhibit strong interactions (tuneable with the optical lattice) by measuring their 3D momentum distribution with single-atom precision (using the combination of MCPs and delay lines). A platform with such capacities is ideally suited for the study of momentum correlations between a large number of particles in strongly correlated systems. In this chapter, the first of a series of analyses that follow that line of thought is presented. These findings are the result of an investigation [32] into the characteristics of a system that exhibits strong correlations on account of strong interactions giving rise to non-linear quantum fluctuations. Even though experimental observations of such non-Gaussian correlations have been sparse so far, strongly-correlated materials represent one of the most intriguing aspects of quantum many-body physics.

Indeed, weakly-interacting systems are often characterized by Gaussian correlations, meaning that quantum fluctuations around the mean-field ground state are small and can be adequately described by a Gaussian distribution¹. In assuming that the probability distribution of the correlations is Gaussian, and thus fully characterized by its mean and variance, the correlations in the system are completely determined once the mean values and the variances of the relevant operators are known². This assumption simplifies the analysis and often allows for analytical or semi-analytical solutions. However, in strongly correlated systems or systems with significant quantum fluctuations, higher-order correlations beyond the mean and variance become important, and the Gaussian approximation may break down.

1. Mathematically, the assumption of Gaussian correlations implies that the probability distribution of a set of operators representing observables in the system can be written in terms of a Gaussian functional.

2. Note that the term "Gaussian" here is used in the context of probability distributions and statistical mechanics, and it doesn't imply that the physical observables themselves are necessarily Gaussian-distributed. Instead, it refers to the distribution of fluctuations around the mean values.

One famous example of the successful application of a Gaussian approximation is Bogoliubov theory for describing Bose gases in the context of weak interactions. This theory is a central cornerstone of descriptions of quantum fluids and superfluidity, having correctly predicted the linear spectrum of excitations, as well as the existence of a non-condensed fraction in the many-body ground state resulting from interactions. Due to momentum conservation, this so-called quantum depletion is made up of pairs of atoms with opposite momenta that are described as two-mode squeezed states, which are Gaussian and thus exhibit linear correlations.

The analysis presented in this chapter seeks out to investigate the transition from the weakly-interacting Bose gas, characterized by Bogoliubov theory and Gaussian correlations, to the strongly-correlated regime beyond Bogoliubov theory in search of complex non-Gaussian quantum fluctuations. The specific observables used to characterize the state of the system are correlation functions between two (or more) atoms in momentum space. The interaction-induced correlations between pairs of atoms at opposite momenta predicted by Bogoliubov theory were first observed on the Helium Lattice experiment [23]. The Gaussian assumption of Bogoliubov theory translates to neglecting correlations between more than two atoms, a simplification that is justified in the weakly-interacting regime. By increasing the interactions beyond the realm of the approximations that underly Bogoliubov theory, the Gaussian assumption is expected to break down due to the emergence of non-negligible correlations between more than two particles. The consequences of the arisal of such higher-order correlations for the pairing signal are unclear; there is no theory to analytically predict its behavior for larger interactions. Its evolution as a function of increasing interactions is the main focus of this chapter.

To set the context for this analysis, the first part of the chapter lays out the main aspects of Bogoliubov theory, followed by the presentation of the initial observation of the opposite-momentum pair correlation signal, with the experiments carried out with weakly-depleted BECs. In the following, interactions are increased and the evolution of the pairing signal is studied. The observed suppression of the pairing signal is associated to the emergence of complex non-Gaussian correlations stemming from the increased interactions. Finally, the behavior of the pairing signal is compared with numerical simulations which qualitatively confirm the experimental picture.

3.1 . Description of the weakly-interacting Bose gas

While problems of interacting many-particle assemblies can be addressed using quantum field theory and Green's functions, physical intuition can often become clearer by employing a more direct approach that involves simplifying the Hamiltonian in second quantization and using approximations that render the problem exactly solvable. Canonical transformations of the creation and destruction operators in the occupation-number Hilbert space do not alter the original commutation relations that completely define these operators. In the case of the interacting Bose gas, the approximation of weak interactions allows for the diagonalization of the quadratic part of the Hamiltonian through a unitary transformation conceived by N. Bogoliubov in a landmark contribution to the understanding of quantum fluids and superfluid phenomena [22]. The foundational framework that he laid in inferring both the excitation spectrum and the form of the many-body ground state stands as a cornerstone of the field of weakly-interacting Bose gases until today. By approximating the interacting system as a non-interacting one, on top of which interaction-induced quantum fluctuations [113] are incorporated as a perturbation, Bogoliubov deduced the nature of the low-lying excitations as being collective oscillations of the condensate density that give rise to superfluid behavior. Lee, Huang and Yang later gave a correction to Bogoliubov's mean field result [114-116] that included a contribution from atoms outside the $\mathbf{k} = 0$ mode the many-body ground state. Bogoliubov deduced that the processes imparting finite momentum to these atoms occur pairwise due to momentum conservation, with both atoms carrying opposite momentum. In this way, momentum correlations evolve intuitively from the non-interacting starting point. Bogoliubov theory played a foundational role at the outset of the study of emergent phenomena in many-body quantum systems, and its key aspects are briefly detailed in the following. Since the main focus of this chapter concerns the physics beyond the weakly-interacting regime, the reader is referred to the group's previous theses [52,53] for a more detailed exposition of Bogoliubov theory and the initial observation of its predicted momentum correlated pairs on the Helium Lattice experiment [23].

3.1.1 . Bogoliubov approximation

Consider a homogeneous Bose gas in a box of volume L^3 . In the absence of interactions, there are no correlations between the populations of different momentum modes \mathbf{k}_i , with fluc-

tuations of their populations having an entirely incoherent (thermal) origin. Correlations arise in the presence of interactions. In their most basic form, two incoming modes \mathbf{k}_1 and \mathbf{k}_2 are coupled to two outgoing modes \mathbf{k}_3 and \mathbf{k}_4 in a four-wave mixing process. Two-body repulsive contact interactions can be modeled by the potential $\delta(\mathbf{r} - \mathbf{r}')$ with interaction strength $U = 4\pi\hbar^2 a_s/m$ and s -wave scattering length $a_s > 0$ [117]. Modeling interactions with this potential is reasonable when the gas is dilute and the mean distance between atoms is much larger than the scattering length $a_s n^{1/3} \ll 1$, where n is the density and $a_s = 7.5$ nm for He*. In second quantization this system's Hamiltonian is given by

$$\hat{H} = \int \frac{\hbar^2}{2m} \nabla \hat{\Psi}^\dagger(\mathbf{r}) \nabla \hat{\Psi}(\mathbf{r}) d\mathbf{r} + \frac{U}{2} \int \hat{\Psi}^\dagger(\mathbf{r}) \hat{\Psi}^\dagger(\mathbf{r}') \delta(\mathbf{r} - \mathbf{r}') \hat{\Psi}(\mathbf{r}) \hat{\Psi}(\mathbf{r}') d\mathbf{r}' d\mathbf{r} \quad (3.1)$$

The field operators $\hat{\Psi}$ and $\hat{\Psi}^\dagger$ can be written in the plane wave basis:

$$\hat{\Psi}(\mathbf{r}) = \frac{1}{L^{3/2}} \sum_{\mathbf{k}} \hat{a}_{\mathbf{k}} e^{i\mathbf{k}\cdot\mathbf{r}} \quad (3.2)$$

and

$$\hat{\Psi}^\dagger(\mathbf{r}) = \frac{1}{L^{3/2}} \sum_{\mathbf{k}} \hat{a}_{\mathbf{k}}^\dagger e^{-i\mathbf{k}\cdot\mathbf{r}} \quad (3.3)$$

with $\hat{a}_{\mathbf{k}}$ and $\hat{a}_{\mathbf{k}}^\dagger$ the operators that destroy and create a particle of momentum \mathbf{k} , respectively, and that satisfy the Bose commutation relations

$$\left[\hat{a}_{\mathbf{k}}, \hat{a}_{\mathbf{k}'}^\dagger \right] = \delta_{\mathbf{k},\mathbf{k}'} \quad \text{and} \quad \left[\hat{a}_{\mathbf{k}}, \hat{a}_{\mathbf{k}}^\dagger \right] = \left[\hat{a}_{\mathbf{k}'}, \hat{a}_{\mathbf{k}'}^\dagger \right] = 0 \quad (3.4)$$

Using the momentum space decompositions (3.2) and (3.3) the Hamiltonian (3.1) can be written in the plane wave basis:

$$\hat{H} = \sum_{\mathbf{k}} \epsilon_{\mathbf{k}} \hat{a}_{\mathbf{k}}^\dagger \hat{a}_{\mathbf{k}} + \frac{U}{2L^3} \sum_{\mathbf{k},\mathbf{k}',\mathbf{k}''} \left(\hat{a}_{\mathbf{k}}^\dagger \hat{a}_{\mathbf{k}'}^\dagger \hat{a}_{\mathbf{k}''} \hat{a}_{\mathbf{k}+\mathbf{k}'-\mathbf{k}''} + \text{c.c.} \right) \quad (3.5)$$

with the kinetic energy of a particle in momentum mode \mathbf{k} given by

$$\epsilon_{\mathbf{k}} = \frac{\hbar^2 k^2}{2m} \quad (3.6)$$

With weak interactions being a key assumption of a theory primarily concerned with low energy excitations, scattering processes are presumed to be elastic, and thus momentum is conserved in the interaction term of (3.5), which translates the phase-matching condition $\mathbf{k}_1 + \mathbf{k}_2 = \mathbf{k}_3 + \mathbf{k}_4$.

An ideal Bose gas ($U = 0$) is entirely Bose condensed at zero temperature with all particles occupying the single-particle ground state, which corresponds essentially to the $\mathbf{k} = \mathbf{0}$ mode: the BEC. Bogoliubov's approximation of weak interactions manifests itself in the assumption that as U takes on a finite but small value, the departure from a perfect BEC is sufficiently insignificant in terms of the occupation numbers to assume that the single-particle ground state will continue to be strongly populated, $\langle N_0 \rangle \gg 1$. Mathematically, this translates to neglecting the operator character³ of \hat{a}_0 and \hat{a}_0^\dagger and instead treating them as ordinary numbers, $a_0, a_0^\dagger \approx \sqrt{N_0}$. This amounts to treating the condensate mode as a classical field. Treating the interaction potential as a weak perturbation provides the basis for a systematic expansion of the Hamiltonian (3.5): $\hat{H} = \sum_{\mathbf{k}} \epsilon_{\mathbf{k}} \hat{a}_{\mathbf{k}}^\dagger \hat{a}_{\mathbf{k}} + \hat{V}_{\text{int}}$ where the interaction potential is now approximated as $\hat{V}_{\text{int}} \approx \hat{V}^{(2)} + \hat{V}^{(3)} + \hat{V}^{(4)}$ with the individual orders equal to

$$\hat{V}^{(2)} = \frac{UN_0^2}{2L^3} + \frac{U}{2L^3} \sum_{\mathbf{k} \neq \mathbf{0}} \left(\hat{a}_{\mathbf{k}}^\dagger \hat{a}_{-\mathbf{k}}^\dagger + \text{c.c.} \right) \quad (3.7a)$$

$$\hat{V}^{(3)} = \frac{U\sqrt{N_0}}{\sqrt{2}L^{3/2}} \sum_{\mathbf{k}, \mathbf{k}' \neq \mathbf{0}} \left(\hat{a}_{\mathbf{k}+\mathbf{k}'}^\dagger \hat{a}_{-\mathbf{k}}^\dagger \hat{a}_{\mathbf{k}} + \text{c.c.} \right) \quad (3.7b)$$

$$\hat{V}^{(4)} = \frac{U}{2L^3} \sum'_{\mathbf{k}, \mathbf{k}', \mathbf{k}''} \left(\hat{a}_{\mathbf{k}+\mathbf{k}'-\mathbf{k}''}^\dagger \hat{a}_{\mathbf{k}''}^\dagger \hat{a}_{\mathbf{k}'} \hat{a}_{\mathbf{k}} + \text{c.c.} \right) \quad (3.7c)$$

where the sum \sum' in the last term excludes $\mathbf{k}_i = \mathbf{0}$ and $\mathbf{k} + \mathbf{k}' + \mathbf{k}'' = \mathbf{0}$.

3.1.2 . Many-body ground state

In a further implication of Bogoliubov's approximation of weak interactions, the number of particles outside the $\mathbf{k} = \mathbf{0}$ mode is presumed to be small, while the vast majority of particles will continue to occupy the single-particle ground state, $N_{\mathbf{k}=\mathbf{0}} = N_0 \approx N$, with only a small fraction

³. Specifically, the approximation is that, with $\langle N_0 \rangle \gg 1$ strongly populated, the prefactors $\sqrt{N_0}$ and $\sqrt{N_0 + 1}$ for \hat{a}_0 and \hat{a}_0^\dagger , respectively, are considered equal, and thus their commutator vanishes.

of the total atom number N removed from the BEC by interactions. Under these conditions the interaction potential \hat{V}_{int} can be truncated and only the quadratic term (3.7a) is retained, which neglects all interactions outside of the condensate⁴. The Hamiltonian in Bogoliubov approximation is thus given by

$$\hat{H} = \frac{Un_0N_0}{2} + \sum_{\mathbf{k} \neq \mathbf{0}} (\epsilon_{\mathbf{k}} + 2Un_0) \hat{a}_{\mathbf{k}}^\dagger \hat{a}_{\mathbf{k}} + \frac{Un_0}{2} \sum_{\mathbf{k} \neq \mathbf{0}} (\hat{a}_{\mathbf{k}}^\dagger \hat{a}_{-\mathbf{k}}^\dagger + \text{c.c.}) \quad (3.8)$$

with the spatial density in the condensate mode $n_0 = N_0/L^3$.

The first of these terms corresponds to the interaction energy of the particles occupying the $\mathbf{k} = \mathbf{0}$ mode; the second to the kinetic energy and Hartree and Fock terms of the interaction between particles in the $\mathbf{k} = \mathbf{0}$ and $\mathbf{k} \neq \mathbf{0}$ modes, respectively; and the final term to the creation or annihilation of pairs of atoms in finite momentum modes at opposite momenta \mathbf{k} and $-\mathbf{k}$ (diagrammatically shown in fig. 3.1).

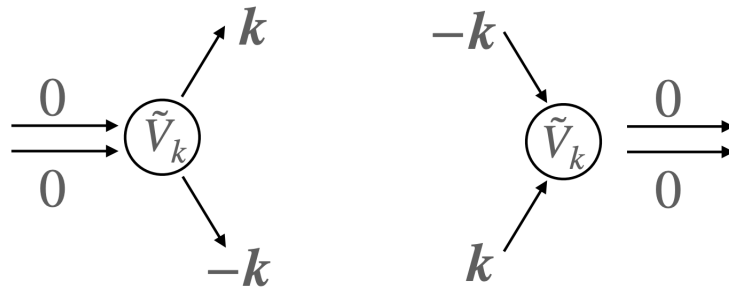


Figure 3.1 – Diagram of the pair creation and annihilation processes induced by interactions. The interactions described by $\hat{V}^{(2)}$ induce correlations between the momentum modes \mathbf{k} and $-\mathbf{k}$. Taken from [118].

Neglecting orders above $V^{(2)}$ in the interaction potential amounts to linearizing the quantum fluctuations, as now only pairwise correlations remain, with phase matching ensuring their opposition in momentum.

4. Note that it is this approximation of retaining only terms up to $\hat{V}^{(2)}$ in \hat{V}_{int} that will be relinquished in the second part of the chapter where interactions are larger and higher-order processes can no longer be neglected.

3.1.3 . The excitation spectrum

With quantum fluctuations linearized, the Hamiltonian (3.8) describes a bosonic Gaussian state, since it is a quadratic form in the creation and destruction operators. As such, it can be solved exactly by diagonalizing it with a canonical transformation. The so-called Bogoliubov transformation [22] consists in introducing the quasi-particle creation and annihilation operators $\hat{b}_{\mathbf{k}}^\dagger$ and $\hat{b}_{\mathbf{k}}$ defined by

$$\hat{b}_{\mathbf{k}} = u_{\mathbf{k}}\hat{a}_{\mathbf{k}} + v_{-\mathbf{k}}^*\hat{a}_{-\mathbf{k}}^\dagger \quad (3.9a)$$

$$\hat{b}_{\mathbf{k}}^\dagger = u_{\mathbf{k}}^*\hat{a}_{\mathbf{k}}^\dagger + v_{-\mathbf{k}}\hat{a}_{-\mathbf{k}} \quad (3.9b)$$

In order for the transformation to be canonical, the quasi-particle operators have to fulfill the bosonic commutation relations

$$\langle [\hat{b}_{\mathbf{k}}, \hat{b}_{\mathbf{k}'}^\dagger] \rangle = \delta_{\mathbf{k},\mathbf{k}'} \quad \text{and} \quad \langle [\hat{b}_{\mathbf{k}}, \hat{b}_{\mathbf{k}}^\dagger] \rangle = \langle [\hat{b}_{\mathbf{k}'}, \hat{b}_{\mathbf{k}'}^\dagger] \rangle = 0 \quad (3.10)$$

The first of these conditions is fulfilled by imposing the restriction $|u_{\mathbf{k}}|^2 - |v_{-\mathbf{k}}|^2 = 1$ on the complex numbers $u_{\mathbf{k}}$ and $v_{-\mathbf{k}}$, leaving only their ratio to be determined. This is achieved by requiring that the Hamiltonian be explicitly diagonal in the quasi-particle operators, which imposes the additional condition $\langle \hat{b}_{\mathbf{k}}^\dagger \hat{b}_{-\mathbf{k}}^\dagger \rangle = \langle \hat{b}_{\mathbf{k}} \hat{b}_{-\mathbf{k}} \rangle = 0$. This determines $u_{\mathbf{k}}$ and $v_{-\mathbf{k}}$ as

$$u_{\mathbf{k}} = \sqrt{\frac{\epsilon_{\mathbf{k}} + gn_0}{2E_{\mathbf{k}}} - \frac{1}{2}} \quad (3.11a)$$

$$v_{-\mathbf{k}} = -\sqrt{\frac{\epsilon_{\mathbf{k}} + gn_0}{2E_{\mathbf{k}}} - \frac{1}{2}} \quad (3.11b)$$

with the Bogoliubov dispersion relation giving the quasi-particle energy as

$$E_{\mathbf{k}} = \sqrt{\epsilon_{\mathbf{k}}(\epsilon_{\mathbf{k}} + 2gn_0)} \quad (3.12)$$

and diagonalizing the Hamiltonian in the quasiparticle basis:

$$\hat{H}_{\text{Bogo}} = E_{\text{LHY}} + \sum_{\mathbf{k}} \epsilon_{\mathbf{k}} \hat{b}_{\mathbf{k}}^{\dagger} \hat{b}_{\mathbf{k}} \quad (3.13)$$

which is given by the energy associated to the non-interacting quasiparticles in addition to the Lee-Huang-Yang energy correction E_{LHY} which arises from no longer considering the interaction potential as a delta function [114]. In numerous systems [119–123], experimental observations have confirmed the highly successful prediction of the excitation spectrum (3.12) made by Bogoliubov theory. The system's superfluid characteristics are linked to the linear behavior of (3.12) at low momenta [124]:

$$E_{\mathbf{k}} \xrightarrow{k \rightarrow 0} \hbar k \sqrt{\frac{gn_0}{m}} \quad (3.14)$$

which is the dispersion relation of phonons, with the sound velocity $c = \sqrt{gn_0/m}$ representing the threshold below which an impurity can move through the gas without undergoing scattering. At high momenta, on the other hand, (3.12) approaches the free-particle dispersion relation (3.6):

$$E_{\mathbf{k}} \xrightarrow{k \rightarrow \infty} \epsilon_{\mathbf{k}} \quad (3.15)$$

In this limit the quasi-particle operators become equivalent to the particle operators, since $v_{\mathbf{k}} \xrightarrow{k \rightarrow \infty} 0$ and $u_{\mathbf{k}} \xrightarrow{k \rightarrow \infty} 1$ imply $\hat{b}_{\mathbf{k}} \xrightarrow{k \rightarrow \infty} \hat{a}_{\mathbf{k}}$.

Thus, Bogoliubov quasi-particles as defined by (3.9) are phonons at low momenta and free particles at high momenta. The characteristic length scale associated to the transition between these two regimes occurring at $\epsilon_{\mathbf{k}} \simeq gn_0$ is the so-called healing length

$$\xi = \sqrt{\frac{\hbar^2}{2mgn_0}} \quad (3.16)$$

and represents the spatial extent over which a local perturbation of the density is smoothed back to the bulk density of the condensate.

The Bogoliubov approach characterizes the excitations of the weakly-interacting Bose gas as non-interacting quasi-particles. Consequently, these quasi-particles exhibit ideal bosonic behavior and are populated at finite temperatures according to the Bose distribution:

$$\langle \hat{b}_{\mathbf{k}}^\dagger \hat{b}_{\mathbf{k}} \rangle = \frac{1}{e^{E_{\mathbf{k}}/k_B T} - 1} \quad (3.17)$$

which implies that at zero temperature the quasi-particle population is

$$\langle \hat{b}_{\mathbf{k}}^\dagger \hat{b}_{\mathbf{k}} \rangle_{T=0} = 0 \quad (3.18)$$

Using the quasi-particle operator definitions (3.9), (3.17) can be used to express the population of the free particles as

$$\langle \hat{a}_{\mathbf{k}}^\dagger \hat{a}_{\mathbf{k}} \rangle = (|u_{\mathbf{k}}|^2 + |v_{\mathbf{k}}|^2) \langle \hat{b}_{\mathbf{k}}^\dagger \hat{b}_{\mathbf{k}} \rangle + |v_{\mathbf{k}}|^2 = \frac{|u_{\mathbf{k}}|^2 + |v_{\mathbf{k}}|^2}{e^{E_{\mathbf{k}}/k_B T} - 1} + |v_{\mathbf{k}}|^2 \quad (3.19)$$

which can be seen to contain two contributions: The first term corresponds to the so-called thermal depletion, constituted of quasi-particles excited by finite temperature, since this term vanishes at $T = 0$. The emergence of the second term stems from the non-commutation of the bosonic creation and annihilation operators, signifying an inherently quantum phenomenon. This term is present even at zero temperature and implies that $\langle \hat{a}_{\mathbf{k}}^\dagger \hat{a}_{\mathbf{k}} \rangle_{T=0} \neq 0$. Consequently, the many-body ground state contains a fraction of atoms with finite momentum outside the $\mathbf{k} = 0$ mode: the so-called quantum depletion. These states are not populated by temperature, but rather by the interplay of interactions and quantum fluctuations.

It is of note that correlations between particles at opposite momenta also occur in a plethora of other systems, such as parametric down-conversion [125], dissociation of diatomic molecules [126], and elastic collisions in high-energy physics [127] or with Bose-Einstein condensates [128]. The significant distinction with regards to the mechanism derived in Bogoliubov theory resides in the fact that the $\mathbf{k}/ - \mathbf{k}$ pairs appear in the weakly-interacting Bose gas as a result of quantum fluctuations in an equilibrium state, as opposed to the examples cited above which all constitute out-of-equilibrium effects. Indeed, the many-body ground state is made up of two contributions: The coherent state in the $\mathbf{k} = 0$ mode is in a coherent superposition with two-mode squeezed states of pairs of opposite momenta $\mathbf{k}/ - \mathbf{k}$ [22, 114]. Consequently, the wavefunction of this ground state⁵ is expressed as a coherent superposition of both contributions:

5. (3.20) shares the same form as the Bardeen-Cooper-Schrieffer ground state for superconductive systems [129] that harbor fermionic Cooper pairs at opposite momenta [130].

$$|\Psi_{\text{GS}}\rangle \propto \exp\left(\sqrt{N_0}\hat{a}_0^\dagger + \sum_{\mathbf{k} \neq \mathbf{0}} \frac{v_{\mathbf{k}}}{u_{\mathbf{k}}} \hat{a}_{-\mathbf{k}}^\dagger \hat{a}_{\mathbf{k}}^\dagger\right) |0\rangle \quad (3.20)$$

It is noteworthy that the thermal depletion is primarily associated with single-particle excitations, except at very small momenta ($k\xi \ll 1$), where a quasi-particle exhibits a pronounced phononic character with $|u_{\mathbf{k}}| \sim |v_{\mathbf{k}}|$. To effectively detect Bogoliubov pairs, it is essential to work at low temperatures, ensuring that the contribution of thermally depleted (incoherent) atoms is minimized. This condition corresponds to entering the low-temperature regime ($k_B T/\mu \ll 1$). In the optical dipole trap, this ratio is approximately unity ($k_B T/\mu \approx 0.75$) [131], given the constraints of evaporative cooling. To mitigate the influence of the thermal depletion, the optical lattice is used to increase the interactions (see chapter 2), and thereby the term gn_0 in (3.11).

In the presence of an optical lattice, a Bogoliubov Hamiltonian of the form of (3.13) can be derived for the Bose-Hubbard model [132,133], involving the effective mass m^* and replacing the interaction constant g with the on-site interaction energy $U = g \int |\text{dr}\omega_{0,0}(\mathbf{t})|^4$. No extension of the theory exists, however, for the system realized in the experiment of 3D lattice bosons with an additional harmonic confinement. Comparisons with theory can therefore only be made via numerical simulations.

3.2 . Normalized two-body correlation functions

Having established the emergence of correlations at opposite momenta in the many-body ground state (3.20) described by Bogoliubov theory, the more practical questions arises of the choice of observable best suited to reveal the presence of these atom pairs in a weakly-interacting Bose gas. As shown in the preceding section, these pairs populate the quantum depletion via interaction processes that correlate them at opposite momentum. By analogy with quantum optics [134,135] such types of momentum correlations can be quantified by two-body correlators in second quantization of the form

$$G^{(2)}(\mathbf{k}, \mathbf{k}') = \langle \hat{a}_{\mathbf{k}}^\dagger \hat{a}_{\mathbf{k}'}^\dagger \hat{a}_{\mathbf{k}} \hat{a}_{\mathbf{k}'} \rangle \quad (3.21)$$

where the normal operator ordering arises from the destruction of the ${}^4\text{He}^*$ atom upon measurement in the same way as it applies to detected photons. The linear nature of Bogoliubov's transformation implies that the Gaussian statistics [136] inherent to the eigenstates of (3.13) pertain not only to the quasi-particles described by (3.9) but also to the real particles, so that Wick's theorem can be applied [137] to decompose (3.21):

$$\begin{aligned} G^{(2)}(\mathbf{k}, \mathbf{k}') &= \langle \hat{a}_{\mathbf{k}}^\dagger \hat{a}_{\mathbf{k}'}^\dagger \rangle \langle \hat{a}_{\mathbf{k}} \hat{a}_{\mathbf{k}'} \rangle + \langle \hat{a}_{\mathbf{k}}^\dagger \hat{a}_{\mathbf{k}'} \rangle \langle \hat{a}_{\mathbf{k}'}^\dagger \hat{a}_{\mathbf{k}} \rangle + \langle \hat{a}_{\mathbf{k}}^\dagger \hat{a}_{\mathbf{k}'} \rangle \langle \hat{a}_{\mathbf{k}'}^\dagger \hat{a}_{\mathbf{k}} \rangle \\ &= |\langle \hat{a}_{\mathbf{k}}^\dagger \hat{a}_{\mathbf{k}'}^\dagger \rangle|^2 + \rho(\mathbf{k})\rho(\mathbf{k}') + |\langle \hat{a}_{\mathbf{k}}^\dagger \hat{a}_{\mathbf{k}'} \rangle|^2 \end{aligned} \quad (3.22)$$

with momentum density $\rho(\mathbf{k}) = \langle \hat{a}_{\mathbf{k}}^\dagger \hat{a}_{\mathbf{k}} \rangle$. The first term of 3.22 is referred to as anomalous two-body correlations and contains correlations between opposite momentum modes \mathbf{k} and $-\mathbf{k}$. The term anomalous stems from the apparent non-conservation of particle numbers. Note, however, that the BEC essentially serves as a reservoir of particles and does not appear in the calculations since it is described as a classical field. Besides the atom pairs in the quantum depletion, quasi-particles at opposite momenta contribute to this term in the low-momentum regime $k\xi \ll 1$ where they behave essentially like phonons. Excluding this contribution, along with the one of the condensed atoms in the $\mathbf{k} = \mathbf{0}$ mode, therefore imposes restrictions on the size of the measurement volume.

In working with lattice superfluids, the momentum distribution consists of the Bragg diffraction pattern of a coherent matter wave released from an optical lattice, with momentum peaks of width $\sim 1/L_{\text{BEC}}^3$ [138] reflecting the periodicity of the latter (as seen for the momentum distributions in fig. 3.2 and 3.4). The extension in momentum space of the quantum depletion, on the other hand, is approximately given by the inverse healing length $1/\xi \gg 1/L_{\text{BEC}}$, which corresponds to a momentum volume much larger than the one occupied by the BEC, a statement that has been shown to also pertain to the thermal depletion at the temperatures of the experiment [139]. In order to exclude the condensed atoms which do not exhibit correlations at opposite momenta, the measurement volume Ω_k for the analysis of the $\mathbf{k}/-\mathbf{k}$ pairs is chosen to exclude the $\mathbf{k} = \mathbf{0}$ mode and probe only the depletion part of the momentum distribution $\Omega_k = 0.15 k_d \leq |k_{x,y,z}| \leq 0.85 k_d$. Since for the minimum value of \mathbf{k} this already corresponds to

$k\xi \approx 0.85 k_d$, this choice of measurement volume also excludes the contribution of thermally depleted atoms to the anomalous correlation signal.

In order to increase the signal-to-noise ratio and reduce the dimensionality of the correlation function from 6D to 3D, 3.22 is computed over the modes \mathbf{k} and $\delta\mathbf{k} - \mathbf{k}$ and integrated over Ω_k :

$$G_A^{(2)}(\delta\mathbf{k}) = \int_{\Omega_k} d\mathbf{k} G^{(2)}(\mathbf{k}, \delta\mathbf{k} - \mathbf{k}) = \int_{\Omega_k} d\mathbf{k} \langle \hat{a}_{\mathbf{k}}^\dagger \hat{a}_{\delta\mathbf{k}-\mathbf{k}}^\dagger \hat{a}_{\mathbf{k}} \hat{a}_{\delta\mathbf{k}-\mathbf{k}} \rangle \quad (3.23)$$

and subsequently normalized to flatten the contribution of the uncorrelated background of the momentum density:

$$g_A^{(2)}(\delta\mathbf{k}) = \frac{\int_{\Omega_k} d\mathbf{k} \langle \hat{a}_{\mathbf{k}}^\dagger \hat{a}_{\delta\mathbf{k}-\mathbf{k}}^\dagger \hat{a}_{\mathbf{k}} \hat{a}_{\delta\mathbf{k}-\mathbf{k}} \rangle}{\int_{\Omega_k} d\mathbf{k} \rho(\mathbf{k}) \rho(\delta\mathbf{k} - \mathbf{k})} \quad (3.24)$$

With the definition of (3.24) a peak at $\delta\mathbf{k} = \mathbf{0}$ in the amplitude of $g_A^{(2)}(\delta\mathbf{k})$ identifies thus the presence of $\mathbf{k}/-\mathbf{k}$ pairs.

3.2.1 . Initial observation of anomalous two-body correlations

As outlined in chapter 2, the experiment begins with the production of a He* BEC in a crossed optical dipole trap [68] which is adiabatically loaded into a 3D optical lattice [97] used to increase interactions and the quantum depletion [23], modeling the Bose-Hubbard Hamiltonian (2.19). This first series of experiments is carried out in a shallow lattice with a value of the Bose-Hubbard parameter $U/J = 5$ corresponding to the weakly-interacting regime. With a condensed fraction of $f_c = N_0/N \simeq 84\%$ the cloud is thus in the superfluid state far from the Mott insulator transition at $U/J = 26(1)$ [140]. A normalized 1D cut of its momentum density is included in fig. 3.4. A total atom number of $N = 5.0(7) \times 10^3$ ensures unity lattice filling and circumvention of interactions during the TOF [99]. As mentioned in the previous chapter, the residual harmonic confinement of the lattice beams implies that the quasi-momentum is not a good quantum number, which leads to a reduction in the amplitudes of correlation functions as compared to those measured in a homogeneous lattice potential. The 3D single-atom resolved distributions measured by the combination of MCPs with delay lines [111] constitute the raw experimental data of in-trap particle momenta [139] from which the correlation functions are calculated. An example of a single shot

of the momentum distribution is shown in fig 3.2. A typical dataset consists of approximately 2500 such shots.

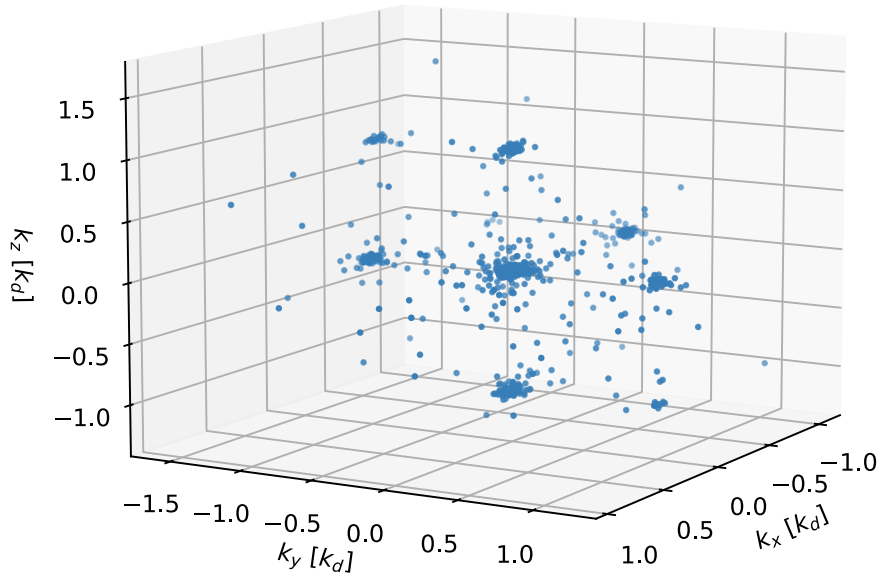


Figure 3.2 - 3D momentum distribution recorded in the experiment. Single-shot experimental distribution of individual atoms in momentum space, from which momentum correlations are computed.

The resulting normalized anomalous two-body correlations (3.24) are plotted in figure 3.3 for all three axes of the optical lattice.

Figure 3.3 shows clear correlation peaks at $\delta\mathbf{k} = \mathbf{0}$ for all three axes of the optical lattice, constituting the first experimental observation of Bogoliubov's correlated atom pairs in the depletion of a weakly-interacting Bose gas [23]. For more details on this observation, refer to the group's previous theses [52, 53], where this correlation signal was among other things shown to disappear with increasing temperature (highlighting its quantum origin) and conform to the characteristics expected for two-mode squeezed states such as linear scaling with the inverse density and relative number squeezing.

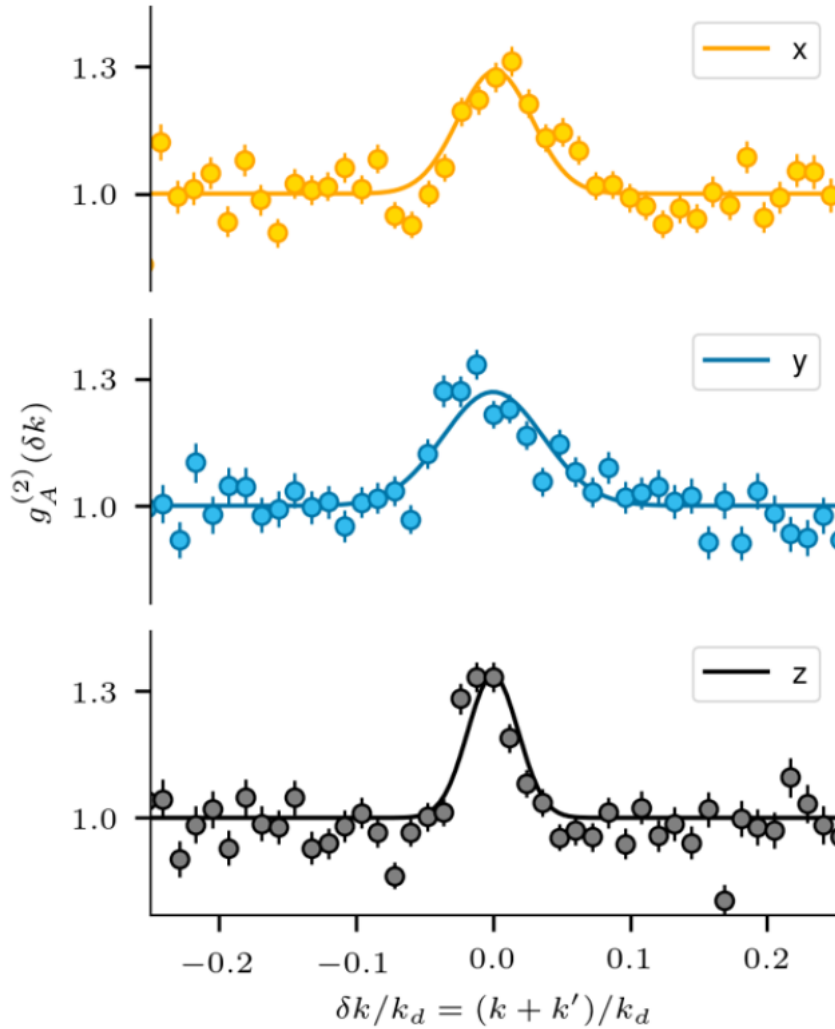


Figure 3.3 – Anomalous correlations revealing pairs of atoms at opposite momenta. One-dimensional cross-sections of $g_A^{(2)}(\delta\mathbf{k})$ are taken along the three lattice axes, with transverse integration using $\delta k_{\perp} = 3.0 \times 10^{-2} k_d$ and a longitudinal voxel size of $\delta k_{\parallel} = 1.2 \times 10^{-2} k_d$. Gaussian functions (solid lines) are used to fit the data, and error bars are determined from the inverse square root of the voxel count.

3.2.2 . Evolution of normalized two-body correlations with interactions

As alluded to in the introduction to this chapter, the main focus of this chapter is on the evolution of this pairing mechanism as interactions are increased beyond the weakly-interacting regime. As outlined in the first part, the theory predicting two-body correlations of the form observed in fig. 3.3 is based on the assumption of interactions being sufficiently weak to lend

themselves to a perturbative treatment. While the initial observation of these momentum correlated pairs has constituted a significant step towards validating Bogoliubov's prediction from over 70 years ago, nothing is said in his theory about the fate of these correlations as interactions are increased beyond the realm of its assumptions. Intuitively, the many-body ground state should continue to contain characteristic signatures of the interaction effects in the system that can be revealed through momentum correlations. Extending the investigation of momentum correlations from the weakly- to the strongly-interacting regime represents thus a natural approach for determining the fate of Bogoliubov's momentum pairing throughout these different regimes and possibly establishing the limit of validity of Bogoliubov theory for interacting Bose gases.

The most natural way to extend the analysis presented in the first part of this chapter is to apply the same procedure to experimental data taken with higher values of interaction $U/J > 5$. In an effort to investigate the fate of the correlation signal presented in figure 3.3 as interactions are increased, the experiment is repeated for interaction values in the range $2 \leq U/J \leq 22$, entering the strongly-interacting regime while steering clear of the critical regime at the (finite-temperature) Mott transition at $u_c = 26(1)$ [140]. Correspondingly, figures 3.4a and 3.4b indicate the presence of contrasted Bragg diffraction peaks associated to the presence of large BECs in the momentum density profiles of all datasets, including the one shown in figure 3.3.

Figure 3.4c indicates a decrease from about 90% to about 20% in the condensed fraction $f_c = N_0/N$ as interactions are increased from $U/J = 2$ to 22. In the momentum distributions this manifests as an increase of more than one order of magnitude in the depletion density around the edge of the FBZ at $k = 0.5 k_d$, clearly visible in the semi-logarithmic scale of fig. 3.4b. It is important to note that the reduced temperature T/J is constant (within error bars) for all the datasets [97], implying that this increase in the depletion density is predominantly the result of the change in interactions, rather than being due to heating.

The size of the measurement volume is slightly reduced around the edge of the FBZ with respect to the first part of this chapter in order to increase the amplitudes of the anomalous correlations, which are proportional to the inverse density as a general property of two-mode squeezed states. Ω_k now corresponds to a cubic corona constituting the difference in volume between two

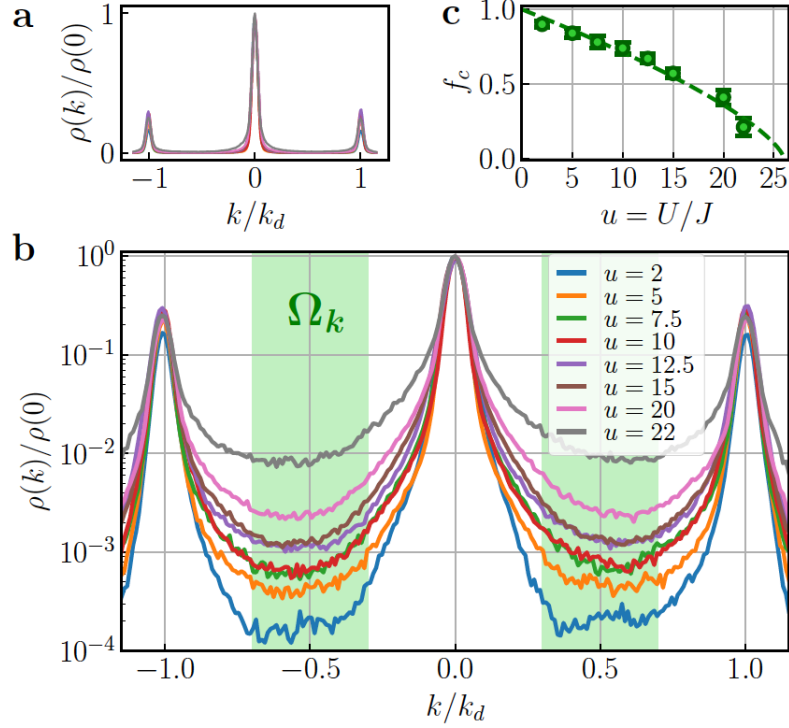


Figure 3.4 - Momentum density profiles. a Normalized 1D cuts of the momentum densities $\rho(k)/\rho(0)$ for the datasets used in this analysis with varying interactions $2 \leq U/J \leq 22$. b Same data as a in semi-log scale. The green shaded area indicates the measurement volume Ω_k of the depletion over which the two-body correlations are computed. c Condensed fraction $f_c = N_0/N$ as a function of the interaction strength, calculated following the procedure outlined in appendix A of [53]. The dashed line is a guide to the eye $\propto (1 - u/u_c)^{2\beta}$ with $\beta = 0.3485$ and $u_c = 26$ [140]. Vertical error bars correspond to fit uncertainties in determining the inflection point of the double structure in the momentum densities [53].

cubes of half-radii $0.7 k_d$ and $0.3 k_d$, which implies $1.8 \leq |k|\xi \leq 3.0$ at $U/J = 2$ and $1.2 \leq |k|\xi \leq 2.0$ at $U/J = 22$ and thereby continues to exclude the phononic part of the thermal depletion ($|k|\xi \ll 1$).

There are two different mechanisms that give rise to peaks in the two-body correlation function $g^{(2)}(\mathbf{k}, \mathbf{k}')$ [23]: The normal and the anomalous correlations. The latter is located at opposite momenta $\mathbf{k}' = -\mathbf{k}$ and is caused by the interaction-induced quantum fluctuations at the heart of Bogoliubov theory defined in (3.24). The former is located at $\mathbf{k}' = \mathbf{k}$ and corresponds to the bosonic bunching of Hanbury-Brown and Twiss (HBT) correlations:

$$g_{\text{HBT}}^{(2)}(0) = \frac{\sum_{\mathbf{k} \in \Omega_k} \langle \hat{a}_{\mathbf{k}}^\dagger \hat{a}_{\mathbf{k}}^\dagger \hat{a}_{\mathbf{k}} \hat{a}_{\mathbf{k}} \rangle}{\sum_{\mathbf{k} \in \Omega_k} \langle N_{\mathbf{k}} \rangle^2} \quad (3.25)$$

As for fig. 3.3 both of these correlation peaks can be fitted with Gaussian functions to extract their amplitudes. The result for all datasets $2 \leq U/J \leq 20$ is show in figure 3.5.

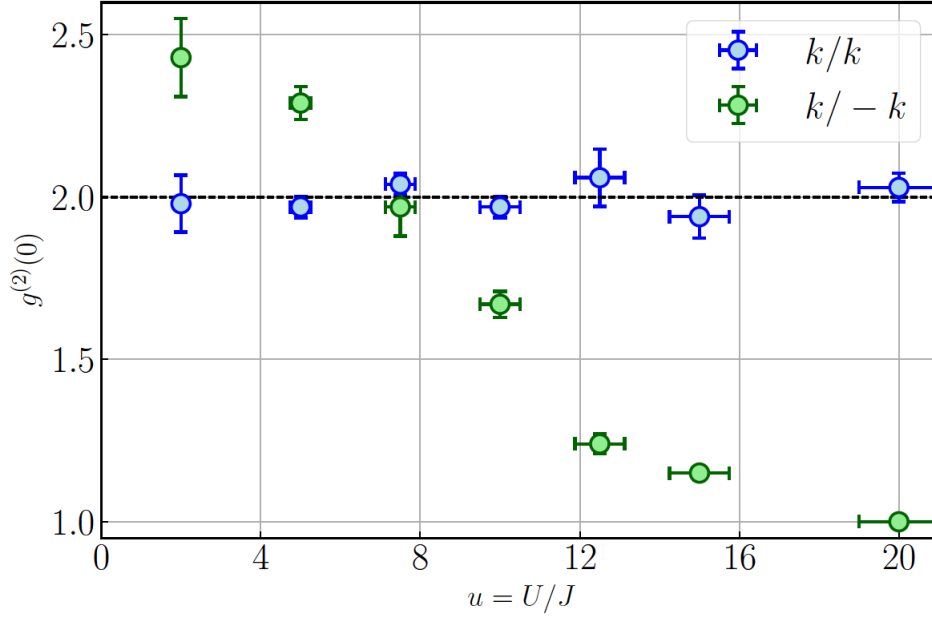


Figure 3.5 – Amplitudes of the normal (HBT) and anomalous (pairing) normalized two-body correlations for increasing interactions. The blue circles are amplitudes of the normal (HBT) and the green ones of the anomalous (pairing) normalized correlations $g_{\text{HBT}}^{(2)}$ (3.25) and $g_A^{(2)}$ (3.24) as a function of the interaction strength u . Vertical error bars correspond to the standard deviations of the amplitudes of $g_{x,y,z}^{(2)}$ while correcting for the effect of transverse integration [53]. Horizontal error bars correspond to average uncertainties on the fit in the parametric heating calibration of the lattice depth shown in fig. 2.8. The dashed line represents a theoretical perfectly contrasted bunching $g_{\text{HBT}}^{(2)} = 2$ expected for any strength of interactions.

Figure 3.5 shows perfectly-contrastted bunching amplitudes $g_{\text{HBT}}^{(2)} = 2.00(5)$ for all regimes of interactions. This observation extends the results of previous work on the experiment [141] to the strongly-interacting regime. In contrast to this consistency, the normalized pairing amplitude decreases monotonously with U/J . As shown in [23, 52, 53], the amplitude of the pairing signal has been confirmed to be inversely proportional to the mode population $g_A^{(2)} - 1 \propto 1/\rho(\mathbf{k})$, as is expected for two-mode squeezed states. Since this decrease is thus compatible with the predictions of Bogoliubov theory, it poses a challenge for drawing a definitive conclusion, as

this reduction is anticipated not only due to the increase in the depletion density but also due to a decrease of the population of the two-mode squeezed states, as would be possible when the system transitions into the strongly-correlated regime where Bogoliubov's approximation breaks down. Consequently, disentangling these two effects poses a significant difficulty. This highlights that normalized correlation functions are inappropriate for establishing a limit of validity for Bogoliubov theory and underscores the need for a different observable. The remainder of this chapter is dedicated to demonstrating that connected correlation functions are able to fulfill this role and quantify the fate of Bogoliubov's momentum pairing at strong interactions in an unambiguous manner.

3.3 . Suppression of Bogoliubov pairing and emergence of non-Gaussian correlations

Increasing the interaction strength beyond the assumptions underlying Bogoliubov theory amounts to having to consider higher orders of interaction processes than merely those described by $\hat{V}^{(2)}$, as strong interactions are expected to give rise to strongly-correlated systems [89, 142] exhibiting large quantum fluctuations with more complex statistics than Gaussian [58, 143]. The truncation of the interaction potential at quadratic order must be relinquished in the context of stronger interactions that deplete the condensate out of the range of validity of the approximation $N_{\mathbf{k}=0} = N_0 \approx N$. With the ratio of particles occupying the quantum depletion increasing monotonously as a function of the interaction strength, higher-order processes involving interactions outside the condensate cease to be negligible, invalidating the linearization of quantum fluctuations as momentum correlations between more than two particles appear out of the the cubic and quartic terms of the interaction potential that cannot be simplified to pairwise interactions, indicating an unmistakable departure from Gaussian states. The impact of the arisal of such higher-order correlations on the two-body pairing signal is unclear, as is the range of interactions for which the predictions of Bogoliubov theory hold true.

Admitting the higher orders $\hat{V}^{(3)}$ and $\hat{V}^{(4)}$ in the interaction potential amounts to the arisal of successive scattering events, that is contrary to Bogoliubov theory, interactions outside the

condensate can no longer be neglected. This leads to additional correlations in momentum besides the two-mode squeezed states already present at weak interactions. Figure 3.6 illustrates the possible scattering events arising from all three constituent terms of \hat{V}_{int} .

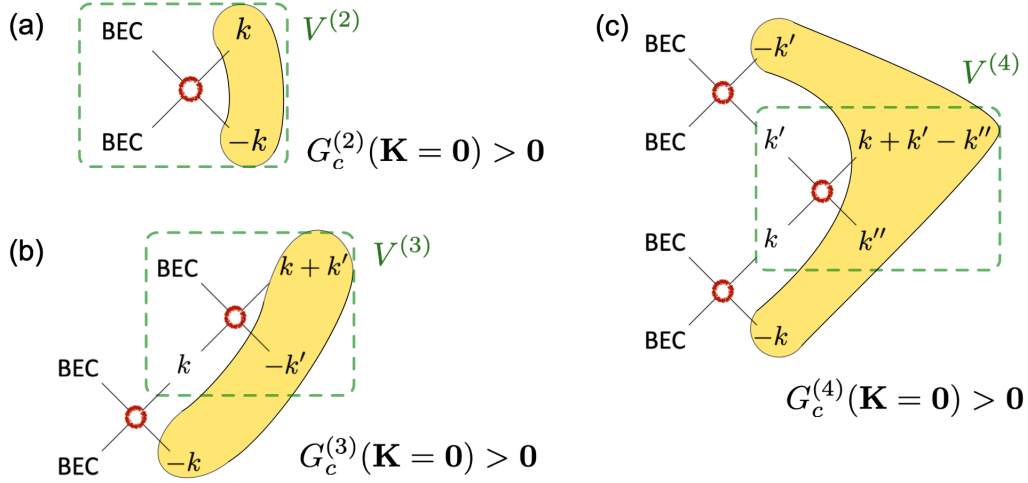


Figure 3.6 – Singular and successive two-body scattering processes from the BEC. With the development of the interaction potential truncated above the quadratic term $\hat{V}^{(2)}$ the only interaction process considered in Bogoliubov theory gives rise to two-mode squeezed states at opposite momenta (a). For stronger interactions collisions outside the condensate constitute successive scattering processes that give rise to momentum correlated triplets (b) and quartets (c), and generally n -uplets with $\sum_{j=1}^n \mathbf{k}_j = \mathbf{0}$ (oranges surfaces).

The cubic and quartic terms of \hat{V}_{int} correlate triplets and quadruplets, respectively, with zero total momentum sums.

3.3.1. Connected correlation functions

With the inaptitude of magnitudes of normalized correlation functions to reveal the fate of the pairing signal for stronger interactions established (see fig. 3.5), a different observable has to be analyzed in order to study the hierarchy of momentum-correlated subsets involving $n > 2$ modes. One such possibility resides in the analysis of connected correlation functions $G_c^{(n)}$, also called n -th order multivariate cumulants or Ursell functions [144], of the momentum density operator $\hat{N}_{\mathbf{k}} = \hat{a}_{\mathbf{k}}^\dagger \hat{a}_{\mathbf{k}}$. They are defined by subtracting the contributions of all lower-order correlations $n' < n$ from the correlator of order n of the populations:

$$G_c^{(n)}(\mathbf{k}_1, \mathbf{k}_2, \dots, \mathbf{k}_n) = \langle N_{\mathbf{k}_1} N_{\mathbf{k}_2} \dots N_{\mathbf{k}_n} \rangle - G_{\text{dis}}^{(n)}(\mathbf{k}_1, \mathbf{k}_2, \dots, \mathbf{k}_n) \quad (3.26)$$

In eliminating $G_{\text{dis}}^{(n)}$ the connected correlations $G_c^{(n)}$ isolate genuine n -mode correlations that are not reducible to correlations of lower order. Explicitly, the second and third order connected correlations of the momentum density operator are given by

$$G_c^{(2)}(\mathbf{k}_1, \mathbf{k}_2) = \langle N_{\mathbf{k}_1} N_{\mathbf{k}_2} \rangle - \langle N_{\mathbf{k}_1} \rangle \langle N_{\mathbf{k}_2} \rangle \quad (3.27)$$

$$\begin{aligned} G_c^{(3)}(\mathbf{k}_1, \mathbf{k}_2, \mathbf{k}_3) &= \langle N_{\mathbf{k}_1} N_{\mathbf{k}_2} N_{\mathbf{k}_3} \rangle - \langle N_{\mathbf{k}_1} \rangle \langle N_{\mathbf{k}_2} N_{\mathbf{k}_3} \rangle \\ &\quad - \langle N_{\mathbf{k}_2} \rangle \langle N_{\mathbf{k}_1} N_{\mathbf{k}_3} \rangle - \langle N_{\mathbf{k}_3} \rangle \langle N_{\mathbf{k}_1} N_{\mathbf{k}_2} \rangle \\ &\quad + 2 \langle N_{\mathbf{k}_1} \rangle \langle N_{\mathbf{k}_2} \rangle \langle N_{\mathbf{k}_3} \rangle \end{aligned} \quad (3.28)$$

Connected correlation functions are not specific to quantum many-body systems, but a widely used tool in statistical mechanics. Indeed, the Ursell function $U_k(\sigma_1, \dots, \sigma_k)$ can be defined for any family of k random variables $\sigma_1, \dots, \sigma_k$ via the exponential generating function [145]:

$$U_k(\sigma_1, \dots, \sigma_k) = \frac{\partial^k}{\partial h_1 \dots \partial h_k} \ln \langle \exp \sum_{i=1}^k h_i \sigma_i \rangle |_{h \equiv 0} \quad (3.29)$$

Solving a quantum many-body problem amounts to gaining knowledge of all its correlation functions. Approximate solutions can be found by considering the degrees of freedom where only a few of the lowest order correlation functions are relevant. Such a choice of basis (i.e. degrees of freedom) where the correlation functions factorize amounts to diagonalizing the many-body Hamiltonian. Analyzing the connected correlation functions (3.26) calculated from the mode populations of the recorded momentum distributions represents an experimental approach to conducting a quantitative investigation of a regime whose correlation structures have thus far eluded understanding with only a few exceptions⁶.

The most relevant quantum correlations induced by interactions, both in Bogolyubov theory and beyond (see fig. 3.6), manifest as connected correlations among momentum modes that sum to zero ($G_c^{(n)}(\mathbf{K} = \mathbf{0})$). Conversely, incoherent (thermal) fluctuations lack a momentum-sum constraint, allowing the momentum sum to fluctuate incoherently. Detecting correlations among

6. See [146] for a theoretical approach in continuum space.

zero-sum modes thus serves as a robust indication of their quantum origin, stemming from processes depicted in fig. 3.6, which illustrates the fact that each higher order of interaction-induced momentum correlated n -uplets is translated by the corresponding connected correlation function $G_c^{(n)}(\mathbf{K} = \mathbf{0})$. Observing non-zero values for these quantities in the experiment is therefore a direct trace about the presence of underlying successive scattering processes leading to high-order correlations that exceed the realm of Gaussian statistics.

In order to continue to investigate the fate of the pairing signal presented in the first part of this chapter, while avoiding the pitfalls associated with the use of normalized correlation functions, the two-mode, zero-sum connected correlations

$$G_c^{(2)}(\mathbf{k}, -\mathbf{k}) = \langle \hat{a}_{\mathbf{k}}^\dagger \hat{a}_{-\mathbf{k}}^\dagger \hat{a}_{\mathbf{k}} \hat{a}_{-\mathbf{k}} \rangle - \langle N_{\mathbf{k}} \rangle \langle N_{-\mathbf{k}} \rangle \quad (3.30)$$

are analyzed. In the context of Bogoliubov theory, these correlations quantify the momentum pairing in the system, with (3.30) being equivalent to $G_c^{(2)}(\mathbf{k}, -\mathbf{k}) = |\langle \hat{a}_{\mathbf{k}}^\dagger \hat{a}_{-\mathbf{k}}^\dagger \rangle|^2$, as can be seen from the following considerations:

The perfectly-contrasted bunching $g_{\text{HBT}}^{(2)} = 2.00(5)$ observed in fig. 3.5 justifies the assumption that the interaction processes described by (3.7) do not induce the appearance of a finite value of $\langle a_{\mathbf{k}} \rangle$ in the depletion, since this would reduce the bunching amplitude. Under this assumption, and relaxing the one of particle-number conservation, the connected correlations of four momentum density operators in the depletion can be expressed as

$$\langle \hat{a}_{\mathbf{k}}^\dagger \hat{a}_{-\mathbf{k}}^\dagger \hat{a}_{\mathbf{k}} \hat{a}_{-\mathbf{k}} \rangle_c = \langle \hat{a}_{\mathbf{k}}^\dagger \hat{a}_{-\mathbf{k}}^\dagger \hat{a}_{\mathbf{k}} \hat{a}_{-\mathbf{k}} \rangle - \left| \langle \hat{a}_{\mathbf{k}}^\dagger \hat{a}_{-\mathbf{k}}^\dagger \rangle \right|^2 - \left| \langle \hat{a}_{\mathbf{k}}^\dagger \hat{a}_{-\mathbf{k}} \rangle \right|^2 - \langle \hat{a}_{\mathbf{k}}^\dagger \hat{a}_{\mathbf{k}} \rangle \langle \hat{a}_{-\mathbf{k}}^\dagger \hat{a}_{-\mathbf{k}} \rangle \quad (3.31)$$

where the last term is equal to $-\langle N_{\mathbf{k}} \rangle \langle N_{-\mathbf{k}} \rangle$. Consequently, (3.30) can be written as⁷

$$G_c^{(2)}(\mathbf{k}, -\mathbf{k}) = \left| \langle \hat{a}_{\mathbf{k}}^\dagger \hat{a}_{-\mathbf{k}}^\dagger \rangle \right|^2 + \left| \langle \hat{a}_{\mathbf{k}}^\dagger \hat{a}_{-\mathbf{k}} \rangle \right|^2 + \langle \hat{a}_{\mathbf{k}}^\dagger \hat{a}_{-\mathbf{k}}^\dagger \hat{a}_{\mathbf{k}} \hat{a}_{-\mathbf{k}} \rangle_c \quad (3.32)$$

As outlined in the first part of this chapter, the approximations underlying Bogoliubov theory imply a linearization of quantum fluctuations and thereby lead to exclusively Gaussian states. For

7. (3.32) is a generic equation applicable to both Gaussian and non-Gaussian states.

such states connected correlations of four operators are zero by definition, i.e. $\langle \hat{a}_{\mathbf{k}}^\dagger \hat{a}_{-\mathbf{k}}^\dagger \hat{a}_{\mathbf{k}} \hat{a}_{-\mathbf{k}} \rangle_c = 0$. Additionally, the theory predicts incoherence among modes at opposite momenta, i.e. $|\langle \hat{a}_{\mathbf{k}}^\dagger \hat{a}_{-\mathbf{k}}^\dagger \rangle|^2 = 0$. With all other terms assumed to vanish, the approximations made in Bogoliubov theory thus predict the connected correlations (3.32) to consist solely of the pairing at opposite momenta:

$$G_c^{(2)}(\mathbf{k}, -\mathbf{k}) = |\langle \hat{a}_{\mathbf{k}}^\dagger \hat{a}_{-\mathbf{k}}^\dagger \rangle|^2 \quad (3.33)$$

3.3.2 . Extracting two-body connected correlations from momentum distributions

The connected correlations at opposite momenta $G_c^{(2)}(\mathbf{k}, -\mathbf{k})$ are extracted from the experimental data shown in fig. 3.4 for momenta \mathbf{k} belonging to the same measurement volume Ω_k as for the analysis of the normalized correlation functions in fig. 3.5. In order to compute the two-body connected correlations (3.30) from the 3D momentum distributions of the type shown in fig. 3.2, the histogram of momentum sums $\mathbf{k}_1 + \mathbf{k}_2$ is calculated for all pairs of atoms detected in a run of the experiment. Removing the disconnected part amounts to subtracting the product of average occupations $\langle N_{\mathbf{k}_1} \rangle \langle N_{\mathbf{k}_2} \rangle$ from this histogram.

Within finite-size systems, correlation functions exhibit a limited range, defined as the correlation volume, the size of which is determined by the size of a single mode (see chapter 4). For the normalized two-body correlations of type $g^{(2)}(\mathbf{k}, -\mathbf{k} + \delta\mathbf{k})$ shown in fig. 3.3, the presence of an isotropic harmonic trap suggests that the function is anticipated to be isotropic. Empirically, it is observed that the function is effectively modeled by an isotropic Gaussian function, an approach that was already employed in the beginning of this chapter where these fits were used to extract the normalized two-body correlation amplitudes at opposite momenta. For these Gaussians, the correlation length l_c is defined as the $1/e^2$ size according to:

$$g_c^{(2)}(\mathbf{k}, -\mathbf{k} + \delta\mathbf{k}) = 1 + \frac{A\sqrt{2}}{\sqrt{\pi}l_c} e^{-2\delta\mathbf{k}^2/l_c^2} \quad (3.34)$$

When defined in such a way, 95% of atoms are expected to be found in the spherical volume given by $|\delta\mathbf{k}| \in [0, l_c]$.

The two-body connected correlation $G_c^{(2)}(\mathbf{k}, -\mathbf{k})$ is determined by integrating $G_c^{(2)}(\mathbf{k}, -\mathbf{k} + \delta\mathbf{k})$ across a cubic volume with a size of Δk :

$$G_c^{(2)}(\mathbf{k}, -\mathbf{k}) = \int_{[-\Delta k/2, \Delta k/2]^3} d\delta\mathbf{k} G_c^{(2)}(\mathbf{k}, -\mathbf{k} + \delta\mathbf{k}) \quad (3.35)$$

Since $G_c^{(2)}(\mathbf{k}, -\mathbf{k} + \delta\mathbf{k}) \propto g^{(2)}(\mathbf{k}, -\mathbf{k} + \delta\mathbf{k}) - 1$, it follows that $G_c^{(2)}(\mathbf{k}, -\mathbf{k}) \propto \left[\text{erf} \left(\frac{\Delta k}{\sqrt{2}l_c} \right) \right]^3$. The volume Δk^3 is selected in such a way that the integral on $d\delta\mathbf{k}$ saturates, setting $\Delta k = 0.18 k_d \simeq 3 \times l_c$ to ensure that $G_c^{(2)}(\mathbf{k}, -\mathbf{k})$ represents 99% of the pairing amplitude in theory.

This is confirmed experimentally for moderate interaction strengths $U/J < 20$, as shown in fig. 3.7, where the integrated version $\overline{G}_c^{(2)}(\mathbf{0}) = \sum_{\mathbf{k}} G_c^{(2)}(\mathbf{k}, -\mathbf{k})$ is plotted normalized by the integration volume Δk^3 .

Indeed, $\overline{G}_c^{(2)}(\mathbf{0})/\Delta k^3$ decays to zero within the expected range of $\Delta k \sim 0.18 k_d$, and the variation $\left[\text{erf} \left(\frac{\Delta k}{\sqrt{2}l_c} \right) \right]^3 / \Delta k^3$ is obtained from the bell-shaped function of the normalized correlations. This observation is analogous to the peak observed in the normalized correlation $g^{(2)}(\mathbf{k}, -\mathbf{k} + \delta\mathbf{k})$ centered on $\delta\mathbf{k} = \mathbf{0}$ for $U/J < 20$.

Conversely, at $U/J = 20$ (and similarly at $U/J = 22$), $\overline{G}_c^{(2)}(\mathbf{0})/\Delta k^3$ exhibits a distinct pattern. While it registers slightly positive values at extremely small Δk values, it remains consistently negative otherwise. This contrasting behavior is responsible for the negative values of $\overline{G}_c^{(2)}(\mathbf{0})$ depicted below. The observation of $\overline{G}_c^{(2)}(\mathbf{0}) < 0$ indicates that the coincidence counts in modes at opposite momenta are fewer than the counts expected in an uncorrelated ensemble of atoms with a similar momentum density $\rho(\mathbf{k}) = \langle \hat{a}_{\mathbf{k}}^\dagger \hat{a}_{\mathbf{k}} \rangle$. Consequently, modes at opposite momenta are inferred to be anti-correlated. Summarizing the above considerations, the histograms are integrated over a cubic volume centered on $\mathbf{k}_1 + \mathbf{k}_2 = \mathbf{0}$ and of size $0.18 k_d$ set by the width of the two-body correlation function. In order to increase the signal-to-noise ratio, the resulting connected correlations are averaged over the modes that constitute Ω_k

$$\overline{G}_c^{(2)}(\mathbf{K} = \mathbf{0}) = \sum_{\mathbf{k} \in \Omega_k} G_c^{(2)}(\mathbf{k}, -\mathbf{k}) \quad (3.36)$$

where the sum is defined over (quasi-) momenta \mathbf{k} contained in Ω_k such that $\mathbf{k} + \mathbf{Q} \neq -\mathbf{k}$, where \mathbf{Q} is a reciprocal lattice vector. These values are multiplied by η^{-2} to account for the finite detection efficiency $\eta = 0.53(2)$ of the detector.

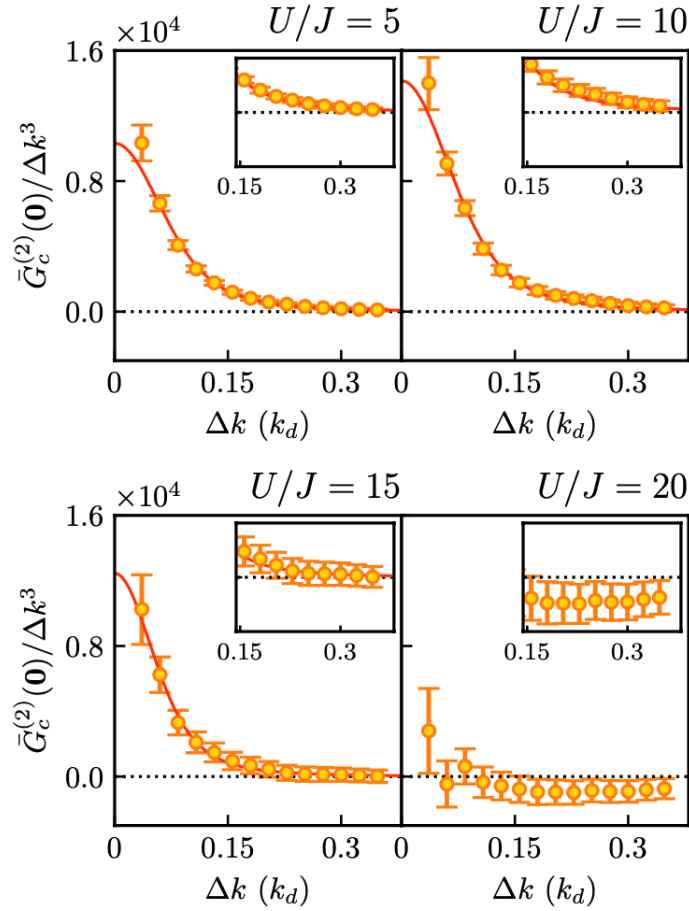


Figure 3.7 - Two-body connected correlations normalized by the integration volume as a function of the latter. The orange circles represent the evolution of $\overline{G}_c^{(2)}(\mathbf{0})/\Delta k^3$ with Δk . The interactions range from weak at $U/J = 5$ to strong at $U/J = 20$. The error bars represent 68%-confidence intervals obtained from a bootstrap method. The red solid line depicts the anticipated variation $\left[\text{erf}\left(\frac{\Delta k}{\sqrt{2}l_c}\right)\right]^3/\Delta k^3$ associated with the correlation length l_c of the normalized two-body correlation $g^{(2)}(\mathbf{k}, -\mathbf{k} + \delta\mathbf{k})$. Insets provide a closer look within the range of $d\delta\mathbf{k} \in [0.14 k_d, 0.38 k_d]$.

3.3.3 . Two-body connected correlations at opposite momenta

The resulting integrated amplitudes $\overline{G}_c^{(2)}(\mathbf{K} = \mathbf{0})$ of the Bogoliubov momentum pairing are plotted in figure 3.8 as a function of the interaction strength.

Figure 3.8 constitutes the main experimental result of this chapter. It shows an initial increase in $\overline{G}_c^{(2)}(\mathbf{0})$. Bogoliubov theory predicts a monotonous increase of the population of the two-mode correlated quantum depletion, indicating the validity of its underlying approximations

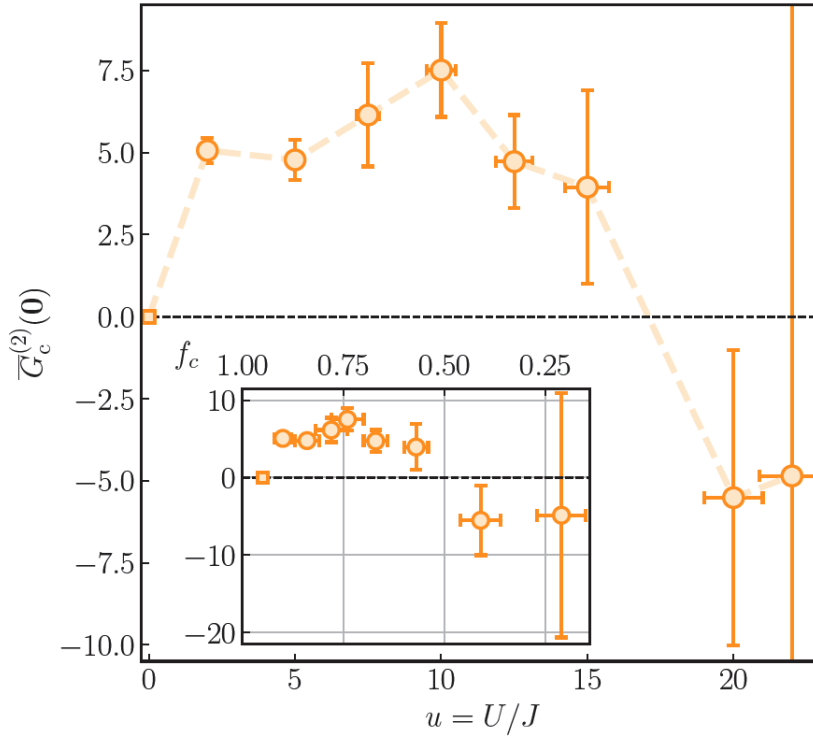


Figure 3.8 – Two-body connected correlations at opposite momenta. Amplitude $\overline{G}_c^{(2)}(\mathbf{K} = \mathbf{0})$ of the Bogoliubov momentum pairing at opposite momenta ($\mathbf{K} = \mathbf{k}_1 + \mathbf{k}_2 = \mathbf{0}$) measured in the volume Ω_k of the depletion of the lattice BEC (orange circles) and of a harmonically-trapped BEC (orange square). The dashed line is a guide to the eye. The vertical error bars represent 68%-confidence intervals obtained from a bootstrap method. The horizontal error bars are the same as in fig. 3.4c. The inset displays $\overline{G}_c^{(2)}(\mathbf{K} = \mathbf{0})$ as a function of the condensate fraction f_c .

in the weakly-interacting regime. However, $\overline{G}_c^{(2)}(\mathbf{K} = \mathbf{0})$ is found to decrease at larger values of U/J , a decrease that occurs for the adiabatic increase of the interaction strength [97] and not due to heating. Furthermore, the inset of fig. 3.8 indicates that location of the maximum aligns with a notably substantial condensate fraction of $f_c \sim 0.75$, far from the Mott transition. This observation strongly indicates that these observations are not specific to lattice bosons at integer filling but are representative of strongly interacting Bose gases in general.

Since a similar decreasing tendency was previously established for the normalized two-body correlation signal at opposite momenta (see fig. 3.5), the difference between the two quantities $\overline{G}_c^{(2)}(\mathbf{K} = \mathbf{0})$ and $g^{(2)}(\mathbf{0})$ is again emphasized at this point:

The normalized correlation function $g^{(2)}(\mathbf{0})$ depends inversely on the population of the depletion

modes in $\Omega_{\mathbf{k}}$ and is therefore undiscernable from the effect of the decrease of f_c shown in figure 3.4c. The connected correlations $\overline{G}_c^{(2)}(\mathbf{K} = \mathbf{0})$ on the other hand contain only contributions of interaction processes at order n , with the effect of the average mode populations that leads to a decrease in the normalized correlations being eliminated via the subtraction of the disconnected part $\langle N_{\mathbf{k}} \rangle \langle N_{-\mathbf{k}} \rangle$ from the n -th order correlator in (3.30).

Figure 3.8 also shows an increase in the size of the error bars of $\overline{G}_c^{(2)}(\mathbf{K} = \mathbf{0})$ as interactions are increased, which indicates a rise of fluctuations for this quantity. Since these fluctuations are sensitive to higher orders of correlation $n > 2$, this increase might be an indication to the increasing complexity of the equilibrium many-body state as the system enters the strongly-interacting regime.

The decrease of $\overline{G}_c^{(2)}(\mathbf{K} = \mathbf{0})$ seen in fig. 3.8 constitutes an experimental observation of non-Gaussian statistics, since it is not predicted by Bogoliubov theory, which encompasses interactions in Bose gases at the Gaussian level. However, a more direct conclusion on non-Gaussian statistics can be obtained from the negative values of $\overline{G}_c^{(2)}(\mathbf{K} = \mathbf{0})$ at the largest interactions for $U/J = 20$ and 22 , as is detailed in the following.

3.3.4 . Experimental signature of non-zero four-particle correlators

In the effort to explore the hierarchy of momentum correlations depicted in fig. 3.6, observing a non-zero value for the integrated three-mode correlations, $\overline{G}_c^{(3)}(\mathbf{0}) = \sum_{\mathbf{k}_1, \mathbf{k}_2} G_c^{(3)}(\mathbf{k}_1, \mathbf{k}_2, -\mathbf{k}_1 - \mathbf{k}_2)$, which quantify genuine three-mode correlations with zero momentum sum, would constitute a direct observation of statistics beyond the Gaussian regime. However, the experimentally measured values of $\overline{G}_c^{(3)}(\mathbf{0})$ are found to be indistinguishable from zero for all interaction strengths $U/J \in [2, 22]$. Measuring $\overline{G}_c^{(3)}(\mathbf{0}) \neq 0$ is not the sole means to demonstrate non-Gaussian statistics in the experimental data. As shown above, the connected two-mode correlations can be expressed in terms of the fourth order cumulant (3.32). Eq. (3.32) reveals that negative values of $\overline{G}_c^{(2)}(\mathbf{K} = \mathbf{0})$ necessarily imply a non-vanishing fourth order cumulant $\langle \hat{a}_{\mathbf{k}}^\dagger \hat{a}_{-\mathbf{k}}^\dagger \hat{a}_{\mathbf{k}} \hat{a}_{-\mathbf{k}} \rangle_c \neq 0$, constituting a direct signature of non-Gaussian statistics. Indeed, negative connected correlations $G_c^{(2)}(\mathbf{k}, -\mathbf{k}) < 0$ amount to anti-bunching, i.e. a number of coincidence counts $\langle \hat{a}_{\mathbf{k}}^\dagger \hat{a}_{-\mathbf{k}}^\dagger \hat{a}_{\mathbf{k}} \hat{a}_{-\mathbf{k}} \rangle$ smaller than the expected uncorrelated gas value $\langle N_{\mathbf{k}} \rangle \langle N_{-\mathbf{k}} \rangle$. Correlations of order $n > 2$ are required to reduce the coincidence counts below $\langle N_{\mathbf{k}} \rangle \langle N_{-\mathbf{k}} \rangle$.

Fig. 3.7 shows a significant shift in the shape of the correlation function $G_c^{(2)}(\mathbf{k}, -\mathbf{k} + \delta\mathbf{k})$ at large interactions $U/J = 20$ (that has also been found to be present at $U/J = 22$). Notably, there is hardly any correlation peak at $\delta\mathbf{k} = 0$, but instead, a constant (negative) offset as a function of $\delta\mathbf{k}$ is observed. In this regime, $\overline{G_c^{(2)}}(\mathbf{0}) < 0$ is observed (see fig. 3.8), and $\sum_{\mathbf{k}} \langle \hat{a}_{\mathbf{k}}^\dagger \hat{a}_{-\mathbf{k}}^\dagger \hat{a}_{\mathbf{k}} \hat{a}_{-\mathbf{k}} \rangle_c \neq 0$. A non-zero fourth-order cumulant serves as a clear indication of non-Gaussian statistics without relying on theoretical modeling, providing compelling evidence for strongly correlated (non-Gaussian) nature of Bose gases at large interactions.

In order to investigate this possibility and explore the evolution of two-mode connected correlations theoretically, the remainder of this chapter is dedicated to a comparison of the experimentally measured connected correlations shown in fig. 3.8 with numerical simulations using quantum Monte Carlo (QMC) simulations on the 3D quantum rotor model. These simulations and their analysis were performed by T. Roscilde (ENS Lyon).

3.4 . Comparison with numerical simulations

To explore the fate of two-mode connected correlations beyond the weakly interacting regime, numerically exact quantum Monte Carlo (QMC) simulations on a 3D quantum rotor model are employed, which capture the essential physics of the Bose-Hubbard model at large, integer filling, and in the absence of confining potentials [147]. While the filling much larger than unity implies that simulations based on this model are not expected to lend themselves to quantitative comparisons with the experimental data of fig. 3.8, they do provide a means to access arbitrary correlations in momentum space without requiring specialized update algorithms [148, 149] at arbitrary temperatures and interactions up to the Mott transition.

Various quantum Monte Carlo approaches are available to explore the equilibrium thermodynamics of the original Bose-Hubbard model [150, 151]. However, these methods commonly employ Fock states in real space as the computational basis, making the momentum distribution an off-diagonal observable. Estimating off-diagonal observables necessitates specialized update schemes referred to as "worm algorithms." While complex worm-like algorithms exist that are

suitable for the investigation of the second moment of the momentum distribution fluctuations in the 1D Bose-Hubbard model [148, 149], probing third moments has never been explored with such algorithms, highlighting the flexibility of the quantum rotor approach.

3.4.1 . QMC simulations on the 3D quantum rotor model

The quantum-rotor model provides an approximation to the Bose-Hubbard model that is valid for large, integer fillings n_{QR} [147]. Using the amplitude-phase decomposition of the bosonic field, $a_i = e^{i\phi} \sqrt{n_i}$, with $[\phi, n_i] = 1$, expressing the density as $n_i = n_{\text{QR}} + \delta n_i$ and assuming that $\sqrt{\langle (\delta n_i)^2 \rangle} \ll n_{\text{QR}}$ (since $n_{\text{QR}} \gg 1$) in all relevant physical regimes, one can write

$$a_i^\dagger a_j + \text{h.c.} \approx 2n_{\text{QR}} \cos(\phi_i - \phi_j) \quad (3.37)$$

neglecting density fluctuations. Quantum fluctuations in the phase still arise due to density-density interactions since $n_i^2 = -\frac{\partial^2}{\partial \phi_i^2}$. The quantum rotor Hamiltonian is obtained by working at integer filling, which eliminates all linear terms in the density:

$$H_{\text{QR}} = -2Jn_{\text{QR}} \sum_{\langle ij \rangle} \cos(\phi_i - \phi_j) - \frac{U}{2} \sum_i \frac{\partial^2}{\partial \phi_i^2} \quad (3.38)$$

Using a coherent-state path-integral approach [147, 152], the quantum statistical physics of the quantum-rotor Hamiltonian (3.38) in d dimensions can be mapped onto an effective classical problem of classical rotors, i.e., planar spins or angles $\phi_{i,p}$, where i represents the spatial position and p is the position in the extra (Trotter) dimension. A QMC simulation of the quantum rotor model amounts to sampling configurations of this $(d+1)$ -dimensional classical model [147, 153]. The approximation in (3.37) allows for the unique association of a momentum distribution $N_p(\mathbf{k}) = \frac{n_{\text{QR}}}{V} \sum_{ij} e^{i\mathbf{k} \cdot (\mathbf{r}_i - \mathbf{r}_j)} e^{-i(\phi_{i,p} - \phi_{j,p})}$ to each configuration of classical rotors $\{\phi_{i,p}\}$ at a given Trotter step p , thereby enabling the reconstruction of arbitrary correlation functions for the momentum populations $N(\mathbf{k})$ by sampling the partition function of the classical rotors.

3.4.2 . Comparison between theory and experiment

The connected two-body correlations $\overline{G_c^{(2)}}(\mathbf{K} = \mathbf{0})$ obtained from QMC simulations on the 3D quantum rotor model are shown in figure 3.9 as a function of the interaction strength u and for different temperatures T . In a previous work the temperature of the experiment was estimated

as $k_B T/J \approx 2$ [97], which corresponds to the data for the quantum rotor model at a temperature $T_J = k_B T/(2Jn_{QR}) = 1$ represented by the green line in fig. 3.9.

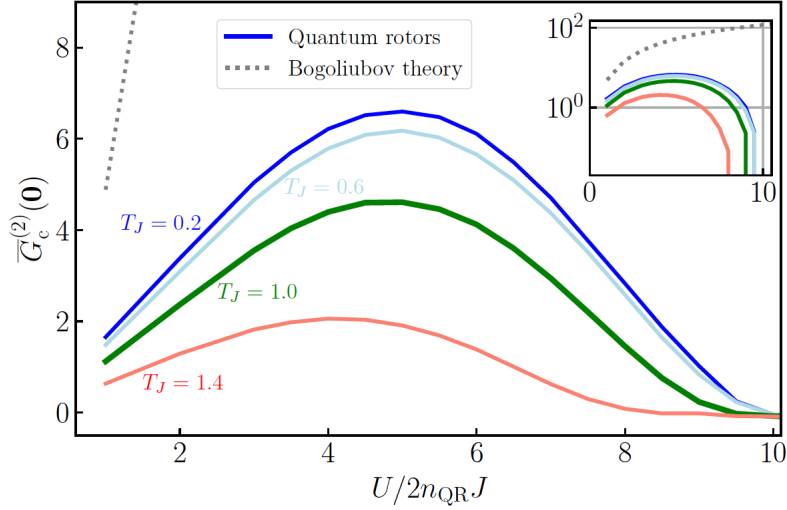


Figure 3.9 – Numerical calculations of connected two-body correlations with the quantum rotor model. Connected correlations $\overline{G}_c^{(2)}(\mathbf{0})$ for two modes, obtained using the quantum rotor model (solid lines), are depicted at various temperatures ranging from $T_J = k_B T/(2Jn_{QR}) = 0.2$ (dark blue) to $T_J = 1.8$ (red). The result from Bogoliubov theory is represented by the dotted line. The inset displays a logarithmic plot of the data from the main panel. The amplitude of $\overline{G}_c^{(2)}(\mathbf{0})$ is normalized to the measured atom number $\langle N_{\Omega_k} \rangle$ (see text).

The connected two-body correlations are integrated over the quasi-momenta in a cubic corona Ω_k between two cubes of sides $2 \times 0.3 k_d$ and $2 \times 0.5 k_d$ for a system of 10^3 cubic lattice sites. The numerically-computed population $\langle N_{\Omega_k}^{\text{th}} \rangle$ of the modes in momentum space is altered depending on the filling n_{QR} , while $\overline{G}_c^{(2)}(\mathbf{K} = \mathbf{0})$ is expected to scale as the square of the density of particles in the measurement volume, $\rho_{\Omega_k} = \langle N_{\Omega_k} \rangle / V_{\Omega_k}$, with the number of modes $V_{\Omega_k} = \sum_{\mathbf{k} \in \Omega_k} 1$, and linearly in the number of modes, i.e. $\overline{G}_c^{(2)} \sim \langle N_{\Omega_k} \rangle^2 / V_{\Omega_k}$. In order to allow for a comparison at least in terms of orders of magnitude between the numerically simulated and experimentally measured two-body connected correlations, the theoretical amplitudes are normalized to the experimentally detected atom number $\langle N_{\Omega_k} \rangle = \sum_{\mathbf{k} \in \Omega_k} \langle N_{\mathbf{k}} \rangle$ by a factor $\sim (\langle N_{\Omega_k} \rangle / \langle N_{\Omega_k}^{\text{th}} \rangle)^2 (V_{\Omega_k}^{\text{th}} / N_{\Omega_k})$ for each interaction strength u . The ratio $r_V = V_{\Omega_k}^{\text{th}} / V_{\Omega_k}$ is purely geometrical and independent of the Hamiltonian parameters. However, making an unambiguous estimation of r_V is not straightforward. Only the core of the atomic cloud, which in principle dictates the size of the momentum modes in momentum space, is expected to be superfluid at the temperature of the experiment

and to contribute to the measured momentum-space correlations. The ratio $r_N = \langle N_{\Omega_k} \rangle / \langle N_{\Omega_k}^{\text{th}} \rangle$, on the other hand, depends significantly on the interaction strength u and can be unambiguously determined. Therefore, the theoretical data for $\overline{G}_c^{(2)}(\mathbf{K} = \mathbf{0})$ are rescaled by r_N^2 , with r_V assumed to be on the order of $r_V \sim \mathcal{O}(1)$. The validity of this assumption is confirmed by the matching orders of magnitude between the experimental values in fig. 3.8 and the rescaled theoretical curve $r_N^2 \overline{G}_c^{(2)}(\mathbf{K} = \mathbf{0})$ in fig. 3.9.

In addition to the right order of magnitude with respect to the experimentally measured connected two-body correlations, the quantum rotor predictions can also be seen to capture the non-monotonic behavior of $\overline{G}_c^{(2)}(\mathbf{K} = \mathbf{0})$ in fig. 3.9. Consequently, the numerical simulations confirm that the decay in the connected two-body correlations $\overline{G}_c^{(2)}(\mathbf{K} = \mathbf{0})$ originates from quantum fluctuations beyond the linearized Bogoliubov regime. The maximum value of $\overline{G}_c^{(2)}(\mathbf{K} = \mathbf{0})$ represents thus a microscopic signature of the Bose gas entering the strongly correlated regime, whose description requires accounting for correlations among $n > 2$ momentum modes.

3.4.3 . Three-mode connected correlations

As outlined at the end of the last section, observing a non-zero value for an order $n > 2$ in the hierarchy of momentum correlations shown in fig. 3.6 would constitute a direct observation a microscopic process leading to non-Gaussian correlations. As seen above, such an observation could not be made from the experimental data. Therefore, the QMC simulations on the 3D quantum rotor model are employed to establish an expected order of magnitude for the integrated three-mode correlations $\overline{G}_c^{(3)}(\mathbf{0}) = \sum_{\mathbf{k}_1, \mathbf{k}_2 \in \Omega_k} G_c^{(3)}(\mathbf{k}_1, \mathbf{k}_2, -\mathbf{k}_1 - \mathbf{k}_2)$ that reveal genuine three-mode correlations with zero momentum sum. More precisely, the above sum is defined over inequivalent pairs of (quasi-) momenta $\mathbf{k}_1, \mathbf{k}_2$, i.e. $\mathbf{k}_1 \neq \mathbf{k}_2 + \mathbf{Q}$ both contained in Ω_k and such that $\mathbf{k}_3 = -\mathbf{k}_1 - \mathbf{k}_2$ is also contained in Ω_k , with reciprocal lattice vector \mathbf{Q} .

The numerically calculated three-mode connected correlations $\overline{G}_c^{(3)}(\mathbf{0})$ computed for quasi-momenta in Ω_k are presented in figure 3.10.

In keeping with the normalization considerations made in the previous section about the numerical simulation data, the simulated values for $\overline{G}_c^{(3)}(\mathbf{0})$ are rescaled by a factor $\sim (\langle N_{\Omega_k} \rangle / \langle N_{\Omega_k}^{\text{th}} \rangle)^3 (V_{\Omega_k}^{\text{th}} / N_{\Omega_k})$ for each interaction strength u , since $\overline{G}_c^{(3)}(\mathbf{0})$ is expected to scale as the cube of the density and as the square of the number of modes, i.e. $\overline{G}_c^{(3)}(\mathbf{0}) \sim \langle N_{\Omega_k} \rangle^3 / V_{\Omega_k}$,

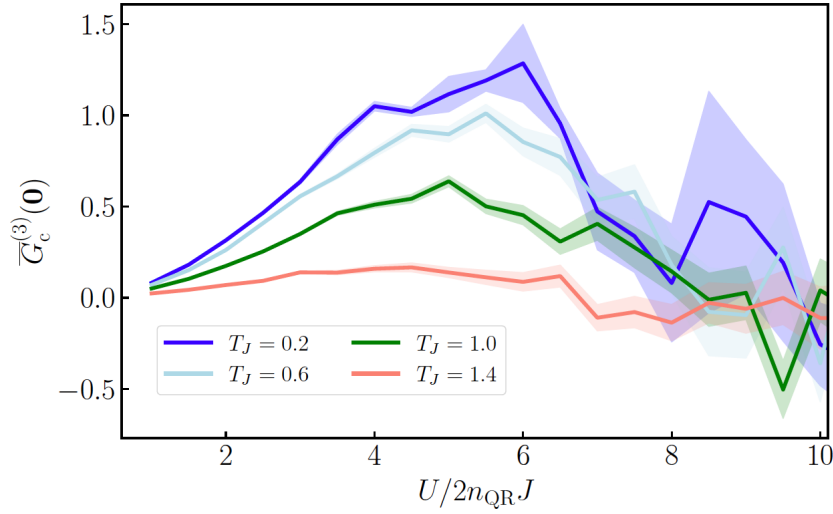


Figure 3.10 – Numerical calculations of connected three-mode correlations with the quantum rotor model. Connected correlations $\bar{G}_c^{(3)}(0)$ for three modes, obtained using the quantum rotor model (solid lines), are depicted at the same temperatures as those for $\bar{G}_c^{(2)}(0)$ in fig. 3.9. The amplitude of $\bar{G}_c^{(3)}(0)$ is normalized to the measured atom number $\langle N_{\Omega_k} \rangle$ (see text).

amounting to a rescaling by n_N^3 .

From fig. 3.10 it is clear that the genuine three-mode correlations in the system are positive, confirming the image proposed in fig. 3.6, and that they rise along with the two-mode correlations. This indicates an incompleteness in the Bogoliubov picture of the Bose gas with intermediate interactions, highlighting the presence of substantial non-Gaussian correlations in the system. However, the three-mode correlations are significantly smaller in magnitude as the two-mode correlations at the same values of interaction and temperature. One potential explanation for this discrepancy may reside in the fact that, while two-mode correlations with a total zero (quasi-)momentum uniquely identify correlated pairs of modes, three-mode correlations with a zero-sum (quasi-)momentum can link every mode to approximately $\mathcal{O}(N)$ pairs of other modes, resulting in considerably weaker correlations within each trio. Upon increasing the number n of modes, correlations are expected to be even more tenuous. Furthermore, detecting triple coincidences of atoms in three modes is challenging due to the finite detection efficiency η of the MCP detector. These factors evidently pose challenges in observing correlations involving more than two modes ($n > 2$). Ultimately, both types of correlations (two-mode and three-mode) diminish as the system transitions into the strongly correlated regime.

3.5 . Conclusion

In conclusion, insights into correlations in an interacting Bose gas beyond the Bogoliubov regime are provided by employing advanced techniques for ultracold gas preparation and detection, along with sophisticated numerical methods. Two-mode correlations, which are predominant in the weakly interacting Bogoliubov regime, are diminished as the system enters the strongly interacting regime. This transition gives way to n -mode correlations ($n > 2$) and the emergence of non-Gaussian correlations. The findings suggest that with increasing interactions, entanglement in momentum space becomes intricate in its multipartite nature and elusive. Each mode is weakly entangled with numerous ($\mathcal{O}(N^{n-2})$) $(n-1)$ -plets of other modes to form n -mode entangled clusters. The theoretical characterization and experimental identification of this complex entanglement structure present intriguing open questions for future studies.

4 - Full-Counting Statistics and High-Order Correlations of Interacting Bosons

One of the main advantages of the single atom detector is the ability to characterize quantum states in small volumes of momentum space with a good signal-to-noise ratio. This ability is on full display in the analysis of full-counting statistics (FCS) which allows for the characterization of quantum states from its many-body coherence properties.

Being able to detect well-contrasted signatures of pure states in experiments is not obvious. At the global level the number statistics of the system is not given by the underlying quantum state, but by the result of the experimental preparation procedure. Such global thermodynamic constraints imply that quantum states described in the grand-canonical ensemble can only be an approximate description of states prepared in the experiment, at least in systems that impose overall particle conservation as is usually the case when working with atoms. As will be shown in this chapter, single-atom detection techniques can offer a way around this intrinsic problem by taking a small sub-volume of the entire measurement volume as system of interest, with the rest of the system effectively acting as a reservoir for this small subsystem, thereby enabling the observation of the signatures of the underlying pure quantum states.

This technique of characterizing quantum states in the experiment is detailed in the following section, followed by the results of applying the technique for the case of two (very different) textbook quantum states: Weakly-interacting lattice superfluids and strongly-interacting Mott insulators. It is shown how the many-body coherence properties of these states reflect their different underlying quantum statistics. A simple heuristic model allows for the quantitative explanation of the measured values of the high-order order correlation functions. Before beginning the analysis, a brief reminder is given concerning the quantum statistics expected for these states when counting atoms in small volumes of momentum space.

One of the main themes of this thesis is the characterization of quantum many-body phenomena through higher orders of the occupation number that is enabled by detecting atoms one by one in 3D. As such, the information about the quantum state that is contained in the statistical quantities extracted from this occupation number can be harnessed. Access to the single-particle resolved 3D momentum distribution opens the way for going beyond the information contained in the average value of the measured momentum densities in investigating the dispersion of momentum occupation numbers in various situations. This approach is conceptually very simple when using a single-particle detector, but as will be shown careful analysis is required to be able to extract the desired quantities beyond simply counting the atoms in a certain part of momentum space. It may be of note that all three of the chapters presenting experimental results are for the most part based upon the very same datasets. This fact illustrates the richness and remarkable information content of datasets that are made up of thousands of atoms, each detected one by one.

4.1 . FCS approach for identifying quantum states in the experiment

Despite the uniqueness of this experimental platform, the extraction of physical properties from the analysis of quantum and thermal noise is not a new approach, as demonstrated by experiments in quantum electronics [154], quantum optics [136] and quantum gases [29, 155, 156]. The FCS is the counting statistics¹ of particles in a given time and/or space interval [157]. Thus, by nature, it relies on the detection of individual particles, and its initial successful implementations have come about as a consequence of the development of single-particle detection techniques for photons and electrons, thus contributing to the fields of quantum optics and mesoscopic conductors [157]. With cold atom experiments protruding into the realm of single-particle detection, FCS has found application in systems based on Rydberg atoms [158–160] and non-interacting atomic gases [41, 161], with the advantage of being less resource-consuming than a full-state tomography [162] while having been shown theoretically to nonetheless be able to shed light on phenomena such as quantum phase transitions [163–165], universality [166, 167], entanglement properties [168] and out-of-equilibrium dynamics [169]. In contrast to the full state tomogra-

1. In theory up to infinite order n , in practice $n > 2$.

phy, FCS only yields information on the diagonal part of the many-body density matrix, a fact that makes this technique amenable to being employed in the characterization of large systems. Nevertheless, knowledge of the populations is already sufficient for identifying a large number of quantum states, similarly to the characterization of light sources from higher order photon correlations [134]². In the context of highly correlated quantum states, the measurement of FCS is expected to reveal non-Gaussian correlations resulting from the nontrivial correlations in the system [29, 170–172] such as the ones shown for strongly-interacting Bose gases in chapter 3. Furthermore, it has been shown that applying unitary transformations before measurement also allows access to the non-diagonal correlators from a measurement of the number statistics [173, 174].

The single-particle detection capabilities for large atom numbers of the Helium Lattice experiment constitute a well-suited platform for this type of analysis. The Bose-Hubbard model described in chapter 2 allows for the realization of different many-body quantum states in equilibrium, such as weakly-interacting lattice superfluids and strongly-interacting Mott insulators. The aim of this chapter is to present the approach for extracting the FCS from the experimental datasets and to discuss the observed many-body coherence properties that allow for the characterization of the different states. It is in large parts based on the work presented in [36]. Prior to delving into the experimental details, however, it is useful to consider the expected structure of the FCS for the different states in order to be able to confirm them experimentally later on.

4.1.1 . FCS for ideal BECs and Mott insulators

For textbook many-body quantum states like ideal BECs and Mott insulators, the FCS, that is the probability distribution of the occupation number, is well-known. While these descriptions are in their most fundamental form made in an ideal and simplified context that implies that one should use caution when expecting experimental measurements to reflect these theoretical predictions, they do represent a useful starting point³ for the expected form of the FCS when probing the actual quantum states in the experiment.

2. For Gaussian states, which have positive Wigner functions [136], this approach is equivalent in its information content to a FCS analysis.

3. As will be shown in the following, in this case the pure state description is much more than simply a starting point but in fact an experimentally observable feature.

BECs have long-range coherence properties with a well-defined phase that results from the spontaneous breaking of gauge symmetry [175]. In the ground state they are thus amenable to a grand-canonical ensemble description⁴ in terms of a coherent state $|\alpha\rangle$. The natural choice of basis for the FCS are the Fock states $|n\rangle$, onto which $|\alpha\rangle$ can be decomposed according to

$$|\alpha\rangle = e^{-|\alpha|^2/2} \sum_n \frac{\alpha^n}{\sqrt{n!}} |n\rangle \quad (4.1)$$

Coherent states are known to have a Poissonian probability distribution of the occupation number that depends only on the mean particle number $|\alpha|^2$:

$$P(n) = |\langle n|\alpha\rangle|^2 = e^{-|\alpha|^2} \frac{|\alpha|^{2n}}{n!} \quad (4.2)$$

On the other hand, ideal Mott insulators, that is uniform and at zero temperature, are diagonal in the Fock state basis of the in-trap position. The absence of coherence between lattice sites leads to the different sites behaving like a series of uncorrelated emitters. Consequently, in the far field Mott insulators have been shown to yield thermal-like statistics [132, 176, 177]. The corresponding FCS is a geometric probability distribution associated to thermal states with a mean particle number \bar{n} :

$$P(n) = \frac{\bar{n}^n}{(\bar{n} + 1)^{n+1}} \quad (4.3)$$

The FCS (4.2) and (4.3) correspond to ideal scenarios describing pure states. As states with Gaussian Wigner functions, these probability distributions are fully determined by the mean particle numbers [136] and their character is therefore unaltered by a finite detection efficiency in the experiment, whose only consequence is the rescaling of the mean particle numbers by the corresponding factor. There are, however, other circumstances intrinsic to experiments, such as finite temperature and coupling to the environment, that make it not at all obvious that a description in terms of pure states should apply to the result of any experiment quite generally, a subject that is still an open question in the domain of experimental quantum simulation. In the following it will be shown how in this case a careful choice of the measurement volume can

4. In a single shot of the experiment, the atom number is of course fixed and the BEC is not a coherent state.

allow for the extraction of pure state statistics.

4.1.2 . Measurement volume for pure state FCS

There are several experimental constraints that limit the size of the measurement volume beyond the issue of sufficient statistics.

A first constraint on the size of the volume used to compute $P(n)$ is that it has to be smaller than the total volume of the system. Should this not be the case, the number statistics will simply reflect the total atom number fluctuations of the final state of experimental preparation, since macroscopic quantities are subject to global thermodynamic constraints imposed by the experiment. As an infinite superposition of Fock states, observing coherent state statistics in systems of massive particles is not obvious⁵, independently of any experimental imperfection: Consider an experiment producing ideal BECs at $T = 0$ with no shot-to-shot fluctuations of the total atom number. If the measurement volume is chosen to be such that it encompasses the entire system⁶ the detected atom number will be constant with the experiment mimicking the canonical (or micro-canonical) ensemble, a fact that has been experimentally demonstrated for extremely stable cold atom machines [33]. Therefore, the statistics of the BEC atom number is not that associated to a coherent state, which can only be observed in a grand-canonical context [178]. This implies that the measurement volume V_Ω needs to be so small as compared to the total system size V_{BEC} that the remainder of the system $V_{\text{BEC}} - V_\Omega \sim V_{\text{BEC}}$ can be considered to be a particle reservoir, thereby circumventing the global thermodynamic constraint on the atom number and allowing for particle number fluctuations of $N_\Omega \ll N$ in a grand-canonical sense.

A second constraint on the measurement volume is that it be no larger than the volume occupied by a single mode in momentum space. This is intuitive in the case of the ideal BEC, since coherent state statistics can only be present in the $\mathbf{k} = \mathbf{0}$ mode, with the thermal and quantum depletion of finite momentum modes displaying thermal chaotic statistics [141]. In the case of the Mott insulator, choosing a measurement volume larger than the volume of a single

5. Note that throughout this chapter the statistical properties of ideal BECs are linked to those of a coherent state; this is to be taken as pertaining exclusively to the number statistics. No statement is made about the phase since the phase of the condensate wavefunction is uncorrelated between different repetitions of the experiment.

6. In the far field this corresponds approximately to $(1.6/L)^3$ where L is the in-trap size of the system [138].

mode in momentum space shifts the FCS from a thermal to a multimode thermal distribution, as will be shown in the following. For an in-trap cloud size L the volume occupied by a mode in momentum space is $V_c = (2\pi/L)^3$, and the constraint on the measurement volume V_Ω thus reads $V_\Omega \lesssim V_c$.

In the case of the BEC the fulfillment of this condition is implied by the previous consideration of $V_\Omega \ll V_{\text{BEC}}$. In the case of the Mott insulator, however, $V_\Omega \lesssim V_c$ is a more stringent condition than $V_\Omega \ll V_{\text{Mott}}$ since Mott insulators are large and dilute clouds in momentum space with V_{Mott} larger than the FBZ. The ability to achieve sufficient statistics when probing such small volumes in momentum space is the essential asset of the Helium Lattice experiment that paves the way for the analysis of FCS of pure states in the experiment and is in large part enabled by the high detection efficiency of the MCP detector.

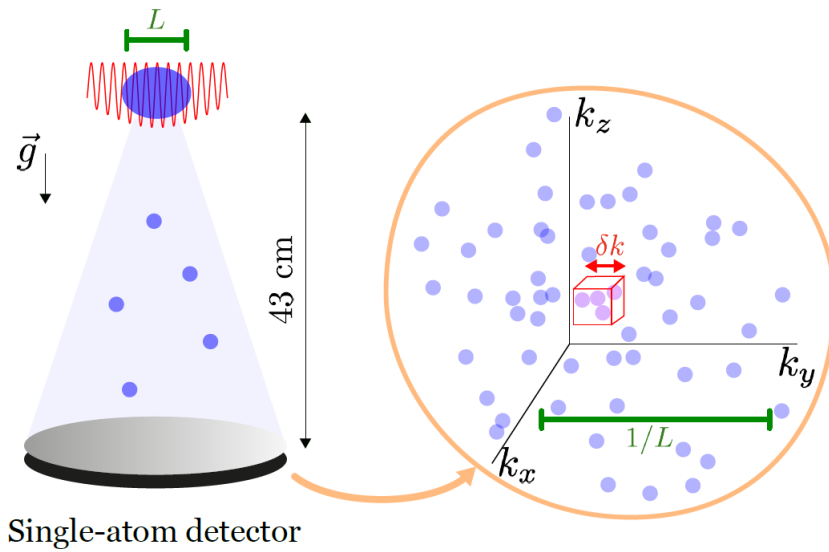


Figure 4.1 - Schematic representation of the FCS measurement. The 3D momentum distribution is recorded in the far field after a long free fall from the optical lattice. The measurement volume $V_\Omega = (\delta k)^3$ has to be chosen to be smaller than the size of a single mode in momentum space $V_c = (2\pi/L)^3$.

Figure 4.1 illustrates the experimental procedure for the measurement of FCS. Atomic clouds of $N \approx 5000$ atoms are adiabatically loaded into the lowest energy band of a 3D optical lattice [97]. After a long TOF the 3D momentum space distribution is recorded by the MCP detector [99, 139]. The length δk of the measurement volume V_Ω is chosen to be smaller than the mode size in

momentum space set approximately by the inverse size of the cloud in the trap L (see below). The atom number N_Ω inside V_Ω then immediately yields the probability distribution of occupation $P(N_\Omega)$ when analyzed over many experimental repetitions. Each dataset for a given value of U/J presented in this chapter is made up of about 2000 realizations of the experiment, with $\langle \cdot \rangle$ used to denote statistical averages⁷. Shot-to-shot fluctuations of the total atom number in the experiment exert a negligibly weak influence on this quantity since by design it is insensitive to global thermodynamic constraints such as the total particle number in a given shot. The long free fall implies a measurement in the far-field regime such that interference effects allow for the FCS to identify quantum states through their many-body coherence [179].

The extracted FCS for weakly-interacting lattice BECs and Mott insulators are presented and discussed in the following sections. The significant difference in the local density of the momentum distributions of these two states necessitates a slightly different analysis procedure for each of these two cases, which is discussed in the context of the respective experimental results.

4.2 . FCS of Mott Insulators

The dilute nature of the momentum distributions of Mott insulators drastically reduces the atom number in volumes of the order of V_c as compared to the $\mathbf{k} = \mathbf{0}$ mode of a BEC⁸. Using a deep lattice at $U/J = 76$ with $N = 6.5(6) \times 10^3$ atoms ensures unity filling at the trap center [176]. In keeping with the above considerations concerning the maximum size of the measurement volume, V_Ω is taken to be a cube of length $\delta k = 6 \times 10^{-2} k_d$. Due to the diluteness of momentum distributions of Mott insulators the statistics within a single such voxel is insufficient to extract a well-contrasted FCS, and increasing the total atom number would induce a filling greater than one atom per lattice site in the trap center. To circumvent the issue of too few counts in a single measurement volume, the entire FBZ is divided into cubic voxels of the same size over which the measured probability distributions are averaged. The resulting FCS is shown in figure 4.2.

From figure 4.2 it is clear that the measured FCS for Mott insulators follows the distribution

7. For instance over all N_{runs} in each dataset, but also over all individual measurement volumes in the case of Mott insulators. $P(n)$ is a measure of correlations within a single shot.

8. For a weakly-interacting lattice superfluid such as the one shown in fig. 4.4 at $U/J = 5$, the average occupation of a volume of size $V_\Omega = (6 \times 10^{-2} k_d)^3$ centered on the origin of momentum space is equal to several hundreds of atoms; for a Mott insulator the occupation of the same volume is nearly on the order of unity.

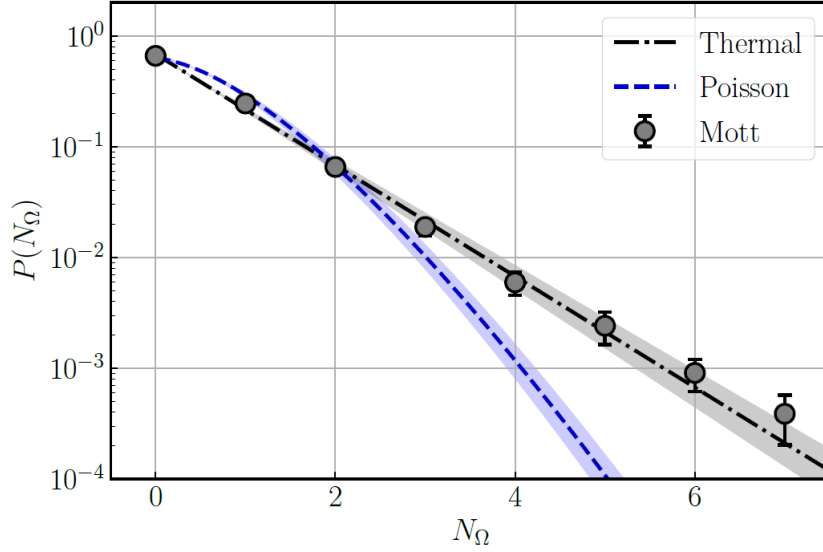


Figure 4.2 - FCS of Mott insulators. The black circles are experimental data of the occupation probability distributions in volumes of size $V_\Omega = 0.9V_c$ averaged over the entire FBZ for a Mott insulator with unity filling. The dashed and dashed-dotted lines correspond to the prediction for thermal and Poissonian statistics, respectively, and are entirely determined by the mean atom number in V_Ω of $\langle N_\Omega \rangle = 0.46(5)$ without any adjustable parameters. The shaded areas represent the uncertainty on $\langle N_\Omega \rangle$. The error bars on the experimental data give the standard deviation estimated via bootstrapping.

expected for a statistical mixture of thermal bosons. The dashed and dashed-dotted lines correspond to the ideal pure state FCS of coherent and thermal states, (4.2) and (4.3) respectively. These theoretical curves are entirely determined by the mean atom number in V_Ω and thus contain no adjustable parameters when $\langle N_\Omega \rangle$ is measured; in this case $\langle N_\Omega \rangle = 0.46(5)$.

4.2.1 . Multimode thermal FCS in large measurement volumes

In order to achieve the best signal-to-noise ratio in terms of statistics, the measurement volume is taken to be as large as possible while still satisfying the condition $V_\Omega \lesssim V_c$. Quantitatively, Mott insulators are shown (see below) to reproduce thermal FCS in momentum space for measurement sizes as large as 90% of the coherence volume, $V_\Omega = 0.9V_c$, as evidenced by the measurement of fig. 4.2. As outlined above, this is based on the notion that a Mott insulator will display thermal statistics in the far-field when probed in volumes that are not larger than that of a single mode V_c . Increasing the measurement volume beyond this size is expected to yield multimode thermal statistics with the probability distribution of occupation morphing from that

of a single mode (4.3) to one reflecting the contributions of M independent modes with average occupation $\langle N \rangle$ according to [41, 180]:

$$P_M(N_\Omega) = \frac{(\langle N_\Omega \rangle + M - 1)!}{\langle N_\Omega \rangle! (M - 1)!} \frac{(\langle N_\Omega \rangle / M)^{N_\Omega}}{(1 + \langle N \rangle / M)^{N_\Omega + M}} \quad (4.4)$$

which contains the single-mode case of (4.3) for $M = 1$. In order to establish up to which volume size the condition $V_\Omega \ll V_c$ is stringent, fig. 4.3 shows the result on the measured FCS of increasing the size of V_Ω from slightly below to significantly above V_c , with the predictions of (4.4) entirely defined by the average atom number $\langle N_\Omega \rangle$ and the number of modes contained in the measurement volume $M = V_\Omega / V_c$. There are therefore no adjustable parameters used to plot the predictions of 4.4 in fig. 4.3.

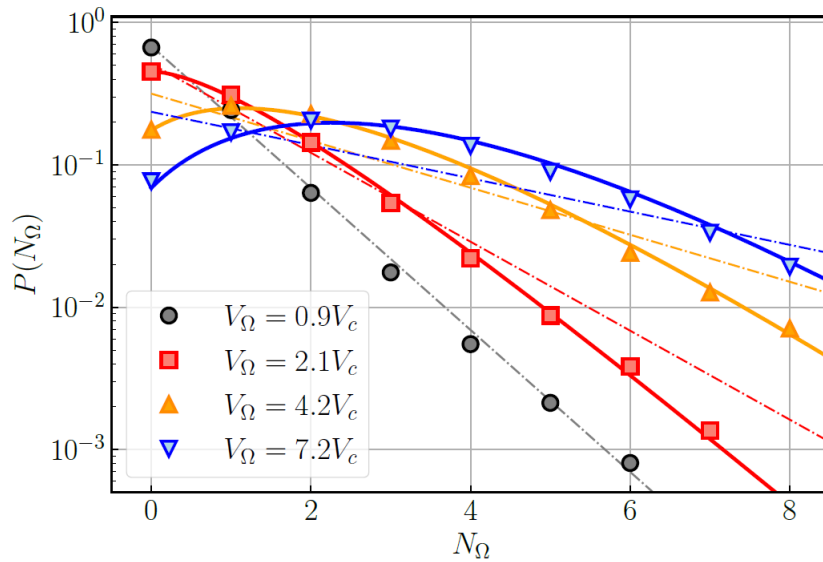


Figure 4.3 - FCS of Mott insulators for different sizes of the measurement volume. The FCS of Mott insulators morphs from a thermal to a thermal multimode description as the size of the measurement volume V_Ω is increased above the coherence volume V_c . The symbols are experimental data and the lines predictions of (4.4) that are given by the measured mean atom number $\langle N_\Omega \rangle$ and the number of modes $M = V_\Omega / V_c$. The black data are the same as in figure 4.2.

Figure 4.3 reveals the condition $V_\Omega \leq V_c$ to be sufficient for the observation of thermal statistics for Mott insulators, with no need to ensure the more stringent $V_\Omega \ll V_c$. As is the case for smaller measurement volumes, the measured probability distributions of occupation are well reproduced by (4.4) for measurement volumes $V_\Omega > V_c$.

4.3 . FCS of weakly interacting BECs

The momentum distribution of lattice BECs in the far field is characterized by a Bragg diffraction pattern that reflects the coherent nature of the matter wave released from a periodic structure. At a shallow lattice depth of $U/J = 5$ the most dominant feature of this distribution in momentum space is a peak of width $\Delta k \simeq 0.15k_d$ centered at $\mathbf{k} = \mathbf{0}$ [23]. The high density of this peak means that sufficient statistics can be achieved for very small measurement volumes that satisfy the condition $V_\Omega \ll V_{\text{BEC}}$ necessary to circumvent the macroscopic constraint of a fixed total atom number impacting the statistics of N_Ω .

For the lattice BECs taking the measurement volume to be a sphere S_Ω of radius $\delta k = 2.5 \times 10^{-2}k_d \ll \Delta k$ is sufficient to obtain a good signal to noise ratio on the measured atom number. For this choice of measurement volume the mean detected atom number is $\langle N_\Omega \rangle \approx 5$, which is roughly an order of magnitude larger than in the case of Mott insulators despite the the measurement volume being only about a third in size. Figure 4.4 shows the measured probability distribution of occupation of S_Ω as a function of the particle number n . The observed FCS is well described by a Poissonian distribution (4.2) and clearly differs from the thermal prediction (4.3). The theory lines are entirely determined by the mean atom number and contain no adjustable parameters. A small deviation from the perfect Poisson law is observed that will be the subject of further discussion in the following.

From comparing figures 4.2 and 4.4 it is clear that the different statistical properties associated to lattice BECs and Mott insulators are well reflected by their respective probability distributions of occupation, highlighting the capabilities of FCS to identify many-body quantum states after an expansion. Furthermore, the respective FCS do in fact reproduce the predictions for pure states (4.2) and (4.3) when the measurement volume is taken to be of appropriate size. Pure states can generally only be approximate descriptions of states realized in experiments due to unavoidable coupling to the environment and macroscopic constraints on thermodynamic variables. The deviation from a perfect Poissonian distribution for lattice BECs visible in figure 4.4 will be further investigated in the following section.

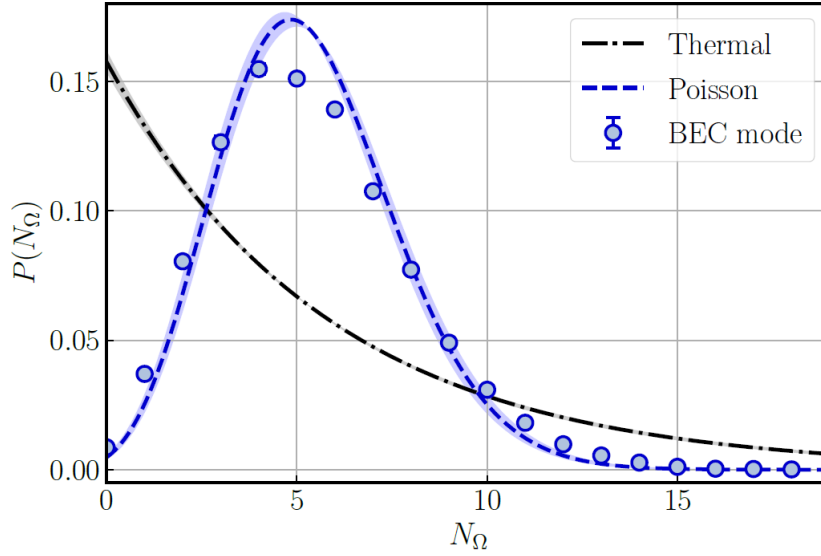


Figure 4.4 - FCS of weakly-interacting lattice BECs. The FCS reveals the underlying Poisson statistics associated to the coherent state of the BEC. Blue circles are experimentally measured probability distributions to find N_Ω atoms in S_Ω for $U/J = 5$ with $\langle N_\Omega \rangle = 5.3(2)$. Error bars indicating the standard deviation via bootstrapping are smaller than the symbols. The blue and black curves are predictions for Poissonian and thermal statistics from (4.2) and (4.3) determined by $\langle N_\Omega \rangle$ without any adjustable parameters. Shaded areas represent the uncertainty on $\langle N_\Omega \rangle$. A small deviation from the Poissonian distribution occurs around the maximum probability that is further discussed in the following.

4.3.1 . Deviation of condensate FCS from Poissonian statistics

The prediction of (4.2) was derived for a pure BEC in a grand-canonical context where all particles in the system are in the condensate and thus describable in terms of a coherent state. However, the fixed experimental particle number at every shot implies that coherent state statistics can only pertain to subvolumes of the entire system. Moreover, in the experiment the BEC is depleted by finite temperature and by interactions (see chapter 3). In a finite-size system, a measurement volume centered on $\mathbf{k} = \mathbf{0}$ of size much smaller than the size of a single mode will necessarily contain contributions from low-energy excited states of the trap, implying that both condensed and depleted atoms contribute to the signal. The thermal depletion is instinctively expected to contribute in an incoherent manner to the statistics, and the quantum depletion has been shown to amount to an incoherent contribution as well when measured in small volumes at nonzero momenta [141]. Since the thermal depletion is approximately constant in the experiment due to the adiabatic loading process into the lattice, the Bose-Hubbard parameter

U/J can be changed at a constant reduced temperature T/J [97]. The remainder of this chapter is dedicated to a quantitative analysis of this deviation from a perfect coherent state statistics by varying the interactions in the experiment and analyzing the higher-order moments of the measured coherence properties.

4.4 . Many-Body Coherence of BECs and Mott Insulators

The probability distributions of occupation presented in the preceding part of this chapter give an initial positive indication to the fact that pure state statistics of many-body quantum states can be retrieved from measurements of single atoms in momentum space. It is not without difficulty, however, to develop a model capable of giving a quantitative explanation for the deviation from a perfect Poissonian FCS in the case of the BEC. Luckily, the measurements of 3D momentum distribution at a single particle level for systems comprised of several thousand atoms are extremely rich datasets and allow for the extraction of other statistical quantities besides the occupation probability of a given volume in momentum space in the quest of identifying the underlying quantum states. One such alternative quantity that can be computed from the same data are correlation functions of high order n , with high n implying significantly larger than $n > 2$ in this case. From a theoretical point of view these quantities are just as well known for the textbooks examples of ideal BECs and Mott insulators as the FCS, with the original idea of making use of them for the characterization of quantum states dating back to R. Glauber's work on photon correlations for light fields [134, 181].

The idea of momentum correlations in the far field reflecting multi-particles interferences in the system and thereby allowing to deduce the many-body coherence properties is directly applicable to atomic gases [179]. As alluded to previously, this approach is even exactly equivalent to the FCS measurement in the case of Gaussian states. In this case, no additional information is contained in the higher orders of correlations since they factorize down to the first order. Therefore, non-Gaussian correlations are expected to be contained in the higher orders in the cases of strongly-correlated non-Gaussian systems [170–172]. Such high orders of correlation functions are not usually measured with atomic gases since they rely on the detection of individual parti-

cles in large systems with strong interactions. Lower orders up to second order have been the subject of measurements on systems of in non-interacting and non-degenerate bosons [31,182] and fermions [183,184], as well as BECs [185], interacting bosons on optical lattices [23,141,186] and interacting fermions [130]. Third order correlations have been measured in BECs [185] and sixth order correlations for non-interacting bosons [182], both making use of the single particle detection capabilities of $^4\text{He}^*$. The measurement of these quantities at high order and in the presence of strong interactions as is the case in strongly-interacting lattice BECs and Mott insulators is thus a novelty in the context of quantum gas experiments, with the testbed of the Bose-Hubbard model able to simulate strongly-correlated systems near the superfluid to Mott insulator transition where the possibility of identifying non-Gaussian states through high order correlation functions presents itself as inspiring future goal.

4.4.1 . Normalized correlation functions

In order to quantify the coherence properties of a quantum state at arbitrarily high orders, Glauber [134] defined the correlation functions $G^{(n)}(x_1, \dots, x_n)$ based on the joint probability of detecting a given number of photons at a given point in spacetime $x_j = (r_j, t_j)$, with the order n set by the number of parallel detectors. It is often convenient to work with the normalized quantity defined as

$$g^{(n)}(x_1, \dots, x_n) = \frac{G^{(n)}(x_1, \dots, x_n)}{\prod_{j=1}^n G^{(1)}(x_j)} \quad (4.5)$$

Crucially, Glauber defined coherent states as having a normalized correlation amplitude of unity:

$$g_{\text{coh}}^{(n)}(x_1, \dots, x_n) = 1 \quad (4.6)$$

for all orders of n and all coordinates x_j . This is in stark contrast to the bosonic bunching displayed by thermal or chaotic states [181], characterized for simultaneous and localized detection $x_1 = \dots = x_n \equiv x$ for correlation functions that grow in amplitude with n according to

$$g_{\text{chaot}}^{(n)}(x, \dots, x) = n! \quad (4.7)$$

as famously showcased in the Hanbury-Brown and Twiss experiment [187].

Even though Glauber's seminal work was motivated by the study of coherence properties of light fields, the approach using normalized correlation functions can be readily transposed to quantum gases measured in momentum space [179], with the coordinates now being given by the momenta \mathbf{k} and thus $g^{(n)}(\mathbf{k}, \dots, \mathbf{k}) \equiv g^{(n)}(0)$. This amplitude of the correlation function at zero separation can then be directly derived from the bosonic commutation rules in second quantization:

$$[\hat{a}(\mathbf{k}), \hat{a}^\dagger(\mathbf{k}')] = \delta_{\mathbf{k}, \mathbf{k}'} \quad (4.8)$$

which leads to the following expression at arbitrary order n :

$$g^{(n)}(0) = g^{(n)}(\mathbf{k}, \dots, \mathbf{k}) = \frac{\langle [\hat{a}^\dagger(\mathbf{k})]^n [\hat{a}(\mathbf{k})]^n \rangle}{\langle \hat{a}^\dagger(\mathbf{k}) \hat{a}(\mathbf{k}) \rangle^n} \quad (4.9)$$

For the purposes of this analysis \mathbf{k} is the momentum indicating the location of the measurement volume V_Ω in momentum space such that $\langle \hat{a}^\dagger(\mathbf{k}) \hat{a}(\mathbf{k}) \rangle = \langle \hat{N}_\Omega \rangle$, with eq. (4.8) implying that the magnitudes of the correlation functions can be directly determined from the measured atom numbers N_Ω via the factorial moments [188–190]:

$$g^{(n)}(0) = \frac{\langle \hat{N}_\Omega (\hat{N}_\Omega - 1) \cdots (\hat{N}_\Omega - n + 1) \rangle}{\langle \hat{N}_\Omega \rangle^n} \quad (4.10)$$

The factorial moments appear out of the power of the number operator due to the normal ordering of creation and annihilation operators $\langle (\hat{a}^\dagger)^n \hat{a}^n \rangle$. In quantum optics this ordering is usually chosen to ensure that the vacuum state has a well-defined expectation value for the photon number and reflects the inevitable destruction of a photon in the detection process. Even though this principle does not usually apply to the detection of atoms, it does so in the case of $^4\text{He}^*$ where any detected atom is for all intents and purposed destroyed from the metastable state since it returns to the ground state. Transposing this approach from quantum optics hence yields the magnitude of the zero-distance correlation functions, which evaluates concretely to, for instance at second order:

$$\begin{aligned}
g^{(2)}(0) &= \frac{\langle \hat{a}^\dagger(\mathbf{k}) \hat{a}^\dagger(\mathbf{k}) \hat{a}(\mathbf{k}) \hat{a}(\mathbf{k}) \rangle}{\langle \hat{a}^\dagger(\mathbf{k}) \hat{a}(\mathbf{k}) \rangle^2} \\
&= \frac{\langle \hat{N}_\Omega (\hat{N}_\Omega - 1) \rangle}{\langle \hat{N}_\Omega \rangle^2} \\
&= \frac{\langle \hat{N}_\Omega^2 \rangle - \langle \hat{N}_\Omega \rangle}{\langle \hat{N}_\Omega \rangle^2} \\
&= 1 + \frac{\sigma_{N_\Omega}^2 - \langle \hat{N}_\Omega \rangle}{\langle \hat{N}_\Omega \rangle^2} \tag{4.11}
\end{aligned}$$

where $\sigma_{N_\Omega}^2 = \langle \hat{N}_\Omega^2 \rangle - \langle \hat{N}_\Omega \rangle^2$ is the variance of the particle number N_Ω in the measurement volume. Equation (4.11) shows that the amplitude of the zero-distance correlation function is determined by the statistical properties of the quantum state. The variance of the probability distributions of occupation (4.2) and (4.3) is well-known and allows immediately for the evaluation of $g^{(2)}$ in the case of ideal BECs and Mott insulators: The Poissonian probability distribution describing coherent states has a variance equal to the mean $\sigma_N^2 = \langle \hat{N} \rangle$ which gives $g^{(2)}(0) = 1$ in accordance with Glauber's definition. The geometric probability distribution describing thermal statistics such as the one of Mott insulators in the far field has a variance equal to $\sigma_N^2 = \langle \hat{N} \rangle^2 + \langle \hat{N} \rangle$ which indicates bosonic bunching at zero distance $g^{(2)}(0) = 2$, an observation that had been confirmed in previous work on the Helium Lattice experiment [176].

On a side note, this manifestation of bosonic bunching in the far field of a Mott insulator that closely resembles that of a thermal state can also be derived directly from the correlation function at second order:

Decompose the momentum operators that enter into the expression for $g^{(2)}(0)$ in the Wannier basis (as is customary for treating Mott insulators), that is using the operators \hat{b}_j^\dagger and \hat{b}_j defined via (2.9) that create and annihilate a particle in the Wannier function of the j -th lattice site:

$$\hat{a}(\mathbf{k}) = \frac{1}{\sqrt{V}} \sum_{j=1}^{N_{\text{site}}} e^{i\mathbf{k}\cdot\mathbf{r}_j} \hat{b}_j \tag{4.12}$$

where N_{site} is the number of lattice sites. Acting on the many-body ground state wave function of an ideal Mott insulator given by (2.25) yields the following type of correlators:

$$g^{(2)}(0) \propto \langle \hat{b}_i^\dagger \hat{b}_j^\dagger \hat{b}_k \hat{b}_l \rangle = \bar{n}^2 (\delta_{i,k} + \delta_{j,l}) - \bar{n} \delta_{i,j,k,l} \quad (4.13)$$

with the mean lattice filling $\bar{n} = N_{\text{tot}}/N_{\text{site}}$. The terms quadratic in \bar{n} run twice over all lattice sites and the term in linear in \bar{n} only once, making the latter negligible for large values of N_{site} (in the experiment $N_{\text{site}} \approx 40^3$). Using $\langle \hat{a}^\dagger(\mathbf{k}) \hat{a}(\mathbf{k}) \rangle^2 = \bar{n}^2$ one is thus left with

$$g^{(2)}(0) = \frac{2\bar{n}^2}{\bar{n}^2} = 2 \quad (4.14)$$

This reasoning is extendable to all higher orders of n where one recovers (4.7), and which corresponds to the bunching at zero distance shown by thermal chaotic states up to negligible terms.

4.4.2 . Measurement volume for fully contrasted correlation functions

In the beginning of the chapter the size of the measurement volume has been shown to play a crucial role in being able to access pure state statistics in the experiment in the context of the measurement of FCS. With the close relationship in information content of that quantity with the normalized correlation functions introduced in the previous part, it comes as little surprise that this question is also of significant importance in this context. The global constraints on macroscopic variables elaborated beforehand still apply in this case, but the physical quantity that is subject to a maximum size condition is now a different one:

Correlation functions do not only contain physically relevant information in the value of their amplitude. The decay distance in the system coordinates of any change in amplitude towards zero distance is also of vital importance. In the far field it represents the typical separation between constituent parts of the system that are uncorrelated and is thus called the correlation length l_c . In the case of Mott insulators where thermal statistics are expected in the far field, the bell-shaped bunching peak towards zero distance in the magnitudes of the correlation functions is well-fitted by Gaussian functions [176] so that the two-body correlation length l_c can be defined from the shape of the second-order correlation function:

$$g^{(2)}(\mathbf{k}_1, \mathbf{k}_2) = g^{(2)}(0) \times \exp\left(\frac{-2|\mathbf{k}_1 - \mathbf{k}_2|^2}{l_c^2}\right) \quad (4.15)$$

As a measure of the decay distance of the correlations in the system, this the correlation length is inversely proportional to the source size, as was famously showcased in the Hanbury-Brown and Twiss experiment [187].

When its light intensity is measured from a great distance, a star can be thought of as a collection of independent emitters of photons, with the far field statistics governed by interferences that take place between emission and detection. In the absence of a coherent mechanism synchronizing the emission of individual photons, the ensuing measured statistics have therefore thermal (chaotic) character. The photon arrival rate of such a source displays thermal statistics in the far field: Bosonic stimulation leads to a strong correlation of intensity fluctuations towards zero distance in both space and time coordinates. The space part of these correlations can be probed by placing two photon detectors at positions \mathbf{r}_1 and \mathbf{r}_2 and varying their separation $|\mathbf{r}_1 - \mathbf{r}_2|$. Hanbury-Brown and Twiss observed a peak caused by the bosonic and chaotic statistics of the starlight in the far field for a detector separation smaller than a certain distance. This decay distance of the correlation function is closely related to the correlation length l_c and could thus be used to determine the angular size of the star.

The detector separation in the HBT experiment is analogous to the size of the measurement volume used to compute atom correlations in this analysis. A finite correlation length implies that if V_Ω is taken to be larger than the correlation volume defined by l_c , the simultaneous fluctuations are measured in part between atoms that are uncorrelated and thus drown out the correlation signal, leading to a reduction in the peak amplitude of $g^{(n)}(0)$. Fully contrasted correlations amplitudes, such as (4.7) in the case of thermal statistics can thus only be measured in volumes smaller than the correlation volume set by l_c . In larger volumes a bunching peak might still be visible, but its amplitude will be reduced with respect to the theoretically expected value. This fact was confirmed by work on the Helium Lattice experiment investigating the amplitude of the third order correlation function at zero distance in Mott insulators [176, 177].

For the Mott insulator data shown in the upper left panel of fig. 4.5 the two-body correlation length fitted using (4.15) is $l_c/k_d = 0.031(2)$, which is commensurate with the expected value given

by the number of lattice sites occupied by the Mott insulator in the trap $l_c/k_d \sim 1/N_{\text{site}}$ [176]. If the correlation length l_c is defined as the $1/e^2$ width of the bunching peak (4.15), its relation to the in-trap system size L in the case of thermal statistics is given by $l_c \simeq \pi/L$. The corresponding coherence volume associated to one mode in momentum space is thus $V_c = (2l_c)^3 = (2\pi/L)^3$. In order to measure fully contrasted correlation amplitudes, the measurement volume must be considerably smaller than this, $V_\Omega \ll V_c$, which is a more stringent condition than the one established in the context of the FCS measurement. Choosing a similar measurement volume size as before such as $V_\Omega = V_c$ would lead to a reduction in the two-body correlation amplitude by a factor of $1/[\sqrt{\pi/8} \operatorname{erf}(\sqrt{2})]^3 \approx 4.7$.

Even though this condition is more stringent than for the FCS measurement, it is fulfilled for the same size of measurement volume S_Ω for lattice superfluids as in the previous case, since $S_\Omega \ll V_c$. The density of the 0 -th order diffraction peak at $\mathbf{k} = \mathbf{0}$ is sufficiently elevated for the extraction of the factorial moments. As in the previous case, however, the situation is drastically different for the Mott insulator which has a very dilute momentum distribution in the far field. On top of that, while V_Ω can be on the order of V_c and still yield single-mode FCS (see fig. 4.3), $V_\Omega \simeq V_c$ is insufficient for the extraction of fully-contrasted correlation function which requires the more stringent $\delta k \ll l_c$. The already low mean detected atom number in V_Ω is thus further diminished by the reduction in the size of the measurement volume in the context of this analysis. In order to achieve sufficient statistics in the face of this additional obstacle anisotropic voxels are now used to bin momentum space $V_\Omega = \delta k \times \delta k_\perp^2$ with a transverse size larger than the correlation length $\delta k_\perp > l_c > \delta k$. This increases the mean detected atom number in V_Ω at the cost of losing the full contrast in the correlation amplitude, a trade-off that is slightly inconvenient but without alternative in the context of the low density exhibited by the far-field momentum distribution of Mott insulators. Similarly to the FCS analysis, the atom number counts $N_{\delta k_\perp}$ extracted from each measurement volume across the FBZ are averaged to increase the signal, with the quantity of interest being now the factorial moments $\hat{N}_{\delta k_\perp}^{(n)}$:

$$\langle \hat{N}_{\delta k_\perp}^{(n)} \rangle = \sum_{j \in \text{FBZ}} \langle N_{\delta k_\perp} (N_{\delta k_\perp} - 1) \dots (N_{\delta k_\perp} - n + 1) \rangle_j \quad (4.16)$$

from which the amplitudes of the normalized correlation functions are directly obtained by

applying the normalization:

$$g_{\delta k_{\perp}}^{(n)}(0) = \frac{\langle \hat{N}_{\delta k_{\perp}}^{(n)} \rangle}{\sum_{j \in \text{FBZ}} \langle N_{\delta k_{\perp}} \rangle_j^n} \quad (4.17)$$

For the second order (4.17) can also be evaluated by computing the histogram of atom pairs instead of the factorial moments [176], which has been verified to yield similar results for the magnitude of $g_{\delta k_{\perp}}^{(2)}(0)$.

The averaging process over the FBZ alone is not sufficient for the extraction of higher order moments, which necessitates the use of the anisotropic measurement volumes. The corresponding reduction in contrast caused by integration over uncorrelated atoms along the directions δk_{\perp} means that the measured magnitudes will be lower than the prediction for thermal statistics (4.7). In order to quantify this effect, figure 4.5 shows the corresponding reduction in amplitude of the correlation functions as δk_{\perp} is increased. The effect is visible at every order from second all the way through sixth.

While this effect is without a doubt undesirable, it does not prevent one from confirming the thermal nature of the obtained statistics. Indeed, the anisotropic geometry of the chosen measurement volume implies that this effect only occurs along two of the three directions of momentum space, which decouple on account of the 3D Gaussian shape of the correlation volume. This decoupling allows for the quantification of the reduction in amplitude of the correlation functions $g_{\delta k_{\perp}}^{(n)}$ along the δk -axis due to the large transverse integration along the two directions δk_{\perp} . Repeated calculation of $g_{\delta k_{\perp}}^{(n)}$ for different values of δk_{\perp} with the longitudinal dimension of V_{Ω} at a constant $\delta k = 1.5 \times 10^{-2} k_d \leq l_c$ then permit the extrapolation of $g_{\delta k_{\perp}}^{(n)}$ in the limit $\delta k_{\perp} \rightarrow 0$, which in turn yields the fully contrasted amplitudes $g^{(n)}(0)$.

4.4.3 . High-order correlation functions of BECs and Mott insulators

Figure 4.6 shows the measured amplitudes of the correlation functions $g^{(n)}(0)$ for Mott insulators and the $\mathbf{k} = \mathbf{0}$ mode of lattice BECs up through sixth order. The difference in amplitude between the correlation functions of the two datasets becomes more and more striking with increasing order as the Mott insulator data is consistent with a thermal scaling according to (4.7) while the BEC appears to remain constant around $g^{(n)} \simeq 1$. At the highest extracted order this leads to a difference of almost three orders of magnitude in the amplitude of the correlation

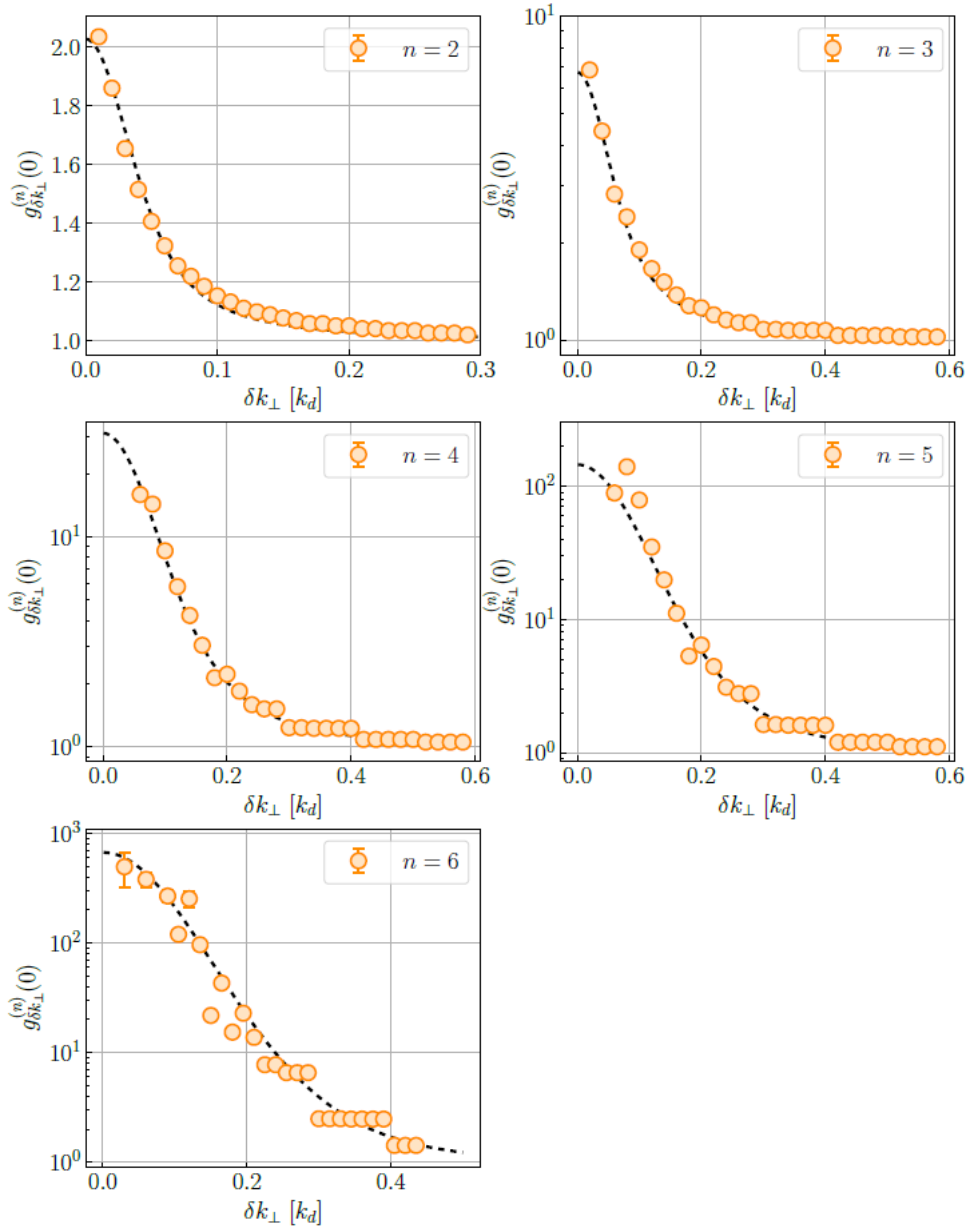


Figure 4.5 - Effect of the transverse integration δk_{\perp} on the amplitudes of the correlation functions $g_{\delta k_{\perp}}^{(n)}$. Varying δk_{\perp} while keeping the longitudinal dimension of V_{Ω} at a constant $\delta k = 1.5 \times 10^{-2} k_d \leq l_c$ allows for the extrapolation of the fully contrasted correlation functions $g^{(n)}$ in the limit $\delta k_{\perp} \rightarrow 0$ (black dashed lines).

functions.

Previous measurements of the second and third order correlation functions of Mott insulators carried out on the Helium Lattice experiment [176] were unable to extract a fully contrasted

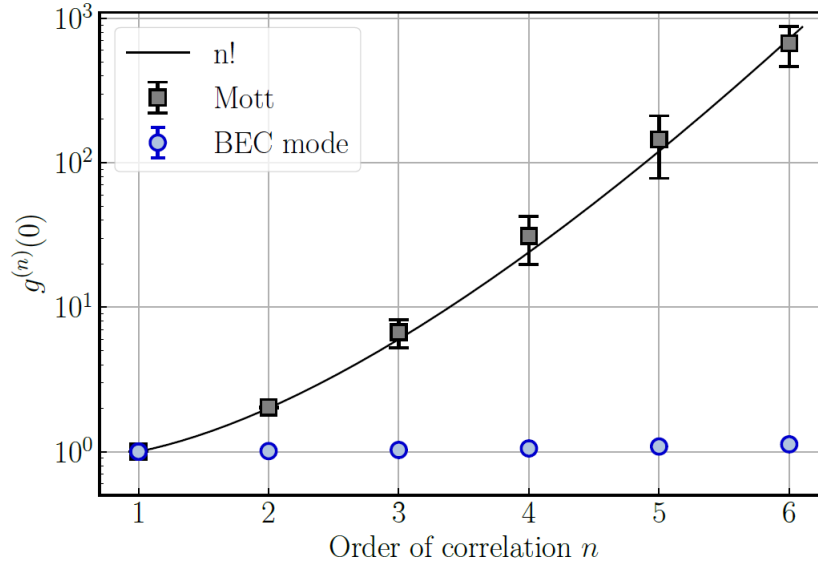


Figure 4.6 – Correlation functions of BECs and Mott insulators for orders $n = 2$ through 6. The Mott insulator follows the expected factorial law (4.7) (black line), while the $\mathbf{k} = \mathbf{0}$ mode of the lattice BEC appears to be consistent with the coherent state prediction (4.6). Error bars for the Mott insulator dataset are the fitting errors from the extrapolation of the correlation amplitude in the limit of vanishing transverse integration (see fig. 4.5). Error bars for the BEC mode are calculated according to (4.18).

correlation amplitude by a considerable margin⁹. Here, the approach detailed above allows for the circumvention of the transverse integration effect and thus the extraction of fully contrasted correlation function amplitudes up to sixth order. The main experimental advancement enabling this measurement is the implementation of the Raman transfer detailed in chapter 2 which has increased the detected atom number in volumes compatible with V_c sufficiently for the extraction of the factorial moments.

The compatibility of the values of $g^{(n)}(0)$ with $n!$ justifies the argument presented above for identifying the far-field momentum space coherence for Mott insulators with those of a thermal state up to negligible factors. The only way to differentiate these two states from the measured momentum distributions is to compare their correlation lengths $l_c^{(n)}$. While both display bunching of the same amplitude and of size $l_c \propto 1/L$, they differ in their in-trap size L due to the incom-

⁹. Due to the limited detection efficiency at the time a much larger measurement volume had to be used with the increase in transverse integration reducing the expected values from 2 to 1.065(10) for $g^{(2)}(0)$ and from 6 to 1.32(5) for $g^{(3)}(0)$. Nonetheless, the correct scaling could be extracted for the ratio $\frac{g^{(3)}(0)-1}{g^{(2)}(0)-1} \simeq 5$.

pressibility of Mott insulators. The latter makes L strongly dependent on the total atom number N_{tot} , while for thermal clouds L is independent of N_{tot} [191]. Despite their apparent similarities in terms of the measured quantities in momentum space, previous work on the experiment has carried out this comparison and thereby confirmed that the states prepared at high values of U/J are indeed Mott insulators and not thermal states [97, 140, 176].

In the log scale used for figure 4.6 the $\mathbf{k} = \mathbf{0}$ mode of the BEC appears to be consistent with Glauber's definition (4.6). Looking more closely at the values around unity, however, reveals a systematic deviation from this value that makes the BEC data incompatible with 1 for all orders above the first, as is shown in figure 4.7.

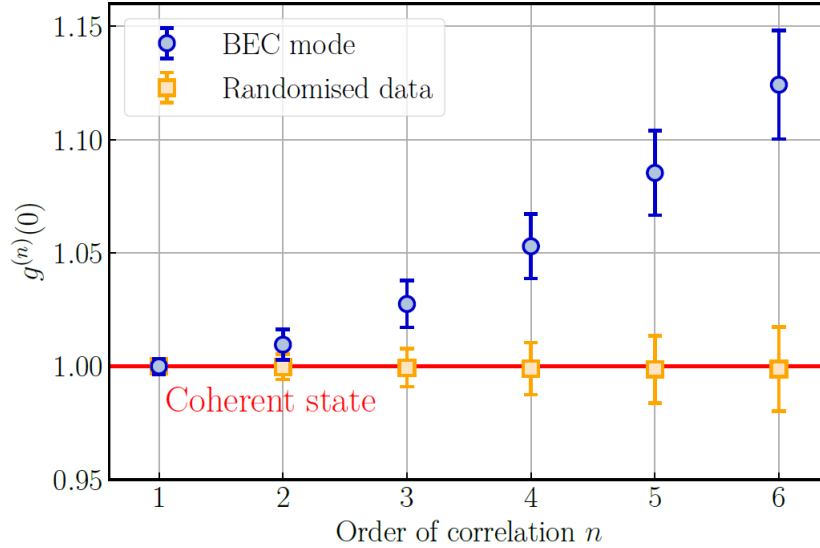


Figure 4.7 - Correlation functions for the weakly-interacting BEC and the randomized dataset. Zooming in on the region around unity for the BEC data shown in fig. 4.6 (blue circles) reveals a deviation from the coherent prediction (4.6) (red line) for all orders $n > 1$. The randomized dataset (orange squares), void of any coherence by construction (see text), adheres to the expected value of unity at all orders up to sixth, indicating that the deviation from the coherent state statistics observed in the blue points is not due to a lack of statistics. Error bars for both datasets are calculated according to (4.18).

The error bars for this dataset are given by

$$\Delta g_{\text{BEC}}^{(n)}(0) = \frac{\Delta N_{\Omega}^{(n)}}{\langle N \rangle^n} \quad (4.18)$$

which is calculated from the standard error of the factorial moments:

$$\Delta N_{\Omega}^{(n)} = \frac{1}{\sqrt{N_{\text{runs}}}} \sqrt{\langle (N_{\Omega}^{(n)})^2 \rangle - \langle N_{\Omega}^{(n)} \rangle^2} \quad (4.19)$$

The deviation increases with n and only the first order of the correlation function amplitude remains at unity¹⁰. Moreover, the way that $g^{(n)}(0)$ deviates from unity seems to resemble the result of a combination of a dominant contribution from coherent state statistics, since the values stay close to 1, with a small addition of some incoherent, thermal-like constituent part adding a small share of $n!$ -like behavior.

In order to verify that the observed deviation is statistically meaningful instead of simply being an artifact of an insufficient number of detection events within the measurement volume S_{Ω} , figure 4.7 also shows the result of the computation of the n -body correlations carried out on an artificial dataset obtained by randomly shuffling the detected atoms across the different runs of the experiment while keeping both the total number of shots and the mean detected atom number per shot constant with respect to the original dataset. Since the correlation between any two atoms from different shots of the experiment is zero, this procedure destroys all many-body coherence effects within a single randomized shot. Thus, the discrete nature of the single particle detection method applied to fully independent events leads to each randomized shot being constituted of a collection of discrete and independent detection occurrences at a fixed rate (due to the randomization). Such conditions give rise to a Poisson distribution, which has a zero-distance amplitude of correlation equal to $g_{\text{Poisson}}^{(n)}(0) = 1$ for all orders n , reflecting the fact that detection events in a Poisson process are independent from another and thus the occurrence of one event has no effect on the likelihood of the occurrence of another one.

It is important to note at this point that, even though the randomized dataset fulfills the conditions for exhibiting Poissonian statistics and therefore an amplitude of the correlation functions equal to unity, this does not occur as a consequence of the same root cause in a physical sense as the one leading to the identical result for the statistics exhibited by a coherent state. Simply put, there are different underlying statistical mechanisms that can give rise to a Poissonian distribution of probability, and while a coherent state is one of them, the relationship is not bijective. The creation of a randomized dataset that contains no correlations between atoms within a sin-

10. Per definition $g^{(1)}(0) = 1$ whatever the nature of the probed state

gle run by construction offers the possibility to test the available statistics to verify the algorithm.

As is evident from fig. 4.7, the magnitudes of the n -body correlations of the randomized dataset adhere perfectly to unity as is expected in the absence of all coherence within a single shot, with amplitudes equal to $g^{(n)}(0) = 1.00(2)$ at any order $n \leq 6$. This randomization method produces the same result when applied to the Mott insulator dataset, validating the computation algorithm for the n -body correlations and confirming the physical origin and significance of the deviation from 1 observed for the BEC mode. This observation is indeed equivalent to the deviation from a perfect Poissonian distribution for the same data in the FCS analysis shown in figure 4.4. The remainder of this chapter is dedicated to a quantitative interpretation of this deviation from pure state statistics that is now evident from two different analyses of the data.

4.4.4 . Establishing the limit of the experimental statistics

The randomization procedure detailed in the context of fig. 4.7 has been shown to allow for a consistency check of the algorithm used to extract the n -body correlations. Fig. 4.8 now presents the extension of this approach on the same dataset at $U/J = 5$ to even higher orders of correlation up to $n = 10$.

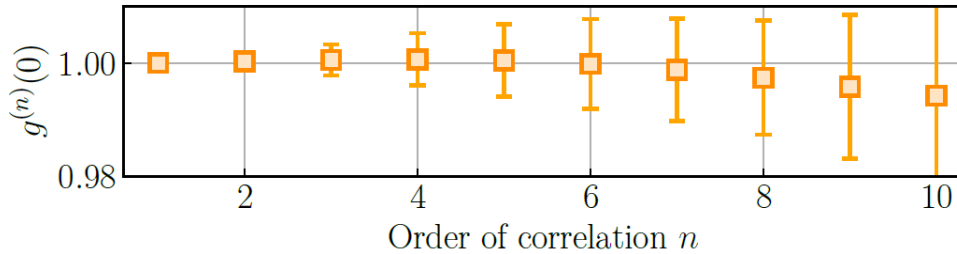


Figure 4.8 - Amplitudes of correlation functions for the randomized dataset extended to higher orders of correlation. The orange points correspond to the same randomized dataset as in fig. 4.7 with the analysis continued through the tenth order of correlation. A systematic deviation towards smaller values occurs for $n > 6$, indicating a limit to the extensibility of the modeling analysis for orders higher than six.

Fig. 4.8 shows the appearance of a systematic trend above $n = 6$ that deviates the randomized data from the $g^{(n)}(0) = 1$ line towards smaller amplitudes. This trend is to be taken as an indication to the fact that the statistics within S_Ω are no longer sufficient to reproduce the theoretically certain result for a dataset known to be completely free of coherence and thus of

any systematic trends in the correlation amplitudes. The appearance of this effect for higher orders constitutes an indication to the fact that the limit of experimental statistics is starting to be tested for $n \geq 7$ with simultaneous detection events of $N_\Omega \geq n$ now representing an increasingly unlikely occurrence. Surpassing this limit would require either a significantly larger number of repetitions of the experiment, or (a considerably more efficient option) an increase in the quantum efficiency η of the single particle detector, with the latter affecting the simultaneous detection of n particles required for a contribution to the factorial moment $\langle \hat{N}_\Omega^{(n)} \rangle$ by a factor of η^n . With the implementation of the Raman transfer detailed in chapter 2, however, it can be assumed that nearly all atoms prepared in the system are transferred to the detected state, and thus increasing η would necessitate a change in the experimental setup, most likely replacing the detector with one with a higher quantum efficiency¹¹.

4.5 . Deviation from Coherent Statistics in Correlations of Lattice BECs

As alluded to in the beginning of the chapter, recovering pure state statistics from experimental data is not an obvious endeavor. The Poissonian FCS and ensuing unity of the correlation function amplitudes rely on the description of the quantum state as an ideal BEC. Unsurprisingly, this state does not correspond to the one prepared in the experiment, where the BEC is depleted by both non-zero temperature and interactions between atoms. Based on previous investigations of the statistical properties of the total depletion [141] these contributions are known to add an incoherent component to the observed local statistics. With the amplitudes of the correlation functions seemingly containing a small incoherent part manifesting in a deviation from unity that increases like some small factor times $n!$ (see fig. 4.7), this incoherent character seems to be reflected in the measured correlation functions and might consequently also account for the deviation from a Poissonian FCS evident in fig. 4.4. Hence, it seems relevant to investigate the role of the depletion in many-body coherence properties for the lattice BECs prepared in the experiment.

11. As of the time of this writing, no MCP detector with a higher quantum efficiency is available on the market.

4.5.1 . The incoherent statistical properties of the depletion

With the enhancement of interactions in the optical lattice [97,141] endowing the experiment with ability to probe the low temperature regime $k_B T \ll \mu$, where μ is the chemical potential, the two contributions to the total depletion are approximately comparable. Concretely, for $U/J = 5$ at $k_B T/\mu \simeq 0.3$ the thermal depletion is on the order of 10% and the quantum depletion on the order of 5% [23]. The origin of the incoherent statistical properties with respect to measurements in small volumes in momentum space differs for the two depletion parts.

On the one hand, the atoms depleted by thermal excitation in the low-temperature regime are known to form a thermal state of noninteracting bosonic Bogoliubov excitations [22] whose population is determined by Gaussian statistics and the temperature. The linearity of Bogoliubov's transformation implies that the Gaussian statistical properties of these quasi-particles carry over to their associated particle momenta, and thus $g^{(n)}(0) = n!$ [132,137,192].

On the other hand, the quantum depletion consists of a superposition of two-mode squeezed states at opposite momenta [23]¹², and is a feature associated to the (zero temperature) ground state of a BEC in the presence of interactions [22]. With the pairs described as being in a coherent superposition with the condensate, the question arises as to why they should lead to an incoherent contribution. The answer lies in the measurement procedure specific to the FCS analysis that requires probing small volumes of momentum space. If located at finite momentum, such small volumes can by construction not contain both partners of a $\mathbf{k}/ - \mathbf{k}$ pair of the quantum depletion, and measuring one while ignoring the other one amounts to performing a partial trace over the second partner of the atom pair at opposite momentum. Correlations measured in small volumes at finite \mathbf{k} thus probe correlations between atoms that belong to different pairs, and the density matrix describing them, which results from the partial trace over the second partner of each pair, has thermal (chaotic) statistics, similarly to the statistics associated with the observation of only one partner of parametric down conversion photons pairs [193] or of atom pairs resulting from two-body collisions [41,194]. Previous work on the Helium Lattice experiment has demonstrated that the quantum depletion exhibits thermal statistics when probed in

12. Note that the considerations outlined in this section are based on the assumption that Bogoliubov theory describes the experimental system. This is certainly justified at small values of U/J . However, following the results presented in chapter 3, this is not the case for the $\mathbf{k}/ - \mathbf{k}$ correlations at larger interaction strengths. Despite that, the quantum depletion is still expected to contribute incoherently to the statistics measured in small volumes of momentum space in this region.

small volumes at nonzero momenta [141]. The overlap of the first excited trap states with the $\mathbf{k} = 0$ mode present in the finite-size experimental system is expected to be sufficiently small for the simultaneous mapping of both opposite momenta into this mode to be a rare occurrence, so that when one partner of a pair is detected in the $\mathbf{k} = 0$ mode, the other one will be most likely be situated at a finite momentum state, and the partial trace argument implies an incoherent contribution to the measured local statistics of the $\mathbf{k} = 0$ mode.

The finite size of the system implies that modes corresponding to the first excited states of the trap contribute to the signal measured in a volume of size much smaller than that of a single mode, implying the presence of atoms belonging to the depletion when probing the $\mathbf{k} = 0$ mode. It is not possible to divide their respective contributions apart in the momentum distributions that make up any single dataset, since it is impossible to attribute any detected atom to either the thermal or the quantum depletion. It is, however, possible to vary the impact of one while keeping the other one more or less constant.

This statement may seem intuitive in the case of temperature, since most quantum gas experiments strive to achieve temperatures that are as low as possible in order to reveal effects associated to quantum degeneracy. As outlined in chapter 2 this is all the more true for the Helium Lattice experiment that sets out to be a platform capable of exploring characteristics of a quantum phase transition that occurs at zero temperature (see chapter 5). Since a considerable effort is undertaken to reduce the temperature of the prepared system as much as possible, it is relatively straightforward from an experimental point of view to achieve what would otherwise be considered a suboptimal cloud temperature¹³. Any procedure resulting in an increase of the thermal depletion is, however, not completely separable from the state of the quantum depletion, at least in the present case of constant total atom numbers for all datasets¹⁴. Since the quantum depletion consists of atoms expelled from the condensate via interactions, a decrease in the condensed fraction f_c brought about by a heating procedure that increases the thermal depletion automatically reduces the number of available atoms in the condensate that can form momentum-correlated pairs via collisions, thereby reducing the quantum depletion. As demon-

13. See for instance the paragraph **Heating procedure** from the **Methods** of [23].

14. As outlined in chapter 2 this condition ensures unity filling of the lattice in the trap center at the Mott transition.

strated in a previous work on the experiment [23] this effect can be made to be sufficiently consequential as to drown out any correlation signal associated to the quantum depletion.

The same consideration naturally holds in the opposite case as well, where a condensate depleted by strong interactions will have less atoms available to be thermally excited into the thermal depletion, even in the case of isentropic loading into the deeper lattice [97]. While these two considerations are to be kept in mind when attributing differences in datasets at different values of T/J or U/J to a single variable, it is also clear that the effect is not dominant and indeed assumed to be sufficiently small in the context of the datasets presented in this chapter at different values of U/J in the superfluid phase that one can consider differences in datasets to be primarily attributable to differences in quantum depletion and thereby the quantum depleted fraction only.

With these considerations in mind, the idea for attributing the deviation from coherent state statistics observed in fig. 4.4 and 4.7 to the presence of atoms from the depletion in the measurement volume consists in increasing the contribution of the depletion to quantify the change in this deviation as the overall depleted fraction of atoms increases. In principle, either one of the outlined mechanism might be used to increase the incoherent contribution of the atoms outside the condensate, but increasing the interactions by tuning the Bose-Hubbard parameter U/J offers far greater control and precision than increasing the temperature of the cloud. Additionally, the ensuing states may still be compared in the context of varying many-body equilibrium states at similar temperature, emphasizing the role of the many-body ground state properties significantly more than increasing temperature but leaving the parameters of the Hamiltonian of the system unchanged.

The set of experiments realized in the quest to quantify and interpret the deviation from coherent state statistics consists thus in increasing the lattice depth to augment the interactions and consequently the quantum depletion, and conducting the same analysis as for the BEC mode as in the previous part of the chapter to investigate the role of the depletion in setting the many-body coherence properties of the quantum system.

An additional context for this series of experiments is given by previous measurements of

the same quantities in lattice BECs [185]. These experiments, carried out on a different $^4\text{He}^*$ experiment, reported second- and third-order momentum correlations of amplitudes consistent with Glauber's definition for coherent states $g^{(2)}(0) = g^{(3)}(0) = 1$ without any systematic deviation from unity. Explaining this discrepancy with respect to the data shown in fig. 4.7 represents a further aim of this analysis.

4.5.2 . Increasing the incoherent contribution via interactions

In keeping with the above considerations about the role of the depletion in the measured many-body coherence properties, the experiment is performed for a range of increasing interactions set by the Bose-Hubbard parameter U/J while keeping to the superfluid part of the phase diagram. Concretely, U/J is increased from the low interaction value of $U/J = 5$ (corresponding to the data shown in fig. 4.4, 4.6 and 4.7) all the way to $U/J = 20$, where the BEC is strongly depleted due to interactions but is still well shy of entering the Mott insulating regime with the critical value located at $(U/J)_c = 26(1)$ [140]. As a consequence the condensed fraction is decreased from $f_c \approx 84\%$ at $U/J = 5$ all the way down to $f_c \approx 15\%$ at $U/J = 20$. Having established that the reduced temperature T/J remains constant as U/J is increased [97], it is the quantum depletion that is mostly responsible for this increase in the condensate depletion. All other experimental parameters are kept constant¹⁵ with respect to the initial experiment at $U/J = 5$. The resulting n -body correlations are shown in figure 4.9.

From figure 4.9 it is clear that increasing the interaction strength increases the deviation of the n -body correlations from the coherent state statistics (4.6). In addition to increasing with U/J across all datasets for any given order n , the deviation also increases as a function of n within any single dataset, as already observed in fig. 4.7. This behavior is reminiscent of that of a state with thermal statistics for which the n -body correlations increase with n according to (4.7). As implied by the equivalence in information content between FCS and n -body correlations, a gradual deviation from the Poissonian FCS is also observed in the FCS of the datasets for $5 \leq U/J \leq 20$. With the increase in quantum depletion being the main differing feature between these momentum distributions, this result confirms the intuition formulated at the outset, namely that of the de-

¹⁵. Technically speaking, increasing U/J also increases the frequency of the harmonic trap as an unavoidable side effect of increasing the intensity of the lattice laser beams due to their harmonic confinement effect.

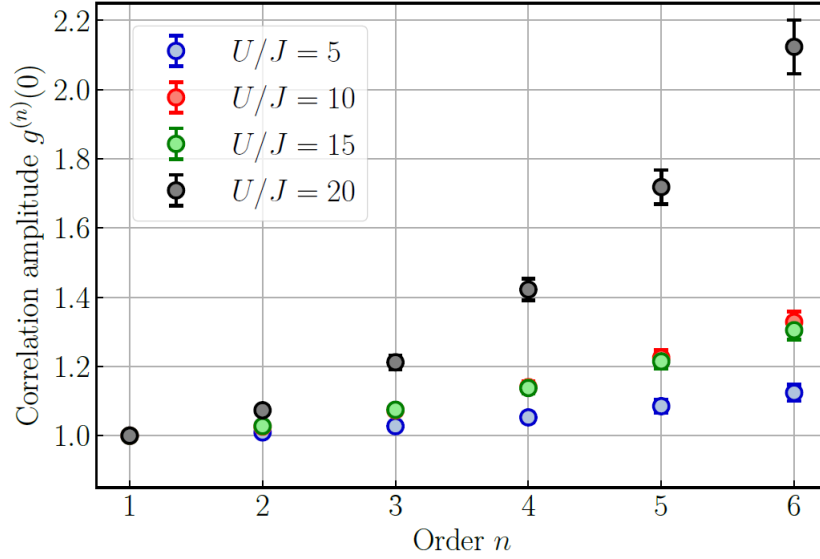


Figure 4.9 – Correlation functions of lattice BECs at increasing interactions U/J . As interactions increase, so does the deviation from unity for the amplitudes of the correlation functions $g^{(n)}(0)$ obtained from the factorial moments of the occupation of the measurement volume S_Ω . The dataset at $U/J = 5$ is the same as in fig. 4.4, 4.6 and 4.7. As observed in fig. 4.7, within each dataset this deviation also increases with the order of correlations, reminiscent of the behavior of states with thermal statistics that exhibit a scaling according to (4.7). Error bars for all datasets are calculated according to (4.18).

viation from coherent state statistics being due to an incoherent contribution of the depletion, at least qualitatively. In the following a heuristic model is introduced in order to describe the impact of the condensate depletion on the n -body correlations in a quantitative manner.

4.5.3 . Modeling the role of condensate depletion in many-body coherence

Since no theoretical analytical prediction exists for the description of large 3D systems of interacting lattice bosons in a harmonic trap, a simple model is developed in an effort to quantitatively represent the role of the condensate depletion in the many-body coherence properties of the system. In addition to supposing that the BEC statistics can be described by those of a coherent state and that the depletion exhibits thermal statistics in S_Ω , the model is based on the simple, but by no means trivial, assumption that atoms in the condensate and in the depletion contribute independently to the measured counting statistics in the measurement volume [178]. This assumption is reasonable in the weakly-interacting regime where the condensate depletion is treated as a perturbation on top of the BEC.

It is emphasized that many of the central aspects of this model arise from the small size of the measurement volume, which, as has been outlined throughout this chapter, is of vital importance in the quest of extracting pure state statistics from experimental data. The reason behind the importance of this fact in the context of setting up the heuristic model is that if the measurement volume were to encompass the entire system, a strong correlation would naturally prevail between the condensed and the depleted atoms, which in the absence of technical imperfections pertaining to the experiment (such as a finite detection efficiency) would amount to $N_{\text{tot}} = N_{\text{BEC}} + N_{\text{dep}}$, implying perfect correlation between the two quantities in the canonical ensemble. The reality of measuring inside the small sphere S_{Ω} of radius $\delta k = 2.5 \times 10^{-2} k_d$, however, implies probing a region of momentum space far smaller than the extension of the depletion. So long as the condensed fraction stays relatively large, i.e. in the Bogoliubov regime, approximating no correlations between condensed and depleted atoms inside S_{Ω} that are imposed by constraints on macroscopic observables seems reasonable. When moving towards the strongly interacting regime where the condensate is significantly depleted and the depletion constitutes no longer just a perturbation on top of the BEC, on the other hand, the validity of this assumption remains an open question and can only be justified by the success of the model that is based upon it in describing the observed effects (see below).

With these assumptions in mind, the model is created from expressing the expectation value of the number operator for the measured occupation of S_{Ω} in terms of the creation and annihilation operators of the parts contributing to the statistics in the measurement volume, that is

$$N_{\Omega} = \langle \hat{N}_{\Omega} \rangle = \langle \hat{a}_{\text{BEC}}^{\dagger} \hat{a}_{\text{BEC}} \rangle + \langle \hat{a}_{\text{dep}}^{\dagger} \hat{a}_{\text{dep}} \rangle = N_{\text{BEC}} + N_{\text{dep}} \quad (4.20)$$

where the assumption of independent contribution of atoms belonging to the condensate and the depletion has entered in the form of neglecting their correlators $\langle \hat{a}_{\text{BEC}}^{\dagger} \hat{a}_{\text{dep}} \rangle = 0$. Note that from here on out all quantities subscripted $_{\text{BEC}}$ and $_{\text{dep}}$ are meant to be understood in the context of the measurement volume, so that for instance N_{dep} refers to the number of atoms from the (quantum or thermal) depletion falling inside S_{Ω} rather than the total number of depleted atoms in the system.

With \hat{a}_{BEC} and \hat{a}_{dep} assumed to be uncorrelated, the n -th power of \hat{a}_Ω can be expressed simply as

$$\hat{a}_\Omega^n = \sum_{p=1}^n \binom{n}{p} (\hat{a}_{\text{BEC}})^p (\hat{a}_{\text{dep}})^{n-p} \quad (4.21)$$

from which follows the expectation value for the n -th factorial moment of the atom number in S_Ω :

$$\langle \hat{N}_\Omega^{(n)} \rangle = \langle (\hat{a}_\Omega^\dagger)^n \hat{a}_\Omega^n \rangle = \sum_{p=1}^n \binom{n}{p}^2 \langle (\hat{a}_{\text{BEC}}^\dagger)^p (\hat{a}_{\text{BEC}})^p (\hat{a}_{\text{dep}}^\dagger)^{n-p} (\hat{a}_{\text{dep}})^{n-p} \rangle \quad (4.22)$$

With the amplitude of the n -body correlation function being essentially given by a normalization applied to the factorial moments, the models yield thus as analytic expression for the n -body correlations:

$$g^{(n)}(0) - 1 = \frac{\langle (\hat{a}_\Omega^\dagger)^n \hat{a}_\Omega^n \rangle}{\langle \hat{a}_\Omega^\dagger \hat{a}_\Omega \rangle^n} - 1 = \sum_{p=1}^{n-1} \left[(n-p)! \binom{n}{p}^2 - \binom{n}{p} \right] (f_{\text{coh}})^p (1 - f_{\text{coh}})^{n-p} \quad (4.23)$$

where the single parameter upon which $g^{(n)}(0)$ depends has been introduced as the coherent fraction:

$$f_{\text{coh}} \equiv \frac{N_{\text{BEC}}}{N_\Omega} = \frac{\langle \hat{a}_{\text{BEC}}^\dagger \hat{a}_{\text{BEC}} \rangle}{\langle \hat{a}_\Omega^\dagger \hat{a}_\Omega \rangle} \quad (4.24)$$

Thus f_{coh} represents the fraction of atoms inside the measurement volume that contribute in a coherent fashion to the measured statistics, which by assumption for this models means the fraction of atoms in S_Ω belonging to the condensate.

Having derived an analytic formula for the n -body correlations from a small set of simple assumptions, and given the close relationship between the amplitudes of the correlation functions and the FCS, one naturally wonders if a similar result can be derived for the probability distributions of occupation. However, despite their strong connection and in some cases even strict equivalence in terms of information content, it is not at all straightforward to derive $P(N_\Omega)$

from $g^{(n)}(0)$. In fact, the neat separation between the contributions of the condensate and the depletion (4.20) does not carry over to the probability distributions, with the latter containing a complex convolution of $P(N_{\text{BEC}})$ and $P(N_{\text{dep}})$. This is in line with a more universal understanding that probability distributions of a random variable are notoriously difficult to derive from its moments in quite a general context [195, 196].

4.5.4 . Establishing the predictive capacities of the model

With the analytical formula (4.23) for the n -body correlations at hand, the model is put to the test by fitting the experimental data of the magnitudes $g^{(n)}(0)$. A successful reproduction of the experimental observations might be seen as a positive indication, though certainly no proof, regarding the justification of the assumptions underlying the model. A failure to reproduce the experimental data, on the other hand, would certainly constitute a strong case for their invalidity.

Figure 4.10 shows the n -body correlations at $U/J = 5$ from fig. 4.7, with the added dashed line corresponding to the model prediction from (4.23).

With (4.23) being a function of a single parameter, fitting this analytic expression to the experimental data yields a value for the coherent fraction of $f_{\text{coh}} = 0.9960(5)$. One can argue about whether or not it is warranted to label this fit as being a prediction, since it contains an adjustable parameter. What fig. 4.10 does certainly reveal, however, is that with the resulting value for f_{coh} the expression (4.23) reproduces the observed data with an accuracy of 5×10^{-4} , thereby constituting a first step towards a potential validation of the assumptions the model is based on.

The value of f_{coh} is close to unity, which is in line with the expectation that for weakly-interacting lattice BECs the number of depleted atoms in S_{Ω} is small. Despite the incoherent fraction $1 - f_{\text{coh}}$ being less than half a percent of the atoms in the measurement volume, it affects the statistical properties of the many-body state in such a way as to confirm its incompatibility with those of a completely coherent state from the second order on. The ability to extend the measurement to orders as high as six results in an uncertainty on the fit parameter that is significantly smaller than the experimental error bars, making this experimental approach extremely sensitive to even small deviations in the many-body coherence properties. It is worthwhile to note that, based on the mechanism employed to increase the incoherent fraction, this shift is directly related to parameters in the Hamiltonian of the system and thus the many-body ground state,

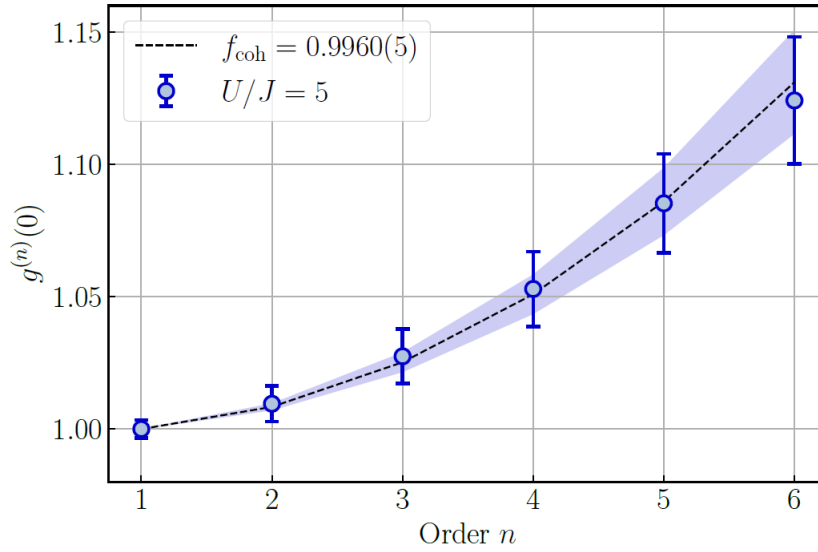


Figure 4.10 - Application of the model to the experimentally observed n -body correlations for the weakly-interacting BEC. The blue points are the same experimental data and error bars as in fig. 4.7. The dashed line is a fit of (4.23) to the experimental data with f_{coh} as only adjustable parameter. The blue shaded region indicates the uncertainty on the fit. The model (4.23) succeeds in confirming the deviation from unity in the correlation amplitudes observed in the experiment and reproduces the experimental data with an extremely low uncertainty on the fit parameter f_{coh} .

as opposed to being simply an artifact of modifying the external conditions of the experimental environment such as the finite temperature. While one has to be careful not to push this line of reasoning too far, since f_{coh} would arguably be larger at zero temperature, comparing the variation of this quantity over datasets that differ nearly exclusively in the value of the parameter driving the unitary dynamics is an exciting prospect that will be pursued in the following, with fig. 4.11 extending the modeling analysis to the other datasets from fig. 4.9.

Figure 4.11 shows that the model likewise succeeds in the reproduction of the experimental data at higher interaction strengths. As expected, the fitted values for f_{coh} decrease with U/J as the stronger interactions successively increase the quantum depletion. Since the measurement volume S_{Ω} is much smaller than the size of a single mode and centered on $\mathbf{k} = \mathbf{0}$, it does not contain the same ratio of condensed to depleted atoms as the system as a whole¹⁶:

¹⁶. It is reminded again that in this section N_{BEC} refers to the quantity measured inside S_{Ω} and not to the total number of detected condensed atoms.

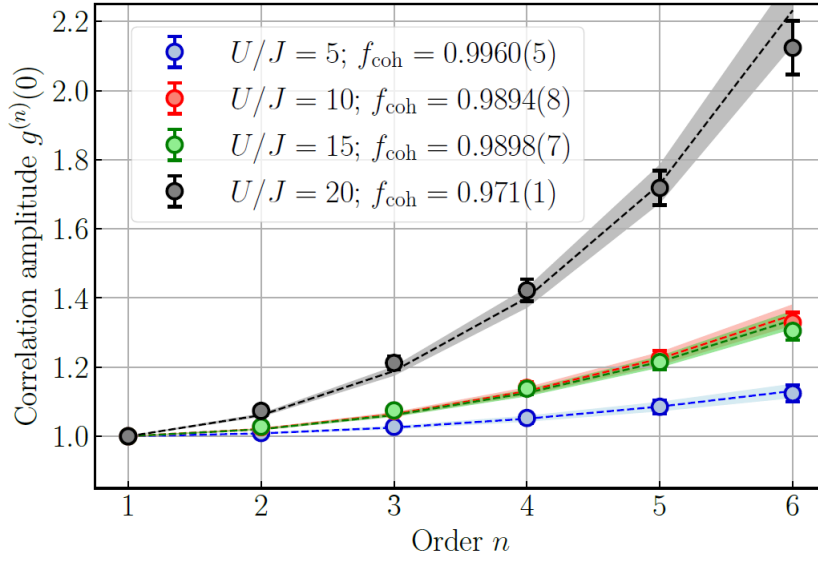


Figure 4.11 – Extension of the application of the model to the experimentally observed n -body correlations for BECs with stronger interactions. The points are the same experimental data and error bars as in fig. 4.9. The dashed lines are fits of (4.23) to the experimental data with f_{coh} as only adjustable parameter. The shaded regions indicate the uncertainties on the fits. The model (4.23) continues to succeed in confirming the deviations from unity in the correlation amplitudes observed in the experiment and to reproduce the experimental data with a low uncertainty on the fit parameters f_{coh} even in the context of strong interactions.

$$f_{\text{coh}} = \frac{N_{\text{BEC}}}{N_{\Omega}} \neq \frac{N_{\text{BEC}}^{\text{tot}}}{N_{\text{tot}}} = f_c \quad (4.25)$$

The relationship between f_{coh} and its approximate counterpart at the macroscopic scale f_c is the subject of the final part of this chapter.

4.5.5 . Extrapolating depletion densities below the BEC

Since it is impossible to attribute a detected atom within S_{Ω} to either the condensate or the depletion, the quantity N_{BEC} cannot be extracted from the experimental data. No quantitative analytical prediction exists for N_{BEC} in large 3D systems of trapped interacting lattice bosons. In the absence of a possible direct comparison between the fitted value of f_{coh} and the experimental value of $N_{\text{BEC}}/N_{\Omega}$, other quantities have to be examined in order to evaluate the validity of the assumptions underlying the model. Although the successful reproduction of the experimental data observed in the preceding part of this section is a positive indication towards this end, the reliance on an adjustable parameter does not allow for a universal conclusion on this point.

Consequently, seeking further validation of the model from the comparison of its predictions with other quantities seems appropriate.

One such possible quantity for comparison is given by 1D cuts of the momentum densities $\rho(k)$. Such a comparison can necessarily only be of qualitative nature, since, even though the profile of the BEC mode centered on $\mathbf{k} = \mathbf{0}$ is well known [138], no analytical formula exists for describing the shape of the depletion distribution in this region of momentum space. In an effort to arrive at some quantitative indications nonetheless, the tails of the momentum distribution far from the $\mathbf{k} = \mathbf{0}$ mode in the range $0.2 \leq k/k_d \leq 0.5$ are fitted by bell-shaped functions; an approach that has been heuristically established to produce the best quantitative agreement when using Lorentzian functions, which are thus employed without any physical justification. The extrapolation of these curves into the region $k/k_d < 0.2$ beneath the BEC can then be compared with the fit result for the incoherent fraction $1 - f_{\text{coh}}$. The results of this analysis for one weakly- and one strongly-interacting dataset at $U/J = 5$ and 20 , respectively, are shown in figure 4.12.

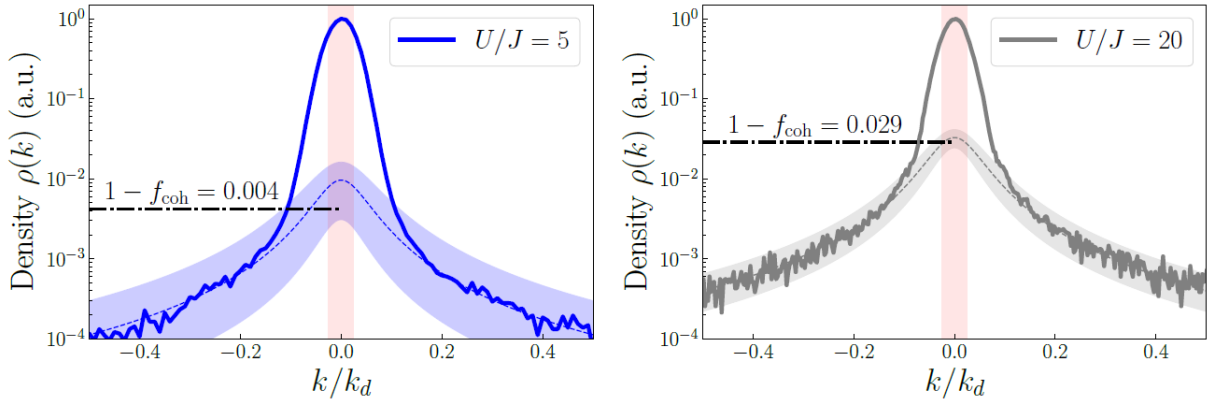


Figure 4.12 – Comparison of the model predictions with 1D density cuts of the momentum densities of lattice BECs. The solid lines are normalized 1D cuts of the experimentally measured momentum densities $\rho(k)$ for weakly- (left) and strongly- (right) interacting BECs. The dashed lines are Lorentzian fits to the tails of $\rho(k)$ in the region $0.2 \leq k/k_d \leq 0.5$ and extrapolated to $k = 0$. The shaded areas around these lines represents the uncertainty of the fits to the tails. The red shaded area centered at the origin indicates the extension of the measurement volume S_Ω . The black dash-dotted lines indicate the values of the incoherent fractions in S_Ω resulting from the fits of f_{coh} in fig. 4.11.

Figure 4.12 shows the momentum densities $\rho(k)$ for two of the datasets presented in figure 4.11 computed with a small transverse integration so as to increase the signal to noise ratio of the depletion tails at high momenta while keeping them from being distorted at the same time.

Normalization with respect to the maximum at $\mathbf{k} = \mathbf{0}$ makes for an immediate comparability of the values with the incoherent fraction $1 - f_{\text{coh}}$. The depletion densities extrapolated to the origin of momentum space are consistent with the values resulting from the fits of f_{coh} , an agreement that is found to prevail over a range of interactions that make for a variation in both quantities of more than one order of magnitude.

4.5.6 . Relationship between the condensed and the coherent fraction

A final comparison made to ascertain the validity (insofar as feasible) of the model concerns the link between the the coherent and the condensed fraction (4.25). While the coherent fraction has been the subject of extended discussion throughout this chapter, little has been said so far about its approximate counterpart at the macroscopic scale of the system. While conceptually simple in its definition, this quantity results from a separate measurement procedure [53] that is entirely independent from the analysis of f_{coh} . For the reasons elaborated in the discussion of the results shown in fig. 4.11, f_{coh} and f_c are not expected to be exactly equivalent. As it turns out, a relationship between these two quantities can be derived based in part¹⁷ on the same assumptions that underlie the model (4.23) presented above.

The approach employed in the comparison with 1D cuts of the momentum densities is carried forward in maintaining the assumption that the depletion density is described by a Lorentzian function along each lattice axis, considered independently:

$$n_{\text{dep}}(k) = \rho_{\text{dep}}(0) \prod_{j=x,y,z} \left(\frac{\sigma_{\text{dep}}^2}{4k_j^2 + \sigma_{\text{dep}}^2} \right) \quad (4.26)$$

A further supposition, although based on considerably more established ground [138], consists in assuming a 3D isotropic Gaussian for the form of the BEC in the FBZ:

$$n_{\text{BEC}} = \rho_{\text{BEC}}(0) e^{-k^2/2\sigma_{\text{BEC}}^2} \quad (4.27)$$

In the preceding equations σ_{dep} and σ_{BEC} refer to the RMS-widths of the corresponding momentum distributions. In approximation, the coherent fraction can be expressed in terms of the momentum densities of the constituent parts of N_{Ω} :

17. As mentioned in the following, in this part some additional assumptions are made in the derivation of (4.33) that are not required for the derivation of the model (4.23).

$$f_{\text{coh}} = \frac{N_{\text{BEC}}}{N_{\text{BEC}} + N_{\text{dep}}} \simeq \frac{\rho_{\text{BEC}}(0)}{\rho_{\text{BEC}}(0) + \rho_{\text{dep}}(0)} \quad (4.28)$$

On a macroscopic scale the same approach leads to the condensed fraction:

$$f_c = \frac{N_{\text{BEC}}^{\text{tot}}}{N_{\text{BEC}}^{\text{tot}} + N_{\text{dep}}^{\text{tot}}} \simeq \frac{\int_{\text{FBZ}} d\mathbf{k} n_{\text{BEC}}(\mathbf{k})}{\int_{\text{FBZ}} d\mathbf{k} [n_{\text{BEC}}(\mathbf{k})n_{\text{dep}}(\mathbf{k})]} \quad (4.29)$$

Since the BEC width is significantly smaller than the momentum range of the FBZ (fig. 4.12 shows a decrease of roughly four orders of magnitude in density between the center and the middle of the FBZ), the integration over the FBZ can be replaced with one extending over all momentum space for the BEC. This allows for the condensed fraction to be expressed as a function of the maximum densities of the respective momentum distributions:

$$f_c \simeq \frac{\rho_{\text{BEC}}(0)\mathcal{V}_c}{\rho_{\text{BEC}}(0)\mathcal{V}_c + \rho_{\text{dep}}(0)\mathcal{V}_d} \quad (4.30)$$

where the normalized total volumes of momentum space occupied by the BEC and the depletion are given by

$$\mathcal{V}_c \simeq \frac{\int_{-\infty}^{\infty} d\mathbf{k} n_{\text{BEC}}(\mathbf{k})}{\rho_{\text{BEC}}(0)} = \left(\sqrt{2\pi}\sigma_{\text{BEC}}\right)^3 \quad (4.31)$$

and

$$\mathcal{V}_d \simeq \frac{\int_{\text{FBZ}} d\mathbf{k} n_{\text{dep}}(\mathbf{k})}{\rho_{\text{dep}}(0)} = \left[\sigma_{\text{dep}} \arctan\left(\frac{k_d}{\sigma_{\text{dep}}}\right)\right]^3 \quad (4.32)$$

Combining (4.28) and (4.30) thereby yields an approximate expression relating the coherent to the condensed fraction that depends only on the ratio $\mathcal{V}_c/\mathcal{V}_d$ of the total volumes occupied by the BEC and the depletion:

$$f_{\text{coh}} \simeq \frac{f_c}{f_c + (1 - f_c)\mathcal{V}_c/\mathcal{V}_d} \quad (4.33)$$

The ratio $\mathcal{V}_c/\mathcal{V}_d$ can be calculated from the widths σ_{BEC} and σ_{dep} extracted from fits to the momentum densities, as already shown in fig. 4.12 in the case of the depletion. σ_{BEC} shows a constant behavior as a function of U/J as the successive reduction in size of the condensate

and increasing trap frequency mutually cancel each other out (see appendix B). Moreover, σ_{dep} is also found to remain constant for all examined interaction strengths, but with the Lorentzian fitting function being a purely pragmatic choice, establishing a physical reason for this consistency is more subtle. However, the constant size of both σ_{BEC} and σ_{dep} implies that their ratio $\mathcal{V}_c/\mathcal{V}_d$ can be taken to be fixed for the purposes of this analysis, with the consequence of making f_{coh} immediately determined by the value of f_c . To proceed, the average value of the ratio of the volumes $\overline{\mathcal{V}_c/\mathcal{V}_d} \simeq 0.3(1)$ over all datasets is used, with the error given by the standard deviation. Consequently, f_{coh} can be continuously extrapolated from f_c for all values $0 \leq f_c \leq 1$ via (4.33), rather than being limited to the discrete data points of each dataset. The result is a continuous prediction for f_{coh} as a function of f_c without adjustable parameters. The variation of the coherent fraction as a function of the condensed fraction is shown in figure 4.13.

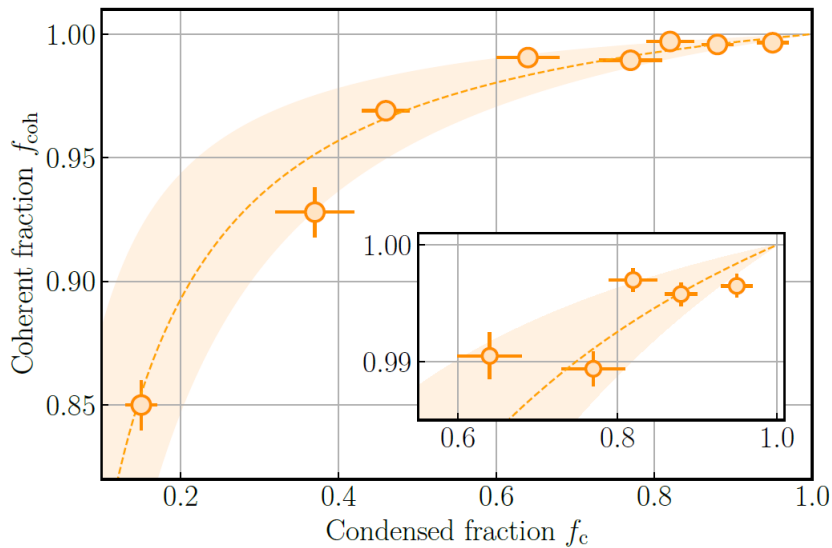


Figure 4.13 – Coherent fraction as a function of the condensed fraction. The data points correspond to the values of f_{coh} resulting from the fits to the n -body correlations of each dataset shown in fig. 4.11. The corresponding condensed fraction is determined following the procedure outlined in appendix A of [53] in each case. Error bars represent uncertainties of the respective fits. The dashed line represents the continuous prediction of (4.33) for the average ratio of volumes with the shaded area translating the uncertainty on this average value. The inset shows a magnification of the region of highest coherent fraction. Since f_c decreases with U/J , the horizontal axis runs in opposite direction to the interaction strength.

Figure 4.13 shows that the values for the coherent and condensed fractions found from the fits on the n -body correlations and momentum densities are in quantitative agreement within

the uncertainties of the continuous prediction of (4.33) using the average ratio of volumes with no adjustable parameters. Since f_{coh} and f_c are the result of an entirely independent analysis from one another with f_{coh} obtained from fits to $g^{(n)}(0)$ and f_c from the momentum density [139], this congruence may be seen as a further validation of the model presented in this chapter.

The non-linearity of the prediction of (4.33) illustrates the difference in the extend to which the condensed and depleted atoms contribute in the two different measurement volumes considered for f_{coh} and f_c , respectively. With S_Ω centered on the $\mathbf{k} = \mathbf{0}$ mode and of size much smaller than $2\pi/L$, the contribution of condensed atoms naturally dominated this part of momentum space. This implies that for a considerable system-wide increase of $1 - f_c$ with U/J , the ensuing change of $1 - f_{\text{coh}}$ is barely noticeable, unless $f_c \ll 1$. Prior to that moment, the majority of N_Ω is predominantly contributed by N_{BEC} , since atoms that are depleted from N_{BEC} are unlikely to end up in the incoherent contribution inside S_Ω but much rather outside of S_Ω altogether. Therefore, unlike $\langle N_{\text{tot}} \rangle$, $\langle N_\Omega \rangle$ is not conserved as U/J is changed, and f_{coh} and f_c do not show a linear relationship.

The fact that 4.33 is able to correctly predict this non-linear behavior between f_{coh} and f_c without any adjustable parameters is a further robust indication towards the validity of the heuristic model. The fact that it is able to do so even in the regime where f_c tends towards very small values is remarkable, however, and its full understanding would undoubtedly require a more sophisticated theoretical framework than the one outlined in this chapter.

4.6 . Conclusion

While the multiple validating indications of the model presented in this chapter are intuitive in the context of weak interactions where the assumptions underlying it are on reasonably solid ground, the prevalence of these agreements when analyzed for stronger interactions is not trivial. For the largest values of U/J analyzed in the superfluid regime, the interaction effect on the depletion of the BEC is such that the condensed fraction decreases to below 20%. This makes it all the more remarkable that a model whose foundational presupposition of uncorrelated BEC and

depletion operators can only be asserted with confidence in the context of weak interactions is nonetheless capable of reproducing the experimental observations with quantitative accuracy. Specifically, one of the principal hypotheses is that of the BEC and the depletion contributing in an independent manner to the statistics observed in the small measurement volumes, which is not entirely counter-intuitive, but still complicated to conclusively substantiate from theoretical perspective alone. In this context the validation of the model results *a posteriori* from its agreement with the experimental data across all compared quantities, a statement which suggests by no means that a more sophisticated theoretical approach than the one presented here might not be of vital interest in explaining the observed impact of the condensate depletion on the many-body coherence.

In giving a positive indication to the attribution of the deviation of the n -body correlations from unity to the presence of the quantum and thermal depletion of the condensate, the results confirm the coherent character of the BEC up to sixth order. Previous experiments had reached a similar conclusion up to third order [185], but failed to observe the effect of the depletion already evident at second order in this analysis. As a matter of fact, the measurement volumes probed in [185] were significantly larger than V_c in order to offset a smaller detection efficiency, which convolutes uncorrelated atoms and leads to a reduction in the amplitude of correlation functions as discussed in this chapter. This fact is illustrated by the observed values of $g^{(2)}(0) = 1.022(2)$ and $g^{(3)}(0) = 1.061(6)$ in that work which are well below the full contrast given by $g^{(2)}(0) = 2$ and $g^{(3)}(0) = 6$, respectively, highlighting the complexity associated to obtaining sufficient statistics in small volumes required for the characterization of many-body quantum states from their many-body coherence properties.

In summary, this chapter has been dedicated to the presentation of measurements of Full Counting Statistics and high-order correlations in interacting lattice Bose gases based on the work published in [36]. It has been demonstrated that the approach developed here is capable of identifying quantum states based on their many-body coherence properties. Based on the factorial moments of the detected atom number in small volumes in momentum space, perfectly contrasted n -body correlations were obtained between up to $n = 6$ individual atoms as illus-

trated by the measured amplitudes $g^{(n)}(0) = n!$ in Mott insulators. The FCS of Mott insulators and BECs were established to conform to those predicted for thermal and coherent states respectively, manifested by their thermal and Poissonian probability distributions and confirming their effective description in terms of pure states when constraints on macroscopic quantities are released. Additionally, it has been shown that the coherence properties of interacting Bose superfluids deviate from those of a coherent state due to the presence of the condensate depletion, particularly the quantum depletion. This underscores the capability of the Helium Lattice experiment to obtain sufficient statistics in volumes of smaller dimension than the system's correlation length, constituting a key advantage for quantitatively probing many-body correlations, an approach that indicates potential for the exploration of a variety of interacting quantum states and phase transitions [165–167, 197]. With its remarkable sensitivity to many-body coherence effects at high orders, a future extension of this technique into the quantum critical region above the superfluid to Mott insulator transition where fluctuations are expected to intensify (see chapter 5) and coherence properties undergo substantial changes is expected to hold great promise for the possible revelation of complex non-Gaussian n -body correlations [173, 174].

5 - BEC Atom Number Fluctuations Across the Mott Transition

This chapter is dedicated to the analysis of the fluctuations of the condensate order parameter across the superfluid to Mott insulator phase transition at finite temperature. Contrary to the classical normal gas condensation transition which is driven by a variation of the temperature, the Mott transition is driven by interactions, and piloted by the quantum fluctuations that these interactions induce. The transition is described in terms of an order parameter (the condensate wave function), which takes on a non-zero average value in the ordered (superfluid) phase and vanishes (on average) in the quantum disordered (Mott insulating) phase. In theory, properties of universal behavior associated to the phase transition can be extracted from (higher moments of) the order parameter when measured across the phase transition. However, sharp features for such quantities are only to be expected in the thermodynamic limit, where the order parameter goes to zero at a sharp boundary that characterizes the quantum phase transition. In finite size systems, cusps are rounded off and shifted, hindering such an analysis of universal scaling. One possible solution to this is to construct quantities that are independent of the system size, such as the Binder parameter.

The goal of this analysis is first and foremost to establish the experimental observation of the order parameter fluctuations associated to the superfluid to Mott insulator phase transition. Measuring the BEC atom number N_{BEC} and analyzing its fluctuations amounts to probing the second-order moment of the order parameter. As shown below, these fluctuations are expected to be enhanced in the ordered phase upon approaching the critical regime, but separating them from the inherent technical noise fluctuations of an average quantum gas experiment is not trivial. Secondly, a brief study is conducted into the variations of the order parameter fluctuations in the critical regime as the system size is changed. This analysis is somewhat limited in its extent due to the small overall range of the atom number available in the experiment. Finally, the Binder cumulant is computed from the measured fluctuations, and while the quantitative extrac-

tion of numerical values associated to universal behavior is not possible in this experiment on account of its harmonic trapping potential rendering the system inhomogeneous, qualitatively interesting behavior such as a sharp variation of the Binder parameter at the transition suggests the potential of this type of investigation for finite-size scaling analysis when applied to homogeneous systems.

The main difficulty in the experimental investigation of these order parameter fluctuations, and presumably the primary reason why few experiments have ever been able to gather experimental evidence for them, is that they are easily drowned out by the inherent technical fluctuations present in a typical quantum gas experiment. In order to render their observation possible, one either has to reduce the other sources of fluctuations to a large degree by conceiving an extremely stable experiment from the outset, or one has to be able to accurately separate the technical from the order parameter fluctuations in post-analysis. The possibility to achieve the latter is given by the single-particle detection capabilities of the Helium Lattice experiment. In the first section of this chapter a brief overview is given of the physics of the order parameter in the context of a second order quantum phase transition. The second section details previous observations of fluctuations of the order parameter in the context of the classical superfluid to normal gas transition. The following section delineates how a measurement of the same quantity has been achieved in the context of the Helium Lattice experiment by using precise post-selection and careful modeling of the major sources of fluctuations in the experiment. The remainder of the chapter presents the experimental observation of the order parameter fluctuations across the superfluid to Mott insulator phase transition, their scaling with the total atom number and the measurement of the Binder cumulant from higher order moments of the order parameter. Preliminary numerical simulations by T. Roscilde (ENS Lyon) based on the quantum rotor model are shown to be in qualitative agreement with the experimental observations.

5.1 . Second order phase transitions

This section gives a broad background on second order phase transitions, their distinction with regards to discontinuous transitions and differences between classical and quantum phase

transitions.

5.1.1 . Classical phase transitions

Ehrenfest classified [198] a phase transition between two phases A and B as being of n -th order when the n -th derivative of the chemical potential $\mu(T, P)$ has a jump:

$$\left(\frac{\partial^m}{\partial T^m}\right)_P (\mu_A - \mu_B) \begin{cases} = 0 & (m < n) \\ \neq 0 & (m = n) \end{cases} \quad (5.1)$$

Theoretical treatment of the transition usually starts with the choice of a macroscopic quantity that occurs a characteristic change at the transition point, e.g. the volume for a liquid to gas transition or the magnetization for a ferromagnetic transition. Nowadays it is the behavior of this so-called order parameter ψ at the transition that labels¹ the order of the transition:

$$\bar{\psi} = \begin{cases} \text{discontinuous} & \text{(1st order transition)} \\ \text{continuous} & \text{(2nd order transition)} \end{cases} \quad (5.2)$$

First-order transitions are thus characterized by a discontinuous jump of ψ at the transition point. When the discontinuity in this jump approaches zero, the transition is said to be of second order. In first case there can be coexistence of the two phases at the transition temperature T_c ², contrary to the second case where this is not possible³. While in many cases there is a seemingly natural choice for ψ , this choice is not unique (any power of an order parameter is itself an order parameter for instance). Some examples of commonly used order parameters are:

$$\psi = \begin{cases} M/M_0 & \text{(ferromagnetic)} \\ \sqrt{\rho_0/\rho} & \text{(BEC)} \\ \sqrt{\rho_s/\rho} & \text{(\lambda transition)} \\ (v - v_c)/v & \text{(gas - liquid)} \end{cases} \quad (5.3)$$

1. This is with the exception of topological phase transitions, which are not characterized by order parameters.

2. As is the case for water and ice at 0° C, for instance.

3. Think for example of the continuous destruction of the regular ordering of magnetic moments in the ferromagnetic transition of iron.

where M is the magnetization, ρ_0 the condensate density and ρ_s the superfluid density. The square root appears in the second and third case because the underlying quantity is the macroscopic wavefunction. In the case of Bose-Einstein condensation the number of condensed particles N_0 changes continuously, implying a phase transition of second order. The order parameter is a thermodynamic quantity whose average value is zero in one phase and non-zero in the other, leading to the phases being referred to as the ordered and the disordered phase:

$$\bar{\psi} \begin{cases} = 0 & T \geq T_c \quad (\text{disordered phase}) \\ \neq 0 & T < T_c \quad (\text{ordered phase}) \end{cases} \quad (5.4)$$

Though its thermodynamic average is zero in the disordered phase, the fluctuations of the order parameter are not. The spatial correlation length ξ of these fluctuations increases upon approaching the critical point. Second-order phase transitions are characterized by the fact the increase in the order parameter fluctuations ends in a divergence of their correlation length at the transition point:

$$\xi \propto |t|^{-\nu} \quad (5.5)$$

ν is referred to as the correlation length critical exponent and t quantifies the distance from the critical point in a dimensionless manner, e.g. in the case of temperature it might be defined as $t = |T - T_c|/T_c$. The long range of the order parameter fluctuations manifests itself not just in space but also in time, with the correlation time τ_c (the decay time scale of the fluctuations) diverging as

$$\tau_c \propto \xi^z \propto |t|^{-\nu z} \quad (5.6)$$

Here z is referred to as the dynamic critical exponent. Critical exponents such as ν and z can be thought of as a measure of the strength of the singularity. Say an observable X depends on a the distance t from the critical point via a power law with critical exponent n : $X \propto t^n$. Then all derivatives $d^m X/dt^m$ with $m > n$ diverge as $t \rightarrow 0$, and the value of n dictates how soon this occurs.

The critical phenomena associated to the phase transition are a consequence of the divergencies (5.5) and (5.6): Since at the transition point the correlations are of infinite range in both space and time, the order parameter fluctuations are present on all length and time scales. A system for which this condition holds true is said to be scale-invariant, with all observables depending on the external parameters via power laws [89]. As a consequence, knowledge of the corresponding so-called critical exponents completely characterizes the critical behavior of the system in the vicinity of the phase transition [89].

Remarkably, systems can be grouped together based on their space dimensionality and symmetry properties of the order parameter such that the critical exponents of their phase transitions are the same for an entire class of very different physical systems. This feature of continuous phase transitions is referred to as universality. It, too, is rooted in the divergencies (5.5) and (5.6): With correlation lengths and times diverging at the critical point, the microscopic details of the Hamiltonian are washed out and rendered unimportant by the system effectively averaging over large volumes in space and time. Systems belonging to the same universality class show identical macroscopic behavior, even though the details of their microscopic interactions might be completely different.

In principle, universality should thus allow for the exact determination of the critical exponents of a phase transition by studying any simple model system that belongs to the same universality class. Naturally, the study of such critical exponents has been a field of great interest in both theoretical [199–201] and experimental [202, 203] condensed matter physics.

5.1.2 . Quantum phase transitions

The above considerations apply to classical phase transitions, so defined because they are driven by fluctuations in temperature and result thus from a competition between energy and entropy. With the critical point being associated to a certain temperature T_c , quantum mechanical effects will play no significant⁴ role for $|t| < T_c^{1/\nu z}$, which makes the critical behavior asymptotically close to the transition amenable to a classical description and is the reason why all finite-temperature transitions are referred to as "classical".

Contrary to that, quantum phase transitions occur at zero temperature through the variation of

4. Quantum mechanics may be important for the behavior on a microscopic scale, but the macroscopic scales associated to the critical behavior are dominated by thermal fluctuations.

a physical (non-thermal) parameter in the Hamiltonian. They are thus brought about as a result of competition between different ground state phases of the system. These types of transitions are induced by quantum fluctuations resulting from the non-commutativity of operators in the Hamiltonian (Heisenberg uncertainty principle). At the Quantum Critical Point (QCP) the fluctuations driving the transition diverge and become scale invariant in space and time. In experiments this critical behavior may still be visible in the low-temperature regime, despite not being at zero temperature, due to the particular excitation spectrum of the quantum critical ground state. With the typical time scale of the long-distance order parameter fluctuations diverging upon approaching the transition, the corresponding frequency scale $\omega_c = \xi^{-z}$ goes to zero, as does the associated energy scale

$$\hbar\omega_c \propto |t|^{\nu z} \quad (5.7)$$

As long as the energy of thermal fluctuations $k_B T$ is smaller than the energy scale associated to the long-distance order parameter fluctuations $\hbar\omega_c$, the system remains in the quantum critical regime even at finite temperature. For $\hbar\omega_c \ll k_B T$ the order parameter fluctuations can be treated classically. The presence or absence of quantum critical behavior at finite temperature depends on whether or not long-range order can exist in the system at finite temperature.

Absence of long-range order

In cases where the existence of long-range order is incompatible with finite temperature⁵ no real phase transition is observable in an experiment. Instead the interplay between quantum and thermal fluctuations leads to different regimes that are separated by smooth crossovers. Universality effects are observable near the QCP in a so-called quantum critical region, the extent of which is given by the scaling of the correlation length of the order parameter fluctuations: The systems appears critical with respect to the tuning parameter as long as

$$k_B T > \hbar\omega_c \propto |r - r_c|^{\nu z} \quad (5.8)$$

5. Consider for instance magnets in two dimensions with SU(2) symmetry, where the Mermin-Wagner theorem rules out long-range order at finite temperature in the thermodynamic limit.

Within this region, the behavior of the system is set by the thermal excitations of the quantum critical ground state, which possesses an excitation spectrum without conventional quasiparticle-like excitations. This bestows the quantum critical region with unusual finite-temperature properties. While the range of values for the external parameter r that correspond to the critical regime actually increases with temperature, the response in amplitude of the system to any excitation may become weaker as temperature increases, generally making the quantum critical effects more difficult to observe.

To either side of the critical region, the system is in a disordered phase for finite temperature, explaining the lack of a true observable phase transition. The causes for the disorder differ between the different sides of the phase transition: While for $r > r_c$ the disorder is brought about by the quantum fluctuations as would be the case at zero temperature, with the corresponding excitation gap leading to a finite temperature state that closely resembles the quantum disordered ground state, the disorder is caused by thermal fluctuations in the opposite case. It is in this region that the presence of any finite temperature has a drastic effect on the system, immediately bringing in out of the ordered phase as soon as $T > 0$. At high temperature thermal fluctuations drown out any quantum fluctuations as soon as $k_B T > \hbar\omega_c$. A schema of the phase diagram corresponding to a system without long-range order at finite temperature is given in figure 5.1 (a).

Presence of long-range order

If, on the other hand, long-range order can exist in the system at finite temperature, additional features appear in the phase diagram, with an ordered phase now surviving the onset of finite temperature fluctuations for values of r below r_c . This implies that a real phase transition can be observed despite the transition being quantum in nature. As outlined above, the fact that this phase transition occurs at finite temperature implies its classical nature, with the QCP representing a zero-temperature endpoint to a line of finite-temperature transitions. This situation is depicted in figure 5.1 (b).

Since in classical systems statics and dynamics decouple while remaining always coupled in quantum systems, and time scales like a length to the power z according to (5.6), a quantum phase transition in d dimensions can be related to a classical phase transition in $(d + z)$ space di-

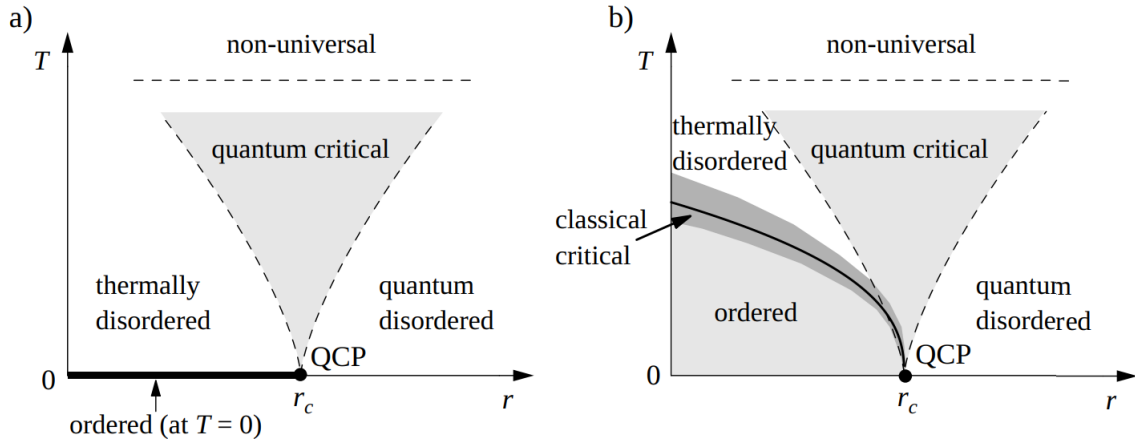


Figure 5.1 – Schematic phase diagrams for continuous quantum phase transitions, temperature as a function of the parameter driving the transition. (a) No long-range order can exist at finite temperature. The only ordered phase exists at $T = 0$. (b) Long-range order can exist at finite temperature. There is an ordered phase above $T = 0$ and below the classical critical line separating it from the thermally disordered phase. In both cases the condition for observing quantum criticality at finite temperature is given by (5.8). Taken from [204].

mensions. Thus, approaching a finite temperature phase transition for a quantum system turns out to be equivalent to a dimensional crossover with the temperature of the quantum problem mapping onto the inverse length of the imaginary time dimension. Static phase transitions are the ones amenable to study with usual statistical physics methods, such as locating non-analyticities in the free-energy density (or in a different relevant thermodynamic potential). In the static case the various phases identified by different behavior of the order parameter are thus equilibrium phases.

5.1.3 . Finite-size scaling

For continuous phase transitions, the non-analyticity of the ground state properties of the system is of higher order than the level crossing associated to first-order transitions and involves an infinite number of many-body eigenstates. Consequently, this type of transition is rounded into a crossover for any finite-size system, with sharp features associated to the collective transition phenomenon only appearing in the thermodynamic limit defined as

$$N \rightarrow \infty, \quad V \rightarrow \infty, \quad v = \frac{V}{N} = \text{const.} \quad (5.9)$$

The fact that sharp phase transitions only occur in the presence of an infinity in the system (usually in the system size) is sometimes referred to as an "extended singularity theorem". Mean field theories do not respect this theorem, but renormalization theories do.

The reason behind this theorem lies in the association of phase transitions to the divergence of some derivative of the free energy (or other thermodynamic potential) at the critical value of the control parameter. Any thermodynamic potential is derived from the partition function, which is a sum of positive terms and as such an analytic function of the parameters in a system with a finite number of degrees of freedom, implying that none of its derivatives can diverge. Thus it is only in the case of the thermodynamic limit where the number of degrees of freedom diverges that a phase transition can occur.

The finite size induces a smoothing of the singularity at the critical point across a parameter space region where $\xi \sim L$. Despite the absence of sharp features and divergences in finite size systems, there is a scaling region characterized by $\xi \gg L$ where peaks form close to where the divergencies would occur in the thermodynamic limit. With increasing system size these peaks become higher and narrower, and their position shifts towards the critical point. This behavior is illustrated in figure 5.2. The way that these peaks behave as a function of the system size is described by finite scaling exponents [205] that relate the value of a physical observable $A_L(t)$ in a system of size L to its value in the thermodynamic limit $A_\infty(t)$, which allows for the extraction of the values of the critical exponents. According to the finite scaling hypothesis, close to the critical point the thermodynamic quantities depend only on the ratio ξ/L of the correlations length to the system size, with the microscopic length scale related to the range of interactions dropping out of the problem.

5.1.4 . The role of the order parameter

The physics at the phase transition is described by long-range fluctuations of the order parameter. The symmetry properties of the order parameter determine the universality class and the existence of low-energy modes. As outlined above, the average value of the order parameter serves to distinguish the phases on either side of the phase transition, with the quantum disordered phase exhibiting a value of zero. Since the order parameter is a thermodynamic quantity, it can fluctuate on both sides of the phase transition, only its thermal average is zero in the disordered phase. Near the critical point, the behavior of the order parameter is governed by critical

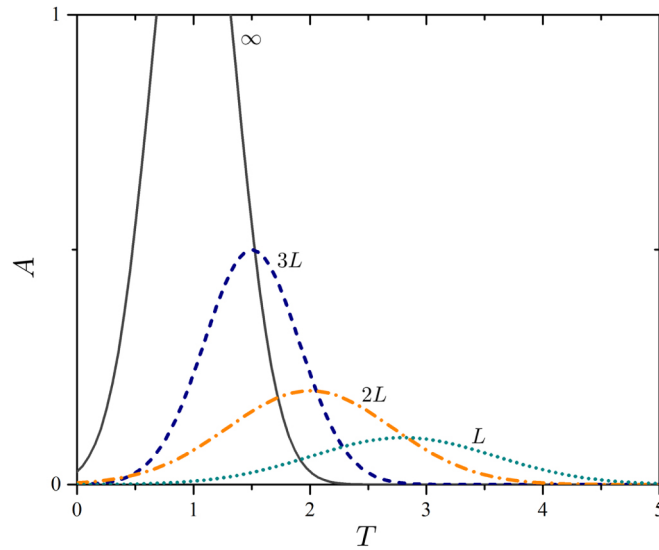


Figure 5.2 – Finite size scaling. Behavior of a physical observable A in the vicinity of the critical point $T_c = 1$ as a function of temperature T for different system sizes L . As L increases, the position and shape of the peak is shifted towards the divergence situation found for $L \rightarrow \infty$. Taken from [206].

exponents that determine the power-law scaling of various thermodynamic quantities as a function of their distance from the transition point. These exponents characterize thus the critical behavior of the system and determine the universality class of the phase transition. Goldstone modes are present when the ordered phase breaks a continuous symmetry.

5.1.5 . Spontaneous symmetry breaking and Goldstone modes

Phases beyond straightforward gases or liquids break one or more of the inherent symmetry properties adhered to by the microscopic interactions among the constituents that constitute these phases, meaning that the microscopic state possesses a symmetry that the low-temperature phase does not.

In the case of the paramagnetic transition at zero field, for instance, a specific direction in space is selected for the net magnetization, even though the Hamiltonian has full rotational symmetry. This symmetry is thus spontaneously broken and the system establishes a corresponding long-range order. The rotational symmetry remains now only in the fact that a simultaneous uniform rotation of all individual magnetizations costs no energy, with all ordered states being equivalent. By continuity, given the fact that a uniform rotation costs no energy, a rotation that is not

uniform but has only long wavelength variations (that is, it varies slowly in space) will cost very little energy. The excitations corresponding to such low energy rotations are called Goldstone modes, and are present in any system with a spontaneously broken continuous symmetry⁶. Goldstone's theorem [207] states that the spectrum of excitations contains one massless scalar particle per generator of a spontaneously broken symmetry, which is referred to as Goldstone boson and represents long-wavelength fluctuations of the corresponding order parameter. In crystalline structure for instance, the low energy collective excitations associated to the spontaneous breaking of translational and rotational symmetries are phonons.

5.1.6 . The Binder cumulant

One valuable tool often employed to locate the critical point in systems with a continuous phase transition is the Binder parameter, or fourth-order cumulant [208, 209], which can be thought of as a variation of the kurtosis of the order parameter for a given system size L . Due to its scaling dimension being zero, the value of this parameter remains invariant with respect to the system size when approaching the critical point. Consequently, the Binder parameters corresponding to various system sizes intersect all at the critical point, which can be identified in this way. The universality class and critical exponent of the system can be determined from the value that the Binder parameter takes at the critical point. This principle is usually applied in the context of spin systems [210], but it is applicable to particle systems as well. Its ease of use and superior convergence properties have made the Binder parameter a useful alternative to other dimensionless variables, such as the ratio of the correlation length to the linear system size. The Binder parameter for an arbitrary order parameter s and for a system of linear size L is defined as follows:

$$U_L = 1 - \frac{\langle s^4 \rangle}{3\langle s^2 \rangle^2} \quad (5.10)$$

The order parameter has a mean value of zero in the disordered phase and its higher moments are given by its Gaussian distribution of variance σ_L : $\langle s^2 \rangle_L = \sigma_L^2$ and $\langle s^4 \rangle_L = 3\sigma_L^4$, which implies $U_L = 0$. In the ordered phase with a spontaneously broken continuous symmetry, the

6. Discrete symmetries rule out the low energy excitations since you cannot slowly transform one state into an equivalent one.

order parameter has a nonzero mean value. In the thermodynamic limit, its distribution can be modeled by a delta function, and thus $U_L = 2/3$. Outside the thermodynamic limit⁷, U_L must exhibit a crossover from one of these regimes to the other.

Different Binder cumulants $U_L, U_{L'}$ for different system sizes L, L' have the same asymptotic values for very large and very small values of the control parameter. Furthermore, for finite-size systems the value of the Binder cumulant at the critical point is independent of the system size L [208], which means that all curves for $U_L, U_{L'}$ etc. cross each other in the same point corresponding to the critical point of the phase transition. This allows for the determination of the critical point from the intersection point of different Binder cumulants, a procedure that has been successfully employed in the study of numerous continuous phase transitions [211]. In numerical simulations for systems such as the 2D Ising model, the value of the Binder parameter at the critical point, U_L^* , has been shown to depend sensitively on the boundary conditions.

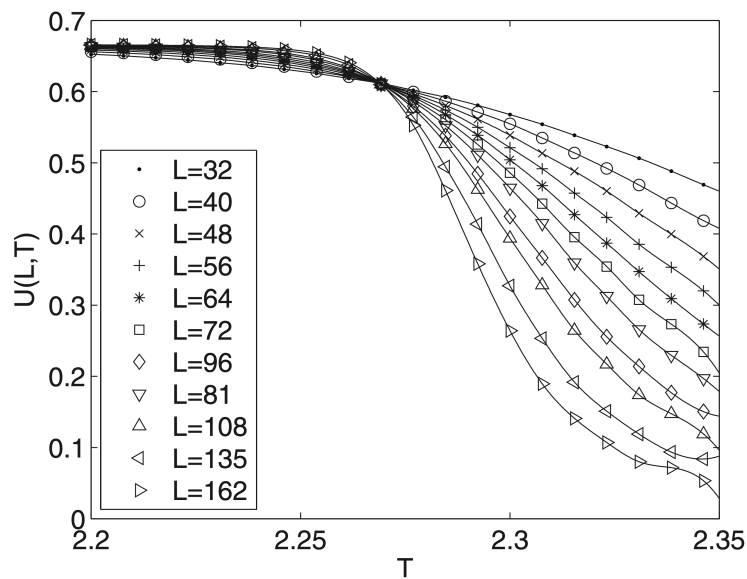


Figure 5.3 – Binder cumulant analysis for the 2D Ising model. Binder cumulants for different system sizes of a 2D Ising model calculated via a Monte Carlo renormalization group technique. The critical temperature (in the thermodynamic limit) is obtained from their interception. Taken from [212].

Figure 5.3 depicts an example of an analysis of the Binder cumulant [212]. U_L was calculated for different system sizes of a 2D Ising model calculated via a Monte Carlo renormalization group

⁷ U_L is a discontinuous function of the control parameter in the limit $L \rightarrow \infty$.

technique. It describes the statistical properties of the order parameter in the system, i.e. the magnetization M . U_L can be seen to depend on the size of the system: For larger systems U_L is larger below T_c and smaller above T_c , and vice versa, implying an inversion of the curves at the critical temperature. Finite size scaling analysis implies that close to the critical temperature all Binder cumulants become independent of the system size, so that the curves representing Binder cumulants of different sizes collapse onto one point. From this interception of different U_L the critical temperature is obtained (in the thermodynamic limit).

5.2 . BEC number fluctuations across BEC transitions

5.2.1 . The superfluid to normal gas transition

The order parameter usually chosen for the treatment of the BEC transition is the wavefunction of the condensate ψ_0 . Its modulus square is equal to the number of condensed particles $N_0 = |\psi_0|^2$. Studying the number of condensed atoms across this phase transition can thus give insight into the critical behavior of the associated order parameter. Moreover, since any power of an order parameter is itself an order parameter, N_0 represents an order parameter in its own right. Being driven by temperature the superfluid to normal gas transition is considered a classical phase transition.

According to grand-canonical theory [213] the occupation fluctuations of the i -th state are given by

$$\Delta N_i^2 = N_i(N_i + 1) \quad (5.11)$$

In a system with a macroscopically occupied ground state, as is the case in BEC, (5.11) leads to unphysically large fluctuations of the order of the total particle number $\Delta N_0 \rightarrow N$, a phenomenon known as grand-canonical catastrophe [214, 215]. Canonical [216] and micro-canonical [217] descriptions that account for the particle conservation in ultracold atom experiments predict the leading contributions to the ground state occupation fluctuations to be equal to

$$\Delta N_0^2 = \left(\frac{\zeta(2)}{\zeta(3)} - \frac{3\zeta(3)}{4\zeta(4)} \right) N \left(\frac{T}{T_c} \right)^3 \quad (5.12)$$

where $\zeta(x)$ is the Riemann zeta function. The second term corresponds to the reduction in fluctuations in the micro-canonical case. Figure 5.4 dresses a rudimentary picture of the variation of the BEC number fluctuations towards the phase transition.

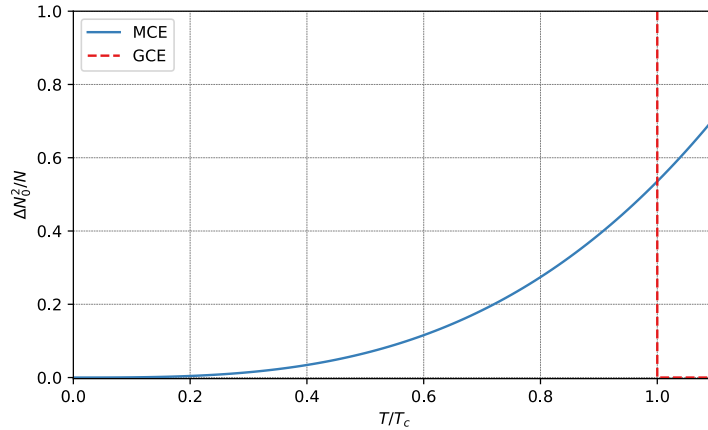


Figure 5.4 – BEC number fluctuations across the normal phase transition. The blue line is the microcanonical prediction of (5.12). The red dashed line corresponds to the grand-canonical prediction (5.11).

The qualitative picture dressed by fig. 5.4 serves the purpose of illustrating the expected behavior of the condensate fluctuations on both sides of the phase transition: Starting at $T = 0$ and increasing the temperature, the fluctuations gradually rise according to the MCE description (5.12). At the critical point there is a sharp drop indicated by the GCE description (5.11) and the fluctuations are expected to vanish in the absence of a condensate.

Beyond this primitive picture, the exact form of the condensate number fluctuations is still topic of theoretical debate. In the weakly-interacting case calculations in the MCE induce a suppression of the predicted peak fluctuations compared to the CE, while the weak interactions shift their position away from T_c [218]. In the strongly-interacting limit exact calculations are more complex still, as outlined below in the context of the Mott insulator transition.

From fig. 5.4 it is clear that the peak fluctuations ΔN_0^2 expected at the transition should approximately be of the order of magnitude of the total atom number, with the standard deviation of the BEC atom number on the order of \sqrt{N} . Observing such small fluctuations represents a considerable challenge for a typical quantum gas experiment that is subject to inherent tech-

nical shot-to-shot fluctuations of the total atom number on the order of $\sim \langle N \rangle$ (for the Helium Lattice experiment $\Delta N / \langle N \rangle \simeq 15\%$ before post-selection.) The only apparatus to ever realize such observations employs an active feedback control during the experimental cycle via non-destructive Faraday imaging [219] to achieve an astonishing stability of the total atom number of $\Delta N / \langle N \rangle < 0.1\%$, i.e. below the shot-noise limit. This unique approach has enabled the observation of BEC number fluctuations in the weakly-interacting regime as T_c is approached from below, with a sharp drop after crossing the critical temperature [33]. The main result of this work is reproduced below.

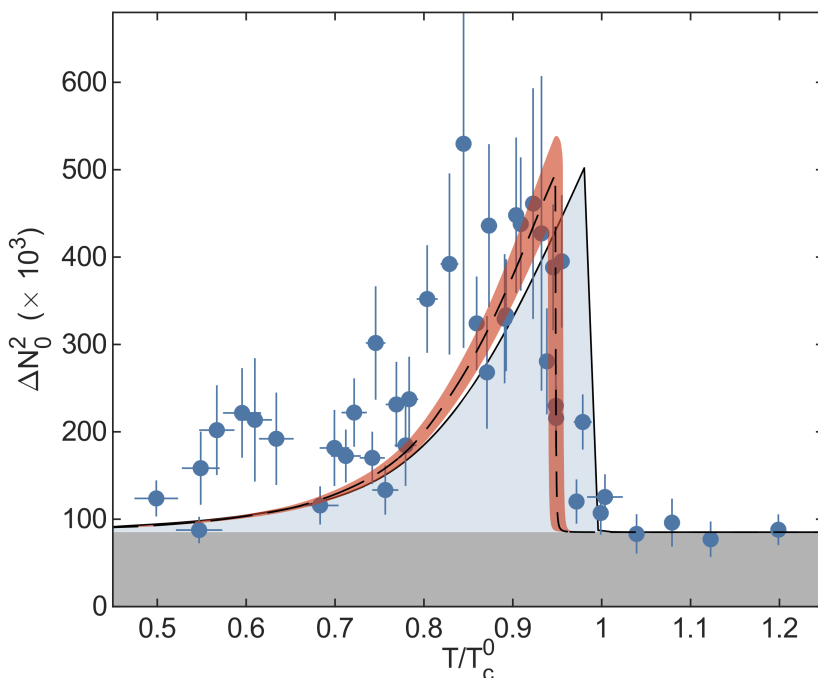


Figure 5.5 - Condensate number fluctuations across the condensation transition observed by Kristensen *et al.* [33]. The blue points correspond to the experimentally observed variance of N_0 for a total atom number of $\langle N \rangle \sim 5 \times 10^5$. The dark grey shaded area represents an offset due to technical fluctuations. The dashed line is a fit to the experimental data using a noninteracting model and the light blue shaded area corresponds to an exact theoretical calculation for a noninteracting gas.

The experimental observation of Kristensen *et al.* shown in fig. 5.5 confirms the initial intuition conveyed by the simplistic analysis of fig. 5.4, with peak fluctuations of the order of the total atom number. It also shows the above-mentioned shift towards smaller temperatures induced by the weak interactions in the system. In a subsequent experiment these fluctuations were re-

vealed to be of microcanonical rather than canonical nature [34].

As outlined in the first part of this chapter, ψ_0 acquires a random but definite phase upon condensation, constituting a spontaneous breaking of a continuous symmetry, with the randomness being due to the lack of a phase stabilization force in the system. The thermal fluctuations of the ensuing Goldstone mode that drive the superfluid to normal gas transition shown in fig. 5.5 are predicted to scale anomalously with the size of the system, with the scaling exponent in the thermodynamic limit of $\Delta N_0^2/N \propto N^\gamma$ where $\gamma = 1/3$ [220–222]. In the subsequent experiment [34] such an anomalous scaling was in fact observed, with a scaling exponent of $\gamma = 0.134(5)$. As outlined below, however, despite the fact that this scaling is predicted to conserve its anomalous character for an arbitrary range of interactions (at least in homogeneous systems) [222], such an anomalous scaling is not expected in the case of the Mott insulator transition, which is not driven by Goldstone mode fluctuations.

The findings [33, 34] represent the only observation of BEC atom number fluctuations and pertain to a classical phase transition driven by temperature. However, increasing the temperature in a weakly-interacting system is not the only means by which one can decrease the population of the BEC mode, even though the number statistics of the condensate occupation in systems where interactions are prominent remain largely unknown. Investigating these number fluctuations in the context of an interaction driven BEC transition can shed light on the delicate balance between quantum coherence and many-body correlations. The lack of theoretical models capable of predicting these fluctuations beyond the weakly-interacting limit poses a significant challenge in unraveling the complex behavior of these systems. Thus, the goal of this analysis is to investigate the BEC number fluctuations in the context of a quantum phase transition, i.e. the superfluid to Mott insulator transition.

5.2.2 . The superfluid to Mott insulator transition

As outlined in chapter 2, the 3D Bose-Hubbard model exhibits a quantum phase transition from a superfluid to a Mott insulator as a result of the competition between the two energy terms in the Hamiltonian \hat{H}_{BH} associated to on-site interaction U and tunnel-coupling J . This phase transition belongs to the 3D XY universality class [95], a class of phase transitions charac-

terized by the presence of short-range interactions, $O(2)$ symmetry and a two-component order parameter (in this case the condensate wave function with its phase and amplitude). According to (5.7) the energy scale associated to the long-wavelength order parameter fluctuations goes to 0 upon approaching the transition. In the case of the superfluid to Mott insulator transition this leads to the transformation of the excitation spectrum of \hat{H}_{BH} from the gapless Bogoliubov excitations spectrum in the superfluid phase to a gapped particle-hole excitation spectrum in the Mott insulating phase.

On-site number fluctuations

When talking about number fluctuations in the case of this transition, there can arise a slight ambiguity with regards to the state whose occupation is fluctuating: On the one hand there is the occupation of the single-particle ground state N_0 , which is linked to the order parameter ψ_0 by modulus square. Fluctuations of this quantity diverge at the critical point in the grand-canonical ensemble. On the other hand one can talk about on-site fluctuations of the atom number, which are large in the superfluid regime because of the long-wavelength coherence of the condensate wavefunction, but go to zero at the transition when the atom number becomes pinned to an integer on each lattice site.

The well defined phase on each lattice site implies that the onsite particle number is quantum mechanically uncertain in the case of the superfluid, as it corresponds to a superposition of different numbers. Measuring the onsite occupation thus yields random numbers according to a Poisson distribution. Increasing the interactions narrows the number distribution, which results in a fixed atom number on each site deep in the Mott insulating regime.

BEC occupation fluctuations

No theoretical prediction of the condensate occupation fluctuations exists across the superfluid to Mott insulator phase transition. However, theoretical investigations of these fluctuations at zero temperature where only quantum fluctuations contribute to ΔN_0^2 show an increase of the fluctuations with U/J , as shown in figure 5.7.

The zero-temperature BEC occupation fluctuations have been predicted by Zwerger [222]:

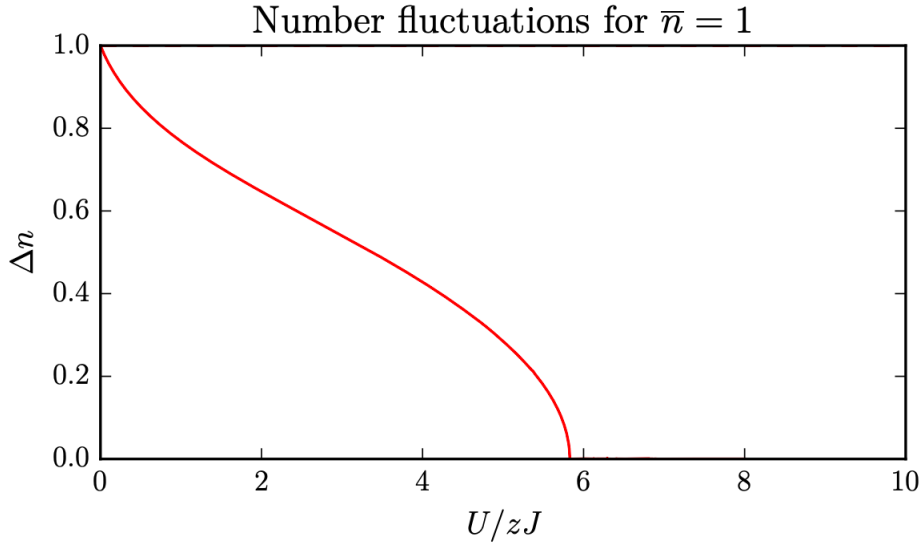


Figure 5.6 – Onsite number fluctuation across the superfluid to Mott insulator phase transition. Contrary to the condensate number fluctuations N_0 , the onsite fluctuations vanish upon approaching the phase transition but remain large in the superfluid region due to the long-wavelength coherence of the condensate wavefunction. Taken from [223].

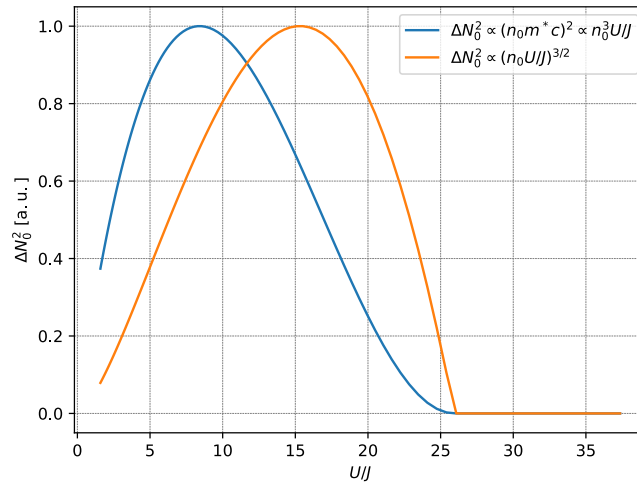


Figure 5.7 – Theoretical predictions of $T = 0$ BEC fluctuations as a function of U/J . The blue line is a prediction of (5.19) and the orange line a prediction of (5.20). The zero-temperature condensate density n_0 contains itself a dependence on U/J .

$$\langle \Delta \hat{N}_0^2 \rangle|_{T=0} \simeq 2 \left(\frac{n_0(T=0)}{n} \right)^2 \left(\frac{mc}{2\hbar} \right)^2 \frac{1}{2\pi^2} \Lambda V \quad (5.13)$$

where $n_0(T = 0)$ is the condensate density at zero temperature and Λ is the momentum cutoff; and by Giogini *et al.* [220]:

$$\langle \delta \hat{N}_0^2 \rangle|_{T=0} = 2\sqrt{\pi}(an_0)^{3/2}V \quad (5.14)$$

Both (5.13) and (5.14) can be applied to the Helium experiment in a rather primitive, ad-hoc approach by replacing m is with the effective mass m^* :

$$m^* = \frac{\hbar^2}{2Jd_{\text{latt}}^2} \quad (5.15)$$

where J is the tunnel coupling and $d_{\text{latt}} = 1550/2$ nm is the lattice spacing; and c with the sound velocity in the lattice:

$$c = \frac{1}{\sqrt{\kappa m^*}} \quad (5.16)$$

with the compressibility given by

$$\kappa = \frac{1}{Un_0} \quad (5.17)$$

where U is the onsite interaction and n_0 is the zero-temperature condensate density, assumed to vary according to the critical scaling law:

$$n_0 \propto \left(1 - \frac{U/J}{(U/J)_c}\right)^{2\beta} \quad (5.18)$$

where $\beta = 0.3485$ for the 3D XY universality class and $(U/J)_c = 25.2(8)$ for the considered datasets (see below). A quantitative agreement certainly not be expected, therefore the variation of the fluctuations is evaluated in arbitrary units (normalized to its maximum). Expressing only the dependence of the parameters on U/J , the ground state occupation fluctuations of (5.13) behave thus according to

$$\langle \delta \hat{N}_0^2 \rangle|_{T=0} \propto (n_0 m^* c)^2 \propto \frac{U}{J} n_0^3 \quad (5.19)$$

and those of (5.14) scale as

$$\langle \delta \hat{N}_0^2 \rangle |_{T=0} = 2\sqrt{\pi}(an_0)^{3/2}V \propto (Um^*n_0)^{3/2} \propto \left(\frac{U}{J}n_0\right)^{3/2} \quad (5.20)$$

While by no means indicative of any physics associated to the Mott transition, these two generic formulas still indicate a rise of quantum fluctuations with increasing interactions, until the condensate density becomes too small upon approaching the transition. The question thus arises whether a similar observation of an increase of the condensate fluctuations towards the phase transition followed by a sharp drop can be made as those shown in fig. 5.5. The remainder of this chapter is dedicated to answering this question.

It is emphasized once again at this point that the Helium Lattice experiment, like any experiment, naturally does not create systems in a zero-temperature context. However, the certified adiabatic loading process into the optical lattice [97] implies that the Bose-Hubbard phase diagram can be traversed at constant entropy per particle, with the most significant part of increasing the condensate depletion due to interaction induced quantum fluctuations and not thermal fluctuations. In such a situation where quantum fluctuations drive the phase transition, the critical regime is expected to mirror the behavior of the ground state (i.e. at $T = 0$) even for a finite temperature in the experiment.

5.3 . Measurement of ΔN_{BEC}^2 across the Mott transition

5.3.1 . The measurement volume for condensate number fluctuations

Due to the randomness of on-site particle numbers within a superfluid, the most direct method of revealing its presence in any experiment is through the utilization of interference. If a superfluid is released from an optical lattice, the far field corresponds to a perfect matter wave interference pattern because of Bragg diffraction, similarly to a coherent laser beam being diffracted on an optical grating. In both cases the far field intensity distribution is a diffraction pattern with a peak separation that corresponds to the inverse spacing of the diffracting element.

Due to the finite size of the MCP detector in relation to the long time-of-flight, some of the diffraction peaks of lattice superfluids fall outside detector even for the first order at $\pm k_d$. Thus it is not

possible to account for all condensed atoms from the trap by counting the atoms in all diffraction peaks. We therefore restrain our measurement volume to the FBZ. N_0 represents therefore not the total number of condensed atoms, but only the atoms in the 0-th order diffraction peak measured in a cube of size $0.3 k_d$ centered on the origin of momentum space. The different measurement volumes are depicted in figure 5.8.

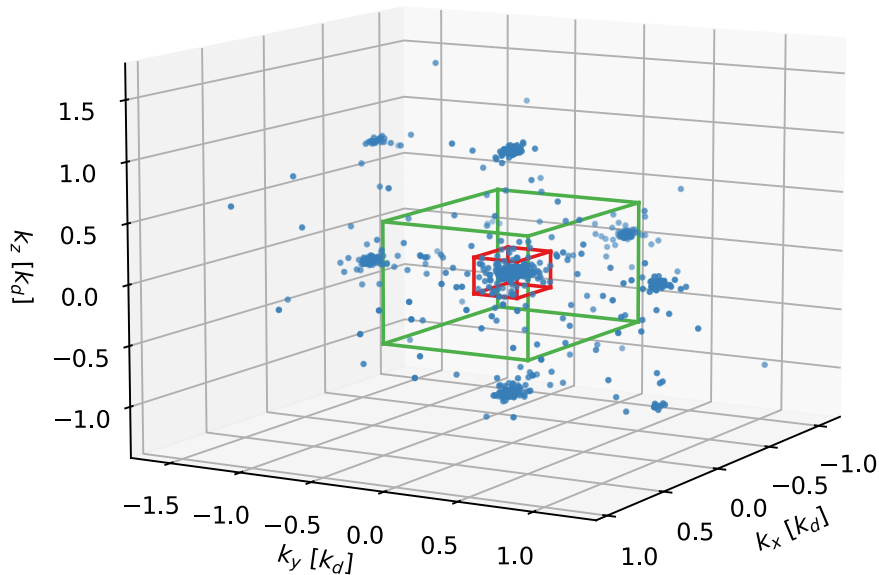


Figure 5.8 – Measurement volume for condensate fluctuations. Same 3D momentum distribution as shown in fig. 3.2, with the different measurement volumes highlighted. The BEC atom number is evaluated by counting the atoms in the 0-th order diffraction peak in a cube of size $0.3 k_d$ (red). It is set into relation with the condensed fraction not via comparison with the total atom number, but the atom number in the FBZ only (green).

The crystalline symmetry of the lattice suggests a strong correlation between quantities measured in the FBZ and their equivalents on a system-wide scale. However, a strict equivalence between the two cannot simply be taken as a given. The amplitude of the density in the higher order diffraction peaks is dictated by the envelope of the modulus square of the Fourier trans-

formed Wannier functions: $N(\mathbf{k}) \propto |\tilde{w}(\mathbf{k})|^2$, where the Wannier functions on each lattice site are given by

$$w_{n,j}(\mathbf{x}) = \sqrt{\frac{d}{2\pi}} \int_{\text{FBZ}} d\mathbf{q} \psi_{n,\mathbf{q}}(x) e^{-ij\mathbf{q}d} \quad (5.21)$$

where $j \in \mathbb{Z}$ corresponds to the index of the lattice site and $n = 0$ (omitted hereafter) to the index of the lowest lattice band in the tight-binding limit. The Fourier-transformed Wannier functions are denoted $\tilde{w}(\mathbf{k})$. In a 3D cubic lattice they factorize, so the atom number in momentum space is related to

$$N(\mathbf{k}) \sim |\tilde{w}(\mathbf{k})|^2 = |\tilde{w}(k_x)|^2 \times |\tilde{w}(k_y)|^2 \times |\tilde{w}(k_z)|^2 \quad (5.22)$$

The other condensed atoms $N_{\text{BEC}} - N_0$ are dispersed over the diffraction peaks of order > 1 : $N_{\text{BEC}} \sim \sum_{\mathbf{k}}' |\tilde{w}(\mathbf{k})|^2$, where the sum runs over all diffraction peaks including the 0th order. For instance, for the second-order diffraction peak at $\mathbf{k}/k_d = (1, -1, 0)$: $|\tilde{w}(\mathbf{k})|^2 = |\tilde{w}(k_d)|^2 \times |\tilde{w}(-k_d)|^2 \times |\tilde{w}(0)|^2 = |\tilde{w}(k_d)|^4$ with the normalization of the Wannier functions to 1 at the origin. To calculate N_{BEC} for a specific diffraction order $n \in \mathbb{Z}$, the sum runs over all Miller indices $\mathbf{k}/k_d = (h, k, l)$ such that $|h| + |k| + |l| = n$.

Based on these considerations, the quantities measured in the FBZ can be approximately related to system-wide measurements of the equivalent quantities, with the result shown in figure 5.9.

From fig. 5.9 it is clear that quantities measured in the FBZ and their counterparts on a system-wide scale do not differ by an order of magnitude, but rather by a factor $\sim 3 - 4$. Such a corrective factor could thus be applied to all experimentally measured quantities within the FBZ⁸; however for the purposes of this analysis the choice was made to simply present the raw data, with the relation to the usual quantities given by fig. 5.9. Thus, for the remainder of this chapter, the occupation of the $\mathbf{k} = \mathbf{0}$ mode N_0 will take the role of the total condensate occupation N_{BEC} , and the occupation of the FBZ N_{FBZ} that of the total atom number N . The equivalent

8. This calculation is based on assumptions that are strictly-speaking only fulfilled on the Mott insulating side of the phase transition, i.e. a homogeneous repartition of the atoms throughout momentum space. On the superfluid side, however, most of the density is concentrated along the lattice axes themselves, therefore one should use caution in applying the same quantitative factor of three throughout. A more thorough comparison may be amenable via a direct 3D fit to QMC simulations of the momentum density using the experimental parameters.

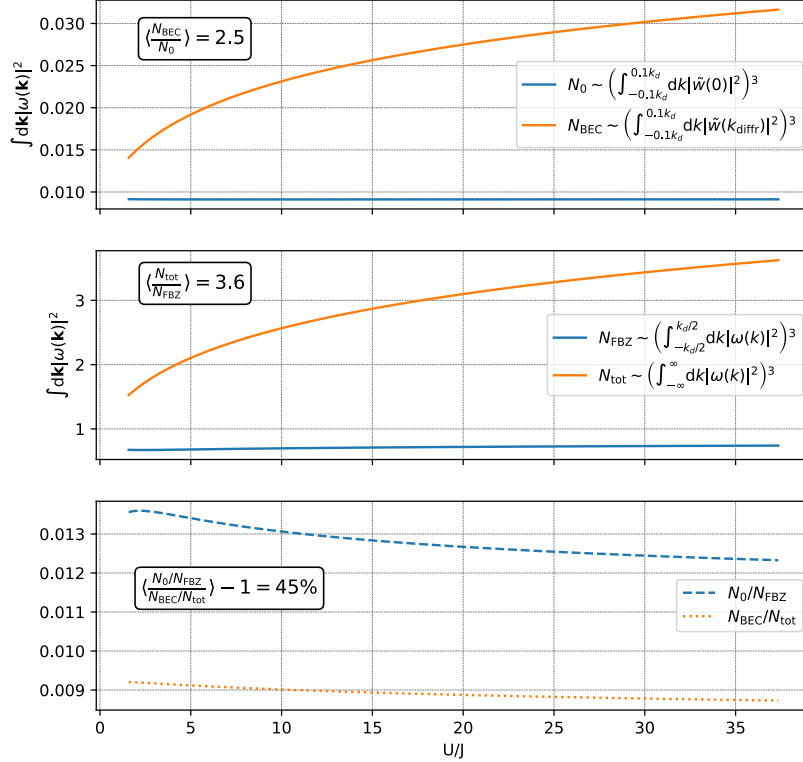


Figure 5.9 – Comparison between quantities measured in the FBZ and on the scale of the entire system. On account of the enlarging of the Fourier transforms of the Wannier functions with U/J the discrepancy grows with increasing interactions, but overall remains of the order of about a factor of three. See footnote in the main text for a caveat when applying the factor of three to measurements on the superfluid side of the phase diagram.

BEC number fluctuations normalized to the total atom number are thus throughout $\Delta N_0^2/N_{\text{FBZ}}$.

An alternative to circumvent the finite size issue of the detector (and increase the statistics of the measured atom number) would reside in the use of band mapping in order to have all the atoms fall onto the detector. However, after the results presented in the previous two chapters, the current investigation is the third one based upon the same datasets spanning the Bose-Hubbard phase diagram, and one that these datasets were not initially set out to support. Since the drawback by limiting the measurement volume to the FBZ is not prohibitive for the purposes

of this analysis, this reason alone does not constitute sufficient ground for employing band mapping and acquiring an entirely new series of datasets.

5.3.2 . Post-selection and noise modeling

Selection of datasets and determination of the critical point

To investigate the fluctuations of the condensate atom number across the phase transition, ensembles of $N = 5000$ atoms are prepared at various values⁹ of the Bose-Hubbard parameter $U/J = u$. Taking data close to the Mott transition represents an increased experimental challenge, since the system is considerably more susceptible to small perturbations such as a slightly suboptimally aligned optical lattice that induces a small amount of heating due to photon scattering or cloud movement while loading if misaligned with respect to the ODT. As a consequence, multiple datasets¹⁰ have been acquired for many values of U/J . The choice between different datasets taken at the same value of U/J but possibly with slightly different temperatures is made by following an approach established in [140] that consists in analyzing the density ρ_0 of the $\mathbf{k} = \mathbf{0}$ mode with respect to the expected critical scaling behavior for the 3D XY universality class:

$$\rho_0(u) = \rho_0^{u=0} |1 - u/u_c|^{2\beta} \quad (5.23)$$

where $\rho_0^{u=0}$ and u_c are fit parameters and $\beta = 0.3485$ [95]. The density is probed in a small volume of size $V_k = (k_d/30)^3$. The result of this analysis carried out for the retained datasets is shown in figure 5.10.

From the analysis of fig. 5.10 the critical point and its uncertainty from the critical scaling fit are determined as $u_c = 25.4(9)$, which is in agreement¹¹ with the value observed in [140]. Going forward the critical regime is indicated on the all plots of atom number fluctuations to facilitate situating the fluctuations with respect to the phase transition.

9. Most of these datasets are the same as the ones presented in the previous two chapters.

10. See for instance p. 136 of [53].

11. Note that the error bars in fig. 5.10 are larger than the ones shown in [140] where they were normalized by the square root of the number of shots.

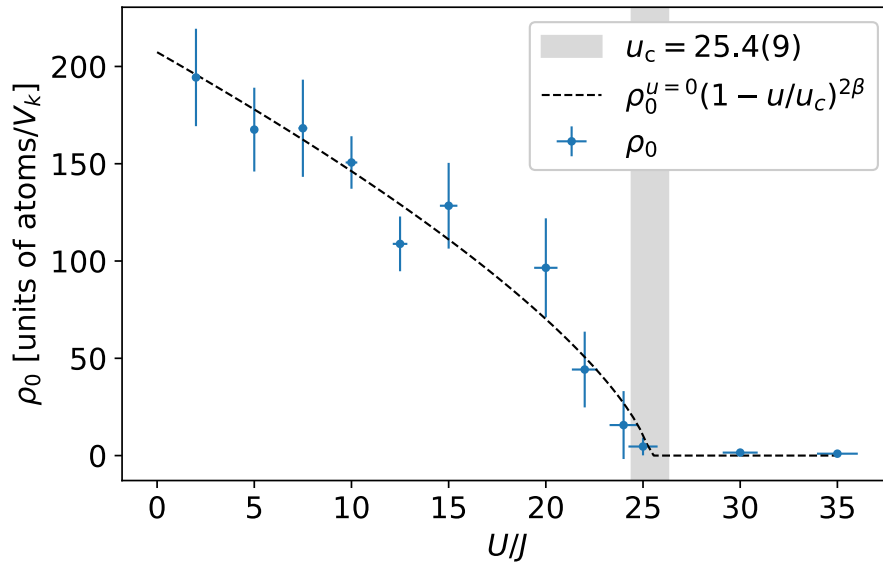


Figure 5.10 - Density of the zero momentum mode. ρ_0 measured in a volume of size $V_k = (k_d/30)^3$ for the datasets used in this analysis. Vertical error bars are one standard deviation on ρ_0 . Horizontal error bars correspond to average uncertainties on the fit in the parametric heating calibration of the lattice depth shown in fig. 2.8. The grey shaded area represents the critical value u_c of the Mott transition and its uncertainty as identified from the fitted dashed line using the critical scaling exponent for the 3D XY universality class.

Post-selection of experimental stability

To observe the order parameter fluctuations above the inherent technical background fluctuations present in any quantum gas experiment, a post-selection technique is employed based on the relatively precisely known atom number. This ensures the necessary experimental stability for the observation of atom number fluctuations in the condensate of the interacting Bose gas.

The post-selection procedure for a typical dataset is detailed in figure 5.11.

As evidenced by fig. 5.11, the precise knowledge of the detected atom number allows to reduce the relative shot-to-shot fluctuations of the total atom number in the experiment, from an initial value of about $\Delta N_{\text{FBZ}}/\langle N_{\text{FBZ}} \rangle \simeq 15\%$ down to only $\Delta N_{\text{FBZ}}/\langle N_{\text{FBZ}} \rangle = 3.5\%$. The trade-off to be made is in terms of the number of shots available for the analysis, which incurs a drop from the original 2953 down to only 499 shots. Even though trading stability for statistics is certainly

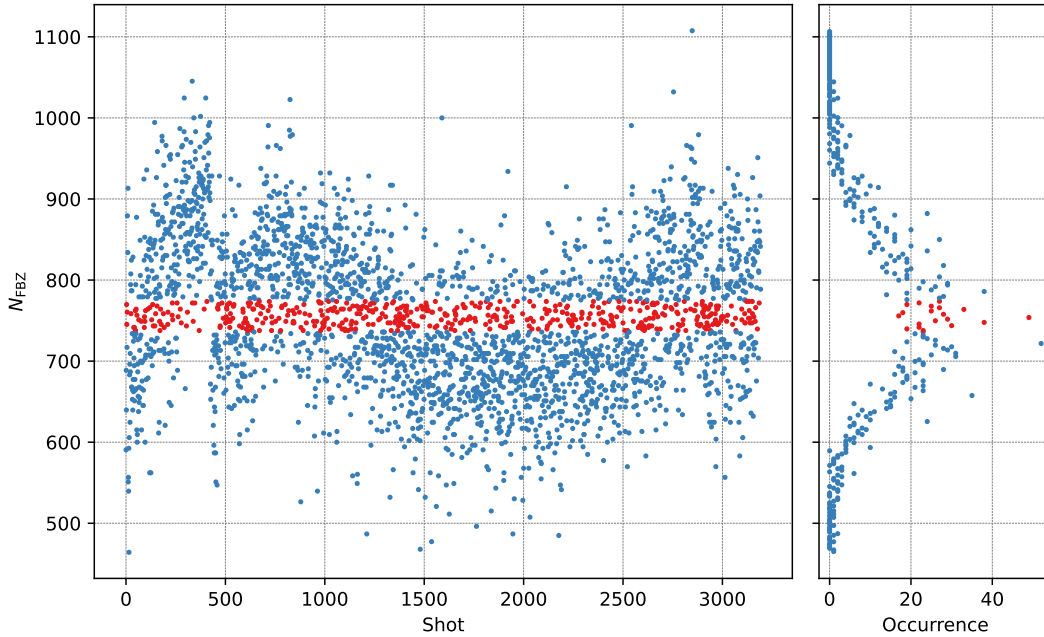


Figure 5.11 – Post-selection procedure. Total detected atom number as a function of repetitions of the experiment. Before post-selection typical technical shot-to-shot fluctuations in the experiment amount to approximately $\Delta N_{\text{FBZ}}/\langle N_{\text{FBZ}} \rangle \simeq 15\%$. The precision of single-atom detection allows to reduce the technical fluctuations in the experiment in post-selection down to low levels. By selecting only the red dots, the fluctuations are reduced down to $\Delta N_{\text{FBZ}}/\langle N_{\text{FBZ}} \rangle = 3.5\%$, at the cost of retaining only 499 out of the original 2953 shots.

not an ideal situation, a balance can be found between the two that is in large part set by the fluctuations associated to the single particle detection, which limit the lower end of the range of the relative stability available in post-selection, as is outlined in the following.

Modeling the experimental noise fluctuations

In order to allow for an unambiguous separation of the order parameter fluctuations from other technical sources of fluctuations in the experiment, the latter have to be modeled and understood precisely. The two main contributions of technical noise fluctuations in the experiment are shot-to-shot variations of the total atom number and fluctuations associated to the detection of single particles with a finite quantum efficiency detector¹².

¹². Saturation effects of the detector are neglected here, as are fluctuations in the total measured atom number due to a combination of the finite detector size and small center of mass fluctuations of the trapped cloud.

In the following a model is constructed to predict the experimental noise fluctuations that contribute within the measurement volume around the $\mathbf{k} = \mathbf{0}$ mode from averaged measurements of the total atom number in the measurement volume around the $\mathbf{k} = \mathbf{0}$ mode and the FBZ. Being determined by average measured values only implies that the experimental noise model predictions can be calculated from experimental data without being sensitive to the order parameter fluctuations, allowing thus to tell the two types of fluctuations apart.

The quantum efficiency of the MCP detector is equal to $\eta = 0.53(2)$. Being for all intents and purposes a stochastic process, the detection mechanism introduces fluctuations that cannot easily be separated from those present in the trapped system. They are modeled with a binomial distribution with a success probability per trial equal to $p = \eta$ and the number of trials given by the in-trap atom number $n = N^{\text{trap}}$. On average their effect is naturally nothing more than to rescale the mean in-trap atom number by the quantum efficiency:

$$\langle N^{\text{meas}} \rangle = \eta \langle N^{\text{trap}} \rangle \quad (5.24)$$

Since the binomial probability distribution resulting from the detection is conditioned by the fluctuations of the total atom number in the trap (about which no assumptions are made in terms of probability distribution), the resulting variance is given by the law of total variance (see eq. (A.1) of appendix A):

$$(\Delta N^{\text{meas}})^2 = \langle (\Delta(N^{\text{meas}}|N^{\text{trap}}))^2 \rangle + (\Delta(\langle N^{\text{meas}}|N^{\text{trap}} \rangle))^2 \quad (5.25a)$$

$$= \langle \eta(1 - \eta)N^{\text{trap}} \rangle + (\Delta(\eta N^{\text{trap}}))^2 \quad (5.25b)$$

$$= \eta(1 - \eta)\langle N^{\text{trap}} \rangle + \eta^2(\Delta N^{\text{trap}})^2$$

$$= (1 - \eta)\langle N^{\text{meas}} \rangle + \eta^2(\Delta N^{\text{trap}})^2 \quad (5.25c)$$

From a mathematical point of view, employing a post-selection procedure on N^{meas} invalidates the use of the law of total variance in going from (5.25a) to (5.25b) since the contributions of the fluctuations due to the detection cannot be disentangled from those occurring already in the trap, so that after post-selection N^{meas} is not strictly conditioned by N^{trap} anymore. This

issue becomes relevant in the limit of a very strict post-selection that starts to cut into the width of the binomial distribution of the detection, as will be discussed further below. In the absence of a more complete model, this consideration is put aside for the time being, and the result of the post-selection on the measured FBZ atom number is simply given by the number resulting from normalizing the standard deviation after post-selecting¹³:

$$\mathcal{N}_{\text{PS}} \equiv \frac{\Delta N_{\text{FBZ}}^{\text{meas}}}{\langle N_{\text{FBZ}}^{\text{meas}} \rangle} \quad (5.26)$$

(5.25c) can then be used to express the variance of the measured FBZ atom number:

$$(\Delta N_{\text{FBZ}}^{\text{meas}})^2 = (1 - \eta) \langle N_{\text{FBZ}}^{\text{meas}} \rangle + \eta^2 (\Delta N_{\text{FBZ}}^{\text{trap}})^2 \quad (5.27a)$$

$$= \mathcal{N}_{\text{PS}}^2 \langle N_{\text{FBZ}}^{\text{meas}} \rangle^2 \quad (5.27b)$$

where the last line is simply the definition (5.26). (5.27a) and (5.27a) can be used to express the variance of the total in-trap FBZ atom number:

$$(\Delta N_{\text{FBZ}}^{\text{trap}})^2 = \eta^{-2} [\mathcal{N}_{\text{PS}}^2 \langle N_{\text{FBZ}}^{\text{meas}} \rangle^2 - (1 - \eta) \langle N_{\text{FBZ}}^{\text{meas}} \rangle] \quad (5.28)$$

The variance of the measured BEC atom number¹⁴, on the other hand, can also be expressed via the law of total variance (5.25c):

$$(\Delta N_0^{\text{meas}})^2 = (1 - \eta) \langle N_0^{\text{meas}} \rangle + \eta^2 (\Delta N_0^{\text{trap}})^2 \quad (5.29)$$

The shot-to-shot fluctuations of the in-trap atom number can be assumed to simply rescale the entire in-trap distribution homogeneously, such that

$$\frac{\Delta N_{\text{FBZ}}^{\text{trap}}}{\langle N_{\text{FBZ}}^{\text{trap}} \rangle} = \frac{\Delta N_0^{\text{trap}}}{\langle N_0^{\text{trap}} \rangle} \quad (5.30)$$

which implies for the variance of the in-trap BEC atom number:

13. No new notation is introduced here to differentiate the atom atom number before and after post-selection in order to avoid rendering the notation heavier than it already is.

14. The order parameter fluctuations are naturally not considered in the derivation of the experimental noise model.

$$(\Delta N_0^{\text{trap}})^2 = \frac{(\Delta N_{\text{FBZ}}^{\text{trap}})^2}{\langle N_{\text{FBZ}}^{\text{trap}} \rangle^2} \langle N_0^{\text{trap}} \rangle^2 \quad (5.31)$$

Finally, (5.29) can be fully expressed in terms of average measured quantities only with the use of (5.31) and (5.28):

$$\begin{aligned} (\Delta N_0^{\text{meas}})^2 &= (1 - \eta) \langle N_0^{\text{meas}} \rangle + \eta^2 \frac{(\Delta N_{\text{FBZ}}^{\text{trap}})^2}{\langle N_{\text{FBZ}}^{\text{trap}} \rangle^2} \langle N_0^{\text{trap}} \rangle^2 \\ &= (1 - \eta) \langle N_0^{\text{meas}} \rangle + \frac{(\Delta N_{\text{FBZ}}^{\text{trap}})^2}{\langle N_{\text{FBZ}}^{\text{trap}} \rangle^2} \langle N_0^{\text{meas}} \rangle^2 \\ &= (1 - \eta) \langle N_0^{\text{meas}} \rangle + \langle N_0^{\text{meas}} \rangle^2 \frac{\mathcal{N}_{\text{PS}}^2 \langle N_{\text{FBZ}}^{\text{meas}} \rangle^2 - (1 - \eta) \langle N_{\text{FBZ}}^{\text{meas}} \rangle}{\langle N_{\text{FBZ}}^{\text{meas}} \rangle^2} \\ &= (1 - \eta) \langle N_0^{\text{meas}} \rangle + \langle N_0^{\text{meas}} \rangle^2 \left[\mathcal{N}_{\text{PS}}^2 - \frac{1 - \eta}{\langle N_{\text{FBZ}}^{\text{meas}} \rangle} \right] \end{aligned} \quad (5.32)$$

Equation (5.32) allows to predict the contribution of experimental noise fluctuations to the total fluctuations measured in the measurement volume around the $\mathbf{k} = \mathbf{0}$ mode.

Note that (5.28) states an implicit lower bound for the post-selection procedure: Since $\Delta N_{\text{FBZ}}^{\text{trap}}$ cannot be negative, the minimal relative fluctuations that can be set on the measured FBZ atom number in post-selection are given by:

$$\mathcal{N}_{\text{PS},\text{min}} = \sqrt{\frac{1 - \eta}{\langle N_{\text{FBZ}}^{\text{meas}} \rangle}} \quad (5.33)$$

Since $\langle N_{\text{FBZ}}^{\text{meas}} \rangle$ varies slightly between different datasets, so does $\mathcal{N}_{\text{PS},\text{min}}$. The mean measured FBZ atom number averaged over all datasets for all values of U/J is $\overline{\langle N_{\text{FBZ}}^{\text{meas}} \rangle} \simeq 450$, which corresponds to a maximum relative stability of $\mathcal{N}_{\text{PS},\text{min}} \simeq 3.2\%$. However, in order to be able to use the same value for all datasets, the minimum value is chosen, $\min(\langle N_{\text{FBZ}}^{\text{meas}} \rangle) \simeq 380$, which gives a slightly higher post-selection bound of

$$\mathcal{N}_{\text{PS},\text{min}} \simeq 3.5\% \quad (5.34)$$

The predictions of the experimental noise model (5.32) are plotted in figure 5.12. In order to alleviate the notations, the superscript ^{meas} is dropped from here on and only measured quanti-

ties are shown.

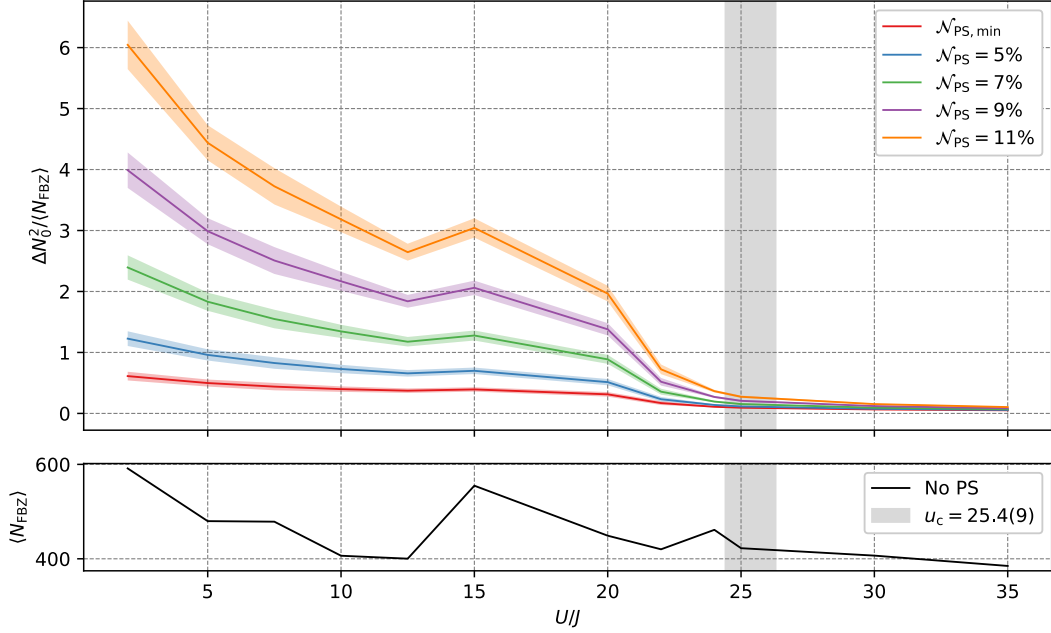


Figure 5.12 – Modeled experimental noise fluctuations. The fluctuations associated to the total experimental noise as resulting from (5.32) are calculated from average experimental values for various values of relative stability \mathcal{N}_{PS} set in post-selection. Shaded areas represent 2σ -uncertainties on average experimental values. The red curve is given by (5.34). The bottom panel shows the variation of $\langle N_{\text{FBZ}} \rangle$ with U/J without any post-selection.

Fig. 5.12 shows that the experimental noise is expected to decrease with U/J , which is not surprising given the dependence of (5.32) on $\langle N_0 \rangle$. The plot of the average occupation of the FBZ shows a positive correlation between $\langle N_{\text{FBZ}} \rangle$ and ΔN_0^2 which stems from the minus sign in front of the corresponding term in (5.32). This effect is more pronounced for large values of \mathcal{N}_{PS} since for small values the contribution of the $\langle N_0 \rangle^2$ term vanishes as the relative fluctuations tend towards their lower limit (5.34). The non-monotonous variation of $\langle N_{\text{FBZ}} \rangle$ with U/J thus explains the similar behavior for the experimental noise fluctuations.

With the experimental noise fluctuations decreasing in amplitude towards the phase transition one might be tempted to conclude that as long as the experimentally measured fluctuations show an increase with U/J similar to fig. 5.5 or 5.7, their identification with the fluctuations of the order parameter might be a foregone conclusion. However, in order to attribute observed

fluctuations to any other source than the experimental noise, the model (5.32) needs validating in a regime where these technical fluctuations are expected to dominate, i.e. far from the phase transition at low values of U/J and for large relative fluctuations \mathcal{N}_{PS} .

5.3.3 . Measurement of order parameter fluctuations

From the experimental data the first two moments of the atom number of the $\mathbf{k} = \mathbf{0}$ mode are extracted, i.e. its average $\langle N_0 \rangle$ and its variance ΔN_0 . The observed fluctuations of the condensate occupation for the same datasets across the superfluid to Mott insulator phase transition are plotted in figure 5.13 alongside the prediction for the experimental noise (5.32) for the lowest level of shot-to-shot fluctuations obtainable in post-selection¹⁵.

Fig. 5.13 shows an increase in the BEC number fluctuations with increasing interactions towards the superfluid to Mott insulator phase transition, starting out at a value corresponding to the offset due to experimental noise (5.32) and rising to a factor on the order of magnitude of the FBZ atom number. Just before the critical regime of the phase transition there is a sudden drop in the fluctuations and they slowly decrease towards the offset of experimental noise as interactions are further increased in the Mott insulating phase. The peak amplitude of the fluctuations is equal to $\max(\Delta N_0^2) = 2.2(1)\langle N_{\text{FBZ}} \rangle$. Following the considerations of fig. 5.9 this translates to the equivalent system-wide quantities $\max(\Delta N_{\text{BEC}}^2) = 0.7(1)\langle N_{\text{tot}} \rangle$ or from (5.25c) in terms of in-trap quantities:

$$\max(\Delta(N_{\text{BEC}}^{\text{trap}})^2) = 1.0(1)\langle N_{\text{tot}}^{\text{trap}} \rangle \quad (5.35)$$

In order to attribute the observed number fluctuations to those of the order parameter at the phase transition, the experimental noise model (5.32) has to be validated in a range of pa-

¹⁵. It should be noted that the the model of experimental noise (5.32) is not expected to yield quantitatively reliable results as soon as the relative fluctuations \mathcal{N}_{PS} start to test the limit of their lower bound (5.34). As explained above, the process of post-selection invalidates the assumption underlying the use of the law of total variance. For large values of \mathcal{N}_{PS} this should not constitute a significant violation since the post-selection does not significantly alter the in-trap distribution. However, when \mathcal{N}_{PS} is close to $\mathcal{N}_{\text{PS},\text{min}}$ this is no longer the case. In the extreme case of a perfectly stable in-trap distribution the fluctuations resulting from the detection process would still have finite variance, implying that the accuracy of the post-selection is intrinsically limited to the width of the binomial distribution associated to the detection process. For this reason the experimental model predictions are shown with a 2σ incertitude since the standard error alone calculated on (5.32) with the standard deviations of experimental average values doubtlessly overestimates the precision of the model.

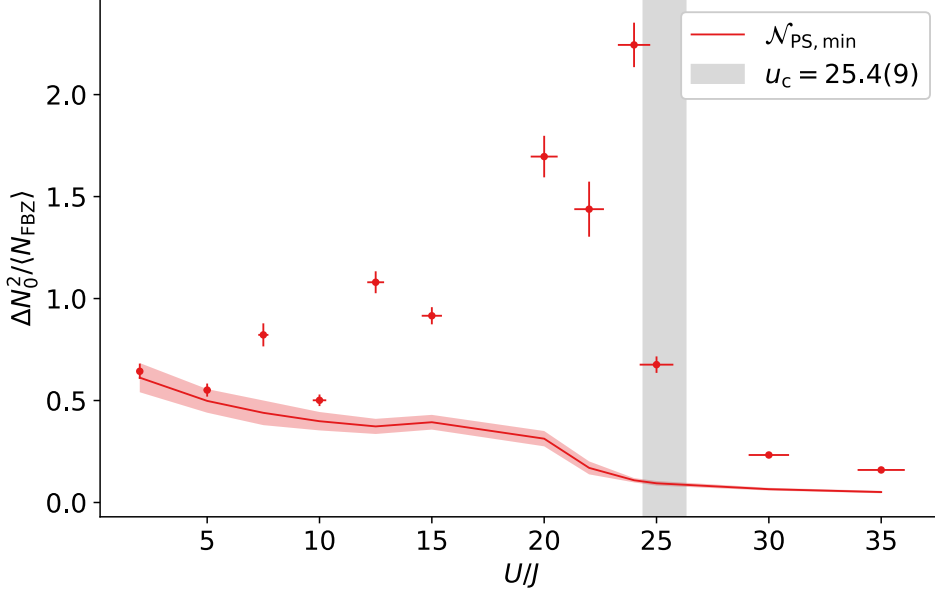


Figure 5.13 – Experimental observation of fluctuations of the condensate occupation across the superfluid to Mott insulator transition. The circles are the second order moments of the BEC atom number distribution extracted from experimental data. Vertical error bars correspond to the standard error of variance (A.3). Horizontal error bars are the same as in fig. 5.10. The line is the prediction from the experimental noise model (5.32) with its shaded area representing 2σ -uncertainties on average experimental values. All quantities are evaluated for a post-selection of experimental shots corresponding to the lower limit of the allowed range of relative fluctuations (5.34).

rameters where its contributions are known to dominate. Intuitively it is clear that increasing the relative fluctuations \mathcal{N}_{PS} increases the role of shot-to-shot fluctuations. The same analysis as in fig. 5.13 is thus repeated for higher values of \mathcal{N}_{PS} , with the results shown in figure 5.14.

Fig. 5.14 shows a satisfactory agreement between the experimental model prediction (5.32) and the second order moments of the BEC atom number distribution in the superfluid regime $15 < U/J$. In this regime experimental noise fluctuations are large due to the significant contribution of the $\langle N_0 \rangle$ dependency of (5.32). For any given value of relative fluctuations \mathcal{N}_{PS} , the experimentally measured fluctuations are found to decrease with U/J as predicted by the model. Furthermore, for values of U/J up to 20, the fluctuations increase as a function of \mathcal{N}_{PS} and are clearly separated, confirming the added contribution of additional shot-to-shot fluctuations included by enlarging the post-selection range of \mathcal{N}_{PS} .

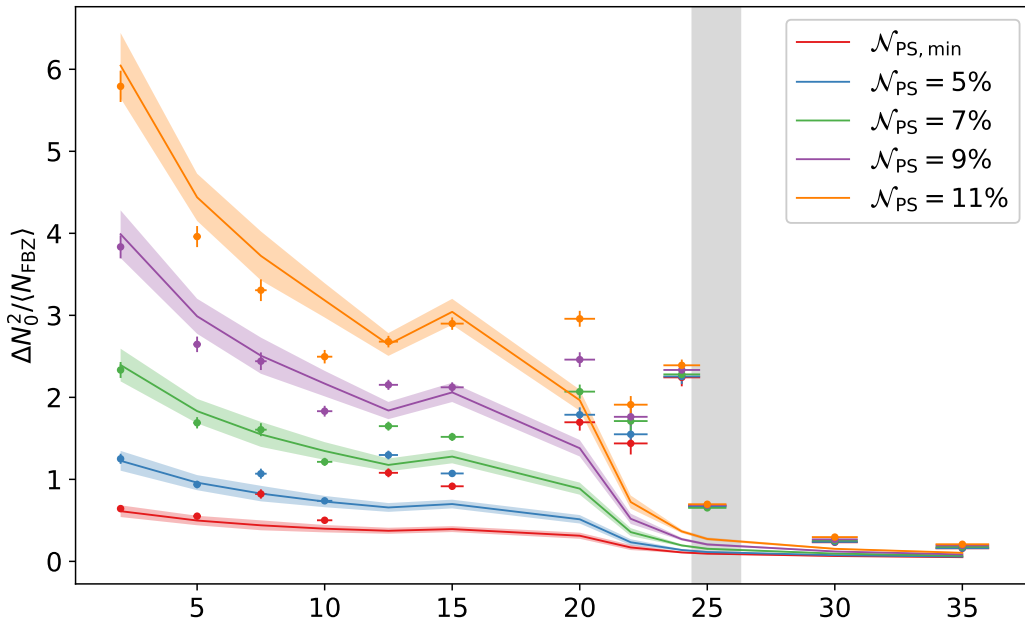


Figure 5.14 – Fluctuations of the condensate occupation across the Mott transition for higher levels of experimental noise. The circles are the second order moments of the BEC atom number distribution extracted from experimental data. Vertical error bars correspond to the standard error of variance (A.3). Horizontal error bars are the same as in fig. 5.10. The lines are the prediction from the experimental noise model (5.32) with their shaded area representing 2σ -uncertainties on average experimental values. All quantities of a given color are evaluated for a given value of relative overall fluctuations established in the post-selection of experimental shots.

Towards the phase transition ($U/J \geq 20$), however, the behavior is radically different: The various curves of experimental noise decrease considerably due to the decrease in $\langle N_0 \rangle$ brought about by a continuing depletion of the condensate. The experimentally measured fluctuations collapse on top of each other for different values of \mathcal{N}_{PS} , indicating that in this regime the experimental fluctuations that can be influenced by post-selection cease to play a significant role in the overall fluctuations of N_0 . For low values of \mathcal{N}_{PS} this region is accompanied by a rise in the amplitude of the fluctuations, while for large values the initial amplitude deep in the superfluid is so significant that no discernible peak can be made out from the overall tendency of the experimental data points. This highlights the crucial role of the post-selection in being able to reduce experimental noise fluctuations sufficiently to be able to make out a fluctuation peak towards the transition, as is evident in the data for the smallest values of \mathcal{N}_{PS} . The collapse of the different series of \mathcal{N}_{PS}

on top of each other implies that the peak amplitudes at $U/J = 24$ are all compatible with each other within error bars.

The transition itself is marked by a sharp drop in fluctuations for all post-selection regimes, or inversely by a sharp onset of fluctuations coming from the Mott insulating side and crossing the BEC transition.

After the transition, finally, the different series continue their joint evolution, as the region of momentum space in which the fluctuations are measured is now sufficiently sparsely populated for experimental noise fluctuations to fade away in amplitude. As shown in fig. 2.7, the inhomogeneous nature of the experimental system implies a wedding cake structure in the trap, so that some superfluid shells survive the initial onset of the transition in the region of u_c . Consequently, the experimentally observed fluctuations do not recede all the way into the background of experimental noise immediately after the transition, but take until $U/J = 35$ to be entirely absorbed by them, indicating the disappearance of the final superfluid constituents in the trap.

The combination of the observation of enhanced fluctuations towards the phase transition and at the same time the quantitative agreement with the experimental noise model that arises jointly from figures 5.13 and 5.14 suggests that the observed fluctuations in the second order moment visible in fig. 5.13 may indeed be associated with fluctuations of the condensate order parameter in the context of a continuous phase transition. The form of the observed fluctuations is qualitatively similar to the observations made in the context of the normal gas condensation transition [33, 34], as is the peak amplitude when converted into units of in-trap quantities measured on the scale of the entire system.

The size of the measurement volume was introduced in the context of fig. 5.8 with little more justification than being slightly larger than the size occupied by the $\mathbf{k} = \mathbf{0}$ diffraction peak in momentum space so as to not cut off any fluctuations. A systematic analysis reveals that the result of the analysis is not very sensitive to the exact size of the measurement volume. The BEC occupation fluctuations for different sizes are compared in figure 5.15.

Figure 5.15 shows that the fluctuations for the smallest value of post-selected shot-to-shot fluctuations shown in fig. 5.13 persist to increase towards the phase transition throughout a

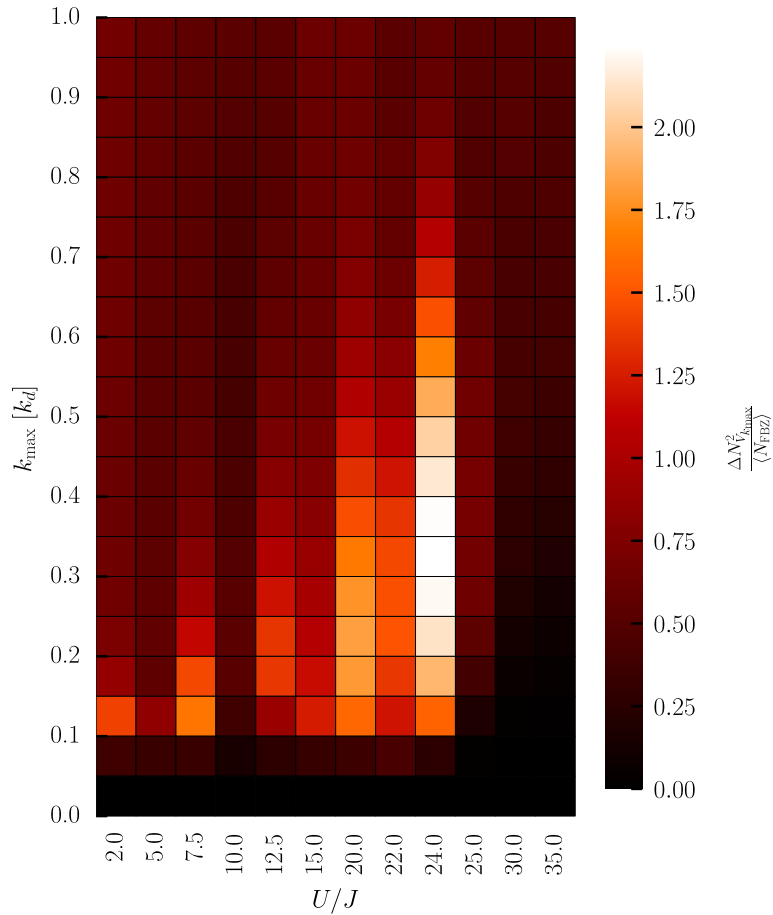


Figure 5.15 – Fluctuations of the condensate occupation across the Mott transition for various sizes of the measurement volume. Second order moments of the BEC atom number distribution measured inside volumes $V_{k_{\text{max}}} = (2k_{\text{max}})^3$ for all datasets for the lowest value of post-selection $\mathcal{N}_{\text{PS},\text{min}}$. The size of the measurement volume used for the figures above is $V_k = (0.3k_d)^3$.

large range of measurement volumes, indicating that the result of the analysis does not depend strongly on this parameter. Intuitively this is not unexpected since increasing the measurement volume slightly above the "true" BEC volume is not likely to recuperate the atoms lost from the BEC in fluctuations, which are on average more likely to populate higher momentum states elsewhere in the depletion region from geometric arguments alone. When the size of the measurement volume is increased so significantly as to encompass the entire FBZ, the value of the observed fluctuations falls back to the value of \mathcal{N}_{PS} established in post-selection as expected.

Besides the observed dependence of the BEC number fluctuations on the size of the measurement volume, there is also a physical reason for choosing $k_{\max} = 0.15k_d$: The BEC number fluctuations are extracted from measurements of $\rho(\mathbf{k})$. The $1/e^2$ size of the diffraction peaks of the lattice is $\sigma_{1/e^2} \simeq 0.043k_d$. Integrating over three times this ranges ($\simeq 0.13k_d$) amounts to counting 99% of the atoms in the peaks. To account for center-of-mass fluctuations of the trapped cloud between shots, k_{\max} is taken to be slightly larger at $0.15k_d$. Both of these values are indicated in fig. 5.16 where the BEC number fluctuations are averaged for all datasets as a function of the size of the measurement volume according to: $\overline{\Delta N_0^2(k_{\max})}/\langle N_{\text{FBZ}} \rangle = \frac{\sum_{U/J} \Delta N_0^2(U/J; k_{\max})/\langle N_{\text{FBZ}} \rangle}{\text{nb. of datasets}}$.

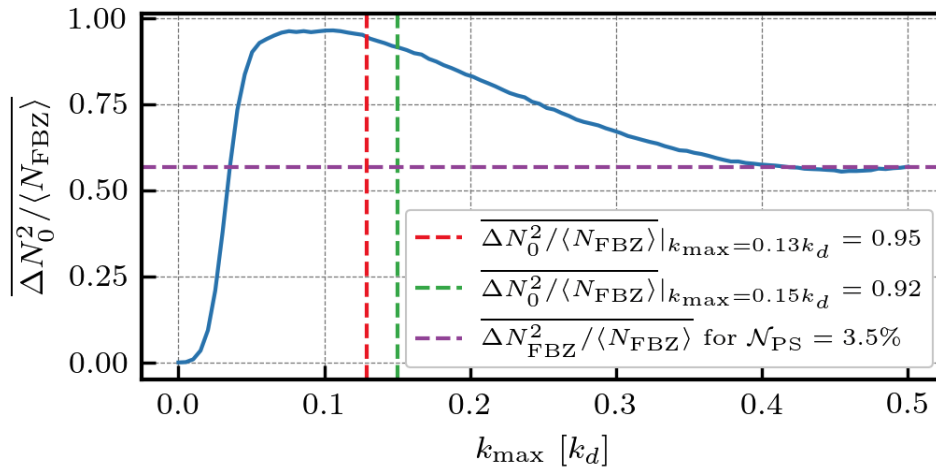


Figure 5.16 – Averaged BEC number fluctuations as a function of the size of the measurement volume. Fluctuations of the atom number inside a volume of size $V_{k_{\max}} = (2k_{\max})^3$ averaged over all datasets. The red line corresponds to three times the $1/e^2$ size of the BEC diffraction peak. The green line corresponds to the value of k_{\max} for this analysis and is taken to be slightly larger to account for center of mass fluctuations of the trapped cloud. For large values ($k_{\max} \rightarrow 0.5k_d$) the average fluctuations reach the level of relative stability \mathcal{N}_{PS} established in post-selection.

Fig. 5.16 confirms that there is a large range of measurement volume sizes $0.06k_d < k_{\max} < 0.12k_d$ where the total average BEC fluctuations are maximal and constant. Upon increasing the measurement volume size further, the fluctuations diminish, until finally saturating at the level of fluctuations set in post-selection \mathcal{N}_{PS} as $k_{\max} \rightarrow 0.5k_d$.

Quantum Rotor Calculations

Numerical simulations of the fluctuations of N_0 across the Mott transition were performed by T. Roscilde (ENS Lyon) using the quantum rotor model described in chapter 3. The results for two different system sizes are shown in fig. 5.17.

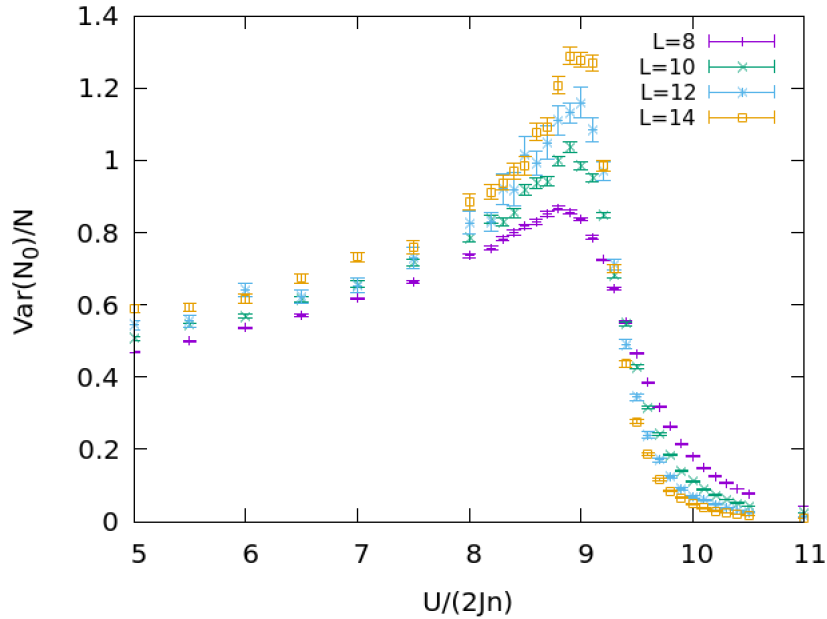


Figure 5.17 – Quantum rotor simulation of the condensate number fluctuations across the Mott transition. The plotted quantity is $(\Delta N_{\text{BEC}}^{\text{trap}})^2 / \langle N_{\text{tot}}^{\text{trap}} \rangle$. The different colors correspond to different system sizes, all evaluated for a reduced temperature of $T/(2Jn) = 1$. Probing different system sizes with the quantum rotor model amounts to probing different atom numbers in the experiment where the size is fixed. However, quantum rotor calculations rely on a lattice filling much larger than unity that does not correspond to the situation in the experiment. In these units the Mott transition occurs at a value of $U/(2Jn) \simeq 9$. Precisely at the transition point the normalized fluctuation amplitudes show an increase with L , illustrating the anomalous scaling of the quantum fluctuations at this particular point.

Fig. 5.17 shows that the quantum rotor simulations produce a qualitatively similar behavior of the condensate number fluctuations across the Mott phase transition as the one observed in fig. 5.13, displaying a continuous rise of the fluctuations with interactions followed by a sudden drop after the phase transition. The plotted quantities are not exactly the same as in the figures showing experimental data; instead they correspond to the quantity $(\Delta N_{\text{BEC}}^{\text{trap}})^2 / \langle N_{\text{tot}}^{\text{trap}} \rangle$ which cannot directly be accessed in the experiment. Given the estimated conversion between the measured atom numbers in the FBZ and the in-trap atom numbers on the scale of the entire system, (5.35)

appears to be in perfect agreement with the simulated peak fluctuation amplitude. However, as outlined in chapter 3, these models rely on the assumption of a lattice filling considerably larger than unity, which is different from the average lattice filling in the experiment of approximately unity. Hence, any observed agreement in fluctuation amplitudes between the measured and simulated data should be considered coincidental.

Fig. 5.17 seems to indicate that at the point of the phase transition the normalized fluctuation amplitudes grow with the system size in the superfluid part of the phase diagram. In order to attempt an experimental observation of such an effect, the fluctuations are analyzed at different total atom numbers in the following.

5.3.4 . Scaling of the number fluctuations with varying system size

In principle one would like to be able to analyze the behavior of these fluctuations as a function of the total system size by varying the total particle number in the system over several orders of magnitude. However, with this experiment relying on optical lattices to create the periodic potential landscape simulating the Bose-Hubbard Hamiltonian, the Gaussian beam waists induce an external harmonic trapping potential that renders the system non-homogeneous, which prevents a straightforward analysis by varying the total atom number over large scales. In fact, such a procedure would modify the critical parameters of the system in non-trivial ways for the different atom numbers, since in the experiment the Mott transition is shifted to different values of U/J depending on whether $N = 5 \times 10^3$ or 5×10^5 . Therefore, in its current state the experimental apparatus is not amenable to varying the total atom number over several orders of magnitude while keeping the realized systems quantitatively comparable.

Moreover, contrary to [34], the BEC transition probed in this experiment is not driven by thermal fluctuations of Goldstone modes populated by finite temperature, which show anomalous scaling with the total atom number according to $\Delta N_0^2 \propto N^{4/3}$ in the thermodynamic limit [220–222]. Instead, zero-temperature quantum fluctuations such as the ones driving the Mott transition exhibit normal scaling with the system size, $\Delta N_0^2 \propto N$ [220, 221]. This statement remains true for all situations of very low temperature values probed across the superfluid phase except exactly at the phase transition, at which point the critical modes (in this case not the Gold-

stone modes but the Higgs modes) show thermally-induced anomalous scaling, but this single point constitutes a particular case.

Despite the experimental constraints on the total atom number, there exists the possibility to make use of post-selection to shift the mean atom number within the limits of remaining reasonably close to unity filling experiment, which corresponds to less than a factor of about 2 in total variation of N . The model (5.32) established to the experimental noise fluctuations can equally be used to predict the scaling behavior of the fluctuations for different datasets. This approach is naturally extremely limited, but is explored nonetheless since the post-selection route offers a straightforward approach to varying the total atom number on already existing datasets. The scaling of the amplitude of the fluctuations of the condensate occupation and that of the experimental noise predictions (5.32) at the lowest limit of post-selection stability $\mathcal{N}_{\text{PS},\text{min}}$ are plotted in figure 5.18 for each dataset.

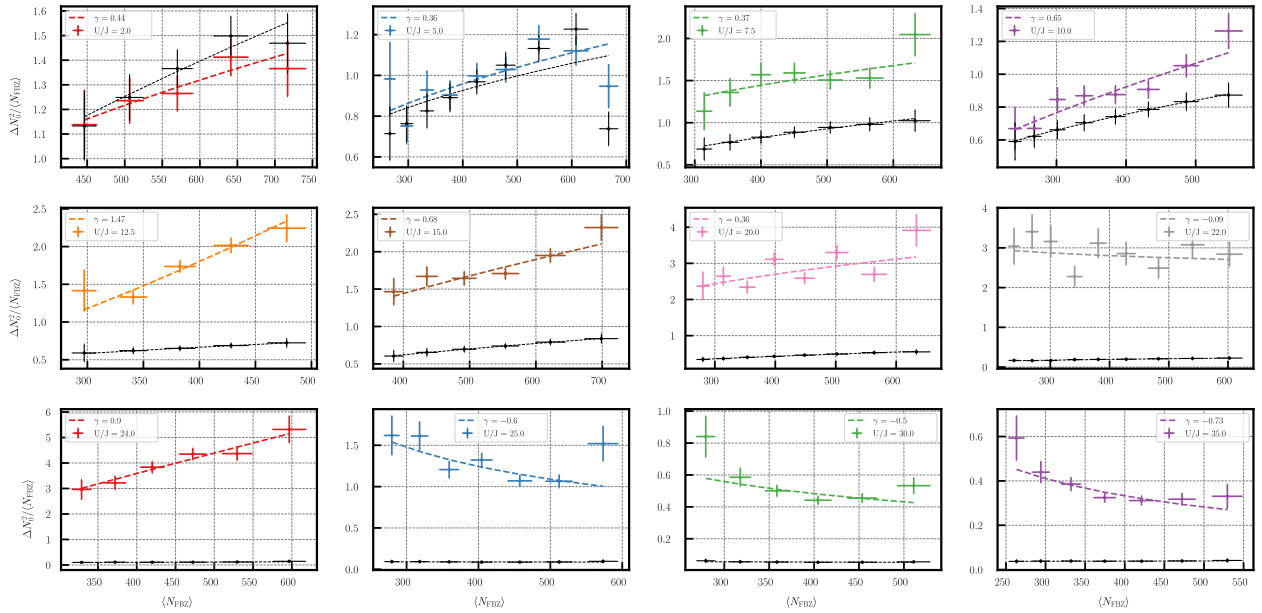


Figure 5.18 – Scaling of the measured fluctuations of the condensate occupation for all datasets across the BH phase diagram. The colored points are experimental data, the black points are predictions for technical noise according to (5.32). The dashed lines are power law fits of of amplitude and exponent according to (5.36). Experimental noise fluctuations are set to the lowest value $\mathcal{N}_{\text{PS},\text{min}}$. Vertical error bars are the standard error on the variance (A.3). Horizontal error bars correspond to one standard deviation of N_{FBZ} .

Figure 5.18 shows first and foremost the differences in amplitudes between the noise model (5.32) and the experimental data that were already visible in fig. 5.13. Most datasets appear to follow a similar scaling trend as the noise model, with the notable exception of the one at the transition at $U/J = 24$. In order to be better able to gauge the different scaling behaviors, the data and the model are fitted with a power law:

$$\Delta N_0^2 / \langle N_{\text{FBZ}} \rangle \propto \alpha \langle N_{\text{FBZ}} \rangle^\gamma \quad (5.36)$$

Due to the small range in values of $\langle N_{\text{FBZ}} \rangle$ far from the origin, these fits cannot be expected to be of great quantitative precision. Indeed, the results were found to depend strongly on the fit parameters¹⁶. Notably the inclusion of an additive offset in 5.36 would render the results for the amplitude and exponent fits over-dependent on initial conditions, and this parameter was discarded with fluctuations naturally expected to die down as $\langle N_{\text{FBZ}} \rangle$ vanishes. The resulting fitted exponents are shown in figure 5.19 for both the experimental data and the noise model (5.32).

As expected from applying the fitting procedure to such a small range of atom numbers, it is not obvious to extract a definite tendency from the experimental data. The experimental noise model (5.32) relies only on average occupation values, which might be why its distribution of fitted exponents as a function of U/J appears more stable. They appear to show a slight tendency throughout the superfluid region to disperse around a value of about 0.5, followed by a drop to approximately 0 at the phase transition. The experimental values of γ are dispersed around the experimental noise values, but their variance is so large that it is hard to read a definitive tendency into them.

5.4 . Measurement of the Binder cumulant across the Mott transition

The Binder cumulant U_L (5.10) for the condensate order parameter can be extracted from the experimental data. Since the system consists of a gas trapped in an inhomogeneous (harmonic) potential, the variation of the Binder cumulant cannot be used to extract critical parameters and exponents in the critical regime: Since the degree of critical behavior is position dependent in an

16. Bounds and initial guesses.

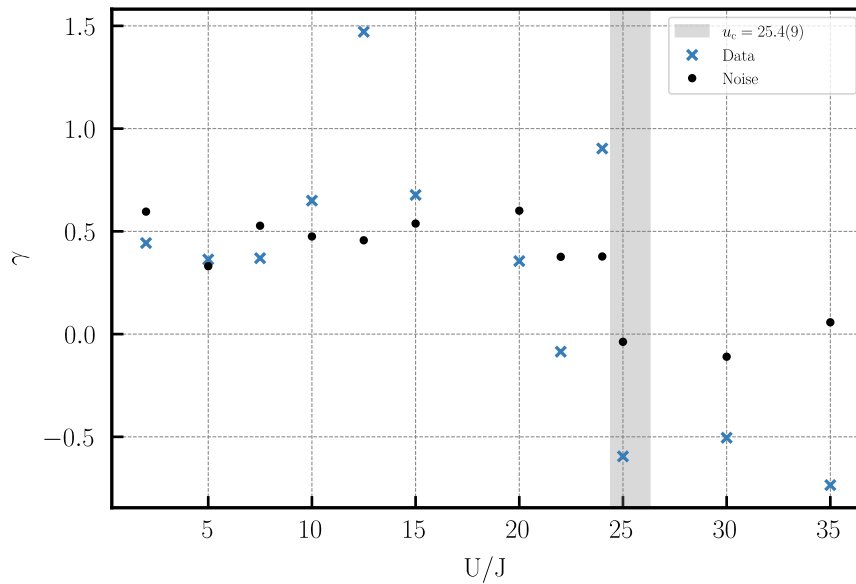


Figure 5.19 – Fitted exponents γ for the scaling across the Mott transition. The blue crosses are fits of (5.36) to the experimental data, and the black points are fits of (5.36) to the predictions from the noise model (5.32).

inhomogeneous system (see fig. 2.7), the Binder cumulant itself is inhomogeneous throughout the system, which makes the comparison between different sizes unfeasible.

When analyzing the fluctuations of the total atom number (in the subsystem of the FBZ), one essentially probes the integral of the order parameter. The considerations concerning the Full Counting Statistics in chapter 4, however, have demonstrated that if one is interested in the actual statistics of the underlying quantum state, one has to choose a measurement volume with a size on the order of the coherence length only. Therefore, the measurement volume is reduced for the analysis of the Binder cumulant to match the one established in chapter 4 to correspond to the coherence volume of a single mode, with a size of $0.038 k_d$.

From its definition in terms of an order parameter (5.10), the Binder cumulant can be expressed in terms of the condensate atom number as follows:

$$\begin{aligned}
U_L &= 1 - \frac{\langle |\psi_{\text{BEC}}|^4 \rangle}{3\langle |\psi_{\text{BEC}}|^2 \rangle^2} \\
&= 1 - \frac{\langle N_0^2 \rangle}{3\langle N_0 \rangle^2}
\end{aligned} \tag{5.37}$$

$$= \frac{2}{3} - \frac{\Delta N_0^2}{3N_0^2} \tag{5.38}$$

From (5.37) the asymptotal values of U_L can be calculated for the superfluid and the Mott insulating regime using the normalized correlation amplitudes defined in terms of the factorial moments (4.11): The expectation value of the second moment in 5.37 can be expressed as $\langle N_0^2 \rangle = \langle N_0 \rangle^2 g^{(2)}(0) + \langle N_0 \rangle$. The ideal values of $g^{(2)}(0)$ in the superfluid and Mott insulating regime established in chapter 4 can thus be used to obtain the asymptotal values of the Binder cumulant in both cases:

Deep in the superfluid regime ($U \rightarrow 0$) the statistics of N_0 is Poissonian ($g^{(2)}(0) = 1$) so that $\langle N_0^2 \rangle = \langle N_0 \rangle^2 + \langle N_0 \rangle$ and the Binder cumulant tends towards

$$U_{L,\text{SF}} = 1 - \frac{\langle N_0^2 \rangle}{3\langle N_0 \rangle^2} = \frac{2}{3} - \frac{1}{3\langle N_0 \rangle} \tag{5.39}$$

Deep in the Mott regime ($U \rightarrow \infty$), on the other hand, the statistics of N_0 is Gaussian ($g^{(2)}(0) = 2$) so that $\langle N_0^2 \rangle = 2\langle N_0 \rangle^2 + \langle N_0 \rangle$ and the Binder cumulant tends towards

$$U_{L,\text{MI}} = 1 - \frac{\langle N_0^2 \rangle}{3\langle N_0 \rangle^2} = \frac{1}{3} - \frac{1}{3\langle N_0 \rangle} \tag{5.40}$$

For all datasets U_L can be directly calculated from the condensate number fluctuations and mean occupation via (5.38). The post selection can be less stringent here since, as it was shown in chapter 4, with the size of the measurement volume corresponding to the correlation volume, the extracted values are mostly insensitive to shot-to-shot fluctuations of the total atom number on the scale of the entire system. \mathcal{N}_{PS} is thus increased to about 5%, increasing the statistics of the available number of shots.

Figure 5.20 shows the Binder cumulant extracted from the experimental data across the superfluid to Mott insulator phase transition.

Fig. 5.20 shows the Binder cumulant to adhere to the asymptotal value expected in the super-

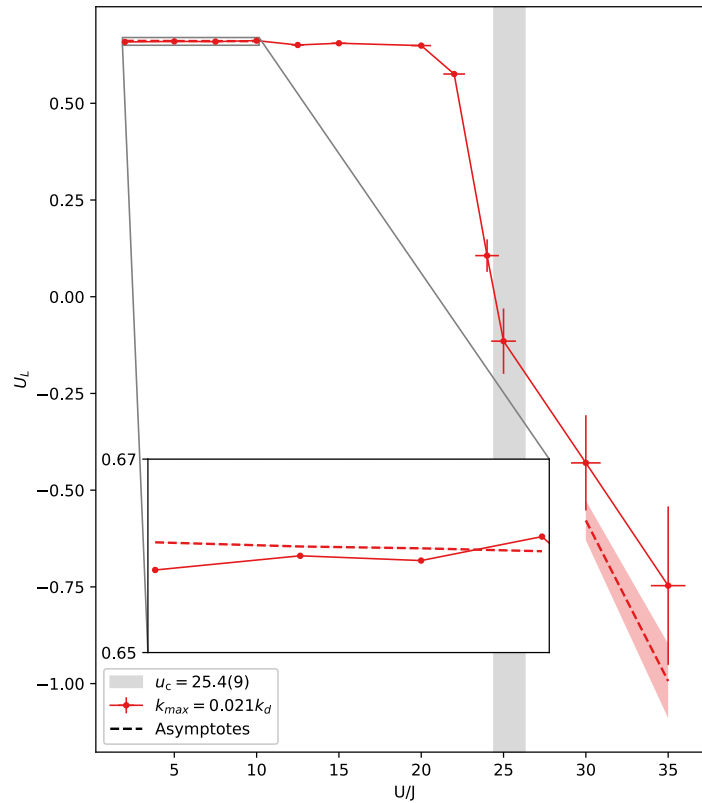


Figure 5.20 - Binder cumulant measured across the Mott transition. Circles are values of the Binder cumulant calculated from experimental data using (5.10) in a volume of size of the correlation volume $(2.1 \times 10^{-2} k_d)^3$. The solid line is a guide to the eye. Vertical error bars represent the combination of the standard error on the variance (A.3) and the standard deviation of the average BEC atom number. Horizontal error bars are the same as in fig. 5.10. The dashed lines represent the asymptotal values (5.39) and (5.40), expected in the superfluid and in the Mott insulating regime, respectively.

fluid regime (5.39), followed by a characteristic drop in amplitude at the phase transition. Once the Mott regime is reached, the statistics in the small volume become insufficient (see chapter 4). It is likely that the error bars in this region are underestimated in fig. 5.20, since U_L is expected to vary monotonously. However, within the dispersion that is present around the asymptotal value (5.40), the Binder cumulant appears to be in the vicinity of the expected value for the Mott regime.

Ideally, one would like to be able to scale the atom number over a sufficiently large range to determine the intersection in the region of the phase transition from the different curves.

However, with the small variations of N available in the datasets, the different curves are too close together to be separated, as is shown in figure 5.21.

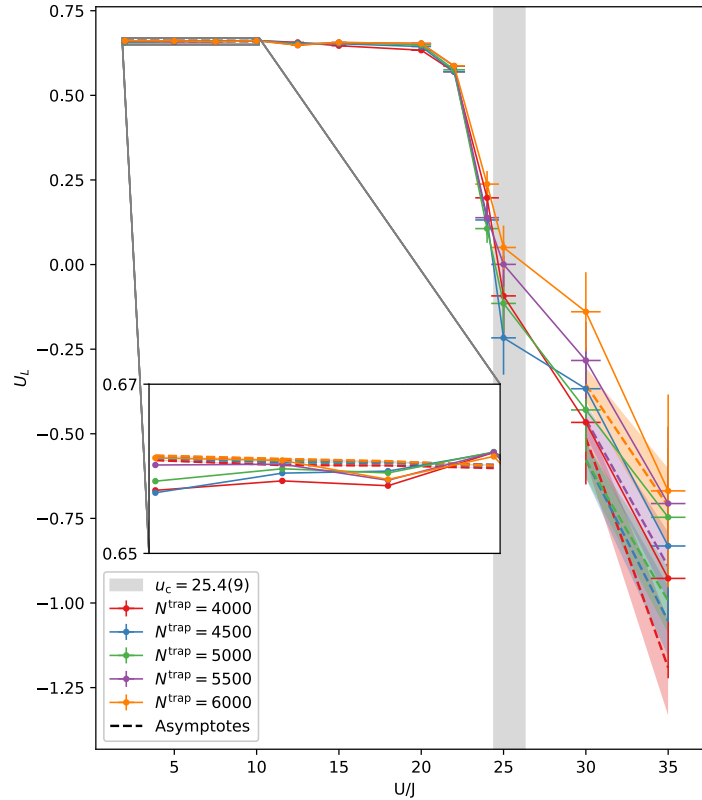


Figure 5.21 – Binder cumulant across the Mott transition for different total atom numbers. Same quantities as is fig. 5.20 for different values of the total atom number varied via post-selection. The different curves are too close to separate and indicate the critical point through their interception.

As seen in chapter 4, the counting statistics of Mott insulators converges towards a Poisson distribution when computed over volumes larger than the correlation volume V_c as a result of the addition of contributions from many (independent) volumes of size V_c . This is confirmed in figure 5.22 where a large measurement volume of the same size as the one used in the analysis of the BEC number fluctuations is used. Consequently, in this situation the system exhibits Poissonian statistics on both sides of the phase transition and U_L becomes almost flat.

If, on the contrary, the size of the measurement volume is reduced below V_c , the occupation of the $\mathbf{k} = \mathbf{0}$ mode becomes so small in the Mott regime that the term in $1/\langle N_0 \rangle^2$ dominates and U_L drops far below its expected asymptotal value, as evidence by fig. 5.22.

In both cases the statistics on the superfluid side remains close to Poissonian, since even for very small a measurement volumes the $k = 0$ mode density is sufficiently large.

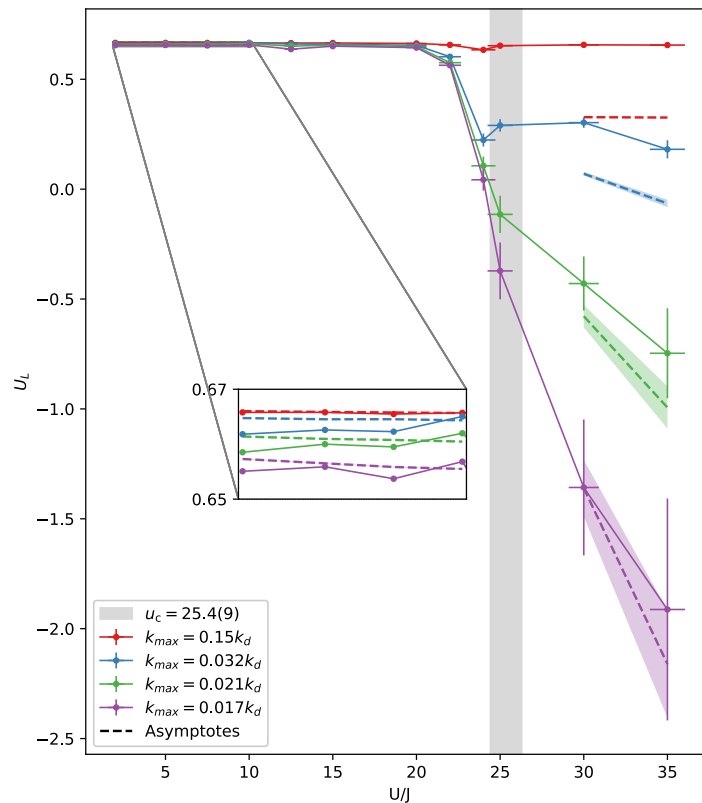


Figure 5.22 – Binder cumulant across the Mott transition for different measurement volumes. Same quantities as in fig. 5.20 for different sizes of the measurement volume. The continuous change on the Mott side from insufficient statistics (smallest volume) to Poissonian statistics on account of averaging over independent contributions (largest volume) can be seen, with the expected asymptotal value for the Mott regime (5.40) approximately compatible with the measurement volume of the size of the correlation volume.

In conclusion, the Binder parameter extracted from experimental data exhibits the characteristic sharp dip at the phase transition. Its expected asymptotal values are confirmed when measured in a volume of the size of the correlation volume, as expected from chapter 4. The external trapping potential renders the system inhomogeneous and prevents the extraction of quantities linked to universal behavior from the value of U_L at the phase transition. However, the approach presented here is in principle readily extendible to homogeneous systems, paving the way to a finite size scaling analysis.

5.5 . Conclusion

BEC number fluctuations were probed across the superfluid to Mott insulator phase transition and found to be peaked at the phase transition, similarly as observations made in the case of the thermally driven superfluid to normal gas transition. The statistical properties of the order parameter are revealed through the extraction of the Binder cumulant, which shows a sharp variation at the phase transition. Though the inhomogeneous nature of the experiment does not allow for the extraction of universal behavior, this approach can be leveraged to pave the way for finite-size scaling analysis in the context of homogeneous systems.

6 - Conclusion

This manuscript has presented investigations into the emergence of complex many-body correlations from the interplay of interactions and kinetic energy based on measurements carried out on lattice Bose gases. The Bose-Hubbard model was simulated by loading BECs of $^4\text{He}^*$ atoms into a 3D optical lattice. The number statistics of occupation of different volumes of momentum space were accessed via electronic detection in 3D of the prepared many-body quantum states. Several dozens of datasets have been acquired in experiments spanning the U/J axis in the Bose-Hubbard phase diagram across the Mott transition isentropically. The resulting datasets, all made up of thousands of shots, each one composed of thousands of individual atoms in momentum space, have permitted to carry out a multitude of analyses in the realm of quantum many-body physics of interacting Bose gases.

Firstly, the weakly-interacting regime of lattice Bose gases was found to be characterized by Bogoliubov's emblematic pair correlation signal between atoms at opposite momenta. This pairing signal was shown to be suppressed upon increasing interactions in favor of more complex correlations between more than two particles, signaling the onset of the strongly correlated regime. This observation was consolidated by a qualitatively similar result obtained by a theory collaborator from numerical simulations based on the quantum rotor model, highlighting the role of non-linear quantum fluctuations in the system. A direct experimental signature of non-Gaussian correlations was obtained via the observation of a non-zero four-operator cumulant at strong interactions, providing insight into the emergence and physical origin of non-Gaussian correlations in ensembles of interacting bosons.

Secondly, an analysis of the Full Counting Statistics of the interacting lattice gases was carried out. Iconic many-body quantum states such as lattice BECs and Mott insulators were characterized by their many-body coherence properties when probed in small volumes of momentum space after an expansion. Mott insulators were found to exhibit thermal FCS characterized by perfectly contrasted bunching amplitudes in the normalized zero-distance correlations that were

probed up to sixth order. Small deviations from Poisson statistics for the BEC were observed that were shown to increase with interactions, highlighting the role of the condensate depletion on many-body coherence.

Finally, the fluctuations of the condensate order parameter were analyzed across the superfluid to Mott insulator phase transition, extracted via measurements of the condensate occupation number. After modeling the principal experimental noise contributions, the order parameter fluctuations were found to be enhanced towards the phase transition, exhibiting a sharp peak of amplitude $\Delta N_0 \sim \sqrt{\langle N \rangle}$ that was deemed incompatible with the modeled experimental noise. This behavior was thus suggested to mirror previous observations made in the context of the normal gas condensation transition driven by temperature and thermal fluctuations [33,34]. Additionally, the Binder cumulant was extracted to probe the statistical properties of the BEC order parameter. This system-size independent quantity was found to exhibit a sharp variation at the phase transition even for the finite size-system probed in the experiment. Though it was outlined that no universal scaling behavior could be extracted from this measurement on account of the harmonic trapping potential rendering the experimental system inhomogeneous, this approach was shown to hold promise for paving the way for finite-size scaling analysis in homogeneous systems.

Appendices

A - Correlations and Statistics

A.1 . Law of total variance

The law of total variance for a probability distribution Y conditioned by another probability distribution X is given by:

$$\text{Var}_Y(Y) = E_X[\text{Var}_Y(Y|X)] + \text{Var}_Y(E_X[Y|X]) \quad (\text{A.1})$$

where $E[X]$ is the expectation value of X .

A.2 . Standard error of variance

Let X_1, \dots, X_n be a random sample from $\mathcal{N}(\mu, \sigma^2)$.

The sample variance is given by

$$S^2 = \frac{1}{n-1} \sum_{i=1}^n (X_i - \bar{X})^2 \quad (\text{A.2})$$

and its standard error by [224]

$$\sigma_{S^2} = S^2 \sqrt{\frac{2}{n-1}} \quad (\text{A.3})$$

B - Evolution of the in-situ cloud size with interactions

Supposing the in-trap density profile of the cloud is parabolic, its radius R can be calculated from the RMS widths σ_{BEC} of the BEC after the TOF. The result is shown in figure B.1 for all datasets.

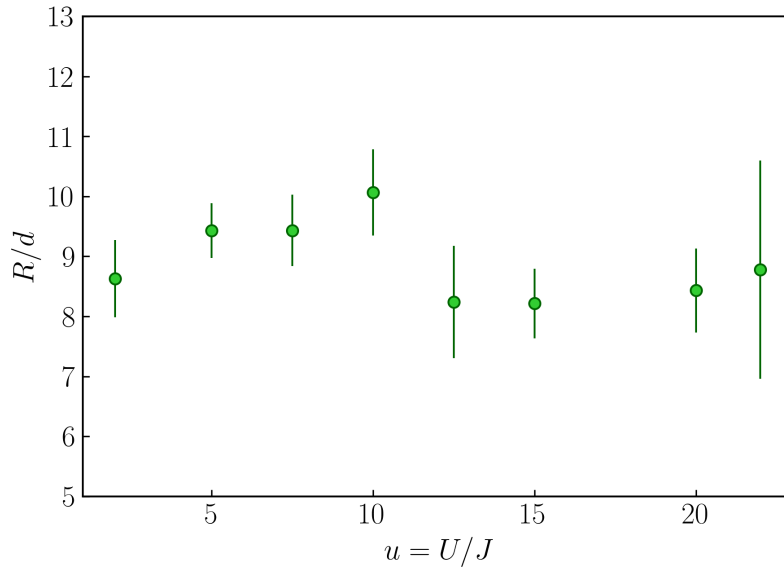


Figure B.1 - In-situ cloud size as a function of interactions. Vertical error bars are one standard deviation on extracted in-situ sizes. The extracted values show no systematic tendency as a function of U/J and are therefore taken to be constant.

Figure B.1 shows that the extracted in-situ cloud sizes show no appreciable tendency as a function of the interaction strength, justifying the approximation made in chapter 4 of considering them to be constant.

List of Figures

2.1	Relevant energy levels of ^4He .	28
2.2	Schema of the metastable Helium source.	29
2.3	Phase-space density at the different stages of the cooling sequence.	32
2.4	Dispersion relations of the lowest three Bloch bands for increasing lattice amplitudes V_0 .	41
2.5	Schematic representation of the two energy terms in the Bose-Hubbard Hamiltonian.	44
2.6	Evolution of the Bose-Hubbard energy terms (a) and their ratio (b) with the lattice amplitude.	47
2.7	Phase diagram (a) and spatial density profile (b) for the inhomogeneous system.	48
2.8	Atom numbers (a) and band calculation (b) for the calibration of the optical lattice intensity via parametric heating.	51
2.9	Bose-Hubbard phase diagram.	52
2.10	Schematic representation of single particle detection of $^4\text{He}^*$ using MCPs and cross delay lines.	59
2.11	Part of the configuration script for the experiment monitoring system.	66
2.12	Experiment monitoring GUI.	67
3.1	Diagram of the pair creation and annihilation processes induced by interactions.	74
3.2	3D momentum distribution recorded in the experiment.	81
3.3	Anomalous correlations revealing pairs of atoms at opposite momenta.	82
3.4	Momentum density profiles and condensed fractions.	84
3.5	Amplitudes of the normal (HBT) and anomalous (pairing) normalized two-body correlations for increasing interactions.	85
3.6	Singular and successive two-body scattering processes from the BEC.	87

3.7	Two-body connected correlations normalized by the integration volume as a function of the latter.	92
3.8	Two-body connected correlations at opposite momenta.	93
3.9	Numerical calculations of connected two-body correlations with the quantum rotor model.	97
3.10	Numerical calculations of connected three-mode correlations with the quantum rotor model.	99
4.1	Schematic representation of the FCS measurement.	106
4.2	FCS of Mott insulators.	108
4.3	FCS of Mott insulators for different sizes of the measurement volume.	109
4.4	FCS of weakly-interacting lattice BECs.	111
4.5	Effect of the transverse integration δk_{\perp} on the amplitudes of the correlation functions $g_{\delta k_{\perp}}^{(n)}$.	120
4.6	Correlation functions of BECs and Mott insulators for orders $n = 2$ through 6.	121
4.7	Correlation functions for the weakly-interacting BEC and the randomized dataset.	122
4.8	Amplitudes of correlation functions for the randomized dataset extended to higher orders of correlation.	124
4.9	Correlation functions of lattice BECs at increasing interactions U/J.	130
4.10	Application of the model to the experimentally observed n-body correlations for the weakly-interacting BEC.	134
4.11	Extension of the application of the model to the experimentally observed n-body correlations for BECs with stronger interactions.	135
4.12	Comparison of the model predictions with 1D density cuts of the momentum densities of lattice BECs.	136
4.13	Coherent fraction as a function of the condensed fraction.	139
5.1	Schematic phase diagrams for continuous quantum phase transitions, temperature as a function of the parameter driving the transition.	150
5.2	Finite size scaling.	152
5.3	Binder cumulant analysis for the 2D Ising model.	154

5.4	BEC number fluctuations across the normal phase transition.	156
5.5	Condensate number fluctuations across the condensation transition observed by Kristensen <i>et al.</i>	157
5.6	Onsite number fluctuation across the superfluid to Mott insulator phase transition.	160
5.7	Theoretical predictions of $T = 0$ BEC fluctuations as a function of U/J.	160
5.8	Measurement volume for condensate fluctuations.	163
5.9	Comparison between quantities measured in the FBZ and on the scale of the entire system.	165
5.10	Density of the zero momentum mode.	167
5.11	Post-selection procedure.	168
5.12	Modeled experimental noise fluctuations.	172
5.13	Experimental observation of fluctuations of the condensate occupation across the superfluid to Mott insulator transition.	174
5.14	Fluctuations of the condensate occupation across the Mott transition for higher levels of experimental noise.	175
5.15	Fluctuations of the condensate occupation across the Mott transition for various sizes of the measurement volume.	177
5.16	Averaged BEC number fluctuations as a function of the size of the measurement volume.	178
5.17	Quantum rotor simulation of the condensate number fluctuations across the Mott transition.	179
5.18	Scaling of the measured fluctuations of the condensate occupation for all datasets across the BH phase diagram.	181
5.19	Fitted exponents γ for the scaling across the Mott transition.	183
5.20	Binder cumulant measured across the Mott transition.	185
5.21	Binder cumulant across the Mott transition for different total atom numbers.	186
5.22	Binder cumulant across the Mott transition for different measurement volumes.	187
B.1	In-situ cloud size as a function of interactions.	195

List of Publications

- Gaétan Hercé, Cécile Carcy, Antoine Ténart, Jan-Philipp Bureik, Alexandre Dareau, David Clément, and Tommaso Roscilde. **Studying the low-entropy Mott transition of bosons in a three-dimensional optical lattice by measuring the full momentum-space density.** Phys. Rev. A, 104(1):1–5, 2021. Used as reference [140] in this manuscript.
- Antoine Tenart, Gaétan Hercé, Jan-Philipp Bureik, Alexandre Dareau, and David Clément. **Observation of pairs of atoms at opposite momenta in an equilibrium interacting Bose gas.** Nat. Phys., 17(12):1364–1368, 2021. Used as reference [23] in this manuscript.
- Gaétan Hercé, Jan-Philipp Bureik, Antoine Ténart, Alain Aspect, Alexandre Dareau, and David Clément. **Full counting statistics of interacting lattice gases after an expansion: The role of condensate depletion in many-body coherence.** Phys. Rev. Res., 5(6):12037, 2023. Used as reference [36] in this manuscript.
- Jan-Philipp Bureik, Gaétan Hercé, Maxime Allemand, Antoine Tenart, Tommaso Roscilde, and David Clément. **Suppression of Bogoliubov momentum pairing and emergence of non-Gaussian correlations in ultracold interacting Bose gases.** arXiv:2401.15340 [cond-mat.quant-gas], 2024. Used as reference [32] in this manuscript.

Bibliography

- [1] Louis De Broglie. Xxxv. a tentative theory of light quanta. *Philosophical Magazine Letters*, 86(7):411–423, 2006.
- [2] Bose. Plancks gesetz und lichtquantenhypothese. *Zeitschrift für Physik*, 26(1):178–181, 1924.
- [3] A. Einstein. *Quantentheorie des einatomigen idealen Gases. Zweite Abhandlung*, pages 245–257. 2024/01/09 2005.
- [4] Steven Chu, L. Hollberg, J. E. Bjorkholm, Alex Cable, and A. Ashkin. Three-dimensional viscous confinement and cooling of atoms by resonance radiation pressure. *Phys. Rev. Lett.*, 55:48–51, Jul 1985.
- [5] J. Dalibard and C. Cohen-Tannoudji. Laser cooling below the doppler limit by polarization gradients: simple theoretical models. *J. Opt. Soc. Am. B*, 6(11):2023–2045, Nov 1989.
- [6] William D. Phillips and Harold Metcalf. Laser deceleration of an atomic beam. *Phys. Rev. Lett.*, 48:596–599, Mar 1982.
- [7] K. B. Davis, M. O. Mewes, M. R. Andrews, N. J. van Druten, D. S. Durfee, D. M. Kurn, and W. Ketterle. Bose-einstein condensation in a gas of sodium atoms. *Phys. Rev. Lett.*, 75:3969–3973, Nov 1995.
- [8] M. H. Anderson, J. R. Ensher, M. R. Matthews, C. E. Wieman, and E. A. Cornell. Observation of bose-einstein condensation in a dilute atomic vapor. *Science*, 269(5221):198–201, 1995.
- [9] Leon N. Cooper. Bound electron pairs in a degenerate fermi gas. *Phys. Rev.*, 104:1189–1190, Nov 1956.
- [10] Marvin E Cage, Kv Klitzing, AM Chang, F Duncan, M Haldane, Robert B Laughlin, AMM Pruisken, and DJ Thouless. *The quantum Hall effect*. Springer Science & Business Media, 2012.
- [11] S. B. Papp, J. M. Pino, R. J. Wild, S. Ronen, C. E. Wieman, D. S. Jin, and E. A. Cornell. Bragg spectroscopy of a strongly interacting ^{85}Rb bose-einstein condensate. *Phys. Rev. Lett.*, 101:135301, Sep 2008.
- [12] N. Navon, S. Nascimbène, F. Chevy, and C. Salomon. The equation of state of a low-temperature fermi gas with tunable interactions. *Science*, 328(5979):729–732, 2010.
- [13] L. Lavoine and T. Bourdel. Beyond-mean-field crossover from one dimension to three dimensions in quantum droplets of binary mixtures. *Phys. Rev. A*, 103:033312, Mar 2021.
- [14] Richard P. Feynman. Simulating physics with computers. *International Journal of Theoretical Physics*, 21(6):467–488, 1982.
- [15] Ehud Altman, Kenneth R. Brown, Giuseppe Carleo, Lincoln D. Carr, Eugene Demler, Cheng Chin, Brian DeMarco, Sophia E. Economou, Mark A. Eriksson, Kai-Mei C. Fu, Markus Greiner, Kaden R. A. Hazzard, Randall G. Hulet, Alicia J. Kollar, Benjamin L. Lev, Mikhail D. Lukin, Ruichao Ma, Xiao Mi, Shashank Misra, Christopher Monroe, Kater Murch, Zaira Nazario, Kang-Kuen Ni, Andrew C. Potter, Pedram Roushan, Mark Saffman, Monika Schleier-Smith, Irfan Siddiqi, Raymond Simmonds, Meenakshi Singh, I. B. Spielman, Kristan Temme,

- David S. Weiss, Jelena Vuckovic, Vladan Vuletic, Jun Ye, and Martin Zwierlein. Quantum Simulators: Architectures and Opportunities. *arXiv*, pages 1–41, 2019.
- [16] Immanuel Bloch, Jean Dalibard, and Sylvain Nascimbène. Quantum simulations with ultracold quantum gases. *Nature Physics*, 8(4):267–276, 2012.
- [17] Markus Greiner, Olaf Mandel, Tilman Esslinger, Theodor W. Hänsch, and Immanuel Bloch. Quantum phase transition from a superfluid to a mott insulator in a gas of ultracold atoms. *Nature*, 415(6867):39–44, 2002.
- [18] D. Jaksch, C. Bruder, J. I. Cirac, C. W. Gardiner, and P. Zoller. Cold bosonic atoms in optical lattices. *Phys. Rev. Lett.*, 81:3108–3111, Oct 1998.
- [19] Immanuel Bloch. Ultracold quantum gases in optical lattices. *Nature Physics*, 1(1):23–30, 2005.
- [20] I. B. Spielman, W. D. Phillips, and J. V. Porto. Condensate fraction in a 2d bose gas measured across the mott-insulator transition. *Phys. Rev. Lett.*, 100:120402, Mar 2008.
- [21] K. Xu, Y. Liu, D. E. Miller, J. K. Chin, W. Setiawan, and W. Ketterle. Observation of strong quantum depletion in a gaseous Bose-Einstein condensate. *Phys. Rev. Lett.*, 96(18):1–4, 2006.
- [22] Nikolai Bogoliubov. On the theory of superfluidity. *Journal of Physics (USSR)*, 11(1):23, 1947.
- [23] Antoine Tenart, Gaétan Hercé, Jan-Philipp Bureik, Alexandre Dareaux, and David Clément. Observation of pairs of atoms at opposite momenta in an equilibrium interacting Bose gas. *Nat. Phys.*, 17(12):1364–1368, 2021.
- [24] Waseem S. Bakr, Jonathon I. Gillen, Amy Peng, Simon Fölling, and Markus Greiner. A quantum gas microscope for detecting single atoms in a hubbard-regime optical lattice. *Nature*, 462(7269):74–77, 2009.
- [25] Lawrence W. Cheuk, Matthew A. Nichols, Melih Okan, Thomas Gersdorf, Vinay V. Ramasesh, Waseem S. Bakr, Thomas Lompe, and Martin W. Zwierlein. Quantum-gas microscope for fermionic atoms. *Phys. Rev. Lett.*, 114:193001, May 2015.
- [26] J. Estève, C. Gross, A. Weller, S. Giovanazzi, and M. K. Oberthaler. Squeezing and entanglement in a bose-einstein condensate. *Nature*, 455(7217):1216–1219, 2008.
- [27] Jacob F. Sherson, Christof Weitenberg, Manuel Endres, Marc Cheneau, Immanuel Bloch, and Stefan Kuhr. Single-atom-resolved fluorescence imaging of an atomic mott insulator. *Nature*, 467(7311):68–72, 2010.
- [28] S. S. Hodgman, R. I. Khakimov, R. J. Lewis-Swan, A. G. Truscott, and K. V. Kheruntsyan. Solving the quantum many-body problem via correlations measured with a momentum microscope. *Phys. Rev. Lett.*, 118:240402, Jun 2017.
- [29] Thomas Schweigler, Valentin Kasper, Sebastian Erne, Igor Mazets, Bernhard Rauer, Federica Cataldini, Tim Langen, Thomas Gasenzer, Jürgen Berges, and Jörg Schmiedmayer. Experimental characterization of a quantum many-body system via higher-order correlations. *Nature*, 545(7654):323–326, 2017.
- [30] A. N. Wenz, G. Zürn, S. Murmann, I. Brouzos, T. Lompe, and S. Jochim. From few to many: Observing the formation of a fermi sea one atom at a time. *Science*, 342(6157):457–460, 2013.

- [31] M. Schellekens, R. Hoppeler, A. Perrin, J. Viana Gomes, D. Boiron, A. Aspect, and C. I. Westbrook. Hanbury brown twiss effect for ultracold quantum gases. *Science*, 310(5748):648–651, 2005.
- [32] Jan-Philipp Bureik, Gaétan Hercé, Maxime Allemand, Antoine Tenart, Tommaso Roscilde, and David Clément. Suppression of bogoliubov momentum pairing and emergence of non-gaussian correlations in ultracold interacting bose gases, 2024.
- [33] M. A. Kristensen, M. B. Christensen, M. Gajdacz, M. Iglicki, K. Pawłowski, C. Klempt, J. F. Sherson, K. Rzazewski, A. J. Hilliard, and J. J. Arlt. Observation of Atom Number Fluctuations in a Bose-Einstein Condensate. *Phys. Rev. Lett.*, 122(16):1–6, 2019.
- [34] M. B. Christensen, T. Vibel, A. J. Hilliard, M. B. Kruk, K. Pawłowski, D. Hryniuk, K. Rzążewski, M. A. Kristensen, and J. J. Arlt. Observation of Microcanonical Atom Number Fluctuations in a Bose-Einstein Condensate. *Phys. Rev. Lett.*, 126(15):1–6, 2021.
- [35] Immanuel Bloch, Jean Dalibard, and Wilhelm Zwerger. Many-body physics with ultracold gases. *Rev. Mod. Phys.*, 80(3):885–964, 2008.
- [36] Gaétan Hercé, Jan-Philipp Bureik, Antoine Ténart, Alain Aspect, Alexandre Dareaux, and David Clément. Full counting statistics of interacting lattice gases after an expansion: The role of condensate depletion in many-body coherence. *Phys. Rev. Res.*, 5(6):12037, 2023.
- [37] Sayan Patra, M. Germann, J.-Ph. Karr, M. Haidar, L. Hilico, V. I. Korobov, F. M. J. Cozijn, K. S. E. Eikema, W. Ubachs, and J. C. J. Koelemeij. Proton-electron mass ratio from laser spectroscopy of hd^+ at the part-per-trillion level. *Science*, 369(6508):1238–1241, 2020.
- [38] Raphael Jannin, Yuri van der Werf, Kees Steinebach, Hendrick L. Bethlem, and Kjeld S. E. Eikema. Pauli blocking of stimulated emission in a degenerate fermi gas. *Nature Communications*, 13(1):6479, 2022.
- [39] Michael Keller, Mateusz Kotyrba, Florian Leupold, Mandip Singh, Maximilian Ebner, and Anton Zeilinger. Bose-einstein condensate of metastable helium for quantum correlation experiments. *Phys. Rev. A*, 90:063607, Dec 2014.
- [40] Kieran F. Thomas, Zhuoxian Ou, Bryce M. Henson, Angela A. Baiju, Sean S. Hodgman, and Andrew G. Truscott. Production of a highly degenerate fermi gas of metastable ^3He atoms. *Phys. Rev. A*, 107:033313, Mar 2023.
- [41] Maxime Perrier, Ziyad Amodjee, Pierre Dussarrat, Alexandre Dareaux, Alain Aspect, Marc Cheneau, Denis Boiron, and Christoph I Westbrook. Thermal counting statistics in an atomic two-mode squeezed vacuum state. *SciPost Phys*, 7(1):002, 2019.
- [42] M. R. Goosen, T. G. Tiecke, W. Vassen, and S. J. J. M. F. Kokkelmans. Feshbach resonances in $^3\text{He}^*$ - $^4\text{He}^*$ mixtures. *Phys. Rev. A*, 82:042713, Oct 2010.
- [43] T. M. F. Hirsch, D. G. Cocks, and S. S. Hodgman. Close-coupled model of feshbach resonances in ultracold $^3\text{He}^*$ and $^4\text{He}^*$ atomic collisions. *Phys. Rev. A*, 104:033317, Sep 2021.
- [44] Cheng Chin, Rudolf Grimm, Paul Julienne, and Eite Tiesinga. Feshbach resonances in ultracold gases. *Rev. Mod. Phys.*, 82:1225–1286, Apr 2010.
- [45] J. S. Borbely, R. van Rooij, S. Knoop, and W. Vassen. Magnetic-field-dependent trap loss of ultracold metastable helium. *Phys. Rev. A*, 85:022706, Feb 2012.

- [46] Lincoln David Turner. *Holographic Imaging of Cold Atoms*. PhD thesis, The University Of Melbourne, 2004.
- [47] S S Hodgman, R G Dall, L J Byron, K G H Baldwin, S J Buckman, and A G Truscott. Metastable Helium: A New Determination of the Longest Atomic Excited-State Lifetime. *Phys. Rev. Lett.*, 103(5):053002, 2009.
- [48] Lynn Hoendervanger. *A New Metastable Helium Machine : An Investigation into the Attributes of Trapping , Cooling and Detecting Metastable Helium*. PhD thesis, Université Paris-Saclay, 2015.
- [49] Quentin Bouton. *Étude microscopique de la distribution en impulsion de condensats de Bose-Einstein d'Hélium métastable*. PhD thesis, Université Paris-Saclay, 2016.
- [50] Hugo Cayla. *Measuring the momentum distribution of a lattice gas at the single-atom level*. PhD thesis, Université Paris-Saclay, 2019.
- [51] Cecile Carcy. *Investigation of the Mott transition with metastable Helium atoms*. PhD thesis, Université Paris-Saclay, 2020.
- [52] Antoine Tenart. *Momentum-space correlations in the depletion of weakly interacting Bose gases*. PhD thesis, Université Paris-Saclay, 2021.
- [53] Gaétan Hercé. *Momentum correlations in strongly-depleted $^4\text{He}^*$ Bose-Einstein condensates*. PhD thesis, Université Paris-Saclay, 2023.
- [54] A. Robert, O. Sirjean, A. Browaeys, J. Poupard, S. Nowak, D. Boiron, C. I. Westbrook, and A. Aspect. A bose-einstein condensate of metastable atoms. *Science*, 292(5516):461–464, 2001.
- [55] F. Pereira Dos Santos, J. Léonard, Junmin Wang, C. J. Barrelet, F. Perales, E. Rasel, C. S. Unnikrishnan, M. Leduc, and C. Cohen-Tannoudji. Bose-einstein condensation of metastable helium. *Phys. Rev. Lett.*, 86:3459–3462, Apr 2001.
- [56] J. M. McNamara, T. Jeltsov, A. S. Tychkov, W. Hogervorst, and W. Vassen. Degenerate bose-fermi mixture of metastable atoms. *Phys. Rev. Lett.*, 97:080404, Aug 2006.
- [57] Donald C Morton, Qixue Wu, and G WF Drake. Energy levels for the stable isotopes of atomic helium(^4He i and ^3He i). *Canadian Journal of Physics*, 84(2):83–105, 2006.
- [58] R. Chang, A. L. Hoendervanger, Q. Bouton, Y. Fang, T. Klafka, K. Audo, A. Aspect, C. I. Westbrook, and D. Clément. Three-dimensional laser cooling at the Doppler limit. *Phys. Rev. A - At. Mol. Opt. Phys.*, 90(6):1–7, 2014.
- [59] A. Aspect, E. Arimondo, R. Kaiser, N. Vansteenkiste, and C. Cohen-Tannoudji. Laser cooling below the one-photon recoil energy by velocity-selective coherent population trapping. *Phys. Rev. Lett.*, 61:826–829, Aug 1988.
- [60] J. Lawall, S. Kulin, B. Saubamea, N. Bigelow, M. Leduc, and C. Cohen-Tannoudji. Three-dimensional laser cooling of helium beyond the single-photon recoil limit. *Phys. Rev. Lett.*, 75:4194–4197, Dec 1995.
- [61] F. M. Penning. Über ionisation durch metastabile atome. *Naturwissenschaften*, 15(40):818–818, 1927.

- [62] Jean Dalibard. *Collisional dynamics of ultra-cold atomic gases*, volume 140: Bose-Einstein Condensation in Atomic Gases of *Proceedings of the International School of Physics "Enrico Fermi"*, pages 321 – 349. IOS Press, 1999.
- [63] F. Bardou, O. Emile, J.-M. Courty, C. I. Westbrook, and A. Aspect. Magneto-optical trapping of metastable helium: Collisions in the presence of resonant light. *Europhysics Letters*, 20(8):681, dec 1992.
- [64] H. C. Mastwijk, J. W. Thomsen, P. van der Straten, and A. Niehaus. Optical collisions of cold, metastable helium atoms. *Phys. Rev. Lett.*, 80:5516–5519, Jun 1998.
- [65] Mitsutaka Kumakura and Norio Morita. Laser trapping of metastable ^3He atoms: Isotopic difference in cold penning collisions. *Phys. Rev. Lett.*, 82:2848–2851, Apr 1999.
- [66] Wim Vassen, Claude Cohen-Tannoudji, Michele Leduc, Denis Boiron, Christoph I. Westbrook, Andrew Truscott, Ken Baldwin, Gerhard Birkl, Pablo Cancio, and Marek Trippenbach. Cold and trapped metastable noble gases. *Rev. Mod. Phys.*, 84:175–210, Feb 2012.
- [67] G. V. Shlyapnikov, J. T. M. Walraven, U. M. Rahmanov, and M. W. Reynolds. Decay kinetics and bose condensation in a gas of spin-polarized triplet helium. *Phys. Rev. Lett.*, 73:3247–3250, Dec 1994.
- [68] Q. Bouton, R. Chang, A. L. Hoendervanger, F. Nogrette, A. Aspect, C. I. Westbrook, and D. Clément. Fast production of Bose-Einstein condensates of metastable helium. *Phys. Rev. A - At. Mol. Opt. Phys.*, 91(6):1–5, 2015.
- [69] Ettore Majorana. Atomi orientati in campo magnetico variabile. *Il Nuovo Cimento (1924-1942)*, 9(2):43–50, 1932.
- [70] Wolfgang Petrich, Michael H. Anderson, Jason R. Ensher, and Eric A. Cornell. Stable, tightly confining magnetic trap for evaporative cooling of neutral atoms. *Phys. Rev. Lett.*, 74:3352–3355, Apr 1995.
- [71] Myoung-Sun Heo, Jae-yoon Choi, and Yong-il Shin. Fast production of large ^{23}Na bose-einstein condensates in an optically plugged magnetic quadrupole trap. *Phys. Rev. A*, 83:013622, Jan 2011.
- [72] Matthew P. A. Fisher, Peter B. Weichman, G. Grinstein, and Daniel S. Fisher. Boson localization and the superfluid-insulator transition. *Phys. Rev. B*, 40:546–570, Jul 1989.
- [73] A. Osterloh, Luigi Amico, G. Falci, and Rosario Fazio. Scaling of entanglement close to a quantum phase transition. *Nature*, 416(6881):608–610, 2002.
- [74] Gabriele De Chiara and Anna Sanpera. Genuine quantum correlations in quantum many-body systems: a review of recent progress. *Reports on Progress in Physics*, 81(7):074002, 2018.
- [75] N. R. Cooper, J. Dalibard, and I. B. Spielman. Topological bands for ultracold atoms. *Rev. Mod. Phys.*, 91:015005, Mar 2019.
- [76] Michael Schreiber, Sean S. Hodgman, Pranjal Bordia, Henrik P. Lüschen, Mark H. Fischer, Ronen Vosk, Ehud Altman, Ulrich Schneider, and Immanuel Bloch. Observation of many-body localization of interacting fermions in a quasirandom optical lattice. *Science*, 349(6250):842–845, 2015.

- [77] Jae yoon Choi, Sebastian Hild, Johannes Zeiher, Peter Schauß, Antonio Rubio-Abadal, Tarik Yefsah, Vedika Khemani, David A. Huse, Immanuel Bloch, and Christian Gross. Exploring the many-body localization transition in two dimensions. *Science*, 352(6293):1547–1552, 2016.
- [78] Alexander Lukin, Matthew Rispoli, Robert Schittko, M. Eric Tai, Adam M. Kaufman, Soonwon Choi, Vedika Khemani, Julian Léonard, and Markus Greiner. Probing entanglement in a many-body-localized system. *Science*, 364(6437):256–260, 2019.
- [79] Daniel Barredo, Sylvain de Léséleuc, Vincent Lienhard, Thierry Lahaye, and Antoine Browaeys. An atom-by-atom assembler of defect-free arbitrary two-dimensional atomic arrays. *Science*, 354(6315):1021–1023, 2016.
- [80] R. Barends, A. Shabani, L. Lamata, J. Kelly, A. Mezzacapo, U. Las Heras, R. Babbush, A. G. Fowler, B. Campbell, Yu Chen, Z. Chen, B. Chiaro, A. Dunsworth, E. Jeffrey, E. Lucero, A. Megrant, J. Y. Mutus, M. Neeley, C. Neill, P. J. J. O’Malley, C. Quintana, P. Roushan, D. Sank, A. Vainsencher, J. Wenner, T. C. White, E. Solano, H. Neven, and John M. Martinis. Digitized adiabatic quantum computing with a superconducting circuit. *Nature*, 534(7606):222–226, 2016.
- [81] Joseph W. Britton, Brian C. Sawyer, Adam C. Keith, C. C. Joseph Wang, James K. Freericks, Hermann Uys, Michael J. Biercuk, and John J. Bollinger. Engineered two-dimensional ising interactions in a trapped-ion quantum simulator with hundreds of spins. *Nature*, 484(7395):489–492, 2012.
- [82] N F Mott. The basis of the electron theory of metals, with special reference to the transition metals. *Proceedings of the Physical Society. Section A*, 62(7):416, jul 1949.
- [83] N. F. Mott. On the transition to metallic conduction in semiconductors. *Canadian Journal of Physics*, 34(12A):1356–1368, 1956.
- [84] N. F. Mott. The transition to the metallic state. *The Philosophical Magazine: A Journal of Theoretical Experimental and Applied Physics*, 6(62):287–309, 1961.
- [85] J. Hubbard. Electron correlations in narrow energy bands. *Proceedings of the Royal Society of London. Series A, Mathematical and Physical Sciences*, 276(1365):238–257, 2023/10/06/ 1963.
- [86] H. A. Gersch and G. C. Knollman. Quantum cell model for bosons. *Phys. Rev.*, 129:959–967, Jan 1963.
- [87] Neil W. Ashcroft and David Mermin. *Solid State Physics*. Holt, Rinehart and Winston, 1976.
- [88] Gregory H. Wannier. The structure of electronic excitation levels in insulating crystals. *Phys. Rev.*, 52:191–197, Aug 1937.
- [89] Subir Sachdev. *Quantum Phase Transitions*. Cambridge University Press, 2 edition, 2011.
- [90] Sara Bergkvist, Patrik Henelius, and Anders Rosengren. Local-density approximation for confined bosons in an optical lattice. *Phys. Rev. A*, 70:053601, Nov 2004.
- [91] Lode Pollet. Recent developments in quantum monte carlo simulations with applications for cold gases. *Reports on Progress in Physics*, 75(9):094501, aug 2012.
- [92] F. Gerbier. Quantum gases in optical lattices. Lecture Notes, <https://www.phys.ens.fr/~chevy/AtomesFroids/OL2015.pdf>, May 2015.

- [93] T. A. Savard, K. M. O'Hara, and J. E. Thomas. Laser-noise-induced heating in far-off resonance optical traps. *Phys. Rev. A*, 56:R1095–R1098, Aug 1997.
- [94] S. Friebel, C. D'Andrea, J. Walz, M. Weitz, and T. W. Hänsch. CO_2 -laser optical lattice with cold rubidium atoms. *Phys. Rev. A*, 57:R20–R23, Jan 1998.
- [95] Massimo Campostrini, Martin Hasenbusch, Andrea Pelissetto, Paolo Rossi, and Ettore Vicari. Critical behavior of the three-dimensional XY universality class. *Phys. Rev. B*, 63:214503, May 2001.
- [96] Matthias Vojta. Quantum phase transitions. *Reports on Progress in Physics*, 66(12):2069, nov 2003.
- [97] Cécile Carcy, Gaétan Hercé, Antoine Tenart, Tommaso Roscilde, and David Clément. Certifying the Adiabatic Preparation of Ultracold Lattice Bosons in the Vicinity of the Mott Transition. *Phys. Rev. Lett.*, 126(4):1–6, 2021.
- [98] F. Gerbier, S. Trotzky, S. Fölling, U. Schnorrberger, J. D. Thompson, A. Widera, I. Bloch, L. Pollet, M. Troyer, B. Capogrosso-Sansone, N. V. Prokof'ev, and B. V. Svistunov. Expansion of a quantum gas released from an optical lattice. *Phys. Rev. Lett.*, 101:155303, Oct 2008.
- [99] Antoine Tenart, Cécile Carcy, Hugo Cayla, Thomas Bourdel, Marco Mancini, and David Clément. Two-body collisions in the time-of-flight dynamics of lattice Bose superfluids. *Phys. Rev. Res.*, 2(1), 2020.
- [100] W Aberth. Microchannel plate for surface-induced dissociation in mass spectrometry. *Anal Chem*, 62(6):609–611, Mar 1990.
- [101] Wesley H Smith. Triggering at LHC experiments. *Nuclear Instruments and Methods in Physics Research Section A: Accelerators, Spectrometers, Detectors and Associated Equipment*, 478(1):62–67, 2002. Proceedings of the ninth Int.Conf. on Instrumentation.
- [102] Lars von der Wense, Benedict Seiferle, Mustapha Laatiaoui, Jürgen B. Neumayr, Hans-Jörg Maier, Hans-Friedrich Wirth, Christoph Mokry, Jörg Runke, Klaus Eberhardt, Christoph E. Düllmann, Norbert G. Trautmann, and Peter G. Thirolf. Direct detection of the 229th nuclear clock transition. *Nature*, 533(7601):47–51, 2016.
- [103] D. Blavette, A. Bostel, J. M. Sarrau, B. Deconihout, and A. Menand. An atom probe for three-dimensional tomography. *Nature*, 363(6428):432–435, 1993.
- [104] Xuetao Zhu, L. Santos, R. Sankar, S. Chikara, C. Howard, F. C. Chou, C. Chamon, and M. El-Batanouny. Interaction of phonons and Dirac fermions on the surface of Bi_2Se_3 : A strong Kohn anomaly. *Phys. Rev. Lett.*, 107:186102, Oct 2011.
- [105] Rebecca Boll, Arnaud Rouzée, Marcus Adolph, Denis Anielski, Andrew Aquila, Sadia Bari, Cédric Bomme, Christoph Bostedt, John D. Bozek, Henry N. Chapman, Lauge Christensen, Ryan Coffee, Niccolò Coppola, Sankar De, Piero Decleva, Sascha W. Epp, Benjamin Erk, Frank Filsinger, Lutz Foucar, Tais Gorkhover, Lars Gumprecht, André Hömke, Lotte Holmegaard, Per Johnsson, Jens S. Kienitz, Thomas Kierspel, Faton Krasniqi, Kai-Uwe Kühnel, Jochen Maurer, Marc Messerschmidt, Robert Moshhammer, Nele L. M. Müller, Benedikt Rudek, Evgeny Savelyev, Ilme Schlichting, Carlo Schmidt, Frank Scholz, Sebastian Schorb, Joachim Schulz, Jörn Seltsmann, Mauro Stener, Stephan Stern, Simone Techert, Jan Thøgersen, Sebastian Trippel, Jens Viehhaus, Marc Vrakking, Henrik Stapelfeldt, Jochen

- Küpper, Joachim Ullrich, Artem Rudenko, and Daniel Rolles. Imaging molecular structure through femtosecond photoelectron diffraction on aligned and oriented gas-phase molecules. *Faraday Discuss.*, 171:57–80, 2014.
- [106] F. B. Dunning, R. D. Rundel, and R. F. Stebbings. Determination of secondary electron ejection coefficients for rare gas metastable atoms. *Review of Scientific Instruments*, 46(6):697–701, 09 1975.
- [107] Joseph Ladislav Wiza. Microchannel plate detectors. *Nuclear Instruments and Methods*, 162(1):587–601, 1979.
- [108] A. L. Hoendervanger, D. Clément, A. Aspect, C. I. Westbrook, D. Dowek, Y. J. Picard, and D. Boiron. Influence of gold coating and interplate voltage on the performance of chevron micro-channel plates for temporally and spatially resolved single particle detection. *Rev. Sci. Instrum.*, 84(2), 2013.
- [109] O. Siegmund, J. Vallerga, P. Jelinsky, X. Michalet, and S. Weiss. Cross delay line detectors for high time resolution astronomical polarimetry and biological fluorescence imaging. In *IEEE Nuclear Science Symposium Conference Record, 2005*, volume 1, pages 448–452, 2005.
- [110] David Clément. *Momentum-space atom correlations in strongly interacting Bose gases*. Habilitation à diriger des recherches, Université Paris-Saclay, Oct 2019.
- [111] F. Nogrette, D. Heurteau, R. Chang, Q. Bouton, C. I. Westbrook, R. Sellem, and David Clément. Characterization of a detector chain using a FPGA-based time-to-digital converter to reconstruct the three-dimensional coordinates of single particles at high flux. *Rev. Sci. Instrum.*, 86(11), 2015.
- [112] Michael L. Edgar, J. S. Lapington, and Alan Smith. The spatial extent of gain depression for MCP-based photon detectors. *Review of Scientific Instruments*, 63(1):816–819, 01 1992.
- [113] L. Pitaevskii and S. Stringari. Uncertainty principle, quantum fluctuations, and broken symmetries. *Journal of Low Temperature Physics*, 85(5):377–388, 1991.
- [114] T. D. Lee, Kerson Huang, and C. N. Yang. Eigenvalues and eigenfunctions of a bose system of hard spheres and its low-temperature properties. *Phys. Rev.*, 106:1135–1145, Jun 1957.
- [115] Nir Navon, Swann Piatecki, Kenneth Günter, Benno Rem, Trong Canh Nguyen, Frédéric Chevy, Werner Krauth, and Christophe Salomon. Dynamics and thermodynamics of the low-temperature strongly interacting bose gas. *Phys. Rev. Lett.*, 107:135301, Sep 2011.
- [116] Nils B. Jørgensen, Georg M. Bruun, and Jan J. Arlt. Dilute fluid governed by quantum fluctuations. *Phys. Rev. Lett.*, 121:173403, Oct 2018.
- [117] L.D. Landau and E.M. Lifshitz. *Quantum Mechanics: Non-Relativistic Theory*, volume 3 of *Course of theoretical physics*. Elsevier Science, 1991.
- [118] Jean Dalibard. Les interactions entre atomes froids dans les gaz quantiques (ii). Cours du Collège de France, https://pro.college-de-france.fr/jean.dalibard/CdF/2022/total_en.pdf, Mar 2022.
- [119] Q. Fontaine, T. Bienaimé, S. Pigeon, E. Giacobino, A. Bramati, and Q. Glorieux. Observation of the bogoliubov dispersion in a fluid of light. *Phys. Rev. Lett.*, 121:183604, Oct 2018.
- [120] Allen Miller, David Pines, and Philippe Nozières. Elementary excitations in liquid helium. *Phys. Rev.*, 127:1452–1464, Sep 1962.

- [121] R. Ozeri, N. Katz, J. Steinhauer, and N. Davidson. Colloquium: Bulk bogoliubov excitations in a bose-einstein condensate. *Rev. Mod. Phys.*, 77:187–205, Apr 2005.
- [122] J. Steinhauer, R. Ozeri, N. Katz, and N. Davidson. Excitation spectrum of a bose-einstein condensate. *Phys. Rev. Lett.*, 88:120407, Mar 2002.
- [123] Petr Stepanov, Ivan Amelio, Jean-Guy Rousset, Jacqueline Bloch, Aristide Lemaître, Alberto Amo, Anna Minguzzi, Iacopo Carusotto, and Maxime Richard. Dispersion relation of the collective excitations in a resonantly driven polariton fluid. *Nature Communications*, 10(1):3869, 2019.
- [124] L. Landau. Theory of the superfluidity of helium ii. *Phys. Rev.*, 60:356–358, Aug 1941.
- [125] David C. Burnham and Donald L. Weinberg. Observation of simultaneity in parametric production of optical photon pairs. *Phys. Rev. Lett.*, 25:84–87, Jul 1970.
- [126] M. Greiner, C. A. Regal, J. T. Stewart, and D. S. Jin. Probing pair-correlated fermionic atoms through correlations in atom shot noise. *Phys. Rev. Lett.*, 94:110401, Mar 2005.
- [127] G. Arnison, A. Astbury, B. Aubert, C. Bacci, R. Bernabei, A. Bézaguët, R. Böck, T.J.V. Bowcock, M. Calvetti, T. Carroll, P. Catz, S. Centro, F. Ceradini, S. Cittolin, A.M. Cnops, C. Cochet, J. Colas, M. Corden, D. Dallman, S. D'Angelo, M. DeBeer, M. Della Negra, M. Demoulin, D. Denegri, D. DiBitonto, L. Dobrzynski, J.D. Dowell, M. Edwards, K. Eggert, E. Eisenhandler, N. Ellis, P. Erhard, H. Faissner, G. Fontaine, J.P. Fournier, R. Frey, R. Frühwirth, J. Garvey, S. Geer, C. Ghesquière, P. Ghez, K.L. Giboni, W.R. Gibson, Y. Giraud-Heraud, A. Givernaud, A. Gonidec, G. Grayer, P. Gutierrez, R. Haidan, T. Hansl-Kozanecka, W.J. Haynes, L.O. Hertzberger, C. Hodges, D. Hoffmann, H. Hoffmann, D.J. Holthuisen, R.J. Homer, A. Honma, W. Jank, P.I.P. Kalmus, V. Karimäki, R. Keeler, I. Kenyon, A. Kernan, R. Kinnunen, H. Kowalski, W. Kozanecki, D. Kryn, F. Lacava, J.P. Laugier, J.P. Lees, H. Lehmann, R. Leuchs, A. Leveque, D. Linglin, E. Locci, T. Markiewicz, G. Maurin, T. McMahon, J.P. Mendiburu, M.N. Minard, M. Moricca, F. Muller, A.K. Nandi, L. Naumann, A. Norton, A. Orkin-Lecourtois, L. Paoluzi, G. Piano Mortari, M. Pimiä, A. Placci, E. Radermacher, J. Ransdell, H. Reithler, J.P. Revol, J. Rich, M. Rijssenbeek, C. Roberts, C. Rubbia, B. Sadoulet, G. Sajot, G. Salvi, G. Salvini, J. Sass, J. Saudraix, A. Savoy-Navarro, D. Schinzel, W. Scott, T.P. Shah, M. Spiro, J. Strauss, K. Sumorok, F. Szoncsó, C. Tao, G. Thompson, J. Timmer, E. Tscheslog, J. Tuominiemi, J.P. Vialle, J. Vrana, V. Vuillemin, H. Wahl, P. Watkins, J. Wilson, M. Yvert, and E. Zurfluh. First observation of correlations between high transverse momentum charged particles in events from the cern proton-antiproton collider. *Physics Letters B*, 118(1):173–177, 1982.
- [128] A. Perrin, H. Chang, V. Krachmalnicoff, M. Schellekens, D. Boiron, A. Aspect, and C. I. Westbrook. Observation of atom pairs in spontaneous four-wave mixing of two colliding bose-einstein condensates. *Phys. Rev. Lett.*, 99:150405, Oct 2007.
- [129] J. Bardeen, L. N. Cooper, and J. R. Schrieffer. Theory of superconductivity. *Phys. Rev.*, 108:1175–1204, Dec 1957.
- [130] Marvin Holten, Luca Bayha, Keerthan Subramanian, Sandra Brandstetter, Carl Heintze, Philipp Lunt, Philipp M. Preiss, and Selim Jochim. Observation of cooper pairs in a mesoscopic two-dimensional fermi gas. *Nature*, 606(7913):287–291, 2022.
- [131] Rockson Chang, Quentin Bouton, Hugo Cayla, C. Qu, Alain Aspect, C. I. Westbrook, and David Clément. Momentum-Resolved Observation of Thermal and Quantum Depletion in a Bose Gas. *Phys. Rev. Lett.*, 117(23):1–5, 2016.

- [132] E. Toth, A. M. Rey, and P. B. Blakie. Theory of correlations between ultracold bosons released from an optical lattice. *Phys. Rev. A - At. Mol. Opt. Phys.*, 78(1):1–19, 2008.
- [133] D. van Oosten, P. van der Straten, and H. T. C. Stoof. Quantum phases in an optical lattice. *Phys. Rev. A*, 63:053601, Apr 2001.
- [134] Roy J. Glauber. The quantum theory of optical coherence. *Phys. Rev.*, 130:2529–2539, Jun 1963.
- [135] C. K. Hong, Z. Y. Ou, and L. Mandel. Measurement of subpicosecond time intervals between two photons by interference. *Phys. Rev. Lett.*, 59:2044–2046, Nov 1987.
- [136] C. Gardiner and P. Zoller. *Quantum Noise: A Handbook of Markovian and Non-Markovian Quantum Stochastic Methods with Applications to Quantum Optics*. Springer Series in Synergetics. Springer, 2004.
- [137] Salvatore Butera, David Clement, and Iacopo Carusotto. Position- And momentum-space two-body correlations in a weakly interacting trapped condensate. *Phys. Rev. A*, 103(1):1–12, 2021.
- [138] J. Stenger, S. Inouye, A. P. Chikkatur, D. M. Stamper-Kurn, D. E. Pritchard, and W. Ketterle. Bragg spectroscopy of a bose-einstein condensate. *Phys. Rev. Lett.*, 82:4569–4573, Jun 1999.
- [139] H. Cayla, C. Carcy, Q. Bouton, R. Chang, G. Carleo, M. Mancini, and D. Clément. Single-atom-resolved probing of lattice gases in momentum space. *Phys. Rev. A*, 97(6):2–6, 2018.
- [140] Gaétan Hercé, Cécile Carcy, Antoine Tenart, Jan-Philipp Bureik, Alexandre Dareaux, David Clément, and Tommaso Roscilde. Studying the low-entropy Mott transition of bosons in a three-dimensional optical lattice by measuring the full momentum-space density. *Phys. Rev. A*, 104(1):1–5, 2021.
- [141] Hugo Cayla, Salvatore Butera, Cécile Carcy, Antoine Tenart, Gaétan Hercé, Marco Mancini, Alain Aspect, Iacopo Carusotto, and David Clément. Hanbury Brown and Twiss Bunching of Phonons and of the Quantum Depletion in an Interacting Bose Gas. *Phys. Rev. Lett.*, 125(16):1–6, 2020.
- [142] Emilia Morosan, Douglas Natelson, Andriy H. Nevidomskyy, and Qimiao Si. Strongly correlated materials. *Advanced Materials*, 24(36):4896–4923, 2012.
- [143] Antoine Georges, Luca de' Medici, and Jernej Mravlje. Strong correlations from hund's coupling. *Annual Review of Condensed Matter Physics*, 4(1):137–178, 2013.
- [144] H. D. Ursell. The evaluation of gibbs' phase-integral for imperfect gases. *Mathematical Proceedings of the Cambridge Philosophical Society*, 23(6):685–697, 1927.
- [145] S. B. Shlosman. Signs of the ising model ursell functions. *Communications in Mathematical Physics*, 102(4):679–686, 1986.
- [146] Eric A. Carlen, Markus Holzmann, Ian Jauslin, and Elliott H. Lieb. Simplified approach to the repulsive bose gas from low to high densities and its numerical accuracy. *Phys. Rev. A*, 103:053309, May 2021.
- [147] Mats Wallin, Erik S. Sørensen, S. M. Girvin, and A. P. Young. Superconductor-insulator transition in two-dimensional dirty boson systems. *Phys. Rev. B*, 49:12115–12139, May 1994.
- [148] Tommaso Roscilde. Bosons in one-dimensional incommensurate superlattices. *Phys. Rev. A*, 77:063605, Jun 2008.

- [149] Bess Fang, Aisling Johnson, Tommaso Roscilde, and Isabelle Bouchoule. Momentum-space correlations of a one-dimensional bose gas. *Phys. Rev. Lett.*, 116:050402, Feb 2016.
- [150] S. Trotzky, L. Pollet, F. Gerbier, U. Schnorrberger, I. Bloch, N. V. Prokofev, B. Svistunov, and M. Troyer. Suppression of the critical temperature for superfluidity near the mott transition. *Nature Physics*, 6(12):998–1004, 2010.
- [151] Stefan Wessel, Fabien Alet, Matthias Troyer, and G. George Batrouni. Quantum monte carlo simulations of confined bosonic atoms in optical lattices. *Phys. Rev. A*, 70:053615, Nov 2004.
- [152] S. L. Sondhi, S. M. Girvin, J. P. Carini, and D. Shahar. Continuous quantum phase transitions. *Rev. Mod. Phys.*, 69:315–333, Jan 1997.
- [153] Tommaso Roscilde, Michael F Faulkner, Steven T Bramwell, and Peter C W Holdsworth. From quantum to thermal topological-sector fluctuations of strongly interacting bosons in a ring lattice. *New Journal of Physics*, 18(7):075003, jul 2016.
- [154] Ya.M. Blanter and M. Büttiker. Shot noise in mesoscopic conductors. *Physics Reports*, 336(1):1–166, 2000.
- [155] E. A. Burt, R. W. Ghrist, C. J. Myatt, M. J. Holland, E. A. Cornell, and C. E. Wieman. Coherence, correlations, and collisions: What one learns about bose-einstein condensates from their decay. *Phys. Rev. Lett.*, 79:337–340, Jul 1997.
- [156] Ehud Altman, Eugene Demler, and Mikhail D. Lukin. Probing many-body states of ultracold atoms via noise correlations. *Phys. Rev. A*, 70:013603, Jul 2004.
- [157] Leonid S. Levitov, Hyunwoo Lee, and Gordey B. Lesovik. Electron counting statistics and coherent states of electric current. *Journal of Mathematical Physics*, 37(10):4845–4866, 10 1996.
- [158] T. Cubel Liebisch, A. Reinhard, P. R. Berman, and G. Raithel. Atom counting statistics in ensembles of interacting rydberg atoms. *Phys. Rev. Lett.*, 95:253002, Dec 2005.
- [159] N. Malossi, M. M. Valado, S. Scotto, P. Huillery, P. Pillet, D. Ciampini, E. Arimondo, and O. Morsch. Full counting statistics and phase diagram of a dissipative rydberg gas. *Phys. Rev. Lett.*, 113:023006, Jul 2014.
- [160] Johannes Zeiher, Rick van Bijnen, Peter Schauß, Sebastian Hild, Jae-yoon Choi, Thomas Pohl, Immanuel Bloch, and Christian Gross. Many-body interferometry of a rydberg-dressed spin lattice. *Nature Physics*, 12(12):1095–1099, 2016.
- [161] Anton Öttl, Stephan Ritter, Michael Köhl, and Tilman Esslinger. Correlations and counting statistics of an atom laser. *Phys. Rev. Lett.*, 95:090404, Aug 2005.
- [162] Steven T Flammia, David Gross, Yi-Kai Liu, and Jens Eisert. Quantum tomography via compressed sensing: error bounds, sample complexity and efficient estimators. *New Journal of Physics*, 14(9):095022, sep 2012.
- [163] D. A. Ivanov and A. G. Abanov. Phase transitions in full counting statistics for periodic pumping. *Europhysics Letters*, 92(3):37008, nov 2010.
- [164] Fernando J. Gómez-Ruiz, Jack J. Mayo, and Adolfo del Campo. Full counting statistics of topological defects after crossing a phase transition. *Phys. Rev. Lett.*, 124:240602, Jun 2020.

- [165] P. Devillard, D. Chevallier, P. Vignolo, and M. Albert. Full counting statistics of the momentum occupation numbers of the tonks-girardeau gas. *Phys. Rev. A*, 101:063604, Jun 2020.
- [166] Viktor Eisler. Universality in the full counting statistics of trapped fermions. *Phys. Rev. Lett.*, 111:080402, Aug 2013.
- [167] Izabella Lovas, Balázs Dóra, Eugene Demler, and Gergely Zaránd. Full counting statistics of time-of-flight images. *Phys. Rev. A*, 95:053621, May 2017.
- [168] Israel Klich and Leonid Levitov. Quantum noise as an entanglement meter. *Phys. Rev. Lett.*, 102:100502, Mar 2009.
- [169] Massimiliano Esposito, Upendra Harbola, and Shaul Mukamel. Nonequilibrium fluctuations, fluctuation theorems, and counting statistics in quantum systems. *Rev. Mod. Phys.*, 81:1665–1702, Dec 2009.
- [170] Pavel E. Dolgirev, Jamir Marino, Dries Sels, and Eugene Demler. Non-gaussian correlations imprinted by local dephasing in fermionic wires. *Phys. Rev. B*, 102:100301, Sep 2020.
- [171] C. Fabre and N. Treps. Modes and states in quantum optics. *Rev. Mod. Phys.*, 92:035005, Sep 2020.
- [172] Mattia Walschaers. Non-gaussian quantum states and where to find them. *PRX Quantum*, 2:030204, Sep 2021.
- [173] Eric Brunner, Andreas Buchleitner, and Gabriel Dufour. Many-body coherence and entanglement probed by randomized correlation measurements. *Phys. Rev. Res.*, 4:043101, Nov 2022.
- [174] Piero Naldesi, Andreas Elben, Anna Minguzzi, David Clément, Peter Zoller, and Benoît Vermersch. Fermionic correlation functions from randomized measurements in programmable atomic quantum devices. *Phys. Rev. Lett.*, 131:060601, Aug 2023.
- [175] L.P. Pitaevskii and S. Stringari. *Bose-Einstein Condensation*. International Series of Monographs on Physics. Clarendon Press, 2003.
- [176] Cécile Carcy, Hugo Cayla, Antoine Tenart, Alain Aspect, Marco Mancini, and David Clément. Momentum-Space Atom Correlations in a Mott Insulator. *Phys. Rev. X*, 9(4), 2019.
- [177] Simon Fölling, Fabrice Gerbier, Artur Widera, Olaf Mandel, Tatjana Gericke, and Immanuel Bloch. Spatial quantum noise interferometry in expanding ultracold atom clouds. *Nature*, 434(7032):481–484, 2005.
- [178] Y. Castin and R. Dum. Low-temperature bose-einstein condensates in time-dependent traps: Beyond the $u(1)$ symmetry-breaking approach. *Phys. Rev. A*, 57:3008–3021, Apr 1998.
- [179] Alain Aspect. Hanbury Brown and Twiss, Hong Ou and Mandel effects and other landmarks in quantum optics: from photons to atoms. In Antoine Browaeys, editor, *Current Trends in Atomic Physics*, pages 428–449. Oxford University Press, 05 2019.
- [180] J.W. Goodman. *Statistical Optics*. Wiley Series in Pure and Applied Optics. Wiley, 2015.
- [181] Roy J. Glauber. Coherent and incoherent states of the radiation field. *Phys. Rev.*, 131:2766–2788, Sep 1963.
- [182] R. G. Dall, A. G. Manning, S. S. Hodgman, Wu RuGway, K. V. Kheruntsyan, and A. G. Truscott. Ideal n-body correlations with massive particles. *Nature Physics*, 9(6):341–344, 2013.

- [183] T. Jelte, J. M. McNamara, W. Hogervorst, W. Vassen, V. Krachmalnicoff, M. Schellekens, A. Perrin, H. Chang, D. Boiron, A. Aspect, and C. I. Westbrook. Comparison of the hanbury brown–twiss effect for bosons and fermions. *Nature*, 445(7126):402–405, 2007.
- [184] Andrea Bergschneider, Vincent M. Klinkhamer, Jan Hendrik Becher, Ralf Klemt, Lukas Palm, Gerhard Zürn, Selim Jochim, and Philipp M. Preiss. Experimental characterization of two-particle entanglement through position and momentum correlations. *Nature Physics*, 15(7):640–644, 2019.
- [185] S. S. Hodgman, R. G. Dall, A. G. Manning, K. G. H. Baldwin, and A. G. Truscott. Direct measurement of long-range third-order coherence in bose-einstein condensates. *Science*, 331(6020):1046–1049, 2011.
- [186] C. Carcy, S. Hoinka, M. G. Lingham, P. Dyke, C. C.N. Kuhn, H. Hu, and C. J. Vale. Contact and Sum Rules in a Near-Uniform Fermi Gas at Unitarity. *Phys. Rev. Lett.*, 122(20):1–5, 2019.
- [187] R. Hanbury-Brown and R. Q. Twiss. A test of a new type of stellar interferometer on sirius. *Nature*, 178(4541):1046–1048, 1956.
- [188] L. Mandel and E. Wolf. *Optical Coherence and Quantum Optics*. EBL-Schweitzer. Cambridge University Press, 1995.
- [189] V. Degiorgio. About photon correlations. *American Journal of Physics*, 81(10):772–775, 10 2013.
- [190] K. Laiho, T. Dirmeier, M. Schmidt, S. Reitzenstein, and C. Marquardt. Measuring higher-order photon correlations of faint quantum light: A short review. *Physics Letters A*, 435:128059, 2022.
- [191] J. Viana Gomes, A. Perrin, M. Schellekens, D. Boiron, C. I. Westbrook, and M. Belsley. Theory for a hanbury brown twiss experiment with a ballistically expanding cloud of cold atoms. *Phys. Rev. A*, 74:053607, Nov 2006.
- [192] L. Mathey, A. Vishwanath, and E. Altman. Noise correlations in low-dimensional systems of ultracold atoms. *Phys. Rev. A*, 79:013609, Jan 2009.
- [193] B. Yurke and M. Potasek. Obtainment of thermal noise from a pure quantum state. *Phys. Rev. A*, 36:3464–3466, Oct 1987.
- [194] Klaus Mølmer, A. Perrin, V. Krachmalnicoff, V. Leung, D. Boiron, A. Aspect, and C. I. Westbrook. Hanbury brown and twiss correlations in atoms scattered from colliding condensates. *Phys. Rev. A*, 77:033601, Mar 2008.
- [195] G.A. Athanassoulis and P.N. Gavriliadis. The truncated hausdorff moment problem solved by using kernel density functions. *Probabilistic Engineering Mechanics*, 17(3):273–291, 2002.
- [196] N. I. Akhiezer. *The Classical Moment Problem and Some Related Questions in Analysis*. Society for Industrial and Applied Mathematics, Philadelphia, PA, 2020.
- [197] Daniele Contessi, Alessio Recati, and Matteo Rizzi. Phase diagram detection via gaussian fitting of number probability distribution. *Phys. Rev. B*, 107:L121403, Mar 2023.
- [198] Gregg Jaeger. The ehrenfest classification of phase transitions: Introduction and evolution. *Archive for History of Exact Sciences*, 53(1):51–81, 1998.
- [199] Michael E. Fisher, Shang-keng Ma, and B. G. Nickel. Critical exponents for long-range interactions. *Phys. Rev. Lett.*, 29:917–920, Oct 1972.

- [200] J. C. Le Guillou and J. Zinn-Justin. Critical exponents from field theory. *Phys. Rev. B*, 21:3976–3998, May 1980.
- [201] N. Saratz, D. A. Zanin, U. Ramsperger, S. A. Cannas, D. Pescia, and A. Vindigni. Critical exponents and scaling invariance in the absence of a critical point. *Nature Communications*, 7(1):13611, 2016.
- [202] C. Voges and H. Pfnür. Experimental determination of the phase-transition critical exponents α and η by integrating methods. *Phys. Rev. B*, 57:3345–3355, Feb 1998.
- [203] C. M. Aegerter, M. Störzer, and G. Maret. Experimental determination of critical exponents in anderson localisation of light. *Europhysics Letters*, 75(4):562, jul 2006.
- [204] Hilbert v. Löhneysen, Achim Rosch, Matthias Vojta, and Peter Wölfle. Fermi-liquid instabilities at magnetic quantum phase transitions. *Rev. Mod. Phys.*, 79:1015–1075, Aug 2007.
- [205] J.M. Thijssen. *Computational Physics*. Cambridge University Press, New York, 2 edition, 2007.
- [206] Eduardo Ibarra-García-Padilla, Carlos Gerardo Malanche-Flores, and Freddy Jackson Poveda-Cuevas. The hobbyhorse of magnetic systems: the ising model. *European Journal of Physics*, 37(6):065103, sep 2016.
- [207] J. Goldstone. Field theories with «superconductor» solutions. *Il Nuovo Cimento (1955-1965)*, 19(1):154–164, 1961.
- [208] K. Binder. Finite size scaling analysis of ising model block distribution functions. *Zeitschrift für Physik B Condensed Matter*, 43(2):119–140, 1981.
- [209] K. Binder, M. Nauenberg, V. Privman, and A. P. Young. Finite-size tests of hyperscaling. *Phys. Rev. B*, 31:1498–1502, Feb 1985.
- [210] Hiroshi Watanabe, Yuichi Motoyama, Satoshi Morita, and Naoki Kawashima. Non-monotonic behavior of the Binder parameter in discrete spin systems. *Progress of Theoretical and Experimental Physics*, 2023(3):033A02, 02 2023.
- [211] Paulo H.L. Martins and Michael Bachmann. Binder cumulants and finite-size scaling for the adsorption transition of flexible polymers under different solvent conditions. *Physics Procedia*, 68:90–94, 2015. Proceedings of the 28th Workshop on Computer Simulation Studies in Condensed Matter Physics (CSP2015).
- [212] G. Palma and D. Zambrano. Cluster-algorithm renormalization-group study of universal fluctuations in the two-dimensional ising model. *Phys. Rev. E*, 78:061134, Dec 2008.
- [213] D.V. Schroeder. *An Introduction to Thermal Physics*. Addison Wesley, illustrated edition, 2000.
- [214] Vitaly V. Kocharovskiy, Vladimir V. Kocharovskiy, Martin Holthaus, C.H. Raymond Ooi, Anatoly Svidzinsky, Wolfgang Ketterle, and Marlan O. Scully. Fluctuations in ideal and interacting bose–einstein condensates: From the laser phase transition analogy to squeezed states and bogoliubov quasiparticles. volume 53 of *Advances In Atomic, Molecular, and Optical Physics*, pages 291–411. Academic Press, 2006.
- [215] Martin Holthaus, Eva Kalinowski, and Klaus Kirsten. Condensate fluctuations in trapped bose gases: Canonical vs. microcanonical ensemble. *Annals of Physics*, 270(1):198–230, 1998.

- [216] H. David Politzer. Condensate fluctuations of a trapped, ideal bose gas. *Phys. Rev. A*, 54:5048–5054, Dec 1996.
- [217] Patrick Navez, Dmitri Bitouk, Mariusz Gajda, Zbigniew Idziaszek, and Kazimierz Rzażewski. Fourth statistical ensemble for the bose-einstein condensate. *Phys. Rev. Lett.*, 79:1789–1792, Sep 1997.
- [218] Maciej Bartłomiej Kruk, Dawid Hryniuk, Mick Kristensen, Toke Vibel, Krzysztof Pawłowski, Jan Arlt, and Kazimierz Rzażewski. Microcanonical and canonical fluctuations in atomic Bose-Einstein condensates – Fock state sampling approach. *SciPost Phys.*, 14:036, 2023.
- [219] M. Gajdacz, A. J. Hilliard, M. A. Kristensen, P. L. Pedersen, C. Klempt, J. J. Arlt, and J. F. Sherson. Preparation of ultracold atom clouds at the shot noise level. *Phys. Rev. Lett.*, 117:073604, Aug 2016.
- [220] S. Giorgini, L. P. Pitaevskii, and S. Stringari. Anomalous fluctuations of the condensate in interacting bose gases. *Phys. Rev. Lett.*, 80(23):5040–5043, 1998.
- [221] F. Meier and W. Zwerger. Anomalous condensate fluctuations in strongly interacting superfluids. *Phys. Rev. A - At. Mol. Opt. Phys.*, 60(6):5133–5135, 1999.
- [222] W. Zwerger. Anomalous Fluctuations in Phases with a Broken Continuous Symmetry. *Phys. Rev. Lett.*, 92(2):4, 2004.
- [223] F. Gerbier. Ultracold quantum gases in optical lattices. Lecture Notes, <https://www.lkb.upmc.fr/boseeinsteincondensates/wp-content/uploads/sites/10/2018/03/cours9.pdf>, Mar 2018.
- [224] M. Kendall and A. Stuart. *The advanced theory of statistics*, volume 1: Distribution theory. Macmillan, New York, NY, 4th edition, 1977.